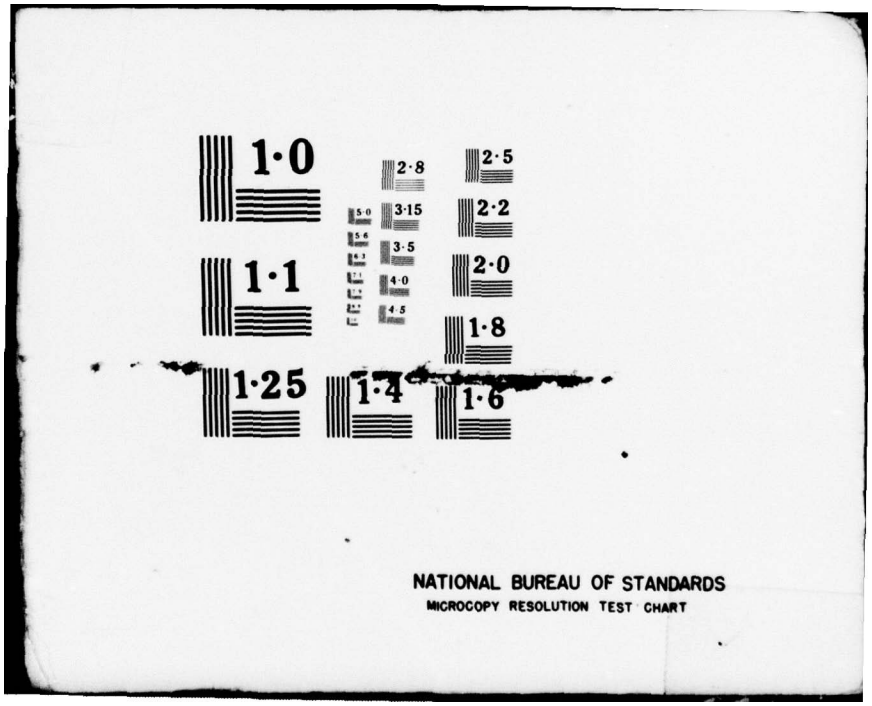
AD-A059 939 TERRA TEK INC SALT LAKE CITY UTAH F/G 18/3
MATERIAL PROPERTIES OF NEVADA TEST SITE TUFF AND GROUT--WITH EM--ETC(U)
NOV 77 D S GARDINER, D O ENNISS, S W BUTTERS DNA001-76-C-0351
UNCLASSIFIED TR-77-96 DNA-4528F NL

1 OF 3
ADA
059939




1·0
1·1
1·25
1·4
1·6
1·8
2·0
2·2
2·5
2·8
3·15
3·5
4·0
4·5
5·0
5·6
NATIONAL BUREAU OF STANDARDS
MICROCOPY RESOLUTION TEST CHART

AD-E300 343

(12) LEVEL II

DNA 4528F

AD A059939

MATERIAL PROPERTIES OF NEVADA TEST SITE TUFF AND GROUT—WITH EMPHASIS ON THE DIABLO HAWK AND HYBLA GOLD EVENTS

Terra Tek, Inc.
420 Wakara Way
Salt Lake City, Utah 84108

DDC FILE COPY

November 1977

Final Report for Period 1 August 1976—30 September 1977

CONTRACT No. DNA 001-76-C-0351

APPROVED FOR PUBLIC RELEASE;
DISTRIBUTION UNLIMITED.

THIS WORK SPONSORED BY THE DEFENSE NUCLEAR AGENCY
UNDER RDT&E RMSS CODE K400076462 J45GAXYX97308 H2590D.

Prepared for
Director
DEFENSE NUCLEAR AGENCY
Washington, D. C. 20305

DDC
RECEIVED
OCT 17 1978
B

78 08 31 001

Destroy this report when it is no longer needed. Do not return to sender.

PLEASE NOTIFY THE DEFENSE NUCLEAR AGENCY, ATTN: TISI, WASHINGTON, D.C. 20305, IF YOUR ADDRESS IS INCORRECT, IF YOU WISH TO BE DELETED FROM THE DISTRIBUTION LIST, OR IF THE ADDRESSEE IS NO LONGER EMPLOYED BY YOUR ORGANIZATION.



UNCLASSIFIED

SECURITY CLASSIFICATION OF THIS PAGE (When Data Entered)

(18) DNA, SBIE (19) 4528F, AD-E300 343

REPORT DOCUMENTATION PAGE

READ INSTRUCTIONS BEFORE COMPLETING FORM

1. REPORT NUMBER: DNA 4528F

2. GOVT ACCESSION NO.

3. RECIPIENT'S CATALOG NUMBER

4. TITLE (and Subtitle): (6) MATERIAL PROPERTIES OF NEVADA TEST SITE TUFF AND GROUT—WITH EMPHASIS ON THE DIABLO HAWK AND HYBLA GOLD EVENTS

5. TYPE OF REPORT & PERIOD COVERED: Final Report for Period 1 Aug 76—30 Sep 77

6. PERFORMING ORG. REPORT NUMBER: (14) TR-77-96

7. AUTHOR(s): (10) D. S. Gardiner, D. O. Enniss, S. W. Butters, A. H. Jones

8. CONTRACT OR GRANT NUMBER(s): (15) DNA 001-76-C-0351

9. PERFORMING ORGANIZATION NAME AND ADDRESS:
Terra Tek, Inc.
420 Wakara Way
Salt Lake City, Utah 84108

10. PROGRAM ELEMENT, PROJECT, TASK AREA & WORK UNIT NUMBERS: Subtask J45GAXYX973-08

11. CONTROLLING OFFICE NAME AND ADDRESS:
Director
Defense Nuclear Agency
Washington, D.C. 20305

12. REPORT DATE: (11) November 1977

13. NUMBER OF PAGES: 284

14. MONITORING AGENCY NAME & ADDRESS (if different from Controlling Office): (9) Final rept. 1 Aug 76–30 Sep 77,

15. SECURITY CLASS (of this report): UNCLASSIFIED

15a. DECLASSIFICATION DOWNGRADING SCHEDULE

16. DISTRIBUTION STATEMENT (of this Report):

Approved for public release; distribution unlimited.

(12) 273 pp

17. DISTRIBUTION STATEMENT (of the abstract entered in Block 20, if different from Report)

(16) J45GAXY (17) X973

18. SUPPLEMENTARY NOTES

This work sponsored by the Defense Nuclear Agency under RDT&E RMSS Code K400076462 J45GAXYX97308 H2590D.

19. KEY WORDS (Continue on reverse side if necessary and identify by block number)

Nuclear Test	Tuff
Hydrostatic	Grout
Uniaxial Strain	Pressure
Triaxial Compression	Load

20. ABSTRACT (Continue on reverse side if necessary and identify by block number)

Material properties testing has been conducted for the Defense Nuclear Agency Field Command. The testing was in support of the Nevada Test Site nuclear test program and covered the period 1 August 1976 through 30 September 1977. The contract number was DNA 001-76-C-0351 and Mr. J. W. LaComb was the Contracting Officer Representative.

next page →

DD FORM 1 JAN 73 1473 EDITION OF 1 NOV 65 IS OBSOLETE

UNCLASSIFIED

SECURITY CLASSIFICATION OF THIS PAGE (When Data Entered)

389 155

20. ABSTRACT (Continued)

The primary task during this period was material evaluations for the Diablo Hawk and Hybla Gold events. Tuff, grout, concrete, saturated sand and "reconstituted" tuff were tested. The material evaluations are used for initial nuclear test site selection, detailed site evaluation (for purposes of insuring successful stemming and containment) and support of related experiments. The majority of the tests were uniaxial strain tests with accompanying physical property and ultrasonic velocity measurements. Additionally, hydrostatic and triaxial compression, heat transfer, burst, and permeability tests were conducted.

PREFACE

The authors would like to express their thanks for the guidance of Mr. J. W. LaComb and to Mr. C. N. Snow for his assistance with geology and core samples. They would also like to thank Mr. T. Tibolla and Mr. M. Fisher for assistance in conducting the laboratory tests and to Ms. J. Grant and Ms. S. Stewart for the transcript preparation.

ACCESSION for
NTIS White Section
DDC Buff Section
UNANNOUNCED
JUSTIFICATION
BY
DISTRIBUTION/AVAILABILITY CODES
Dist. AVAIL. and/or SPECIAL
A

TABLE OF CONTENTS

	Page
Preface	1
Table of Contents	3
Introduction	5
Diablo Hawk Event	11
Containment Analysis	
Material Properties for Diablo Hawk Event	13
Material Properties of U12n.10A DNUG#5 Core Samples	71
Physical and Mechanical Properties of Diablo Hawk Tuff Matching Grout -- ME8-11	79
Structures Properties	
Some Material Properties of Diablo Hawk Tuff Associated With the TRW Experiment	85
Boeing Experiment	
Diablo Hawk Structures Tuff Material Properties -- Boeing Drift	87
High Pressure Mechanical Properties of Lapis Lustre Sand	119
Hybla Gold Event	121
Material Properties for the Hybla Gold Event	123
Material Properties of U12e.20 Tuff Overcores	195
Water and Air Permeability of Concrete from Hybla Gold Pipe	199
Material Properties for Cores from Exploratory Drill Hole U12n.11 UG#1	203
Mechanical Properties of Mighty Epic Grout (Postshot)	213

PRECEDING PAGE BLANK-NOT FILMED

Page

Residual Stress in Thick-Walled Cylinders of Ash-Fall Tuffs and Tuff Matching Grouts Subjected to Internal Pressurization . . . 219

High Temperature Gas Flow Tests on Reconstituted Tuff 233

Physical and Mechanical Properties of Reconstituted Tuff 257

Stanford Research Institute Grout 265

Material Properties of Stanford Research Institute Grout . . . 267

Material Properties of SRI Rock Matching Grout and Modified Granite Simulant 273

INTRODUCTION

Material properties of the containment media (tuff) and related construction materials associated with individual nuclear events at the Nevada Test Site is a vital part of the Defense Nuclear Agency (DNA) nuclear test program. Material properties are primarily needed for purposes of evaluating the potential for successful stemming and containment of the nuclear tests. They are also extensively used in material models designed to predict ground motion and wave propagation.

This report summarizes the materials testing program conducted by Terra Tek from August 1976 through September 1977 for DNA Test Command. The main function of the test program was material characterization for the Diablo Hawk and Hybla Gold events. Tuff, grout, concrete, and saturated sand were tested. Other material evaluations included measurement of mechanical and thermal flow properties of "reconstituted" tuff. During the contract period, reports were published upon completion of testing and distributed to designated agencies. This final report includes those reports plus some additional test data not yet distributed. A synopsis (in some cases, the abstract from the report) of the testing and analysis is provided as follows:

Diablo Hawk Event

The Diablo Hawk event is in the configuration of the new "two-for-one concept" where two separate nuclear tests are planned in the same main tunnel. Substantial cost savings will be incurred resulting from common use of support facilities. Material evaluation focused on structures area

tuff and grout noting the effects of the nearby Mighty Epic event. Additionally, media associated with the TRW and Boeing experiments were evaluated. The Boeing experiment also required extensive testing of saturated sand, the medium to be used in filling a portion of the Boeing drift.

Reports and letters describing the above work are:

- Containment Analysis

  Material Properties for Diablo Hawk Event (TR 77-43)

  Material Properties of U12n.10A DNUG#5 Core Samples

  Physical and Mechanical Properties of Diablo Hawk, Tuff Matching Grout -- ME8-11

- Structures Properties

  Some Material Properties of Diablo Hawk Tuff Associated with the TRW Experiment (TR 77-95)

- Boeing Experiment

  High Pressure Mechanical Properties of Lapis Lustre Sand (TR 77-70)

  Diablo Hawk Structures Tuff Material Properties -- Boeing Drift (TR 77-90)

Hybla Gold Event

The location of the forthcoming Hybla Gold event at the Nevada Test Site is unique in that it is located close to a previously executed nuclear test. Typical site characterization usually assumes that material properties are reasonably consistent and predictable within a given geological layer. This could not be assumed for the Hybla Gold event. The material (tuff) surrounding the Hybla Gold event had been subjected to shock waves from the previous Dining Car event. The magnitude of the shock waves is obviously

a function of distance from the Dining Car working point. Recent work completed by Terra Tek for the "two-for one" concept (multi use of common facilities) suggested, although no conclusions could be made because of a paucity of data, that material properties changes could result from shock loading or from cavity growth. In either case, it was necessary to characterize the Hybla Gold media as a function of location.

The media characterization included mechanical and physical properties. Comparisons are also drawn on the effects of the Dining Car event on the Hybla Gold media. Additionally, water and air permeability tests were conducted on pipe concrete, emplaced near the test site.

Reports and letters describing the work are:

- Some Material Properties for the Hybla Gold Event (TR 77-46)
- Material Properties of U12e.20 Tuff Overcores
- Water and Air Permeability of Concrete from Hybla Gold Pipe

Exploratory Drill Hole U12n.11 UG#1

Site exploration is an essential part of the nuclear test program at the Nevada Test Site. The constant need for new test sites dictates continual exploration. Exploratory drill holes are an economical means of determining site usability for a nuclear test prior to extending tunnels into an area.

Site potential can be determined by examining the material properties of exploratory drill hole cores and comparing results with data from previously tested sites. This report examines both the physical and mechanical properties in an effort to evaluate a particular area's potential as a future test site.

Mighty Epic Grout (Postshot)

Samples of Mighty Epic grout from U12n.10 A, B and C drifts were tested (postshot) for physical and mechanical properties. The properties were used to compare with those of preshot grout.

Mechanical tests were performed to determine the longitudinal and shear wave velocities and uniaxial strain response. The physical properties measured were the as-received density, grain density, and percent water by wet weight. Calculated properties were dry density, porosity, saturation and air void content.

Residual Stress in Thick-Walled Cylinders of Ash-Fall Tuffs and Tuff Matching Grouts Subjected to Internal Pressurization

Field measurements and calculations indicate that the rock material surrounding a postshot cavity is noticeably strengthened by the event. It is thought that this strengthening results from the presence of residual stresses. To investigate this possibility, internal pressurization tests on thick-walled tuff and tuff-matching grout cylinders were conducted to determine whether residual stresses can exist. The report presents the experimental techniques and test results.

Properties of Reconstituted Tuff

In light of the fact that nuclear tests are being located closer together, it is becoming increasingly important to characterize the highly fractured material ("chimney" material) near previous test sites. Material property tests were therefore conducted on tuff material that was crushed and/or pulverized and recompacted to densities commonly seen in such materials in the field. Tests included the measurement of physical, mechanical and thermal flow properties of tuffs of varying particle sizes.

Reports describing the data are:

- Thermal Flow Properties of Crushed Tuff (TR 77-48)
- Physical and Mechanical Properties of Reconstituted Tuff (TR 77-94)

Stanford Research Institute Grout

Stanford Research Institute conducts experiments in support of the DNA test program. Commonly, these experiments involve the use of tuff-matching grout. Mechanical and physical properties of these grouts are determined by Terra Tek to verify the grout properties and to provide data required for predictive calculations. Tests conducted during this contract year are described in:

- Material Properties of Stanford Research Institute Grout (TR 76-41)
- Material Properties of SRI Rock Matching Grout and Modified Granite Simulant

DIABLO HAWK EVENT

Containment Analysis

Material Properties for Diablo Hawk Event

Material Properties of U12n.10A DNUG#5 Core Samples

Physical and Mechanical Properties of Diablo Hawk Tuff Matching Grout -- ME8-11

Structures Properties

Some Material Properties of Diablo Hawk Tuff Associated with the TRW Experiment

Boeing Experiment

Diablo Hawk Structures Tuff Material Properties -- Boeing Drift

High Pressure Mechanical Properties of Lapis Lustre Sand

PRECEDING PAGE BLANK-NOT FILMED

MATERIAL PROPERTIES FOR DIABLO HAWK EVENT

TR 77-43
June 1977

PRECEDING PAGE BLANK-NOT FILMED

TABLE OF CONTENTS

	Page
Table of Contents	14
List of Illustrations	15
List of Tables	20
Introduction	21
Section 1 - U12n.10A Horizontal Drill Hole Summary	22
Section 2 - UE12n#10 Vertical Drill Hole Summary	27
Section 3 - U12n.10A Overcore Summary	29
Section 4 - U12n.10A "N Tunnel" Bypass Drift Superlean Grout Summary	36
References	40
Appendix A - Uniaxial Strain Curves for U12n.10A Drill Holes	41
Appendix B - Uniaxial Strain Curves for UE12n#10 Vertical Drill Hole	64

LIST OF ILLUSTRATIONS

Figure	Description	Page
1-1	Location of drill holes in Diablo Hawk area	22
1-2	Measured permanent compaction of selected drill holes	24
1-3a	Cycled uniaxial strain test on U12n.10A LLCI#1 core samples--mean normal stress versus volume change	26
1-3b	Cycled uniaxial strain test on U12n.10A LLCI#1 core samples--stress difference versus confining pressure	26
2-1	Plan view of Diablo Hawk area showing the UE12n#10 drill hole from which core samples have been tested.	27
2-2	Comparison of UE12n#10 measured permanent compaction values--measured permanent compaction versus drill hole footage	28
3-1	Triaxial compression stress-strain curves for ISS#31-2 overcore samples	31
3-2	Triaxial compression stress-strain curves for ISS#32-1 overcore samples	31
3-3	Triaxial compression stress-strain curves for ISS#33-2 overcore samples	32
3-4	Triaxial compression stress-strain curves for ISS#34-3 overcore samples	32
3-5	Triaxial compression stress-strain curves for GSIS#6 overcore samples	33
3-6	Triaxial compression stress-strain curves for GSIS#6 overcore samples	33
3-7	Failure envelopes for ISS#31-34 overcores--stress difference versus confining pressure	34
3-8	Failure envelopes for GSIS#6 overcores--stress difference versus confining pressure	35
4-1	Triaxial compression stress-strain curves for U12n.10A "N Tunnel" bypass superlean grout	38

Figure	Description	Page
4-2a	Uniaxial strain tests on U12n.10A "N Tunnel" bypass drift superlean grout--mean normal stress versus volume change	39
4-2b	Uniaxial strain tests on U12n.10A "N Tunnel" bypass drift superlean grout--stress difference versus confining pressure	39
A-1a	Uniaxial strain tests on U12n.10A GSCH#1 core samples--mean normal stress versus volume change	42
A-1b	Uniaxial strain tests on U12n.10A GSCH#1 core samples--stress difference versus confining pressure	42
A-2a	Uniaxial strain tests on U12n.10A GSCH#1 core samples--mean normal stress versus volume change	43
A-2b	Uniaxial strain tests on U12n.10A GSCH#1 core samples--stress difference versus confining pressure	43
A-3a	Uniaxial strain tests on U12n.10A GSCH#1 core samples--mean normal stress versus volume change	44
A-3b	Uniaxial strain tests on U12n.10A GSCH#1 core samples--stress difference versus confining pressure	44
A-4a	Uniaxial strain tests on U12n.10A GSCH#1 core samples--mean normal stress versus volume change	45
A-4b	Uniaxial strain tests on U12n.10A GSCH#1 core samples--stress difference versus confining pressure	45
A-5a	Uniaxial strain tests on U12n.10A GSCH#2 core samples--mean normal stress versus volume change	46
A-5b	Uniaxial strain tests on U12n.10A GSCH#2 core samples--stress difference versus confining pressure	46
A-6a	Uniaxial strain tests on U12n.10A GSCH#2 core samples--mean normal stress versus volume change	47
A-6b	Uniaxial strain tests on U12n.10A GSCH#2 core samples--stress difference versus confining pressure	47
A-7a	Uniaxial strain tests on U12n.10A GSCH#3 core samples--mean normal stress versus volume change	48
A-7b	Uniaxial strain tests on U12n.10A GSCH#3 core samples--stress difference versus confining pressure	48

Figure	Description	Page
A-8a	Uniaxial strain tests on U12n.10A GSCH#3 core samples--mean normal stress versus volume change	49
A-8b	Uniaxial strain tests on U12n.10A GSCH#3 core samples--stress difference versus confining pressure	49
A-9a	Uniaxial strain tests on U12n.10A GSCH#3 core samples--mean normal stress versus volume change	50
A-9b	Uniaxial strain tests on U12n.10A GSCH#3 core samples--stress difference versus confining pressure	50
A-10a	Uniaxial strain tests on U12n.10A GSCH#4 core samples--mean normal stress versus volume change	51
A-10b	Uniaxial strain tests on U12n.10A GSCH#4 core samples--stress difference versus confining pressure	51
A-11a	Uniaxial strain tests on U12n.10A GSCH#4 core samples--mean normal stress versus volume change	52
A-11b	Uniaxial strain tests on U12n.10A GSCH#4 core samples--stress difference versus confining pressure	52
A-12a	Uniaxial strain tests on U12n.10A GSHF#3 core samples--mean normal stress versus volume change	53
A-12b	Uniaxial strain tests on U12n.10A GSHF#3 core samples--stress difference versus confining pressure	53
A-13a	Uniaxial strain tests on U12n.10A GSHF#4 core samples--mean normal stress versus volume change	54
A-13b	Uniaxial strain tests on U12n.10A GSHF#4 core samples--stress difference versus confining pressure	54
A-14a	Uniaxial strain tests on U12n.10A GSHF#4 core samples--mean normal stress versus volume change	55
A-14b	Uniaxial strain tests on U12n.10A GSHF#4 core samples--stress difference versus confining pressure	55
A-15a	Uniaxial strain tests on U12n.10A GSHF#6,8,9 core samples--mean normal stress versus volume change . .	56
A-15b	Uniaxial strain tests on U12n.10A GSHF#6,8,9 core samples--stress difference versus confining pressure	56

Figure	Description	Page
A-16a	Uniaxial strain tests on U12n.10A LLCI#1 core samples--mean normal stress versus volume change	57
A-16b	Uniaxial strain tests on U12n.10A LLCI#1 core samples--stress difference versus confining pressure	57
A-17a	Uniaxial strain tests on U12n.10A DNRE#1 core samples--mean normal stress versus volume change	58
A-17b	Uniaxial strain tests on U12n.10A DNRE#1 core samples--stress difference versus confining pressure	58
A-18a	Uniaxial strain tests on U12n.10A DNHF#3 core samples--mean normal stress versus volume change	59
A-18b	Uniaxial strain tests on U12n.10A DNHF#3 core samples--stress difference versus confining pressure	59
A-19a	Uniaxial strain tests on U12n.10A DNHF#3 core samples--mean normal stress versus volume change	60
A-19b	Uniaxial strain tests on U12n.10A DNHF#3 core samples--stress difference versus confining pressure	60
A-20a	Uniaxial strain tests on U12n.10A DNHF#3 core samples--mean normal stress versus volume change	61
A-20b	Uniaxial strain tests on U12n.10A DNHF#3 core samples--stress difference versus confining pressure	61
A-21a	Uniaxial strain tests on U12n.10A DNHF#3 core samples--mean normal stress versus volume change	62
A-21b	Uniaxial strain tests on U12n.10A DNHF#3 core samples--stress difference versus confining pressure	62
A-22a	Uniaxial strain tests on U12n.10A DNRE#2, IFRE#2, DNHF#3 core samples--mean normal stress versus volume change	63
A-22b	Uniaxial strain tests on U12n.10A DNRE#2, IFRE#2, DNHF#3 core samples--stress difference versus confining pressure	63
B-1a	Uniaxial strain tests on UE12n#10 core samples--mean normal stress versus volume change	65
B-1b	Uniaxial strain tests on UE12n#10 core samples--stress difference versus confining pressure	65

Figure	Description	Page
B-2a	Uniaxial strain tests on UE12n#10 core samples--mean normal stress versus volume change	66
B-2b	Uniaxial strain tests on UE12n#10 core samples--stress difference versus confining pressure	66
B-3a	Uniaxial strain tests on UE12n#10 core samples--mean normal stress versus volume change	67
B-3b	Uniaxial strain tests on UE12n#10 core samples--stress difference versus confining pressure	67
B-4a	Uniaxial strain tests on UE12n#10 core samples--mean normal stress versus volume change	68
B-4b	Uniaxial strain tests on UE12n#10 core samples--stress difference versus confining pressure	68
B-5a	Uniaxial strain tests on UE12n#10 core samples--mean normal stress versus volume change	69
B-5b	Uniaxial strain tests on UE12n#10 core samples--stress difference versus confining pressure	69

LIST OF TABLES

Table	Description	Page
1-1	Physical Properties, Uniaxial Strain Permanent Volume Compaction and Ultrasonic Wave Velocities on Individual Tuff Samples Tested	23
2-1	Physical Properties, Uniaxial Strain Permanent Volume Compaction and Ultrasonic Wave Velocities of UE12n#10 Tuffs	28
3-1	Young's Moduli and Poisson's Ratios from Triaxial Compression	30
3-2	Physical Properties and Ultrasonic Velocities of U12n.10A Overcores	30
4-1	Physical Properties, Uniaxial Strain Permanent Volume Compaction and Ultrasonic Wave Velocities of U12n.10A Superlean Grouts	37

INTRODUCTION

The Diablo Hawk event at the Nevada Test Site is a test of a new concept -- the two in one concept -- where two separate nuclear tests are planned in the same main tunnel, U12n.10. Ground zero for Diablo Hawk is located in the main horizontal drift, 500 feet to the portal side of a previously executed nuclear test, Mighty Epic. Since this is a new concept, a more thorough characterization is required for stemming and containment than had been provided for past events. Material properties were determined in all directions from the Diablo Hawk working point to better assess material changes detrimental to successful stemming and containment that resulted from the Mighty Epic event.

Characterization in the horizontal plane of the working point was provided by testing cores from 14 short horizontal and vertical drill holes. The vertical drill hole--UE12n#10-- provided core samples for testing from above and below the working point. Triaxial compression tests were conducted on "N tunnel" bypass grout as well as tuff overcores. The data are presented separately:

Section 1 Horizontal U12n.10A Drill Holes

Section 2 Vertical UE12n#10 Drill Hole

Section 3 Overcore

Section 4 Grout

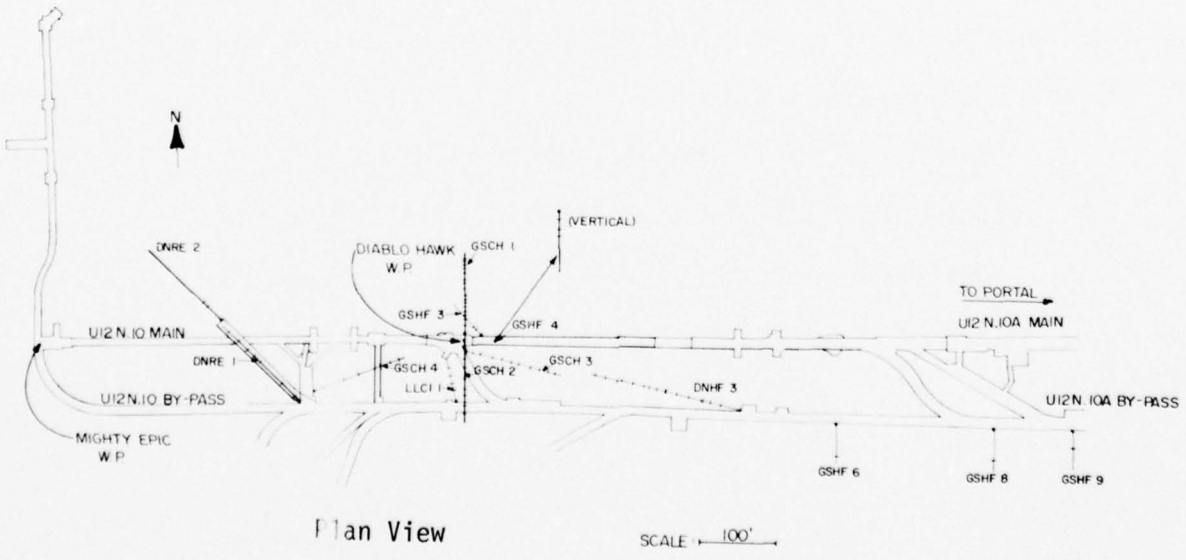
SECTION 1

U12n.10A HORIZONTAL DRILL HOLE SUMMARY

Several horizontal drill holes were emplaced from the U12n.10 main and bypass drifts in tunnel bed three ear the Diablo Hawk working point as shown in Figure 1-1. Material testing has been conducted on ash-fall tuff cores from the following drill holes:

GSCH 1	LLCI 1
GSCH 2	DNRE 1
GSCH 3	DNRE 2
GSCH 4	DNHF 3
GSHF 3	IFRE 2
GSHF 4	
GSHF 6,8,9	

Physical properties, uniaxial strain measured permanent compaction, and ultrasonic velocities are listed in Table 1-1. Figure 1-2 shows plots of uniaxial strain measured permanent compaction versus drill hole footage for select dril holes. Curves showing the uniaxial strain test



Plan View

Figure 1-1. Location of drill holes in Diablo Hawk area. (Small cross marks note the location from which core samples were received and tested)

TABLE 1-1

Physical Properties, Uniaxial Strain Permanent Volume Compaction and Ultrasonic Wave Velocities on Individual Tuff Samples Tested

DRILL HOLE/ FOOTAGE		DENSITY (gm/cc)			WATER BY WET WEIGHT (%)	POROSITY (%)	SATURATION (%)	CALC AIR VOIDS (%)	MEAS PERMANENT COMP (%)	VELOCITY (km/sec)	
		AS-RECEIVED	DRY	GRAIN						LONG	SHEAR
GSCH 1	12	1.74	1.36	2.40	22.0	43.4	88.0	5.2	4.4	1.86	1.30
	19	1.72	1.37	2.43	20.6	43.7	81.3	8.2	---	2.62	1.21
	24	1.78	1.35	2.41	24.3	44.2	97.4	1.2	1.3	2.46	1.24
	30	1.80	1.39	2.37	22.8	41.3	99.1	0.4	1.9	2.64	1.36
	35	1.86	1.50	2.40	19.8	37.8	97.3	1.0	0.7	3.11	1.65
	41	1.87	1.51	2.39	19.4	36.9	98.5	0.6	0.8	2.47	1.16
	44	1.92	1.57	2.40	18.1	34.6	100.0	0	0.3	2.99	1.61
	50	1.70	1.26	2.38	25.9	47.0	93.7	3.0	4.9	2.71	1.42
	59	1.85	1.51	2.43	18.2	37.6	89.7	3.9	4.0	2.66	1.43
	66	1.71	1.34	2.43	21.7	44.8	83.1	7.6	7.6	3.71	1.95
	71	1.85	1.55	2.43	16.2	36.3	82.6	6.3	6.2	1.40	0.83
	79	1.76	1.36	2.42	22.5	43.7	90.6	4.1	2.7	2.21	1.31
	85	1.73	1.37	2.41	20.6	43.0	83.0	7.4	6.5	1.74	0.99
	90	1.66	1.33	2.44	19.8	45.5	72.1	12.7	8.2	2.61	1.46
	95	1.83	1.43	2.42	21.5	40.6	96.9	1.2	0.6	2.42	1.25
	97	1.87	1.56	2.41	16.3	35.1	86.5	4.8	6.2	2.54	1.27
GSCH 2	12	1.86	1.63	2.49	17.0	34.5	97.0	1.0	1.3	2.67	1.28
	25	1.93	1.60	2.54	17.4	37.1	90.7	3.4	0.5	2.52	1.13
	35	1.82	1.42	2.46	22.1	42.3	94.5	2.3	0.7	2.84	1.39
	49	1.85	1.48	2.44	20.0	39.3	94.2	2.3	2.1	3.09	1.63
	65	1.96	1.62	2.52	17.5	35.8	95.6	1.6	1.4	3.01	1.52
	73	1.89	1.54	2.42	18.2	36.3	94.2	2.1	4.4	2.49	1.18
	85	1.84	1.45	2.45	21.1	40.7	95.5	1.8	4.2	2.65	1.12
	96	1.96	1.62	2.49	17.4	35.0	97.3	1.0	0.8	2.87	1.23
GSCH 3	11	1.97	1.64	2.45	16.6	32.9	99.3	0.2	---	3.65	2.05
	22	1.98	1.65	2.52	16.7	34.7	95.1	1.7	0.6	2.86	1.37
	37	1.93	1.59	2.47	17.8	35.8	96.0	1.4	0.7	2.84	1.43
	50	1.88	1.51	2.40	19.6	37.1	99.2	0.3	1.9	3.15	1.54
	62	1.82	1.44	2.46	21.0	41.4	92.0	3.3	1.9	3.05	1.59
	72	1.89	1.50	2.44	19.6	37.8	97.7	0.9	0.3	2.66	1.34
	88	1.95	1.62	2.46	17.0	34.4	95.9	1.4	0.6	2.75	1.38
	101	1.93	1.59	2.48	17.8	35.9	95.5	1.6	0.5	2.90	1.43
	113	1.97	1.64	2.49	16.8	34.1	97.0	1.0	1.2	2.71	1.31
	122	1.92	1.58	2.48	17.7	36.0	94.3	2.1	0.8	2.70	1.28
GSCH 4	12	1.83	1.46	2.42	20.2	39.7	93.2	2.7	0.8	2.62	1.31
	41	1.91	1.60	2.41	16.2	33.5	92.5	2.5	0.2	3.49	1.99
	63	1.79	1.38	2.42	23.1	43.1	96.1	1.7	0.7	2.67	1.34
	93	1.93	1.65	2.35	14.8	30.0	95.7	1.3	0.2	3.33	1.82
	106	1.76	1.39	2.43	21.3	43.1	87.1	5.6	5.2	1.56	0.90
	118	1.89	1.52	2.45	19.7	38.2	97.7	0.9	0.9	2.97	1.77
GSHF 3	10	1.83	1.45	2.44	20.7	40.6	93.4	2.7	3.2	2.51	1.39
	15	1.83	1.45	2.44	20.6	40.3	93.4	2.7	1.5	2.56	1.15
GSHF 4	10	1.83	1.44	2.42	21.4	40.5	96.5	1.4	1.3	2.58	1.23
	15	1.87	1.52	2.43	18.7	37.2	94.0	2.2	2.1	2.86	1.37
	20	1.90	1.55	2.40	18.1	35.4	96.7	1.2	1.1	2.76	1.40
	24	1.70	1.30	2.43	23.9	46.7	87.1	6.0	4.0	1.63	0.93
	32	1.75	1.38	2.39	21.0	42.3	87.0	5.5	5.4	1.97	1.29
	35	1.78	1.41	2.44	20.9	42.4	87.7	5.2	5.7	2.25	0.89
	41	1.78	1.36	2.44	23.7	44.3	95.3	2.1	1.3	2.60	1.28
	48	1.93	1.59	2.42	18.0	34.6	100.0	0	0.5	2.51	1.27
GSHF 6	42	1.86	1.50	2.46	19.3	39.0	92.1	3.1	2.6	2.36	1.33
	8 41	1.74	1.28	2.41	26.1	46.9	96.7	1.6	0.5	2.00	1.15
	9 23	1.72	1.26	2.38	26.9	47.2	98.3	0.8	1.2	2.99	1.87
LLCI 1	15	1.90	1.52	2.52	20.1	39.7	96.1	1.5	0.9	2.56	1.16
	16	1.91	1.54	2.46	19.6	37.5	99.9	0.1	---	3.36	1.28
	25	1.90	1.54	2.49	19.0	38.2	94.6	2.1	1.0	2.55	1.03
	35	1.91	1.56	2.46	18.5	36.6	96.6	1.6	1.6	2.58	1.24
	46	1.92	1.60	2.42	17.0	34.1	95.8	1.4	0.5	3.08	1.72
DNRE 1	10	1.89	1.55	2.41	17.9	35.5	95.6	1.6	0.6	2.89	1.58
	32	1.94	1.64	2.42	15.7	32.3	94.4	1.8	1.5	2.43	1.55
	73	1.93	1.60	2.45	17.2	34.8	95.2	1.7	0.3	3.03	1.58
	83	1.92	1.58	2.44	17.6	35.3	95.7	1.5	0.4	2.89	1.55
	95	1.89	1.52	2.48	19.5	38.7	95.2	1.7	---	----	----
	112	1.91	1.57	2.44	18.0	35.8	96.3	1.3	1.5	2.08	1.86
	128	1.89	1.52	2.47	19.5	38.6	95.4	1.8	0.7	2.90	1.34
DNHF 3	25	1.90	1.55	2.44	18.6	36.5	96.7	1.2	2.8	2.29	1.01
	40	1.88	1.52	2.50	19.4	39.3	93.0	2.8	1.1	2.73	1.25
	49	1.94	1.67	2.45	14.2	31.9	86.5	4.3	2.5	3.71	1.83
	58	1.74	1.30	2.46	25.1	46.9	93.3	3.1	4.4	3.75	2.08
	69	1.84	1.44	2.47	21.5	41.5	95.4	1.9	3.0	2.77	1.32
	84	1.86	1.47	2.44	20.8	39.6	97.6	1.0	2.1	2.93	1.52
	100	2.00	1.70	2.45	14.9	30.4	97.8	0.7	0.3	3.81	2.11
	112	1.85	1.54	2.47	17.1	37.8	83.7	6.2	6.0	----	----
	122	1.85	1.47	2.46	20.4	40.1	94.1	2.4	2.5	2.85	1.66
	130	1.79	1.37	2.45	23.8	44.2	96.4	1.6	2.7	4.13	2.36
	144	2.01	1.69	2.54	15.8	33.5	95.1	1.6	3.0	2.96	1.36
	158	1.99	1.65	2.53	17.0	34.8	97.2	1.0	0.5	2.92	1.35
	165	1.99	1.65	2.53	17.0	34.7	92.2	1.0	0.4	2.99	1.36
	181	1.91	1.57	2.44	17.7	35.8	94.4	2.0	0.7	3.03	1.63
	194	1.99	1.70	2.45	14.3	30.5	92.8	2.2	1.0	3.46	2.02
DNRE 2	24	1.89	1.52	2.50	19.7	39.2	94.8	2.0	2.0	1.99	1.22
	33	2.11	----	----	----	----	----	---	0.1	3.83	1.94
IFRE 2	8	1.96	1.61	2.48	17.1	35.0	95.0	1.7	1.0	2.65	1.63

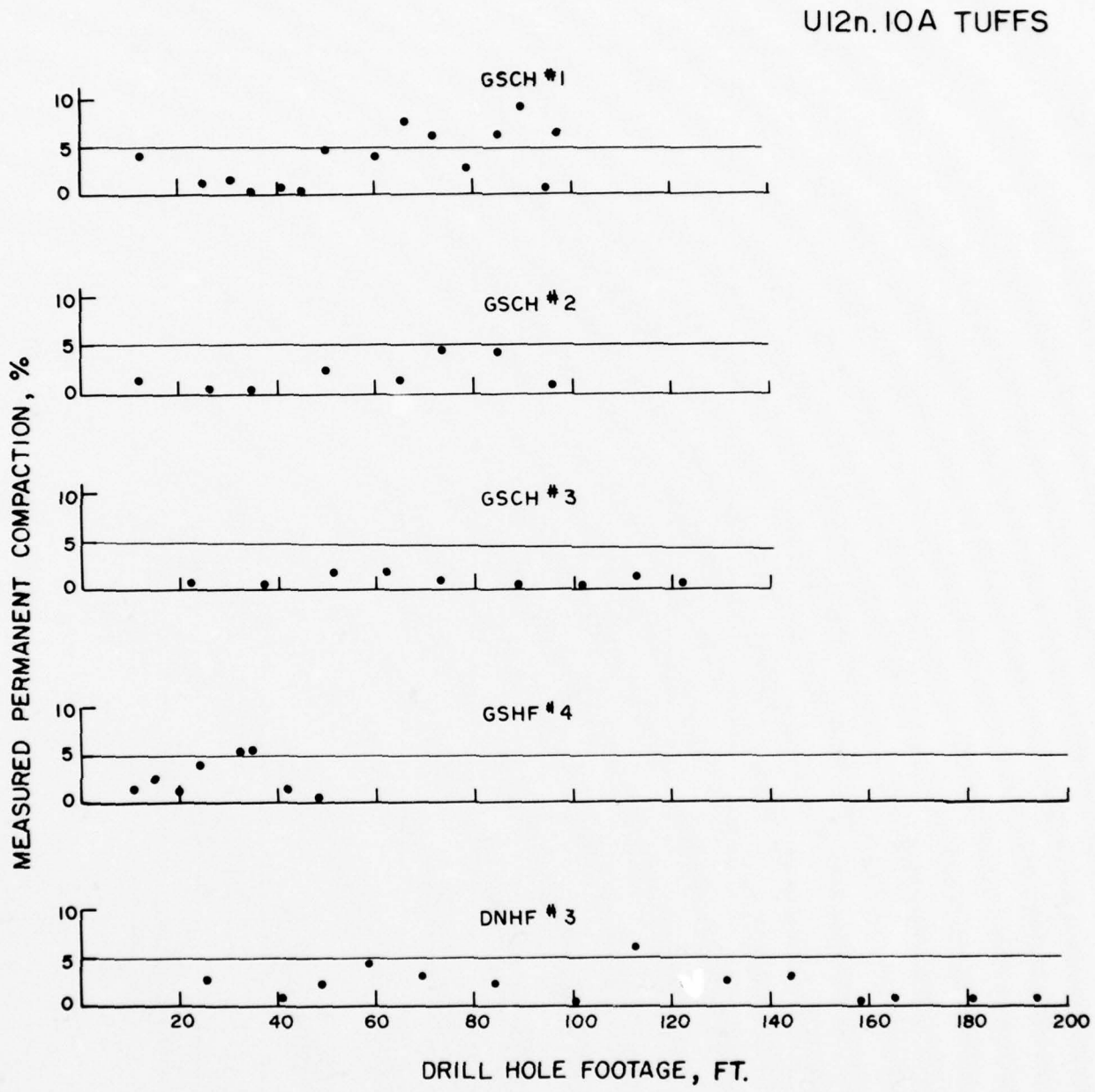


Figure 1-2. Measured permanent compaction of selected drill holes.

results--mean normal stress versus volume change and stress difference versus confining pressure--are contained in Appendix A.

Material properties surrounding the U12n.10A working point show a nearly saturated tuff with scattered areas of high air void contents (i.e. over 2 percent). This trend was also seen in nearby U12n.10 UG#1, 2, and 3 drill holes previously examined by Terra Tek[1]. These high air voids, in most cases, can be identified as a function of lithological beds. GSCH#1 and #2 drill holes at the 50 to 100 foot depths, GSHF#4 drill hole at 20 and 40 feet and drill hole DNHF#4 along most of its length are such areas showing above average air void content.

Cycled Uniaxial Strain Tests

Since the Diablo Hawk working point is close to Mighty Epic ground zero, shock wave loading effects on the site were of interest. In order to recognize those effects, it was decided to compare the mechanical response of postshot tuffs to the response shown in the second cycle of a cycled uniaxial strain test.

One might expect that uniaxial strain tests on postshot tuff would produce results similar to the second cycle of a cycled uniaxial strain test. Specified core footages were therefore subjected to cycled uniaxial strain tests to 4 kbars. A typical 2 cycle uniaxial strain test is shown in Figure 1-3. Note that the second cycle load and unload paths follow the unload path of the first cycle contributing no additional volume strain. Also note that the stress difference is significantly lower during the second cycle for confining pressures less than 4 kbars. This shallow failure curve could be a means of recognizing areas subjected to previous loading (i.e. media surrounding a past event).

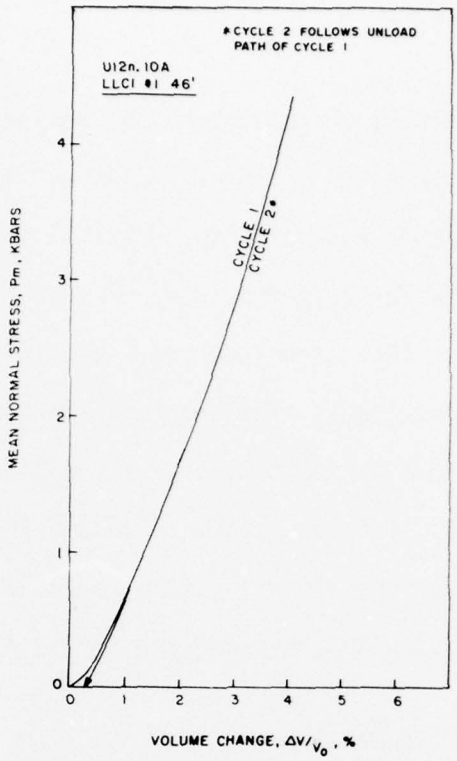


Figure 1-3a. Cycled uniaxial strain test on U12n.10A LLCI#1 core samples--mean normal stress versus volume change.

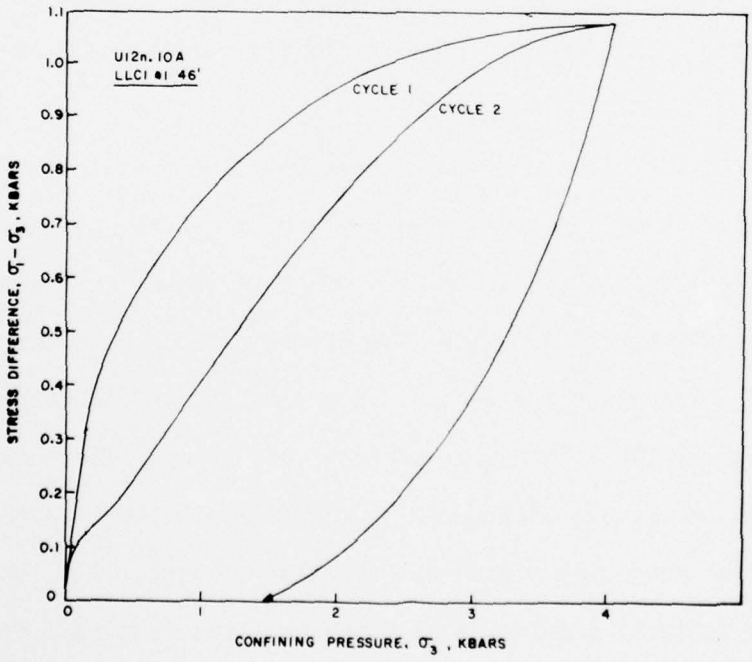


Figure 1-3b. Cycled uniaxial strain test on U12n.10A LLCI#1 core samples--stress difference versus confining pressure.

SECTION 2

UE12n#10 VERTICAL DRILL HOLE SUMMARY

Ash-fall tuff core samples from vertical drill hole UE12n#10 were subjected to uniaxial strain tests, physical property and ultrasonic velocity measurements. The drill hole is located approximately 1000 feet northeast of the working point (see Figure 2-1). Core samples were tested from between 1195 feet through 1417 feet (as measured from the Mesa surface) in approximately 12-foot increments. This range was selected to supply data approximately 100 feet above and 100 feet below the working point.

Physical property and ultrasonic longitudinal and shear wave velocity measurements are listed in Table 2-1. Figure 2-2 is a plot of permanent volume compaction versus drill hole footage for each sample tested. The uniaxial strain test curves are shown in Appendix B.

The data show a nearly saturated tuff with scattered areas of high air void content. A region above the main tunnel elevation (between 1195 through 1241 foot depths) is such an area with air void contents over 2 percent.

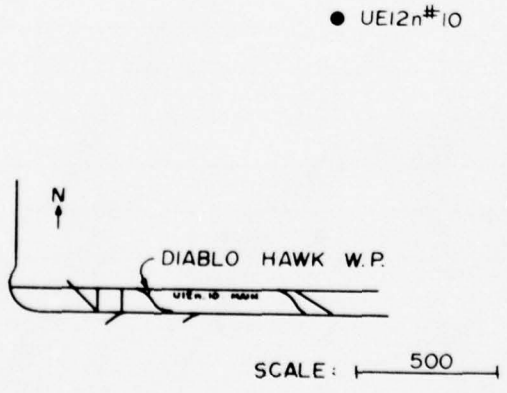


Figure 2-1. Plan view of Diablo Hawk area showing the UE12n#10 drill hole from which core samples have been tested.

TABLE 2-1

Physcial Properties, Uniaxial Strain Permanent Volume Compaction and Ultrasonic Wave Velocities of UE12n#10 Tuffs

DRILL HOLE FOOTAGE	DENSITY (gm/cc)			WATER BY WET WEIGHT (%)	POROSITY (%)	SATURATION (%)	CALC AIR VOIDS (%)	MEAS. PERMANENT COMP. (%)	VELOCITY (km/sec)	
	AS-RECEIVED	DRY	GRAIN						LONG	SHEAR
1195	1.91	1.57	2.47	18.0	36.6	94.0	2.2	1.3	2.86	1.46
1207	1.79	1.42	2.50	20.8	43.3	86.0	6.0	3.6	2.45	1.37
1217	1.69	1.23	2.46	27.1	49.9	91.7	4.1	2.3	2.19	1.25
1230	1.93	1.66	2.41	14.0	31.1	86.8	4.1	4.3	3.06	1.66
1241	1.81	1.47	2.40	18.6	38.6	87.2	4.9	1.0	2.30	1.21
1252	2.00	1.77	2.36	11.6	25.1	92.5	1.8	0.8	3.67	1.82
1265	1.77	1.31	2.45	26.1	46.5	99.1	0.4	2.4	2.93	1.63
1277	1.84	1.46	2.50	20.6	41.5	91.4	3.5	0.6	2.57	1.32
1290	1.79	1.38	2.46	23.1	43.9	93.9	2.7	0.4	2.34	1.06
1298	1.90	1.59	2.40	16.4	33.8	91.8	2.8	0.5	3.51	1.77
1313	1.79	1.36	2.50	24.2	45.7	94.5	2.5	---	2.24	0.97
1325	1.83	1.41	2.54	23.1	44.6	95.0	2.2	1.2	1.96	1.02
1336	1.75	1.32	2.38	24.7	44.5	97.0	1.3	1.2	2.45	1.38
1348	1.79	1.36	2.45	23.8	44.3	96.1	1.7	3.3	2.44	1.11
1360	1.77	1.39	2.44	21.5	43.0	88.3	5.0	1.3	2.54	1.24
1373	1.75	1.30	2.42	25.6	46.1	97.1	1.3	1.5	2.43	1.04
1384	1.76	1.29	2.44	26.5	47.0	99.3	0.3	1.3	1.91	0.99
1395	1.73	1.30	2.40	24.9	45.9	93.9	2.8	1.0	2.62	1.33
1406	1.83	1.44	2.44	21.6	41.1	96.1	1.6	2.0	2.50	1.21
1417	1.79	1.38	2.44	23.2	43.7	95.0	2.2	0.9	2.96	1.48

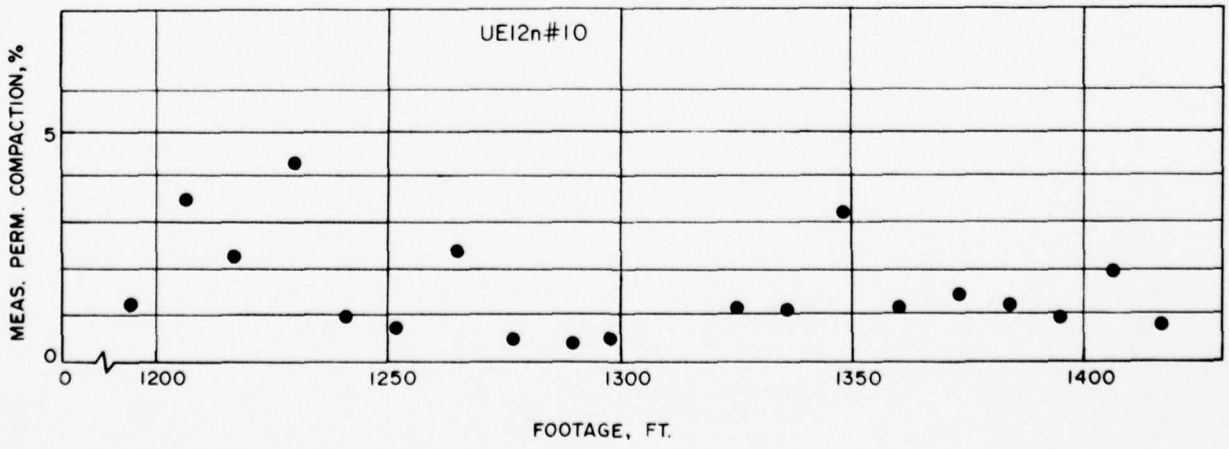


Figure 2-2. Comparison of UE12n#10 measured permanent compaction values--measured permanent compaction versus drill hole footage.

SECTION 3

U12n.10A OVERCORE SUMMARY

Triaxial compression tests were conducted on test samples from the following overcores

GSIS#6
ISS#31
ISS#32
ISS#33
ISS#34

in order to determine the elastic moduli for use by USGS (Special Projects, Denver, Colorado) in evaluating *in situ* stresses[2] These tests were performed at three confining pressures, 1 bar (unconfined), 34.5 bars (500 psi), and 69 bars (1000 psi). The Young's moduli and Poisson's ratios obtained are listed in Table 3-1. Individual stress-strain curves are shown in Figures 3-1 through 3-6. Failure envelopes deduced from the tests are shown in Figures 3-7 and 3-8. Physical properties are listed in Table 3-2.

Both Young's modulus and Poisson's ratio values were scaled from the linear elastic region. For the unconfined compression tests, this was immediately after the initial non-linear stress-strain region associated with microcrack closure. Results showed 140 percent increase in Young's moduli for ISS overcores when confined to 34.5 and 69.0 bars. Young's moduli for GSIS overcores increased approximately 200 and 300 percent for the same respective confining pressures. Poisson's ratios increased only moderately from approximately 0.2 to 0.3 with increased confining pressure for both ISS and GSIS overcores.

TABLE 3-1

Young's Moduli and Poisson's Ratios from Triaxial Compression

Drill Hole/Sample		σ_3 = 1 BAR		σ_3 = 34.5 BARS		σ_3 = 69.0 BARS	
		E(KB)	ν *	E(KB)	ν	E(KB)	ν
ISS#31	#2	30	0.09 ± .01	43	0.28 ± .15	45	0.22 ± .09
ISS#32	#1	19	0.20 ± .03	28	0.24 ± .02	36	0.20 ± .02
ISS#33	#2	58	0.26 ± .13	86	0.17 ± .01	82	0.35 ± .05
ISS#34	#3	19	0.20 ± .03	25	0.32 ± .02	27	0.29 ± .01
GSIS#6	24'	7	0.22 ± .05	13	0.30 ± .04	22	0.26 ± .04
GSIS#6	28'	-	---	14	0.28 ± .01	22	0.28 ± .01

* Poisson's ratios are from an average of two transverse strain measurements.

TABLE 3-2

Physical Properties and Ultrasonic Velocities of U12n.10A Overcores

DRILL HOLE/ SAMPLE	DENSITY (gm/cc)			WATER BY WET WEIGHT (%)	POROSITY (%)	SATURATION (%)	CALC. AIR VOIDS (%)	MEAS. PERMANENT COMP. (%)	VELOCITY (km/sec)	
	AS-RECEIVED	DRY	GRAIN						LONG	SHEAR
ISS#31 #2	1.80	1.48	2.43	18	39	82	7.2	--	2.45	1.21
ISS#32 #1	1.80	1.46	2.45	19	41	83	6.8	--	2.33	0.90
ISS#33 #2	1.85	1.49	2.41	20	38	96	1.6	--	2.36	1.35
ISS#34 #3	1.81	1.45	2.44	20	40	88	4.9	--	2.43	1.22
GSIS#6 24'	1.82	1.49	2.45	18	39	85	6.0	--	1.72	0.67
GSIS#6 28'	1.79	1.44	2.46	20	41	85	6.4	--	1.67	0.75

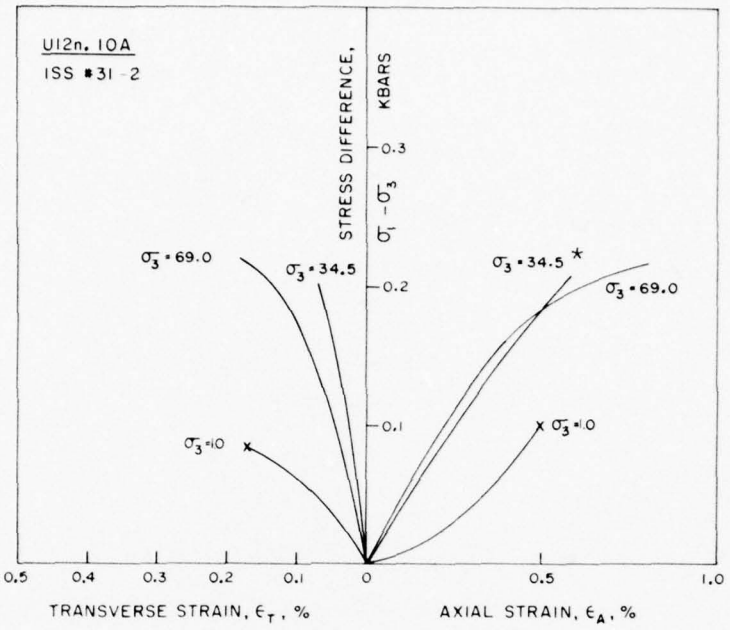


Figure 3-1. Triaxial compression stress-strain curves for ISS#31-2 overcore samples. (*Confining pressure given in bars.)

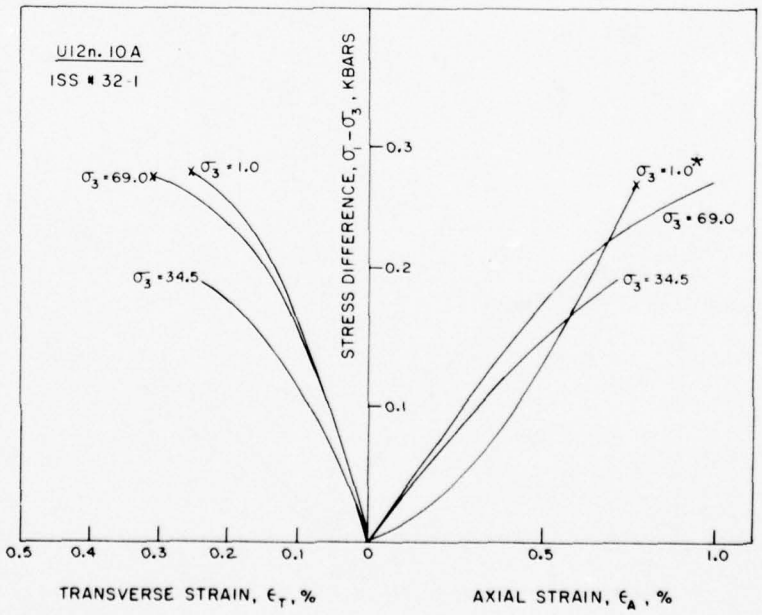


Figure 3-2. Triaxial compression stress-strain curves for ISS#32-1 overcore samples. (*Confining pressure given in bars.)

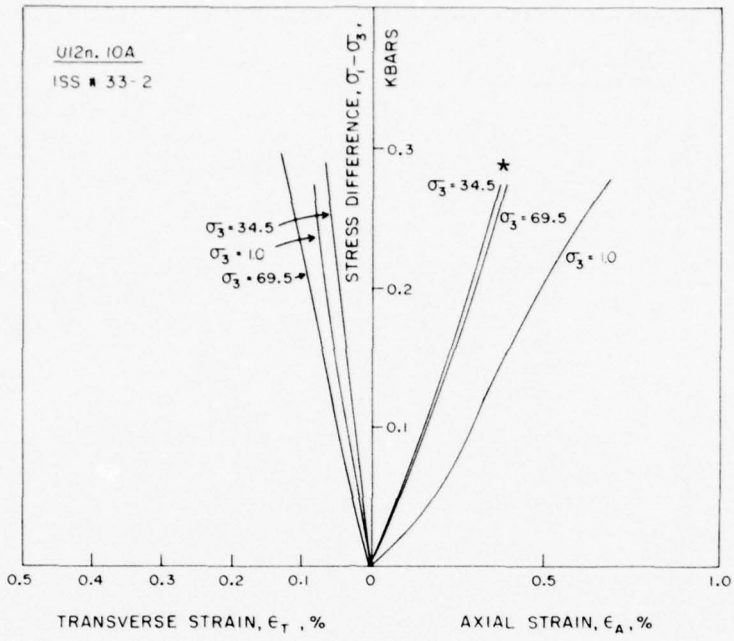


Figure 3-3. Triaxial compression stress-strain curves for ISS#33-2 overcore samples. (*Confining pressure given in bars.)

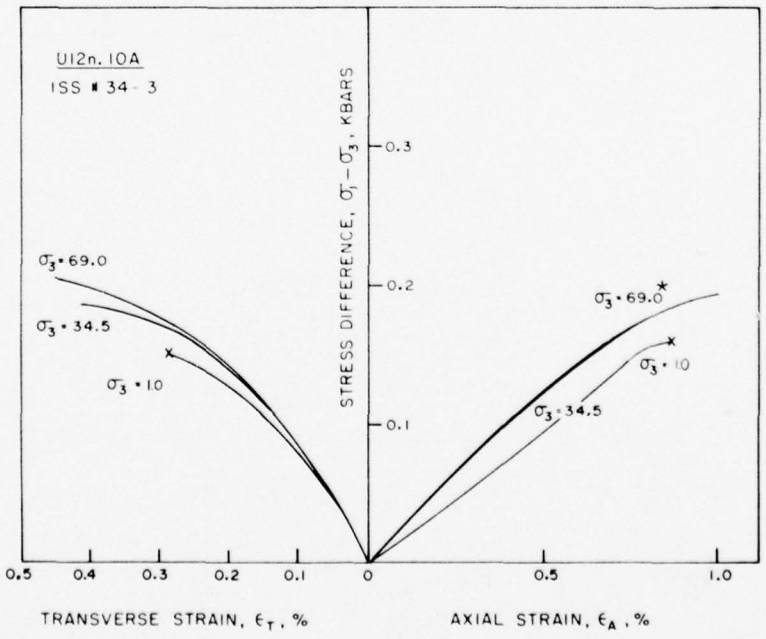


Figure 3-4. Triaxial compression stress-strain curves for ISS#34-3 overcore samples. (*Confining pressure given in bars.)

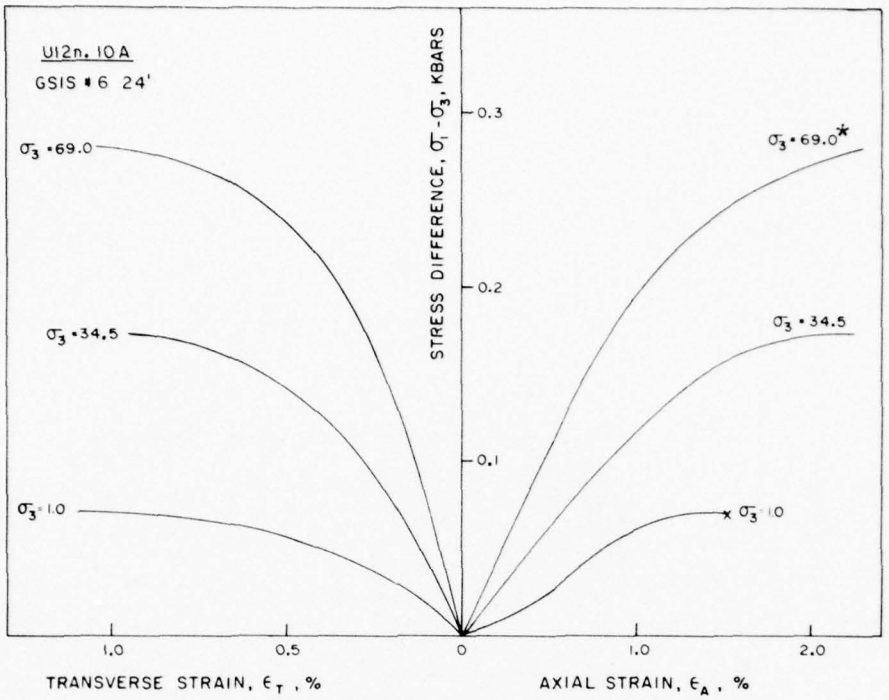


Figure 3-5. Triaxial compression stress-strain curves for GSIS#6 overcore samples. (*Confining pressure given in bars.)

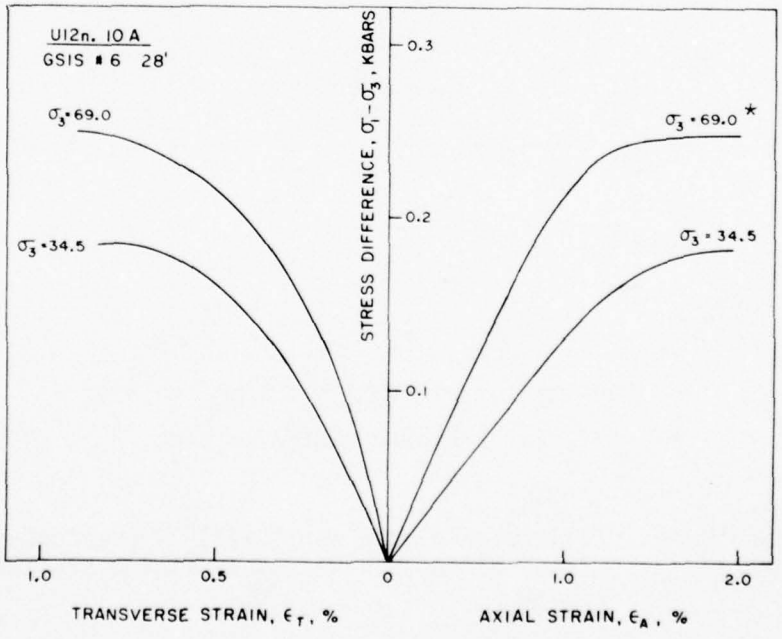


Figure 3-6. Triaxial compression stress-strain curves for GSIS#6 overcore samples. (*Confining pressure given in bars.)

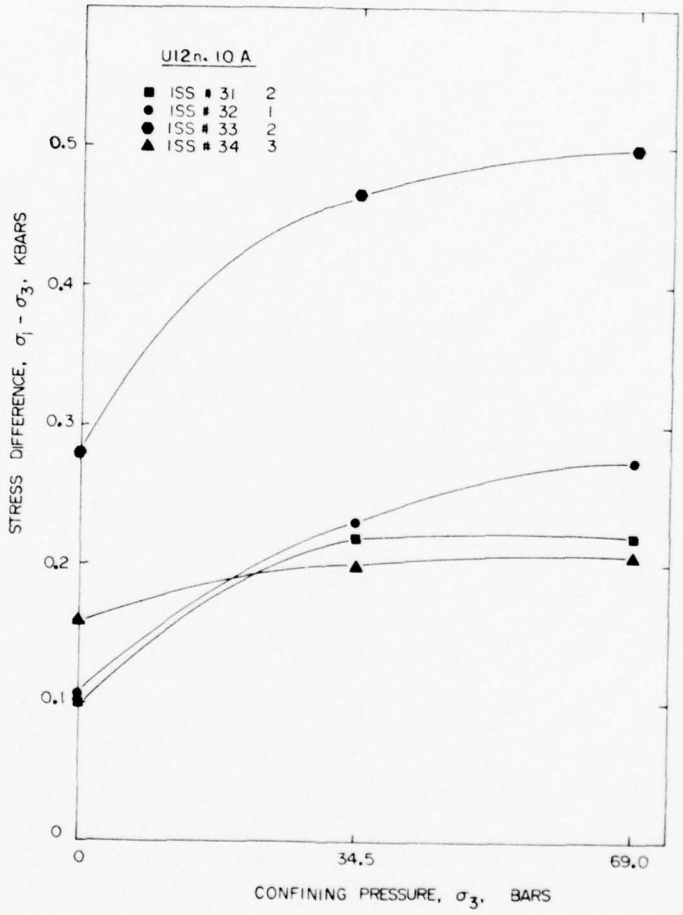


Figure 3-7. Failure envelopes for ISS#31-34 overcores--stress difference versus confining pressure.

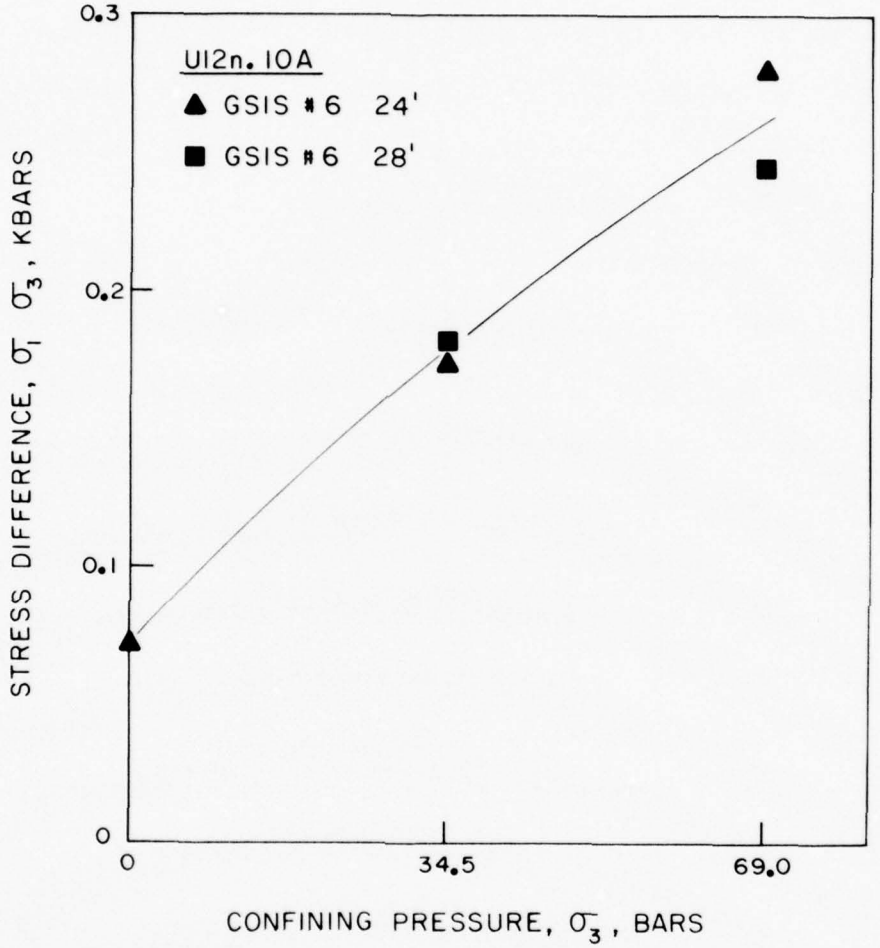


Figure 3-8. Failure envelopes for GSIS#6 overcores--stress difference versus confining pressure.

SECTION 4

U12n.10A "N TUNNEL" BYPASS DRIFT SUPERLEAN GROUT SUMMARY

Superlean grout from U12n.10A "N Tunnel" bypass drift (CS 17+30) was tested for physical and mechanical properties. Longitudinal and shear wave velocities, triaxial compressive response at confining pressures of 0, 0.5, 2.0 and 4.0 kbars and uniaxial strain response up to a mean normal stress of 4.0 kbars were determined.

Physical properties and ultrasonic velocities are listed in Table 4-1. The triaxial compressive data are plotted in Figure 4-1 and the uniaxial strain response is plotted in Figure 4-2.

Physical properties show the grout to be of relatively low density and slightly undersaturated with air void contents near 5 percent. High shear strengths, most probably due to aging, were approximately twice those of superlean grouts previously tested at these stress states[1,3]. Failures occurred near 30 bars for the unconfined tests and 65 bars for the confined tests. Volumetric strain during the uniaxial strain tests ranged from 8 to 9 percent resulting in permanent volume compaction of 4 to 5 percent by volume.

TABLE 4-1

Physical Properties, Uniaxial Strain Permanent Volume Compaction and Ultrasonic Wave Velocities of U12n.10A Superlean Grouts

SAMPLE DESIGNATION	DENSITY (gm/cc)			WATER BY WET WEIGHT (%)	POROSITY (%)	SATURATION (%)	CALC. AIR VOIDS (%)	MEAS. PERMANENT COMP. (%)	VELOCITY (km/sec)	
	AS-RECEIVED	DRY	GRAIN						LONG	SHEAR
1A*	1.75	1.30	2.65	25.4	50.9	87.2	6.5	4.0	2.08	1.09
1B	1.75	1.30	2.63	25.5	50.5	88.4	5.8			
2A	1.75	1.28	2.64	27.1	51.6	92.1	4.1	5.0	2.31	1.03
2B	1.74	1.29	2.62	25.7	50.6	88.4	5.8			

* The number-letter designation indicates core number-test number.

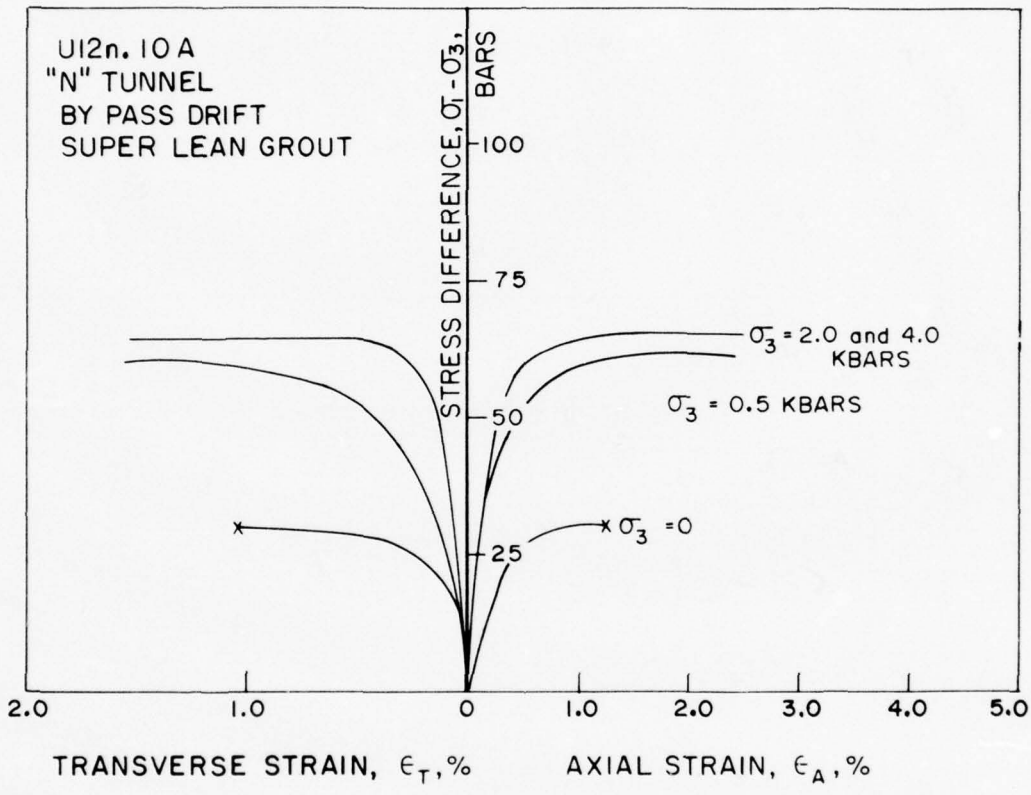


Figure 4-1. Triaxial compression stress-strain curves for U12n.10A "N Tunnel" bypass superlean grout.

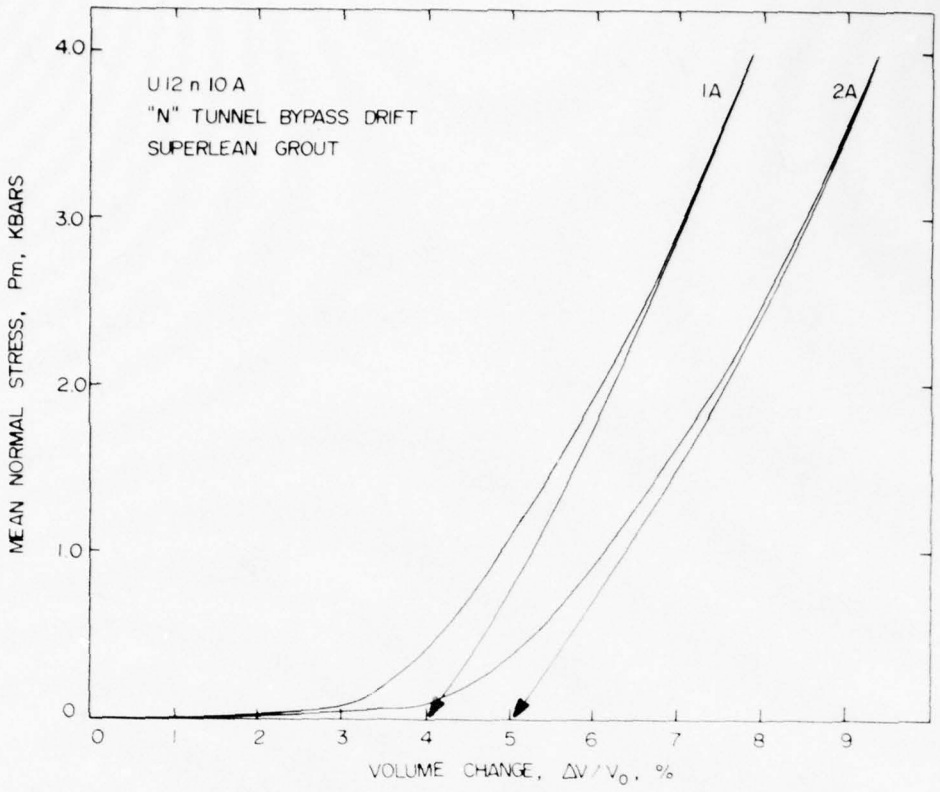


Figure 4-2a. Uniaxial strain tests on U12n.10A "N Tunnel" bypass drift superlean grout--mean normal stress versus volume change.

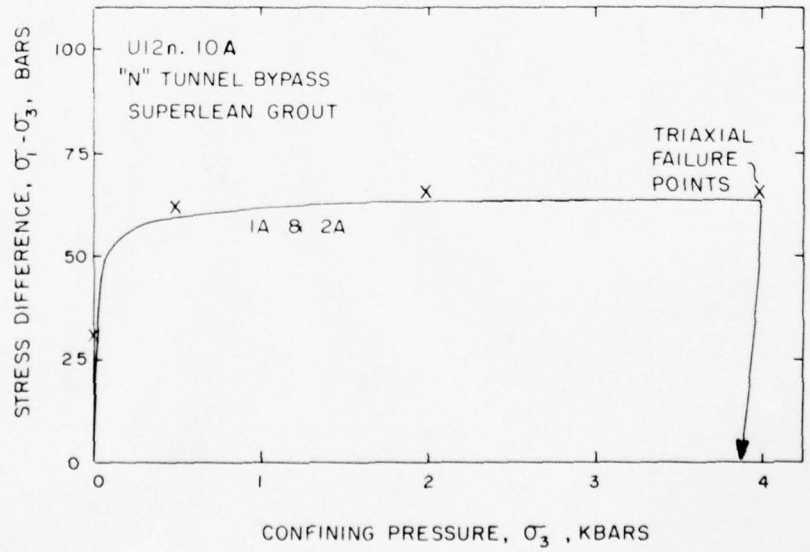


Figure 4-2b. Uniaxial strain tests on U12n.10A "N Tunnel" bypass drift superlean grout--stress difference versus confining pressure.

REFERENCES

1. Butters, S. W., Dropek, R. K, and Jones, A. H., "Material Properties of Nevada Test Site Tuff and Grout with Emphasis on the Mighty Epic Event," Terra Tek Report TR 76-63, November 1976.

2. Ellis, W. L., U.S. Geological Survey, Personal communication, November 1976.

3. Butters, S. W. Nielsen, R. R., Jones, A. H., and Green, S. J., "Mechanical & Physical Properties of Nevada Test Site Tuffs and Grouts from Exploratory Drill Holes," Terra Tek Report TR 73-69, December 1973.

APPENDIX A

Uniaxial Strain Curves for U12n.10A Drill Holes

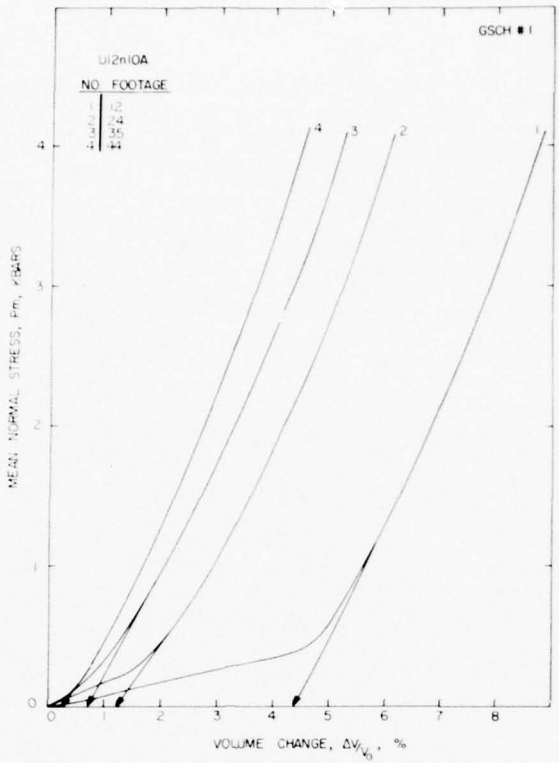


Figure A-1a. Uniaxial strain tests on U12n.10A GSCH#1 core samples--mean normal stress versus volume change.

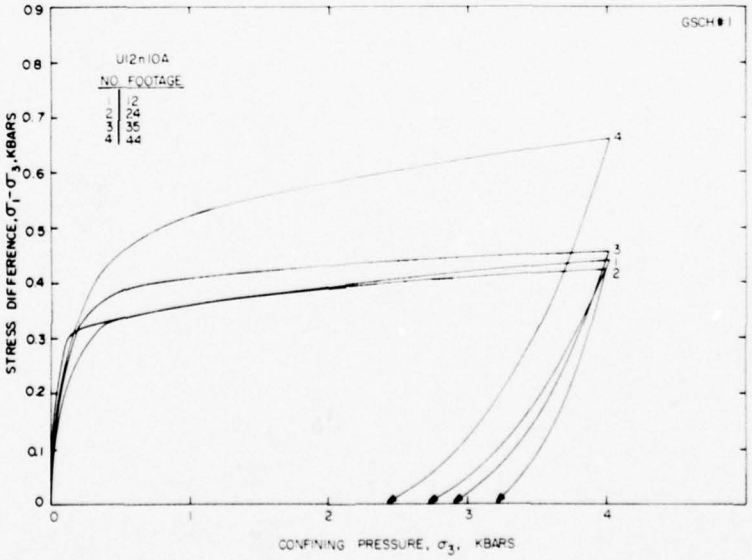


Figure A-1b. Uniaxial strain tests on U12n.10A GSCH#1 core samples--stress difference versus confining pressure.

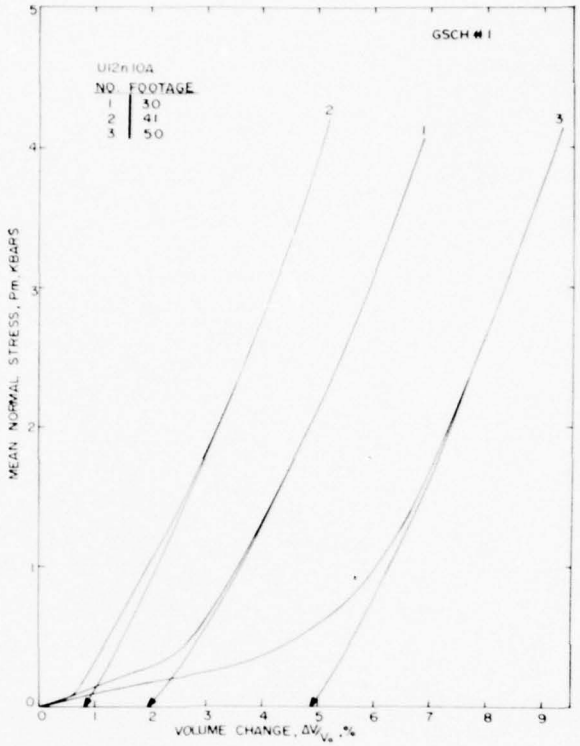


Figure A-2a. Uniaxial strain tests on U12n.10A GSCH#1 core samples--mean normal stress versus volume change.

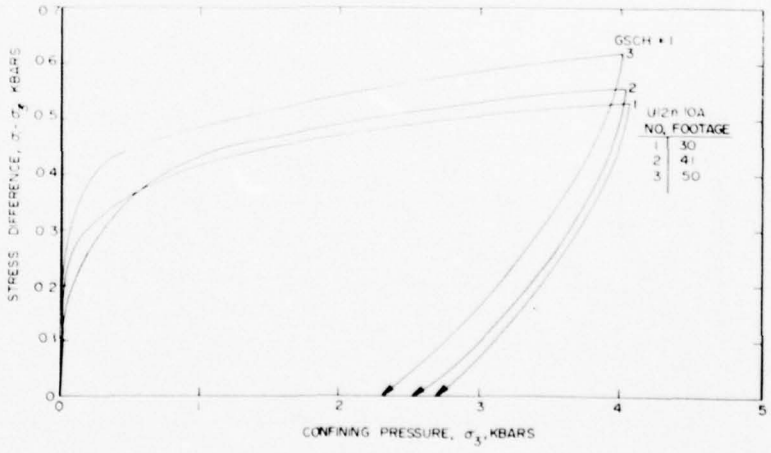


Figure A-2b. Uniaxial strain tests on U12n.10A GSCH#1 core samples--stress difference versus confining pressure.

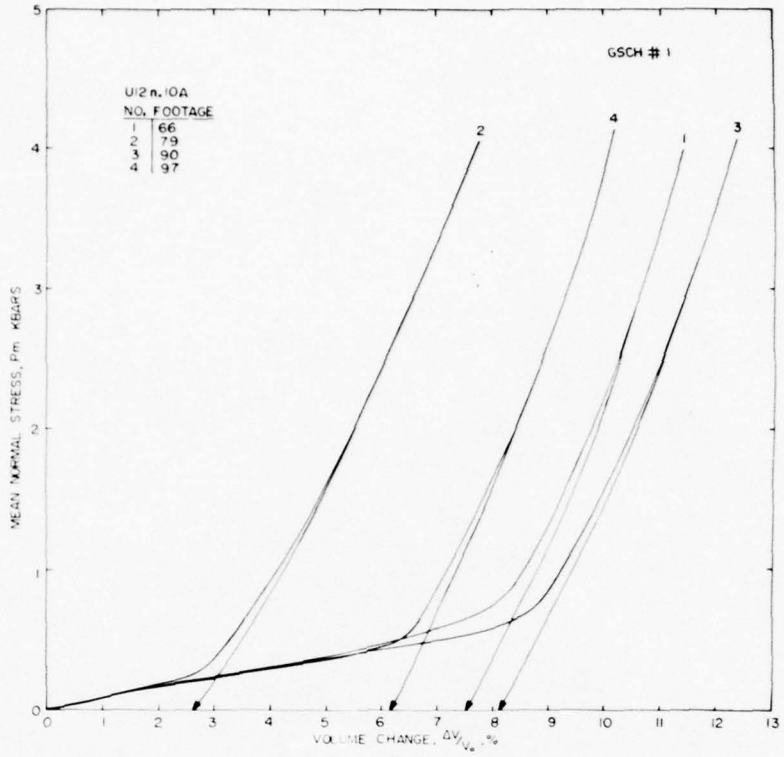


Figure A-3a. Uniaxial strain tests on U12n.10A GSCH#1 core samples--mean normal stress versus volume change.

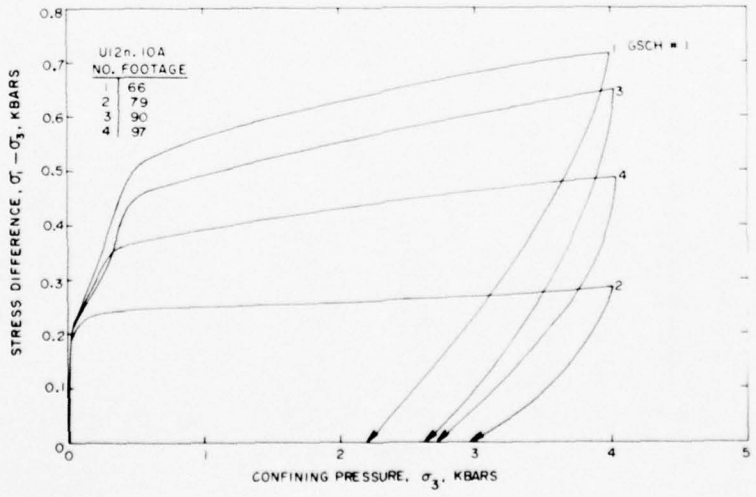


Figure A-3b. Uniaxial strain tests on U12n.10A GSCH#1 core samples--stress difference versus confining pressure.

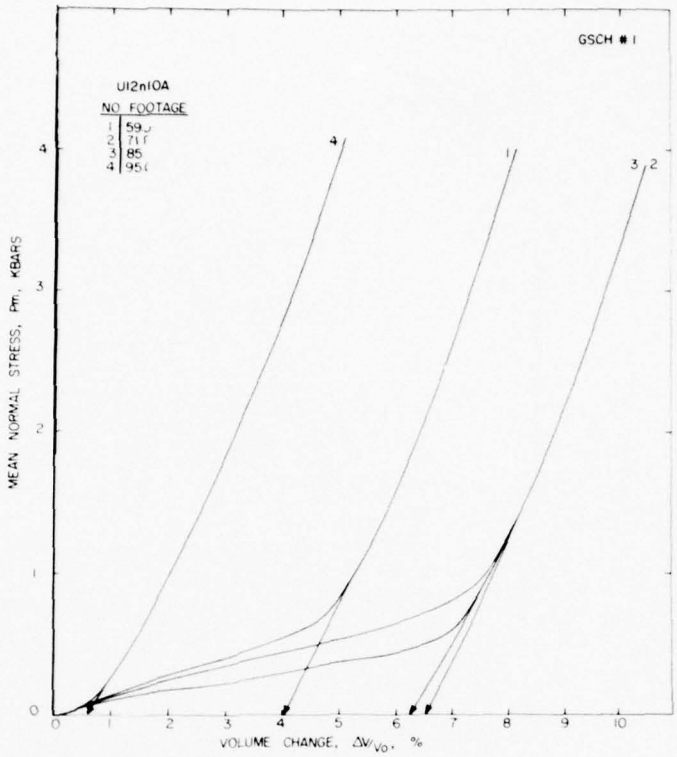


Figure A-4a. Uniaxial strain tests on U12n.10A GSCH#1 core samples--mean normal stress versus volume change.

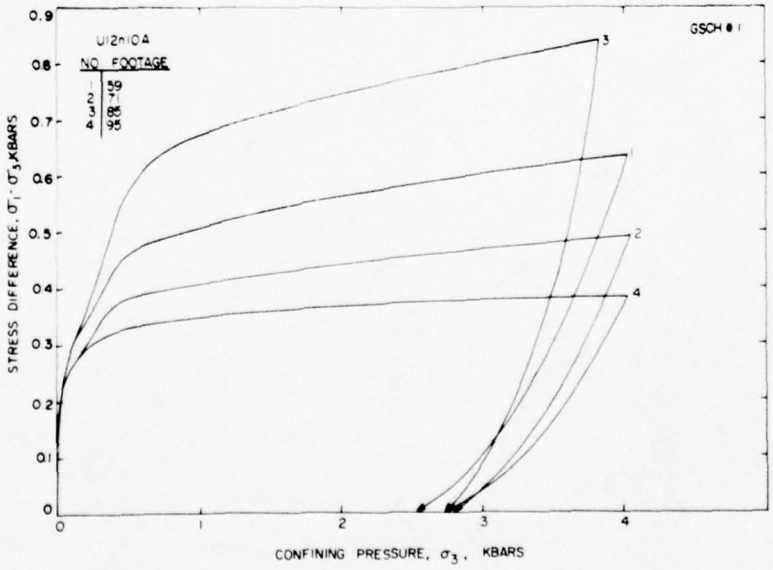


Figure A-4b. Uniaxial strain tests on U12n.10A GSCH#1 core samples--stress difference versus confining pressure.

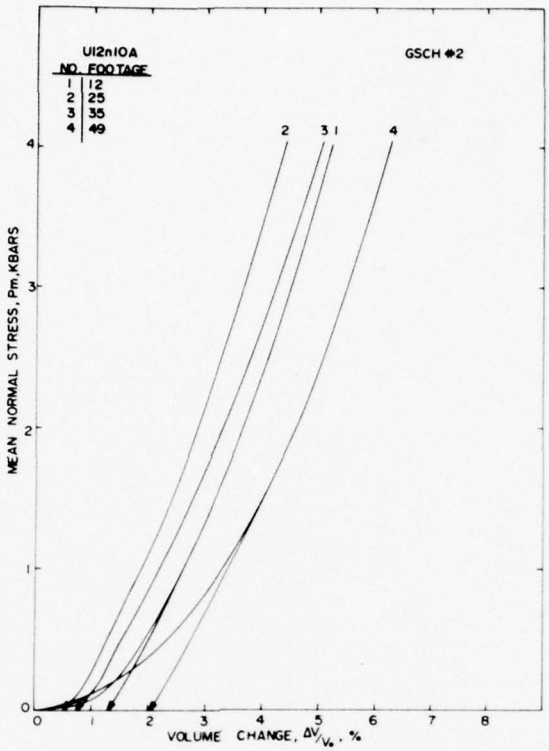


Figure A-5a. Uniaxial strain tests on U12n.10A GSCH#2 core samples--mean normal stress versus volume change.

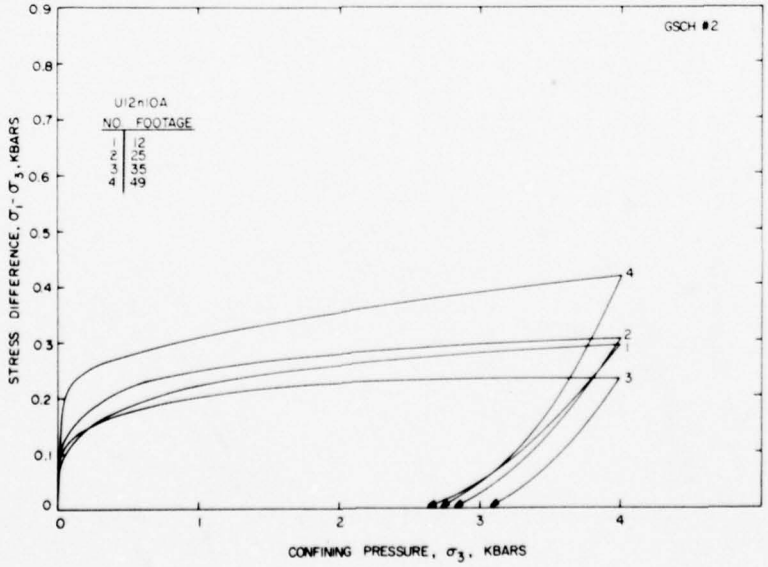


Figure A-5b. Uniaxial strain tests on U12n.10A GSCH#2 core samples--stress difference versus confining pressure.

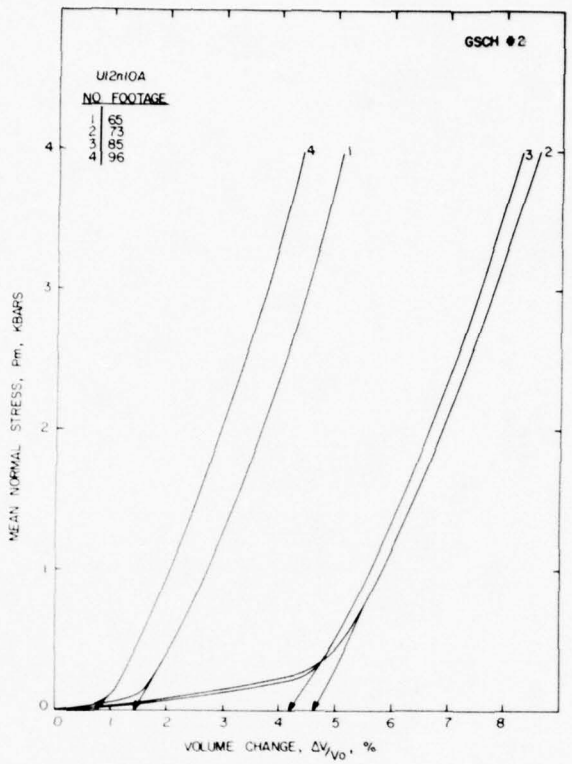


Figure A-6a. Uniaxial strain tests on U12n.10A GSCH#2 core samples--mean normal stress versus volume change.

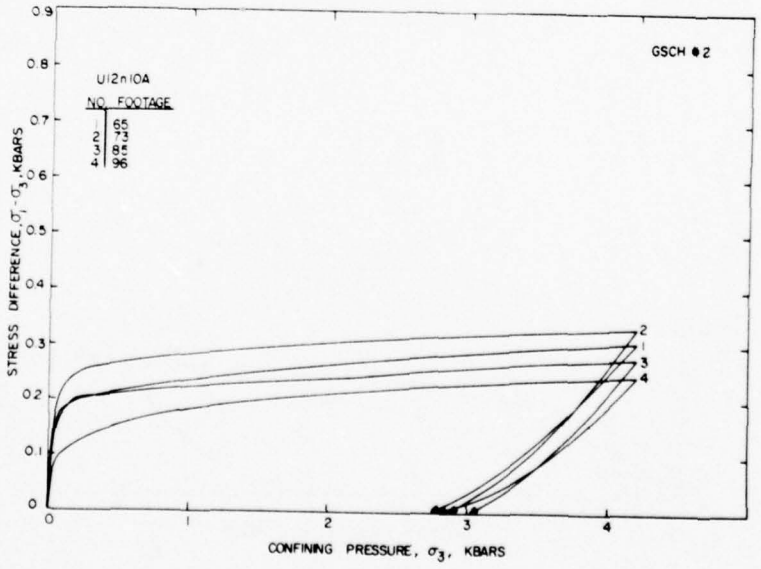


Figure A-6b. Uniaxial strain tests on U12n.10A GSCH#2 core samples--stress difference versus confining pressure.

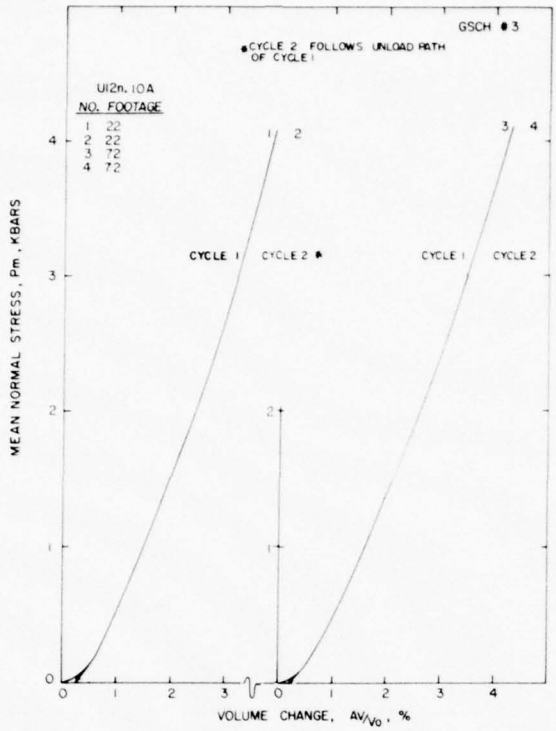


Figure A-7a. Uniaxial strain tests on U12n.10A GSCH#3 core samples--mean normal stress versus volume change.

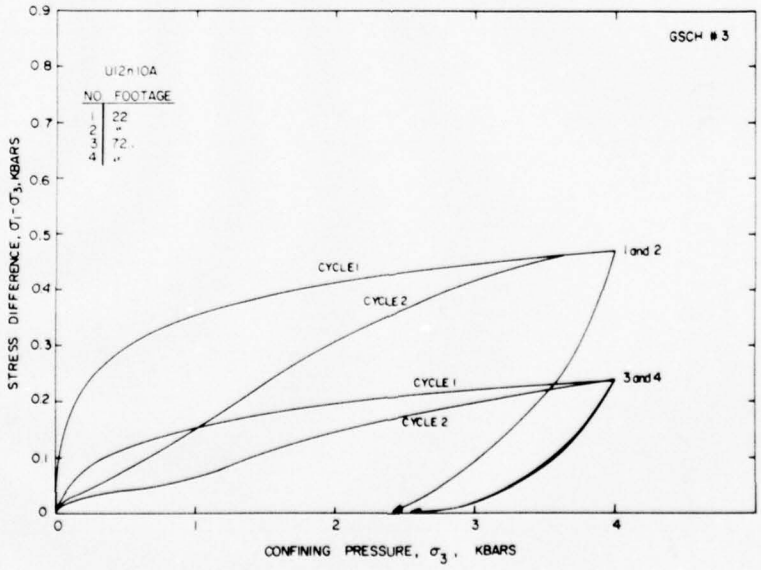


Figure A-7b. Uniaxial strain tests on U12n.10A GSCH#3 core samples--stress difference versus confining pressure.

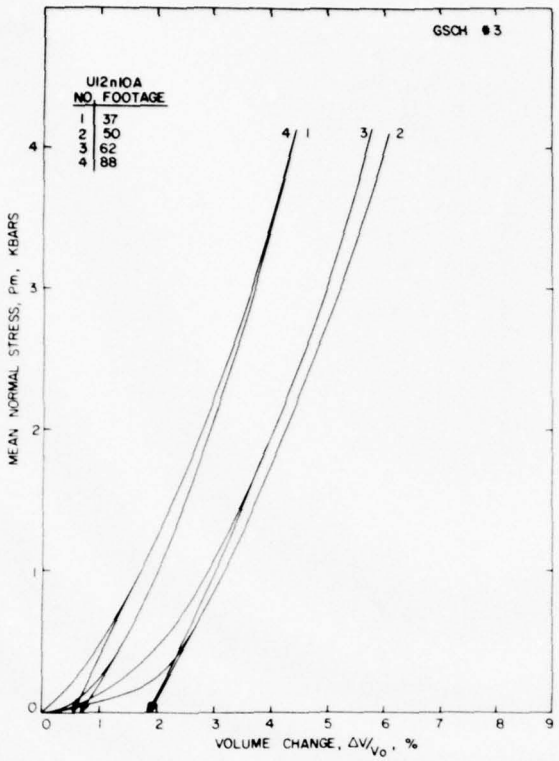


Figure A-8a. Uniaxial strain tests on U12n.10A GSCH#3 core samples--mean normal stress versus volume change.

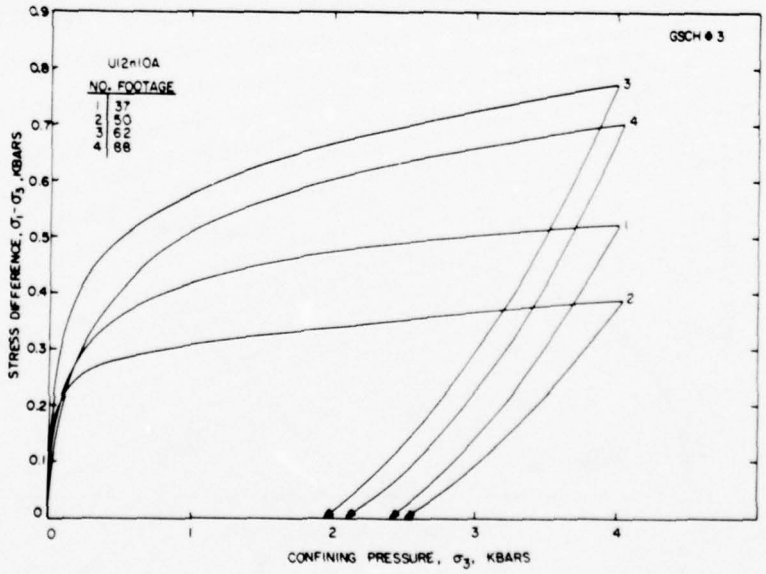


Figure A-8b. Uniaxial strain tests on U12n.10A GSCH#3 core samples--stress difference versus confining pressure.

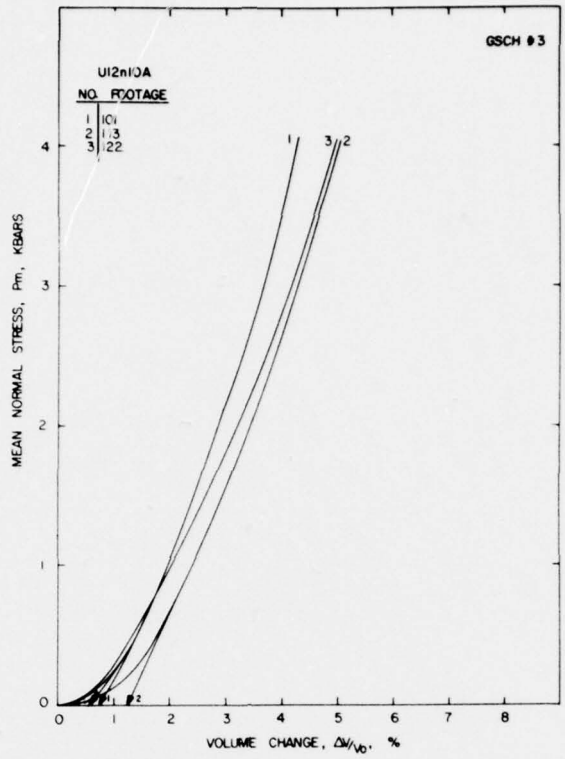


Figure A-9a. Uniaxial strain tests on U12n.10A GSCH#3 core samples--mean normal stress versus volume change.

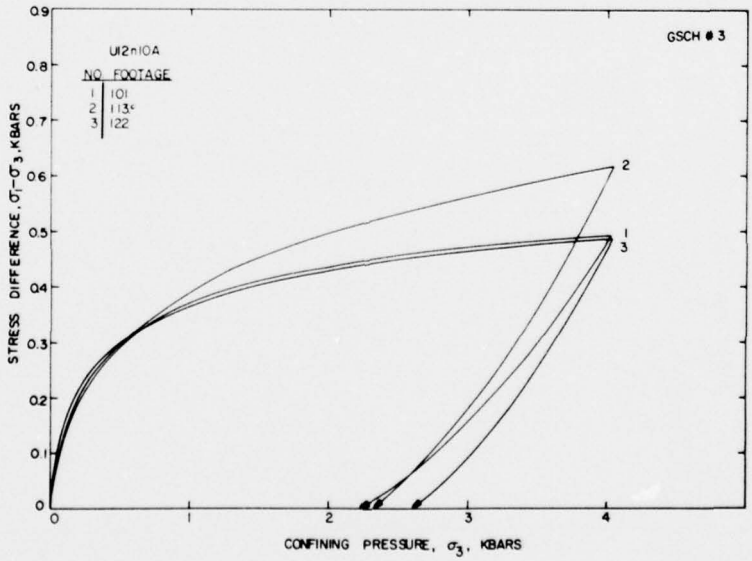


Figure A-9b. Uniaxial strain tests on U12n.10A GSCH#3 core samples--stress difference versus confining pressure.

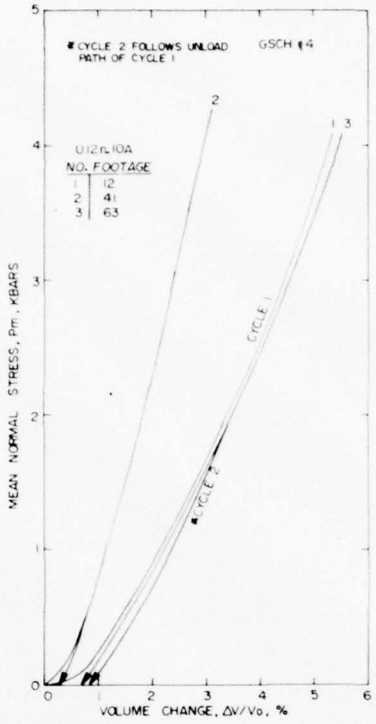


Figure A-10a. Uniaxial strain tests on U12n.10A GSCH#4 core samples--mean normal stress versus volume change.

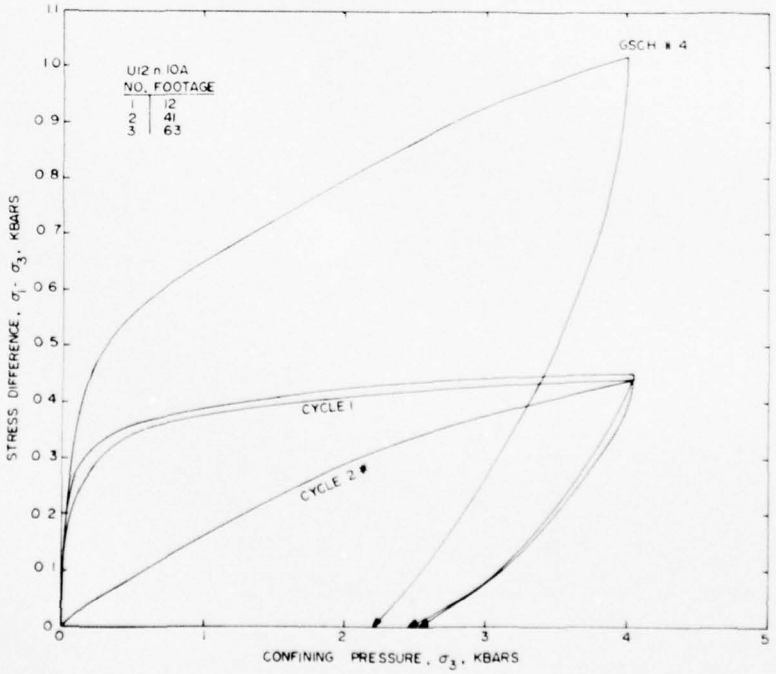


Figure A-10b. Uniaxial strain tests on U12n.10A GSCH#4 core samples--stress difference versus confining pressure.

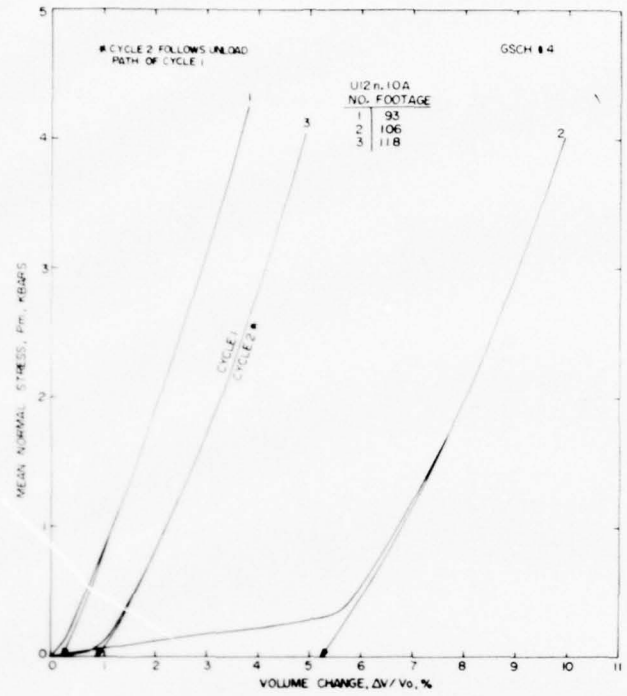


Figure A-11a. Uniaxial strain tests on U12n.10A GSCH#4 core samples--mean normal stress versus volume change.

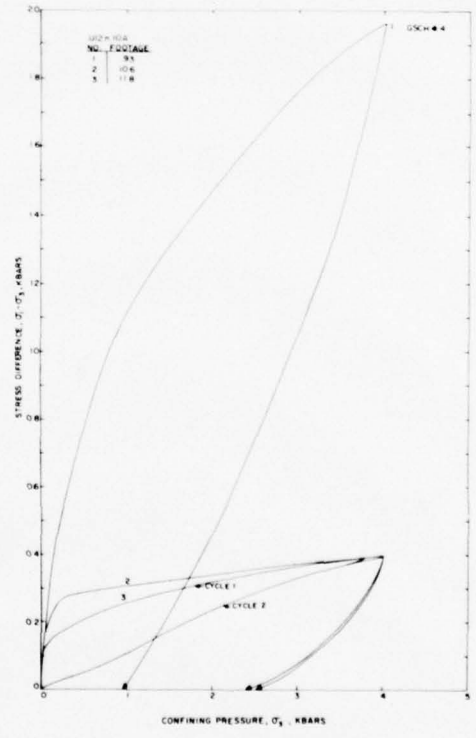


Figure A-11b. Uniaxial strain tests on U12n.10A GSCH#4 core samples--stress difference versus confining pressure.

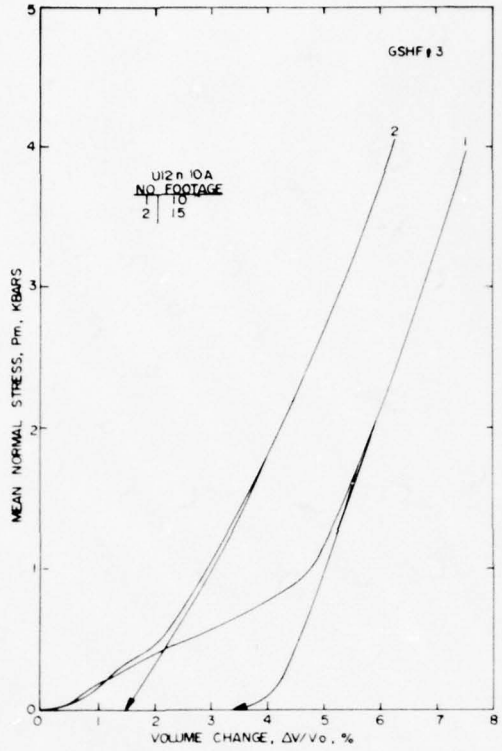


Figure A-12a. Uniaxial strain tests on U12n.10A GSHF#3 core samples--mean normal stress versus volume change.

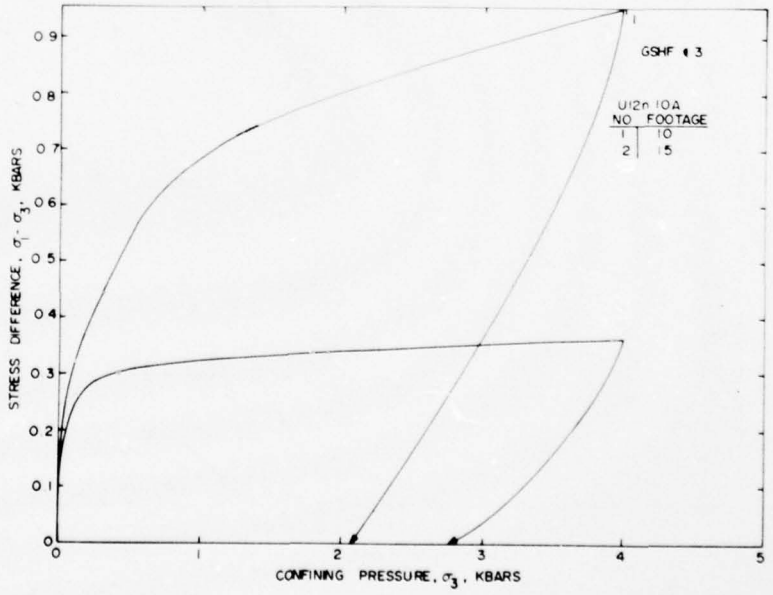


Figure A-12b. Uniaxial strain tests on U12n.10A GSHF#3 core samples--stress difference versus confining pressure.

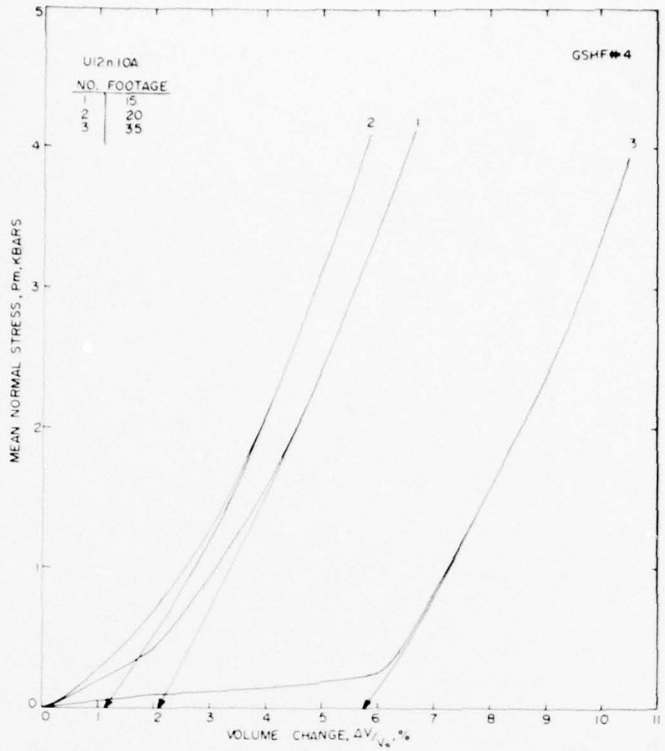


Figure A-13a. Uniaxial strain tests on U12n.10A GSHF#4 core samples--mean normal stress versus volume change.

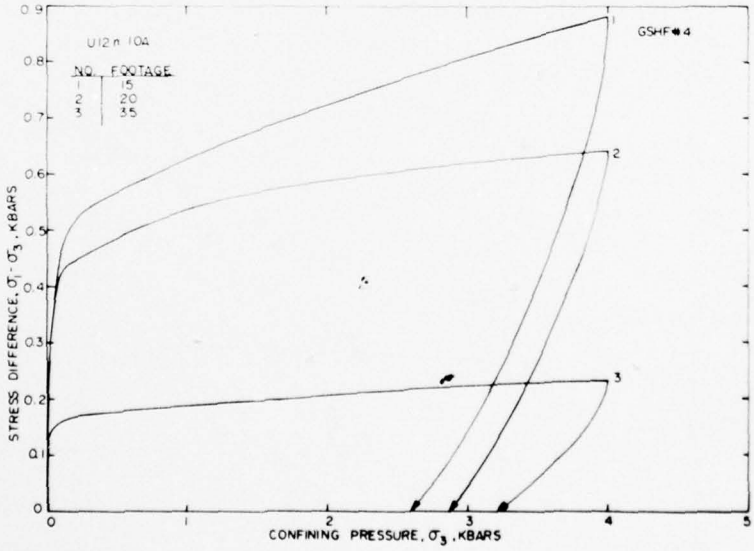


Figure A-13b. Uniaxial strain tests on U12n.10A GSHF#4 core samples--stress difference versus confining pressure.

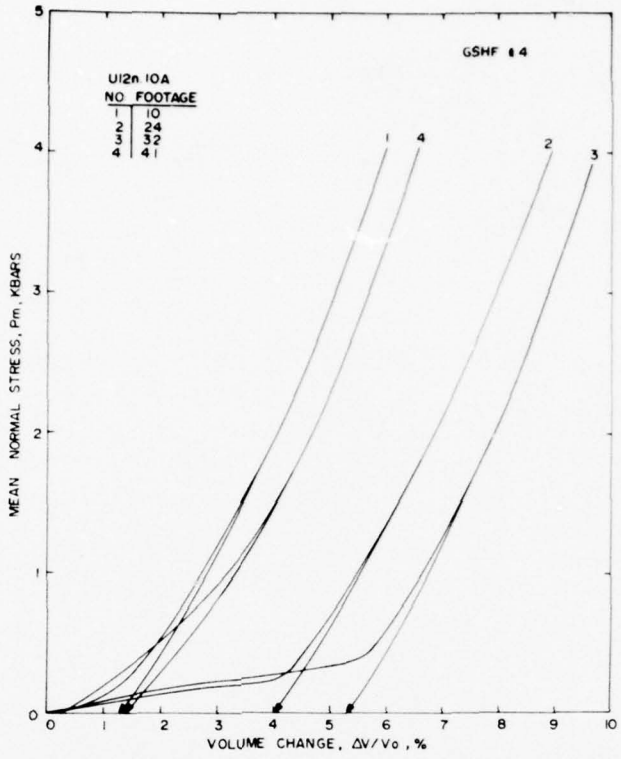


Figure A-14a. Uniaxial strain tests on U12n.10A GSHF#4 core samples--mean normal stress versus volume change.

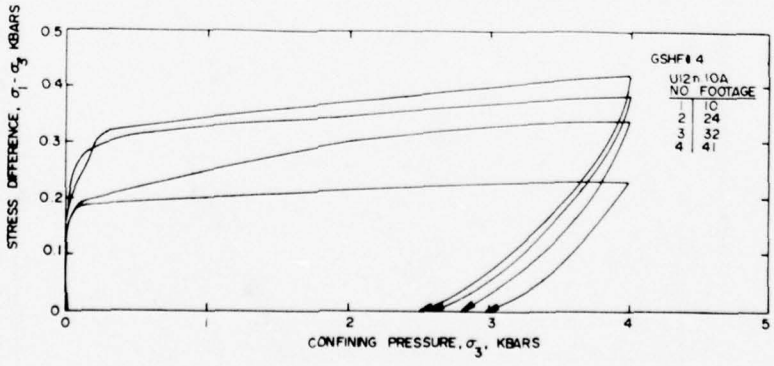


Figure A-14b. Uniaxial strain tests on U12n.10A GSHF#4 core samples--stress difference versus confining pressure.

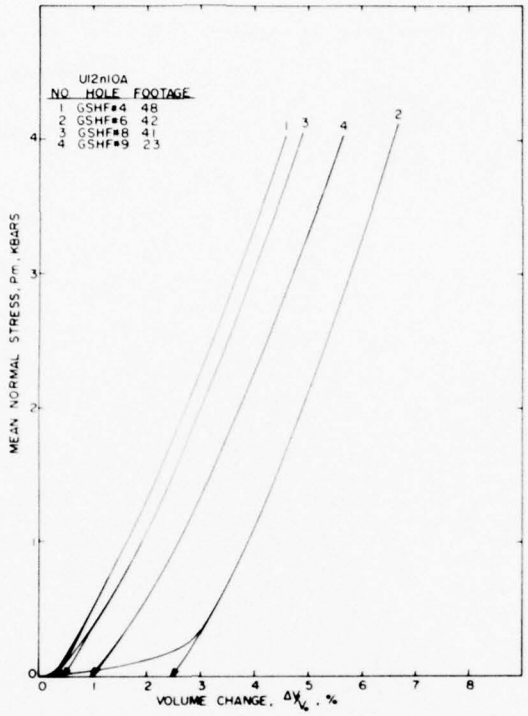


Figure A-15a. Uniaxial strain tests on U12n.10A GSHF#6,8,9 core samples--mean normal stress versus volume change.

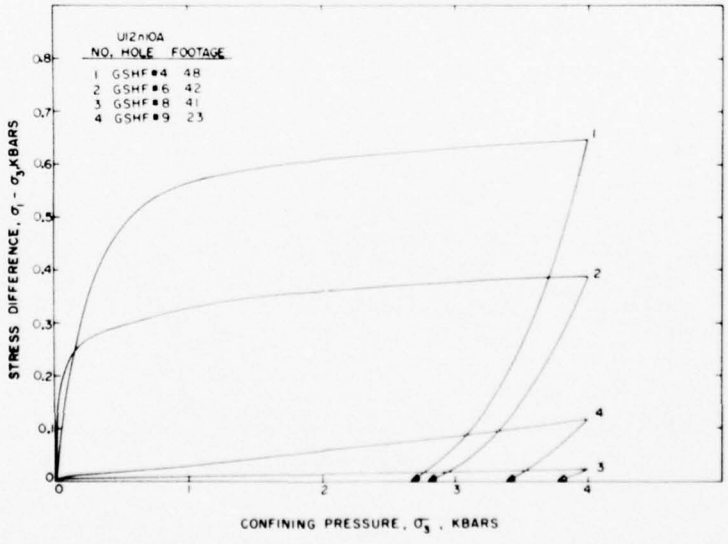


Figure A-15b. Uniaxial strain tests on U12n.10A GSHF#6,8,9 core samples--stress difference versus confining pressure.

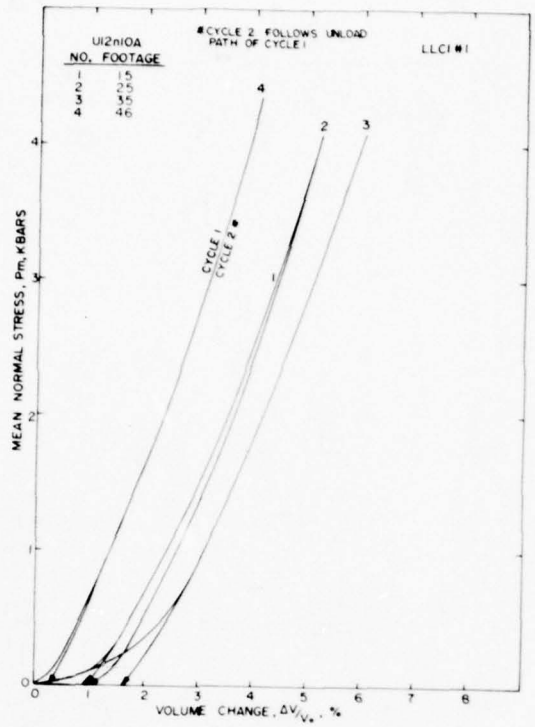


Figure A-16a. Uniaxial strain tests on U12n.10A LLCI#1 core samples--mean normal stress versus volume change.

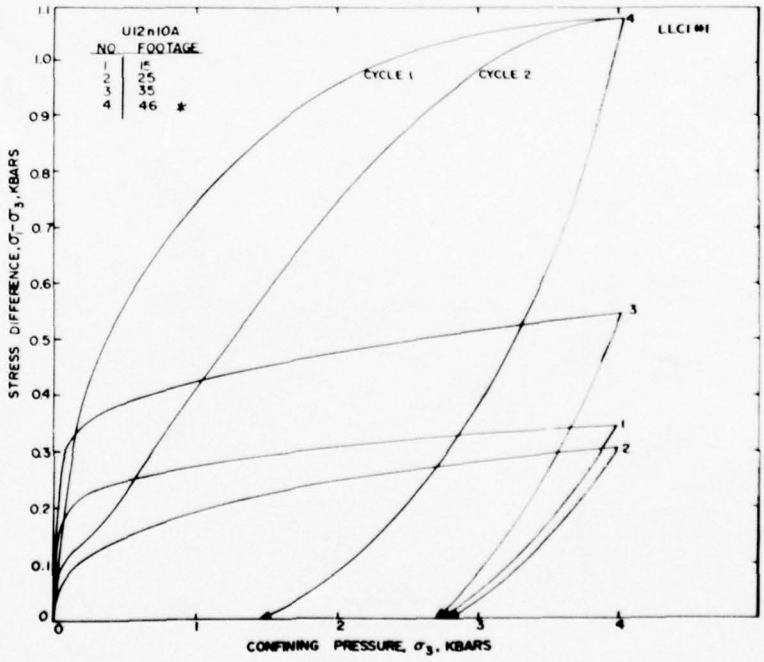


Figure A-16b. Uniaxial strain tests on U12n.10A LLCI#1 core samples--stress difference versus confining pressure.

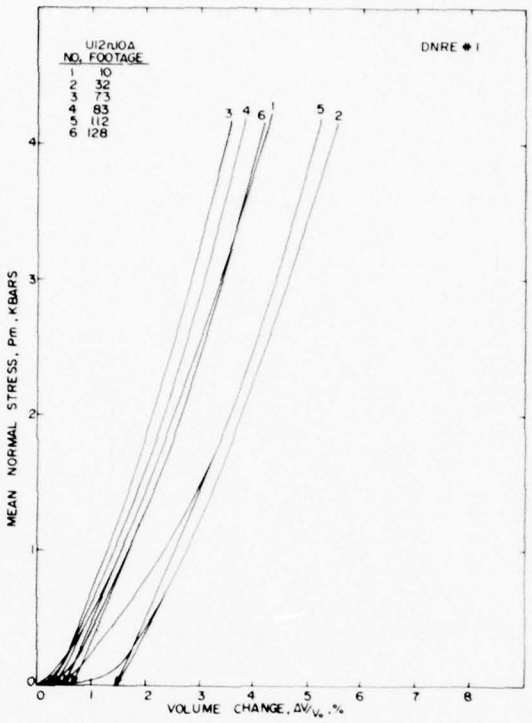


Figure A-17a. Uniaxial strain tests on U12n.10A DNRE#1 core samples--mean normal stress versus volume change.

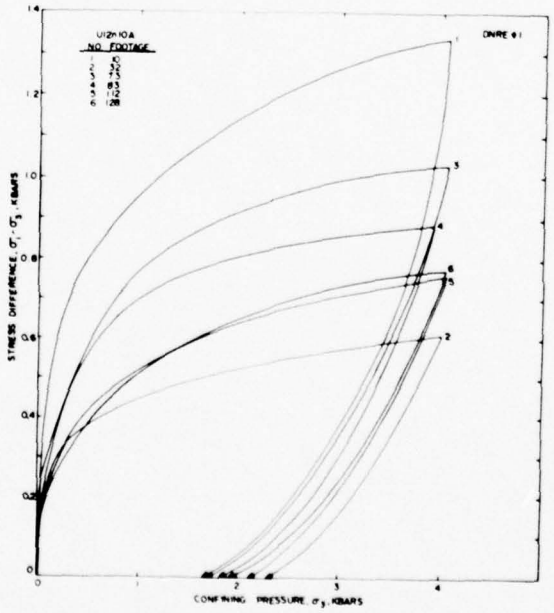


Figure A-17b. Uniaxial strain tests on U12n.10A DNRE#1 core samples--stress difference versus confining pressure.

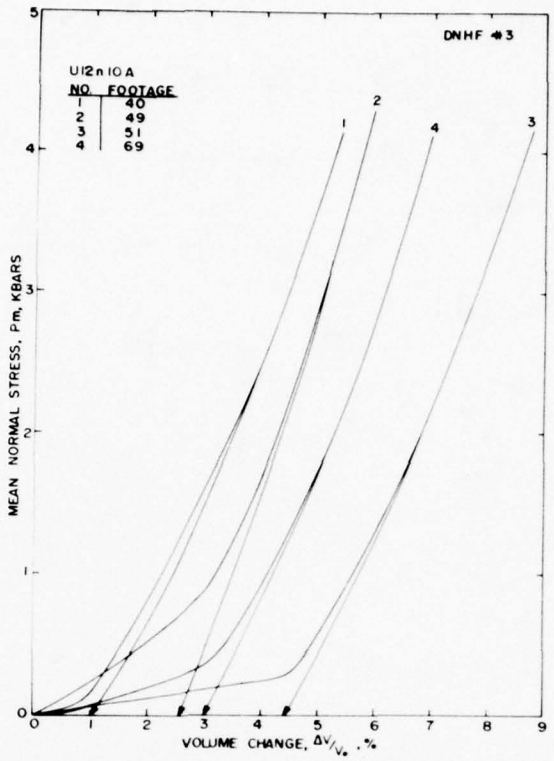


Figure A-18a. Uniaxial strain tests on U12n.10A DNHF#3 core samples--mean normal stress versus volume change.

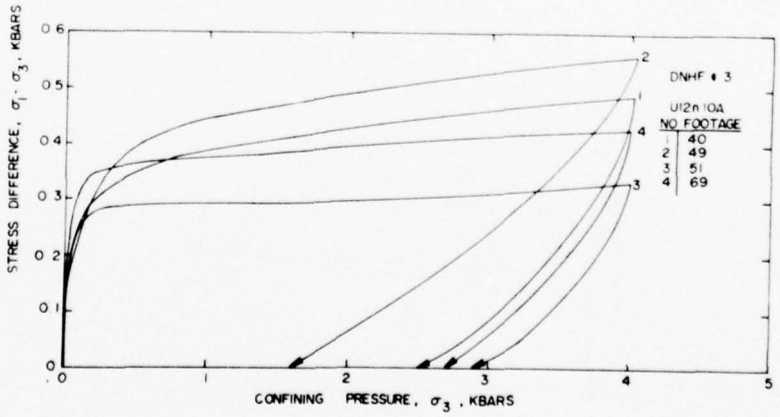


Figure A-18b. Uniaxial strain tests on U12n.10A DNHF#3 core samples--stress difference versus confining pressure.

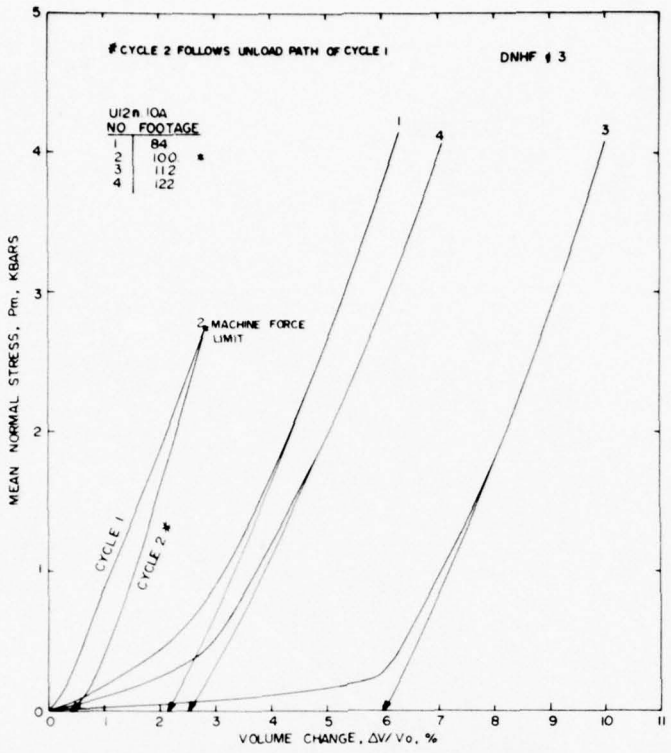


Figure A-19a. Uniaxial strain tests on U12n.10A DNHF#3 core samples--mean normal stress versus volume change.

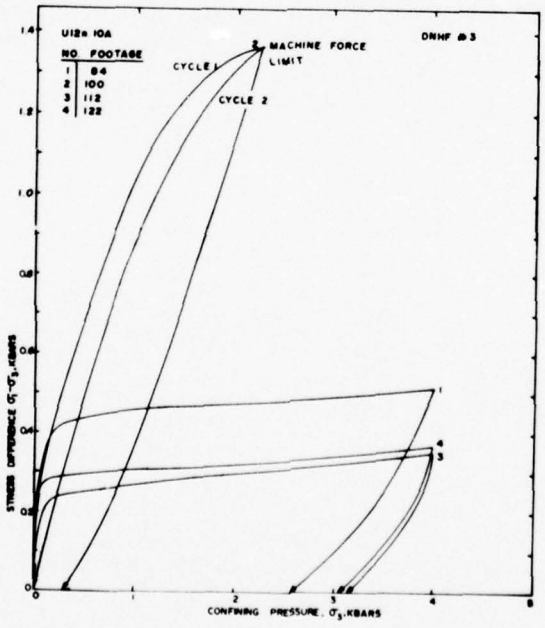


Figure A-19b. Uniaxial strain tests on U12n.10A DNHF#3 core samples--stress difference versus confining pressure.

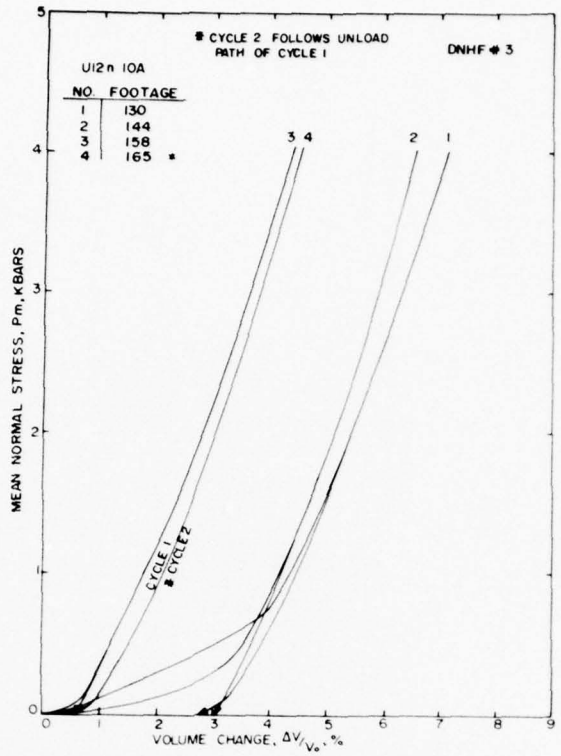


Figure A-20a. Uniaxial strain tests on U12n.10A DNHF#3 core samples--mean normal stress versus volume change.

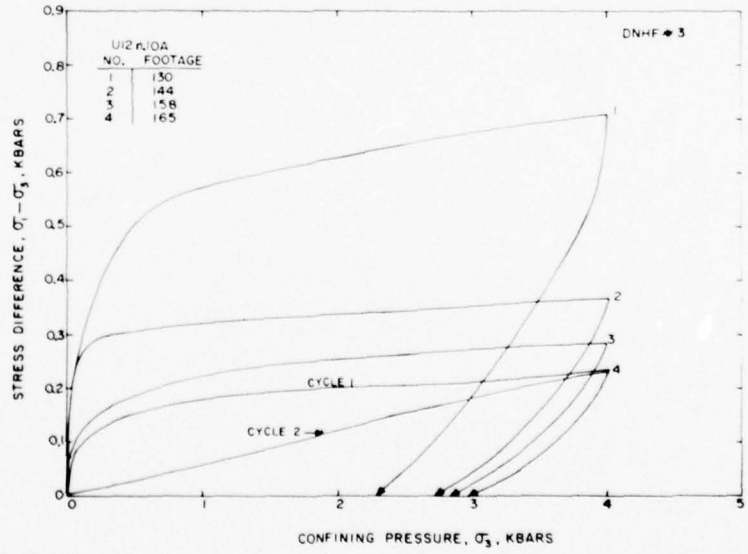


Figure A-20b. Uniaxial strain tests on U12n.10A DNHF#3 core samples--stress difference versus confining pressure.

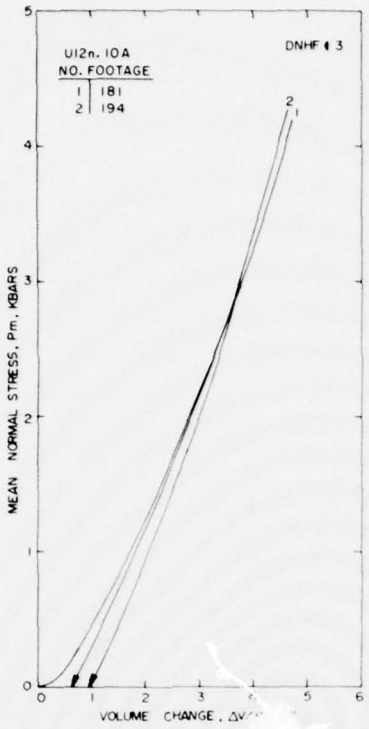


Figure A-21a. Uniaxial strain tests on U12n.10A DNHF#3 core samples--mean normal stress versus volume change.

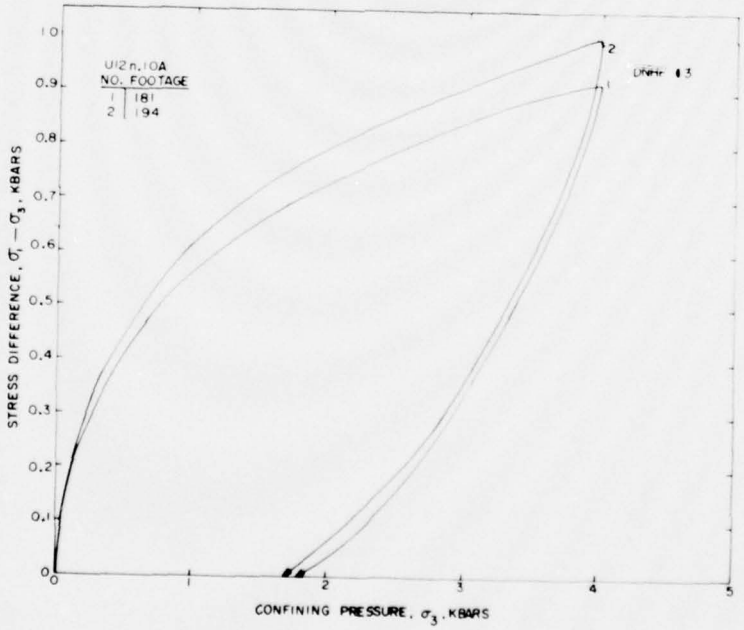


Figure A-21b. Uniaxial strain tests on U12n.10A DNHF#3 core samples--stress difference versus confining pressure.

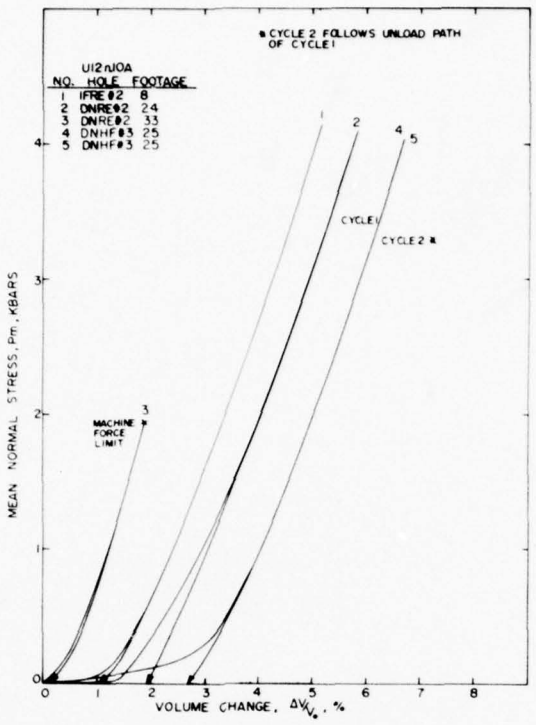


Figure A-22a. Uniaxial strain tests on U12n.10A DNRE#2, IFRE#2, DNHF#3 core samples--mean normal stress versus volume change.

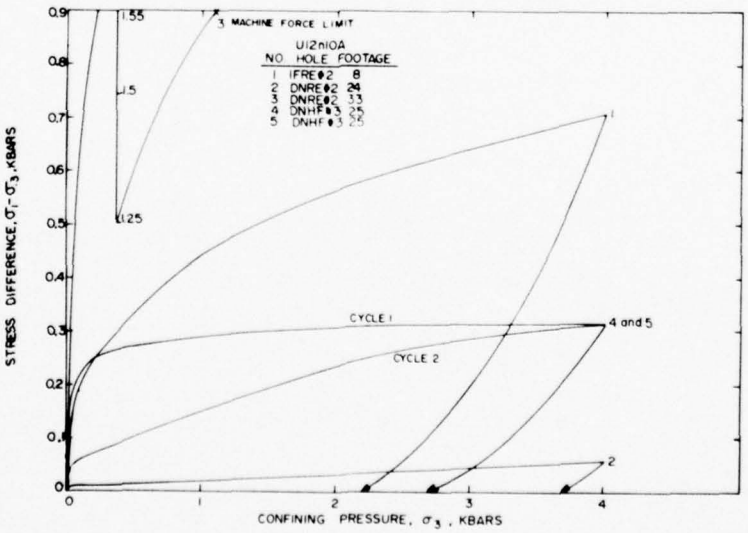


Figure A-22b. Uniaxial strain tests on U12n.10A DNRE#2, IFRE#2, DNHF#3 core samples--stress difference versus confining pressure.

APPENDIX B

Uniaxial Strain Curves for UE12n#10 Vertical Drill Hole

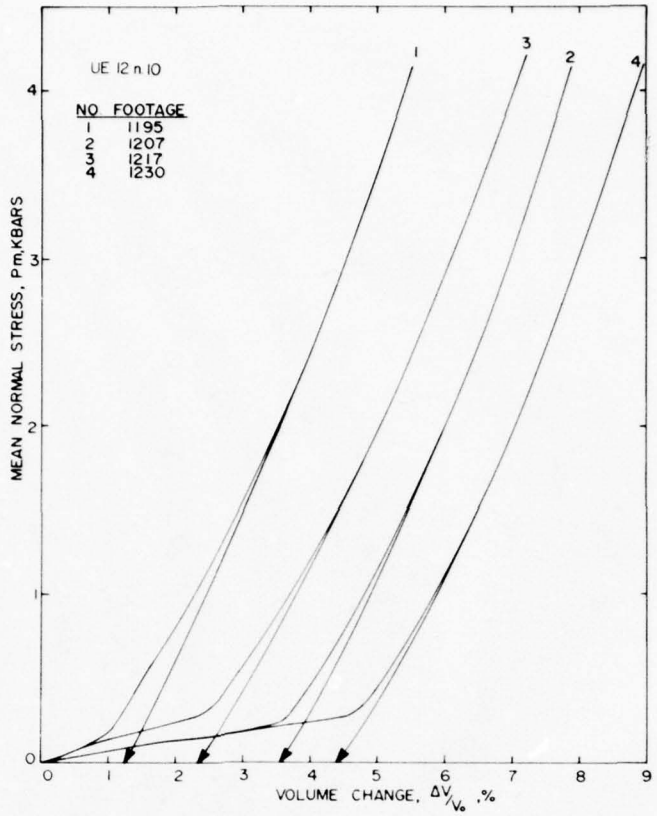


Figure B-1a. Uniaxial strain tests on UE12n#10 core samples--mean normal stress versus volume change.

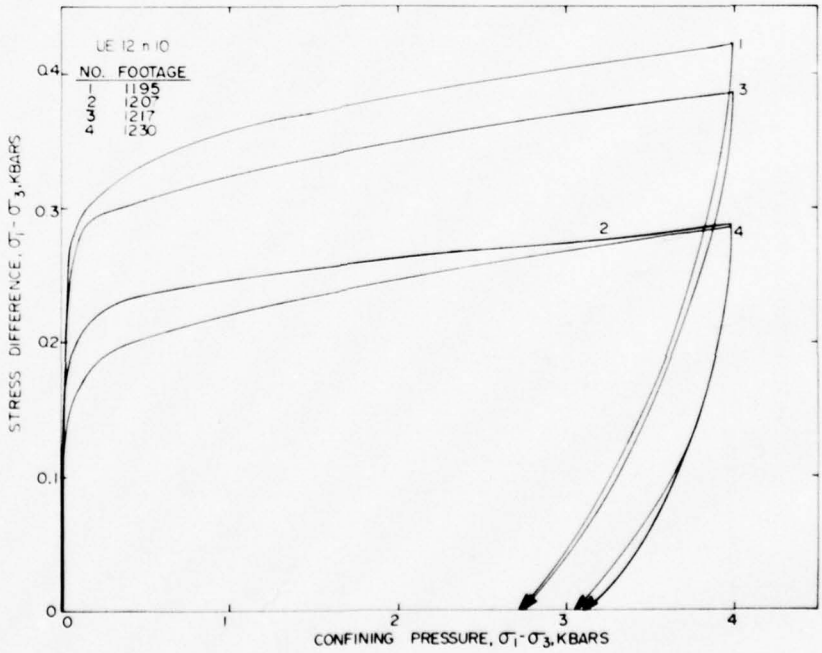


Figure B-1b. Uniaxial strain tests on UE12n#10 core samples--stress difference versus confining pressure.

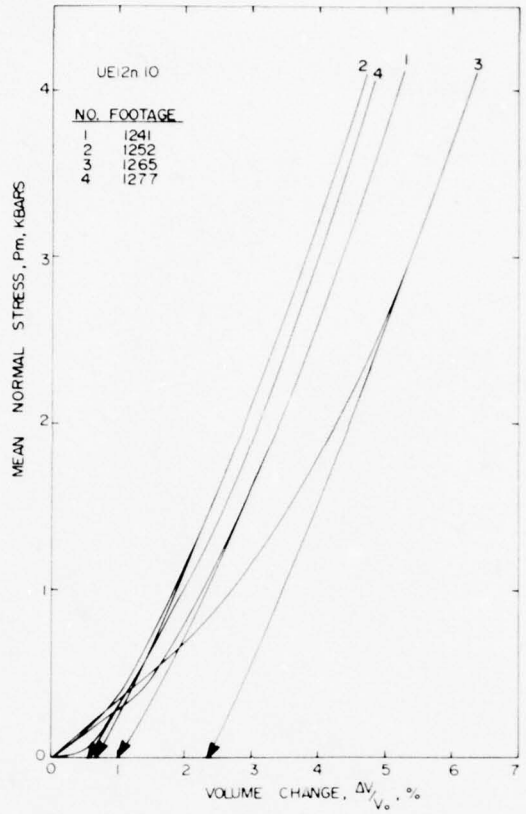


Figure B-2a. Uniaxial strain tests on UE12n#10 core samples--mean normal stress versus volume change.

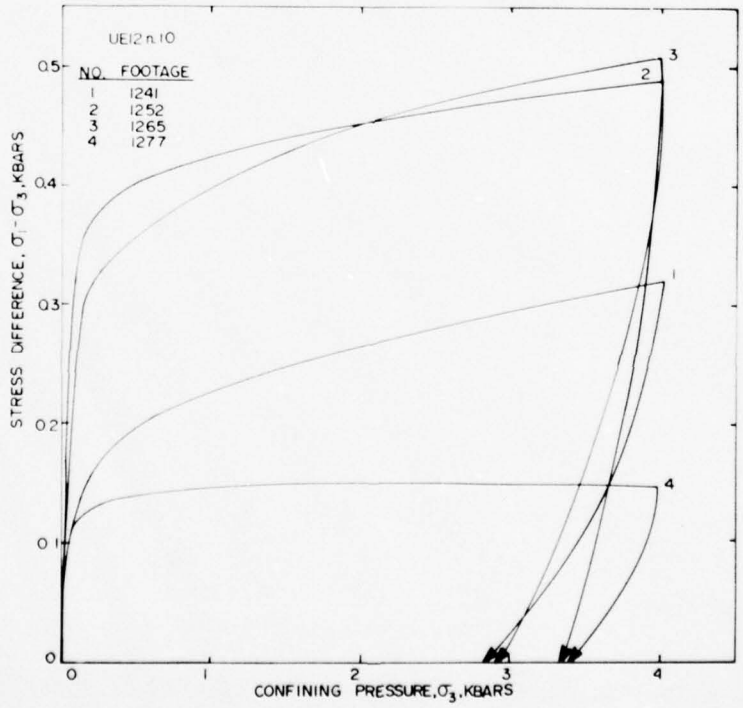


Figure B-2b. Uniaxial strain tests on UE12n#10 core samples--stress difference versus confining pressure.

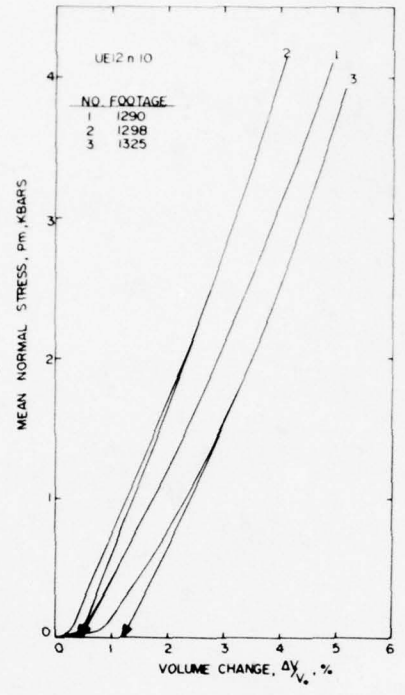


Figure B-3a. Uniaxial strain tests on UE12n#10 core samples--mean normal stress versus volume change.

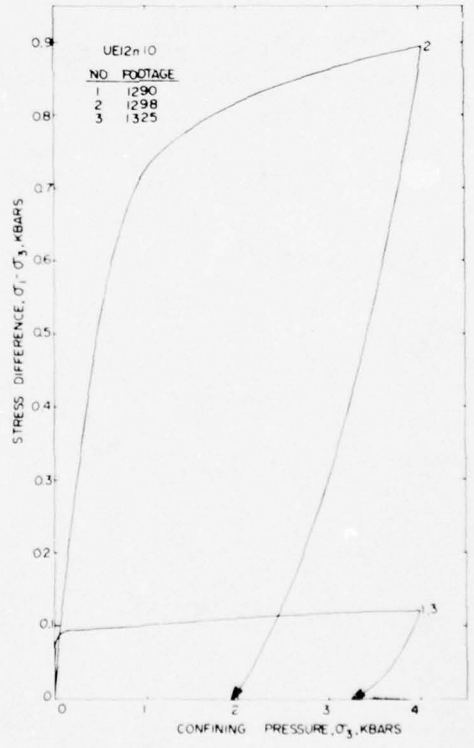


Figure B-3b. Uniaxial strain tests on UE12n#10 core samples--stress difference versus confining pressure.

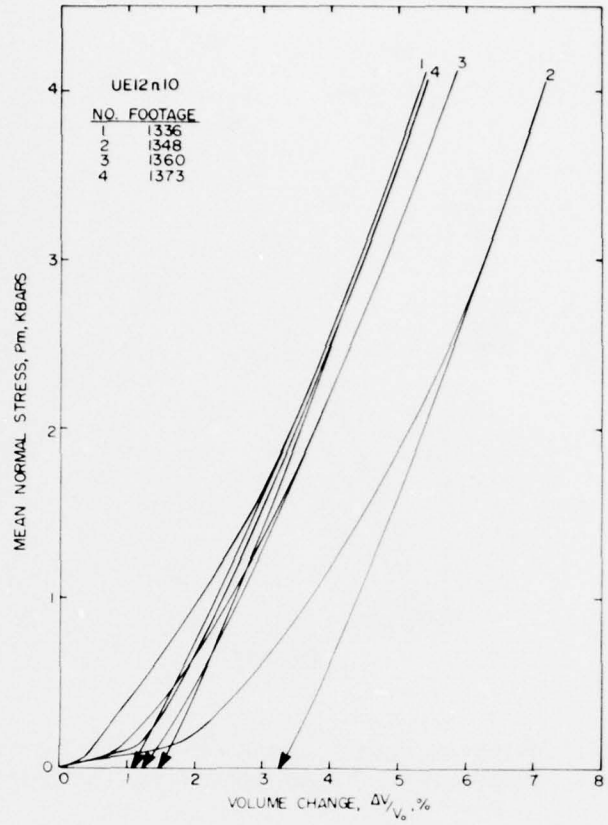


Figure B-4a. Uniaxial strain tests on UE12n#10 core samples--mean normal stress versus volume change.

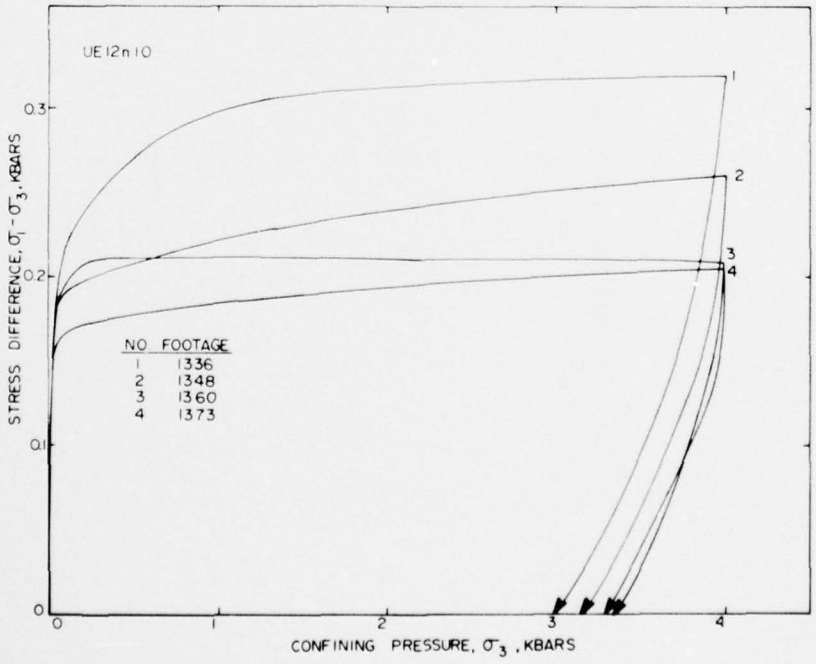


Figure B-4b. Uniaxial strain tests on UE12n#10 core samples--stress difference versus confining pressure.

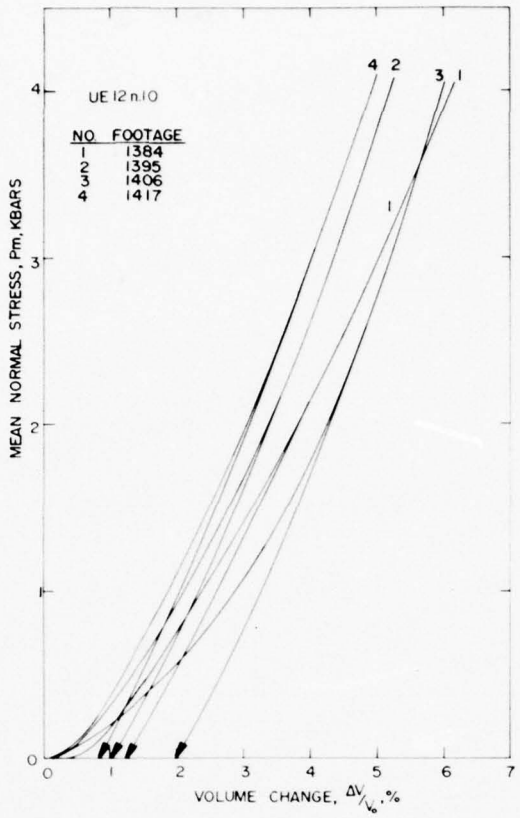


Figure B-5a. Uniaxial strain tests on UE12n#10 core samples--mean normal stress versus volume change.

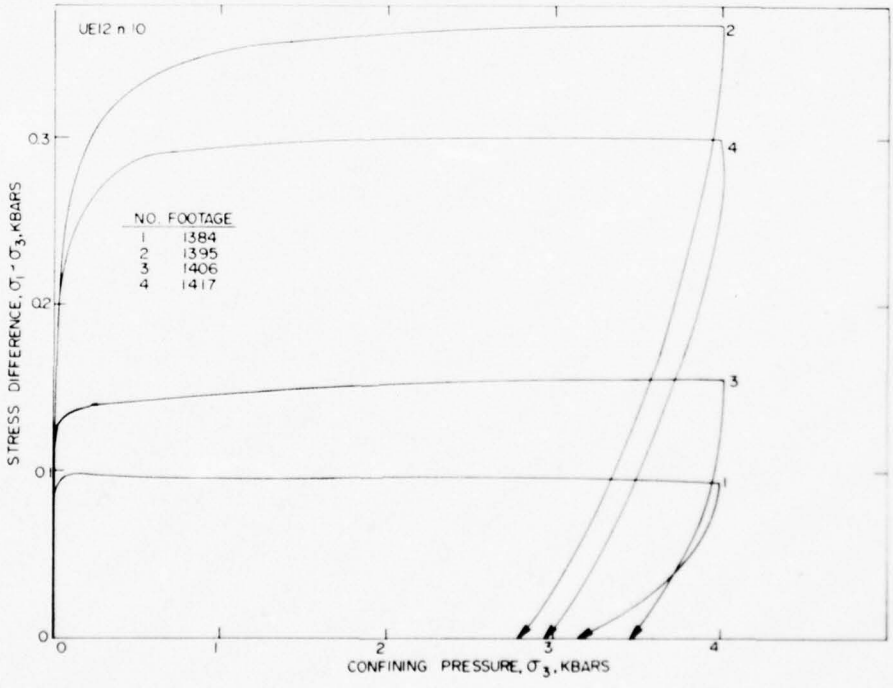


Figure B-5b. Uniaxial strain tests on UE12n#10 core samples--stress difference versus confining pressure.

MATERIAL PROPERTIES OF U12n.10A DNUG#5 CORE SAMPLES

PRECEDING PAGE BLANK-NOT FILMED

U12n.10A DNUG#5 VERTICAL DRILL HOLE SUMMARY

Ash-fall tuff core samples from vertical drill hole U12n.10A DNUG#5 were subjected to uniaxial strain tests, physical property and ultrasonic velocity measurements. The drill hole was collared at the Diablo Hawk working point in the U12n.10 main drift. Core samples tested were from between 12 feet and 99 feet (as measured downward from the tunnel floor) in approximately 10 foot increments. Additional core samples between the 20 foot through 30 foot depths were tested to identify a suspected area of high air void content.

Physical property and ultrasonic longitudinal and shear wave velocity measurements are listed in Table 1. Figure 1 is a plot of permanent volume compaction and calculated air void content versus drill hole footage for each sample tested. The uniaxial strain test curves are shown in Figures 2 through 5.

Test data indicate a nearly saturated tuff along most of the drill hole length with an undersaturated region between 20 feet and 25 feet. Air void content in this undersaturated area is about six percent. Average maximum stress difference at 4 kbars confining pressure appears to be around 0.3 kbars.

TABLE 1

Physical Properties, Uniaxial Strain Permanent Volume Compaction and Ultrasonic Wave Velocities of U12n.10A DNUG#5 Tuffs

DRILL HOLE FOOTAGE DN UG#5	DENSITY (gm/cc) AS-RECEIVED	DRY	GRAIN	WATER BY WET WEIGHT (%)	POROSITY (%)	SATURATION (%)	CALC. AIR VOIDS (%)	MEAS. PERMANENT COMP. (%)	VELOCITY (Km/sec/Ft./sec) LONG	SHEAR
12	1.85	1.51	2.40	18.6	37.1	92.6	2.7	1.5	2.98/9776	1.52/4986
16	1.88	1.55	2.38	17.4	34.7	94.0	2.1	2.3	3.17/10403	1.45/4740
19	1.77	1.44	2.18	18.7	34.0	97.4	0.9	2.3	2.69/8842	1.58/5187
21	1.73	1.35	2.36	21.8	42.7	88.4	4.9	4.6	2.12/6955	1.06/3477
24	1.77	1.44	2.39	18.8	39.9	83.4	6.6	5.9	2.32/7618	1.33/4363
27	1.82	1.45	2.38	20.4	39.1	94.8	2.0	1.3	2.90/9507	1.35/4438
28	1.81	1.41	2.46	22.0	42.6	93.4	2.8	1.8	2.16/7086	0.85/2788
40	1.80	1.39	2.41	22.7	42.4	96.1	1.7	1.4	2.57/8431	1.17/3838
50	1.84	1.46	2.40	20.5	39.0	96.5	1.4	1.6	2.85/9350	1.25/4101
59	1.78	1.32	2.43	25.4	45.5	99.2	0.4	0.6	2.78/9120	1.33/4363
69	1.93	1.58	2.51	18.1	37.0	94.2	2.1	1.0	2.88/9448	1.39/4560
81	1.94	1.60	2.49	17.7	35.9	95.7	1.5	1.4	2.47/8103	1.58/5183
90	1.98	1.69	2.51	14.8	32.8	89.4	3.5	1.6	2.92/9580	1.81/5938
99	1.89	1.53	2.44	19.0	37.2	96.3	1.4	0.5	2.56/8399	1.47/4822

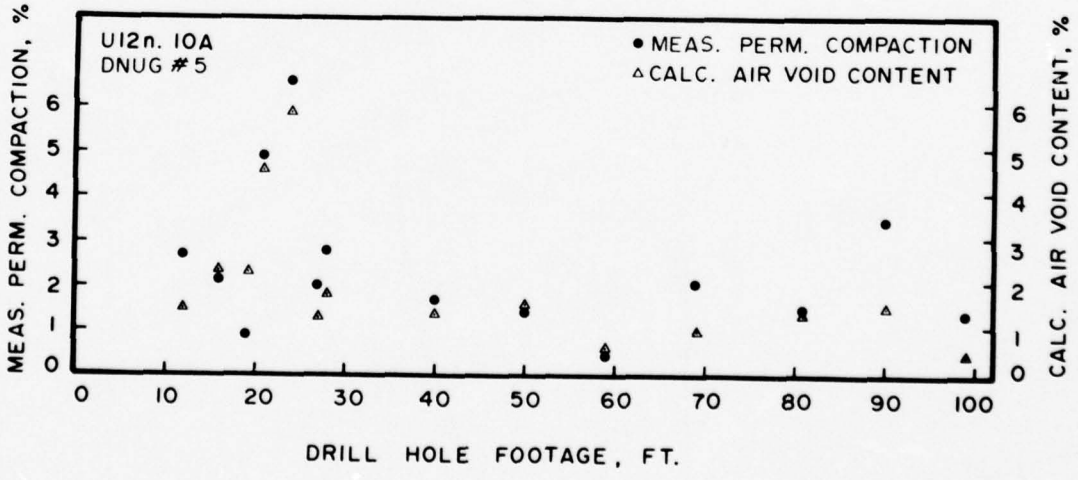


Figure 1. Comparison of U12n.10A DNUG#5 tuff measured permanent compaction and calculated air void content as a function of drill hole footage.

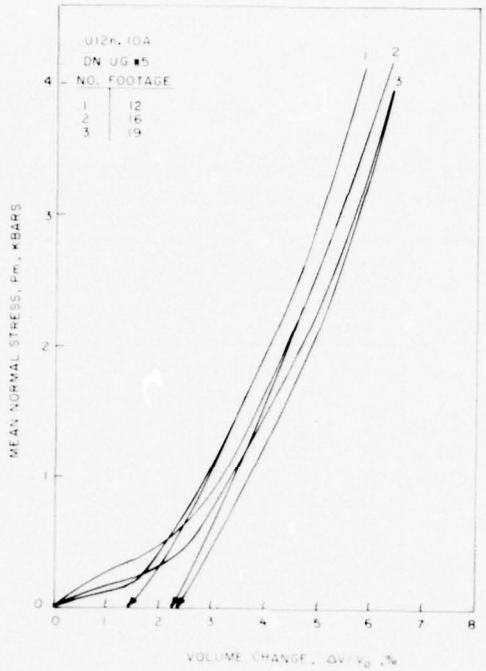


Figure 2a. Uniaxial strain test to 4 kbars confining pressure on U12n.10A DNUG#5 tuff samples -- mean normal stress versus volume change.

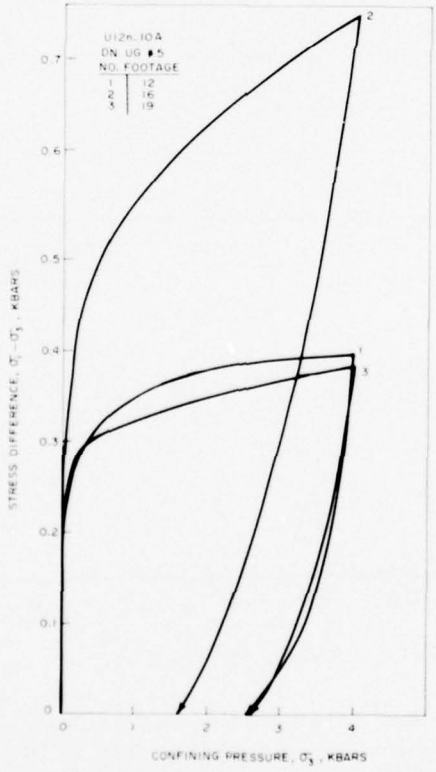


Figure 2b. Uniaxial strain test to 4 kbars confining pressure on U12n.10A DNUG#5 tuff samples -- stress difference versus confining pressure.

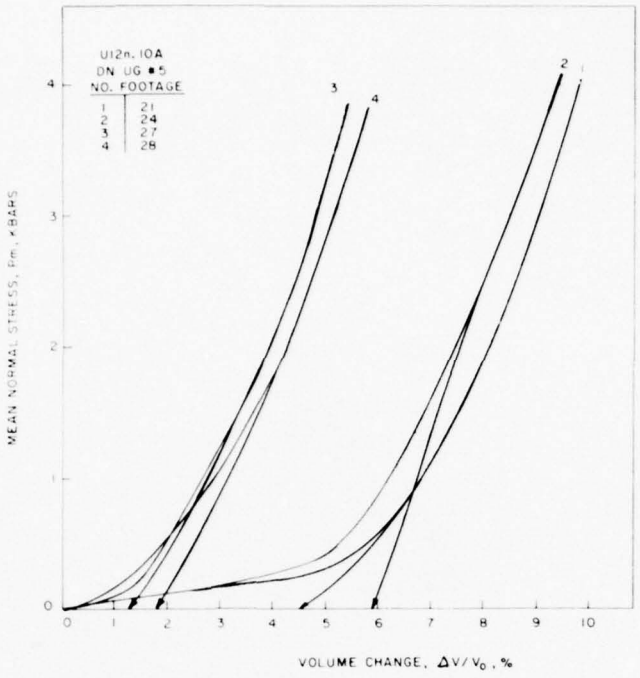


Figure 3a. Uniaxial strain test to 4 kbars confining pressure on U12n.10A DNUG#5 tuff samples -- mean normal stress versus volume change.

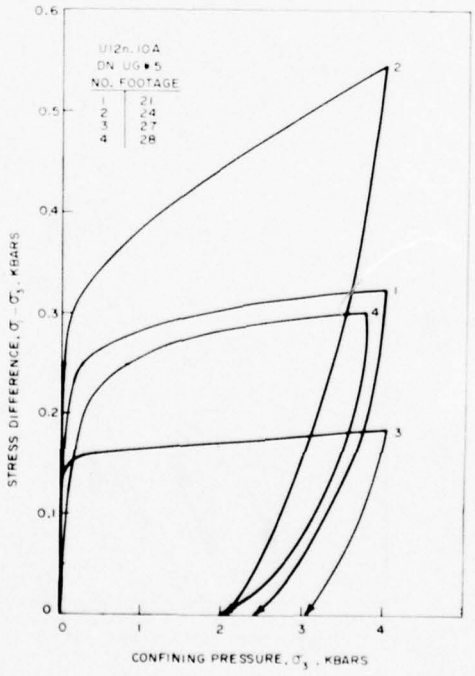


Figure 3b. Uniaxial strain test to 4 kbars confining pressure on U12n.10A DNUG#5 tuff samples -- stress difference versus confining pressure.

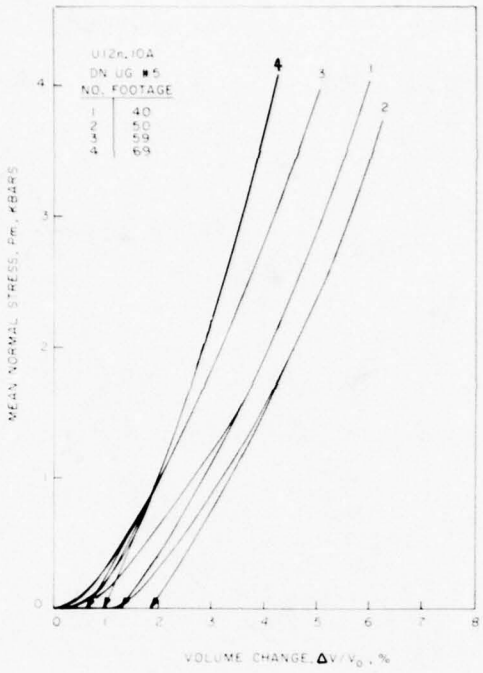


Figure 4a. Uniaxial strain test to 4 kbar confining pressure on U12n.10A DNUG#5 tuff samples -- mean normal stress versus volume change.

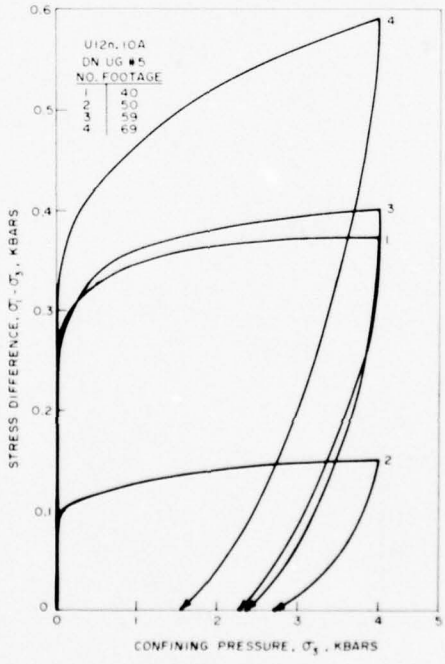


Figure 4b. Uniaxial strain test to 4 kbars confining pressure on U12n.10A DNUG#5 tuff samples -- stress difference versus confining pressure.

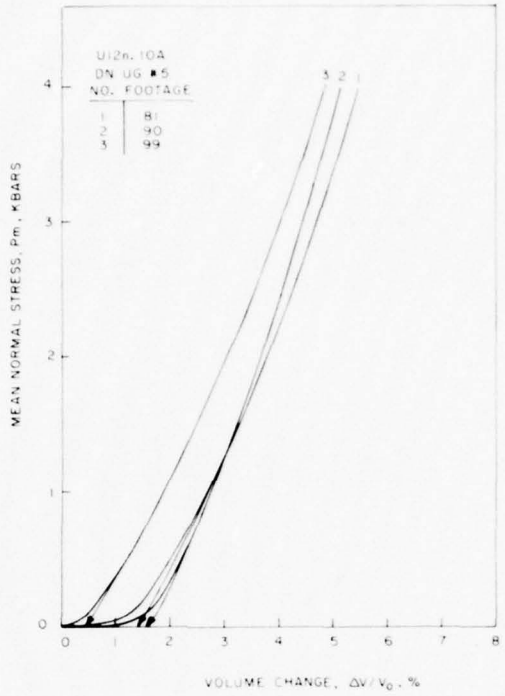


Figure 5a. Uniaxial strain test to 4 kbars confining pressure on U12n.10A DNUG#5 tuff samples -- mean normal stress versus volume change.

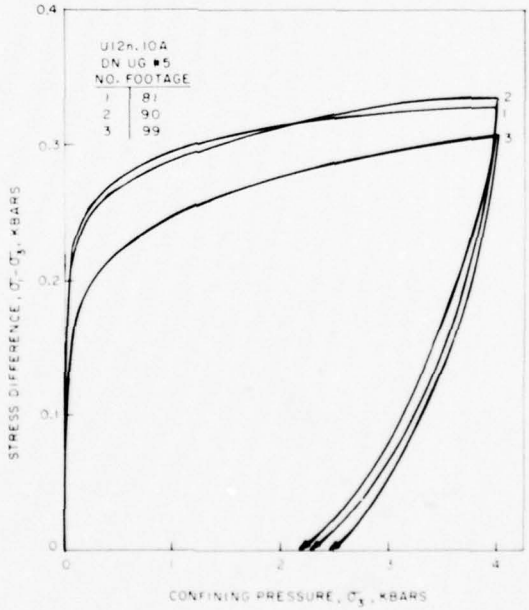


Figure 5b. Uniaxial strain test to 4 kbars confining pressure on U12n.10A DNUG#5 tuff samples -- stress difference versus confining pressure.

PHYSICAL AND MECHANICAL PROPERTIES OF DIABLO HAWK TUFF
MATCHING GROUT -- ME8-11

PRECEDING PAGE BLANK-NOT FILMED

TerraTek

September 14, 1977

Mr. J. W. LaComb
Defense Nuclear Agency
Nevada Test Site
Mercury, NV 89023

Dear Joe:

Enclosed are test results on the Diablo Hawk LOS Drift grouts (ME8-11). Six samples, designated

1. 12 + 58.5
2. 12 + 28
3. 12 + 17
4. 12 + 06
5. 11 + 94
6. 11 + 64

were tested for physical and mechanical properties. Material testing consisted of uniaxial strain tests to 4.0 kbars confining pressure and physical property and ultrasonic velocity measurements.

Test results are listed in Table I. Uniaxial strain test curves are shown in Figures 1 and 2. Test results show the grout to be slightly undersaturated with ~4 percent air voids. Stress difference averaged about 0.3 kbars at 4 kilobars confining pressure.

Also enclosed are average material property data that you requested on Mighty Epic structures area tuffs and Diablo Hawk stemming area tuffs. Select physical properties from these areas are listed in Table II for comparison with the average grout properties. Figure 3 shows the average uniaxial strain stress-stress curve for each group.

If you are in need of any further data for comparative purposes, please give me a call.

Sincerely,

Don Gardiner

D. S. Gardiner
Research Engineer

DSG/jlg

Enclosures

cc: Charles Welch, WES
Cliff Snow, DNA

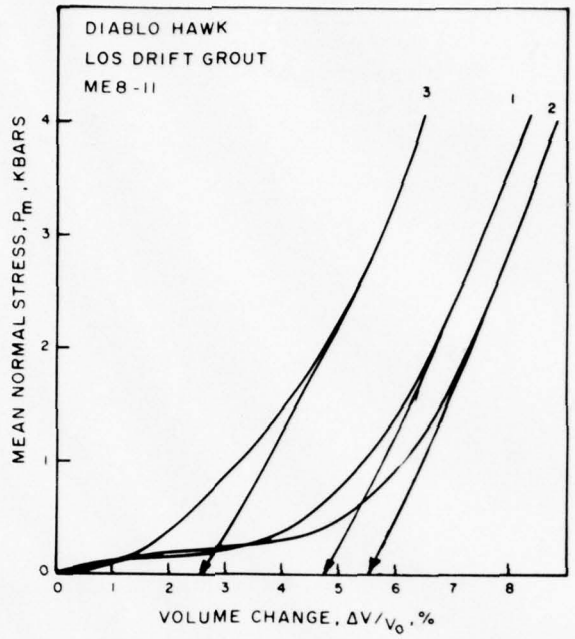


Figure 1a. Uniaxial strain test results on Diablo Hawk LOS Drift grout (ME8-11) -- mean normal stress versus volume change.

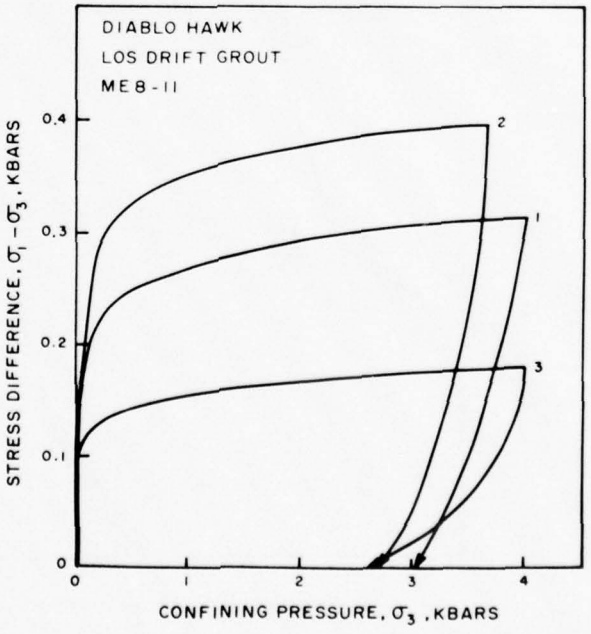


Figure 1b. Uniaxial strain test results on Diablo Hawk LOS Drift grout (ME8-11) -- stress difference versus confining pressure.

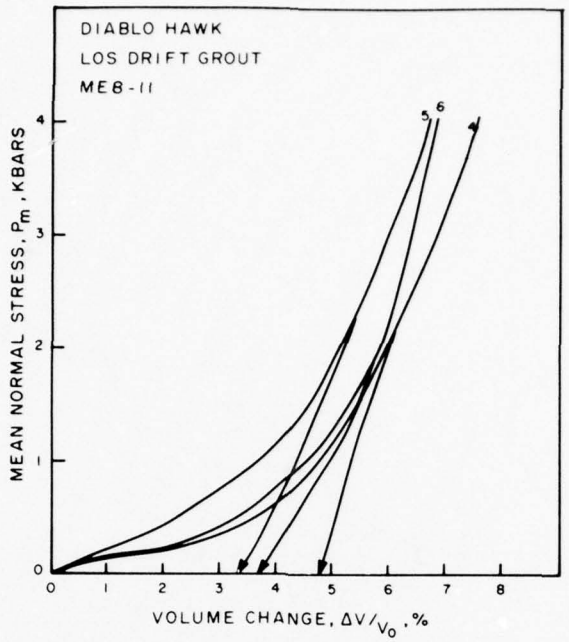


Figure 2a. Uniaxial strain test results on Diablo Hawk LOS Drift grout (ME8-11) -- mean normal stress versus volume change.

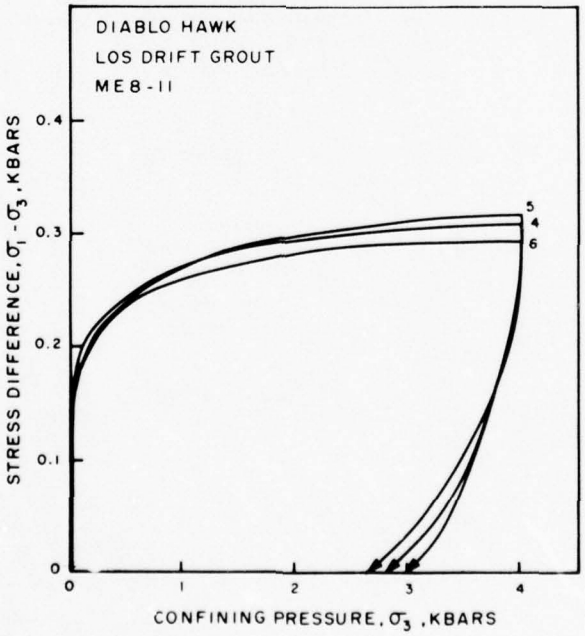


Figure 2b. Uniaxial strain test results on Diablo Hawk LOS Drift grout (ME8-11) -- stress difference versus confining pressure.

TABLE I

Diablo Hawk LOS Drift Grout

SAMPLE DESIGNATION	DENSITY (gm/cc)			WATER BY WET WEIGHT (%)	POROSITY (%)	SATURATION (%)	CALC. AIR VOIDS (%)	MEAS. PERMANENT COMP. (%)	VELOCITY (km/sec)	
	AS-RECEIVED	DRY	GRAIN						LONG	SHEAR
ME 8-11										
1	2.14	1.78	3.01	16.6	40.9	86.7	5.4	4.8	3.39	1.90
2	2.16	1.81	2.95	16.0	38.5	90.1	3.8	5.5	3.33	1.84
3	2.19	1.80	3.01	17.8	40.1	97.0	1.2	2.6	3.42	1.86
4	2.10	1.74	2.92	17.1	40.4	88.6	4.6	4.7	3.37	1.89
5	2.17	1.81	3.15	16.7	42.5	85.1	6.3	3.3	3.42	1.87
6	2.13	1.78	2.98	16.7	40.3	88.3	4.7	3.7	3.41	1.85

TABLE II

Select Average Properties of Tuffs and Grouts Relating to the Diablo Hawk Event

	Mighty Epic* Tuff (Structures)	Diablo Hawk* Tuff (Stemming Area)	Diablo Hawk Grout (LOS Drift)
As Received Density (gm/cc)	1.95 ± 0.05	1.91 ± 0.07	2.15 ± 0.03
Water Content by Wet Weight (%)	15.7 ± 2.6	18.0 ± 2.7	16.8 ± 0.6
Porosity (%)	31.0 ± 7.0	36.7 ± 4.0	40.4 ± 1.3
Air Voids (%)**	1.0 ± 0.4	1.6 ± 1.4	4.1 ± 1.1
Ultrasonic Longitudinal Velocity (km/sec)	3.14 ± 0.3	3.07 ± 0.4	3.50 ± 0.7

* Mighty Epic Tuff - U12n.10 UG#4, UG#6a; see TR 76-63, pg. 210.
Diablo Hawk Tuff - U12n.10 GSCH#3, DNHF#3

** Air void is the permanent volume compaction from the uniaxial strain test.

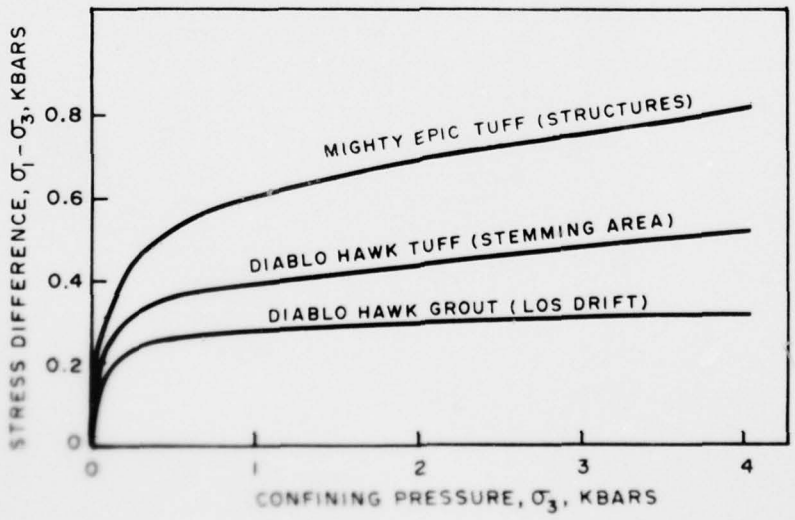


Figure 1. Average uniaxial strain curves for Diablo Hawk tuffs and grouts.

SOME MATERIAL PROPERTIES OF DIABLO HAWK TUFF ASSOCIATED WITH THE TRW EXPERIMENT

TR 77-95
October 1977

SOME MATERIAL PROPERTIES OF DIABLO HAWK TUFF ASSOCIATED WITH THE TRW EXPERIMENT

Material property testing of tuffs associated with the TRW experiment was not completed at the time of submittal of this final report. To maintain continuity, the report, in its entirety, will be published at a later date when testing is completed.

DIABLO HAWK STRUCTURES TUFF MATERIAL PROPERTIES -- BOEING DRIFT

TR 77-90
October 1977

ABSTRACT

An experiment planned for the Diablo Hawk event in Area 12 at the Nevada Test Site involves the emplacement of a horizontal column of saturated sand. A portion of the Boeing drift, located near ground zero, will be used to house the sand column. Mechanical testing of the saturated sand has been conducted to characterize its response under selected stress conditions[1]. This report summarizes the characterization of the Boeing drift media (tuff).

1. Gardiner, D. S., Butters, S. W., "High Pressure Mechanical Properties of Saturated Lapis Lustre Sand," Terra Tek Report TR 77-70, August 1977.

INTRODUCTION

Material properties of the tuff media surrounding the Boeing drift at the Diablo Hawk event (Area 12 NTS) are required for pre-test ground motion calculations. Selected samples of tuff from three specific locations were characterized: (1) near the working point (GSHF#3 and GSCH#4); (2) at the working point end of the Boeing drift (PIFF#1); and (3) near R.S. 400' in the Boeing drift (PIFF#9). Respective locations of these drill holes are shown below in Figure 1.

Material characterization of the tuff was accomplished through measurement of both mechanical and physical properties. Mechanical testing included hydrostatic and triaxial compression and uniaxial strain tests. Confining pressure ranged from 0 (unconfined compression) to 8 kbars. Physical properties measured were "as received" density, content moisture and grain density. Porosity, saturation and air void content were calculated from the measured physical properties.

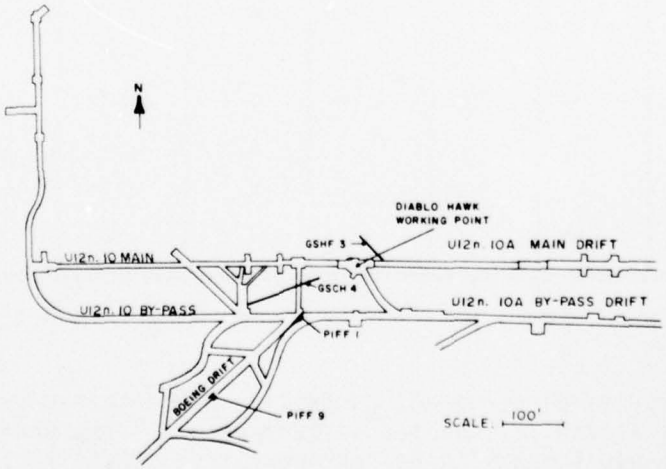


Figure 1. Plan view of Boeing drift and selected drill holes.

TEST RESULTS

Physical properties and measured permanent compaction (from both hydrostatic compression and uniaxial strain tests) are listed in Table 1. Maximum stress difference during triaxial compression is plotted in the form of failure envelopes in Figure 2 through 4 for GSHF#3-GSCH#4, PIFF#1 and PIFF#9 respectively. Stress-strain curves for hydrostatic and triaxial compression tests are shown in the Appendix. Uniaxial strain test results are shown in Figures 5 through 7 as stress difference versus confining pressure. Complete uniaxial strain test curves are also shown in the Appendix.

TABLE 1

Physical Properties and Measured Permanent Compaction on Diablo Hawk Structures Tuff (U12n.10A)

DRILL HOLE FOOTAGE	DENSITY (gm/cc)			WATER BY WET WEIGHT (%)	POROSITY (%)	SATURATION (%)	CALC. AIR VOIDS (%)	MEAS. PERMANENT COMP. (%)	
	AS-RECEIVED	DRY	GRAIN					Hyd.	I-D
PIFF#1 12'	1.84	1.51	2.40	17.8	36.9	88.8	4.1	-0	2.0
PIFF#1 20'	--	--	--	--	--	--	--	4.5	2.0
PIFF#9 5'	1.84	1.52	2.43	17.4	37.4	85.5	5.4	2.1	1.0
PIFF#9 6'	--	--	--	--	--	--	--	5.1	4.1
GSHF#3 20'	1.83	1.47	2.40	19.5	38.6	92.4	2.7	*9.0	2.0
GSCH#4 113	1.94	1.60	2.49	17.1	35.5	93.4	2.4	*7.5	2.0

* Hydrostatic compression permanent compaction was obtained by using 3 times the axial strain (transverse strains were not measured). These high values are not thought to be representative of the *in situ* air void content since both the calculated air voids and the uniaxial strain measured permanent compaction indicate much lower values.

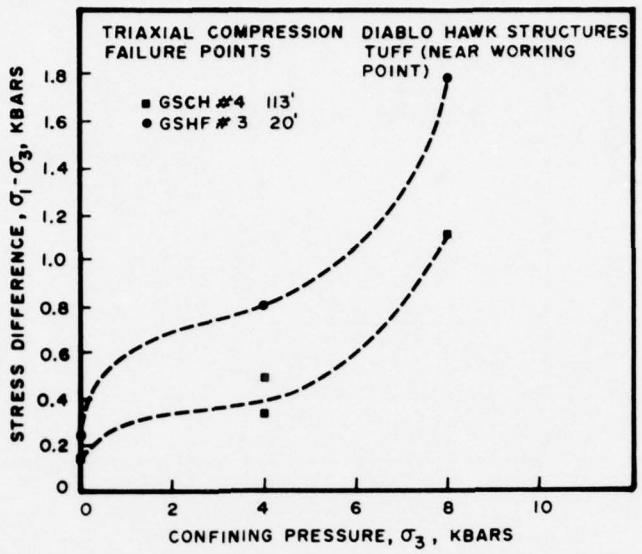


Figure 2. Triaxial compression failure points of GSCH#4 and GSHF#3 tuff samples. Dashed lines are estimates of failure envelopes.

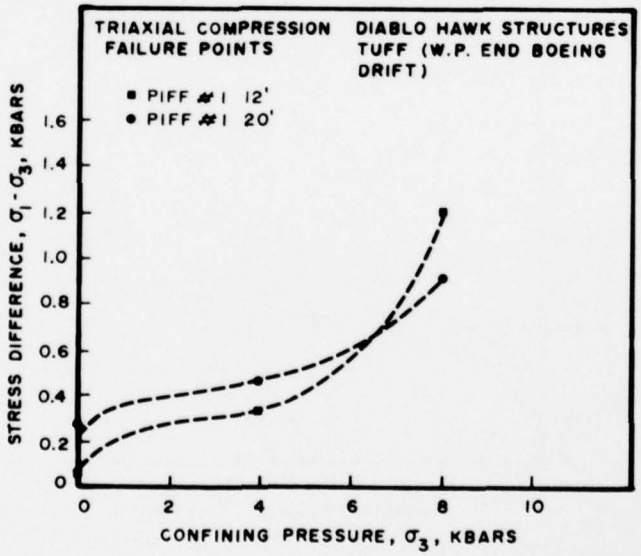


Figure 3. Triaxial compression failure points of PIFF#1 tuff samples. Dashed lines are estimates of failure envelopes.

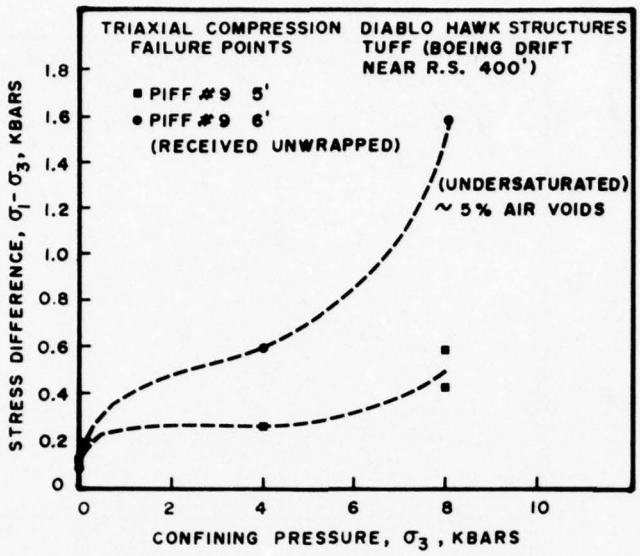


Figure 4. Triaxial compression failure points of PIFF#9 tuff samples. Dashed lines are estimates of failure envelopes.

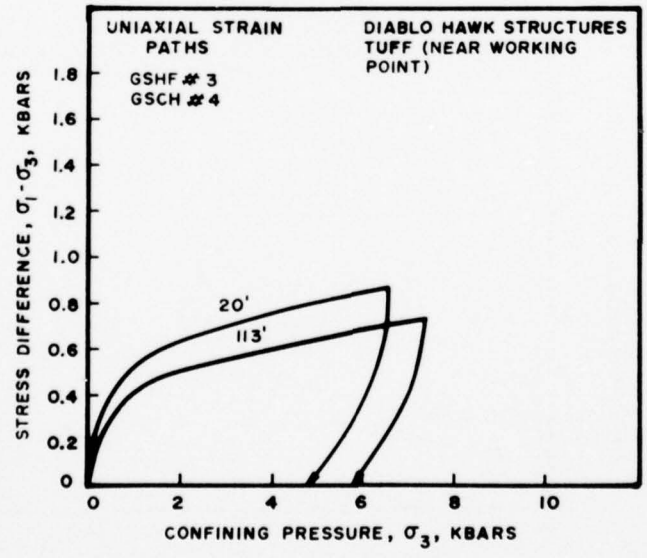


Figure 5. Uniaxial strain paths of GSHF#3 and GSCH#4 tuff samples.

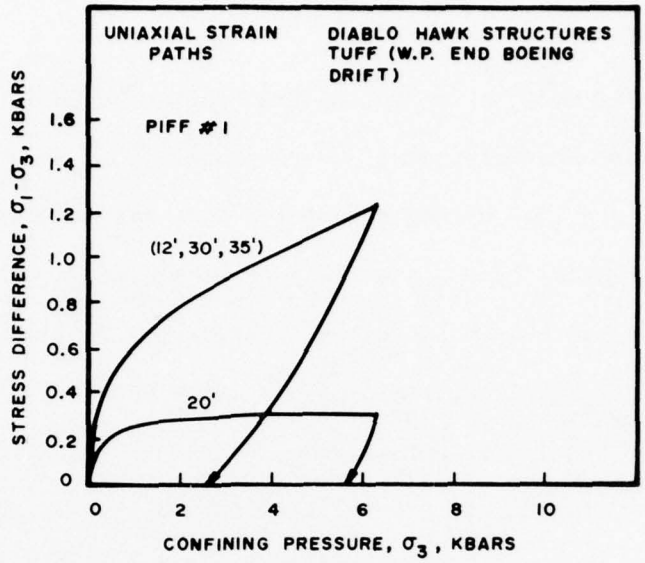


Figure 6. Uniaxial strain paths of PIFF#1 tuff samples.

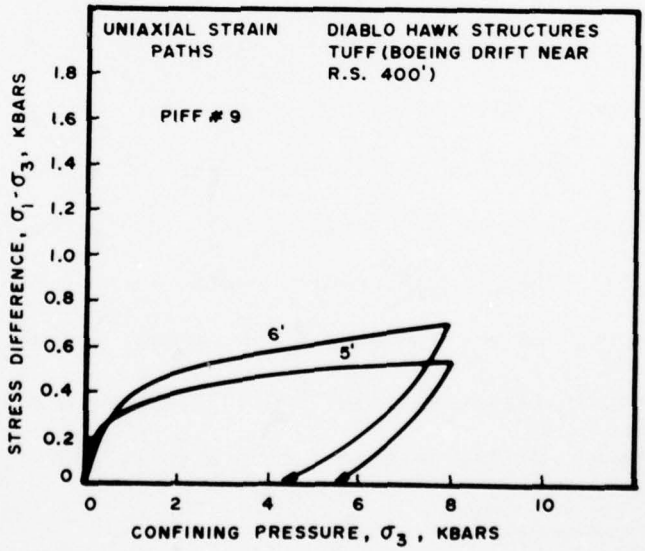


Figure 7. Uniaxial strain paths of PIFF#9 tuff samples.

DISCUSSION

Test results show, as expected, the scatter in tuff response for samples from the various core holes. Percentage air voids varied from sample to sample even though they were taken from the same approximate location. Also, triaxial compression failure points fall both below and above the uniaxial strain path. Since the triaxial compression failure strength should always be above the stress-stress curve generated by the uniaxial strain curves, this is further evidence of the tuff scatter.

With regard to the failure surface, the data up to the 4 kbars confining pressure is typical of previous results[2]. That is, shear strength increases by factors of 2 or 3 with increased confining pressure up to about 0.2 kbars. From ~0.2 kbars to 4 kbars, the increases in shear strength are much less dramatic, on the order of 20-50 percent. From 4 to 8 kbars confining pressure, however, the shear strength again shows substantial increases with increasing confining pressure (i.e. based on data points at 4 and 8 kbars confining pressure).

Although the reasons for this behavior are not completely understood, it is thought that the pore pressure and hence the effective stress play an important role. That is, at the low confining pressure (0 to ~0.2 kbars), the material matrix supports a substantial amount of the stress due to the confining pressure, resulting in low pore pressure and high effective stresses. At the intermediate pressures (0.2 to 4.0 kbars) the

---

2. Butters, S. W., Dropek, R. K., Jones, A. H., "Material Properties of Nevada Test Site Tuff and Grout with Emphasis on the Mighty Epic Event," Terra Tek Report TR 76-63, November 1976.

rock matrix is breaking down and the pore pressure increases with the confining pressure, resulting in very little increase in the effective stress over this confining pressure range. At confining pressures above approximately 4 kbars, the rock matrix has collapsed to the point where it again begins to carry an increased percentage of the added stress and the effective stress increases rapidly as a function of the confining pressure.

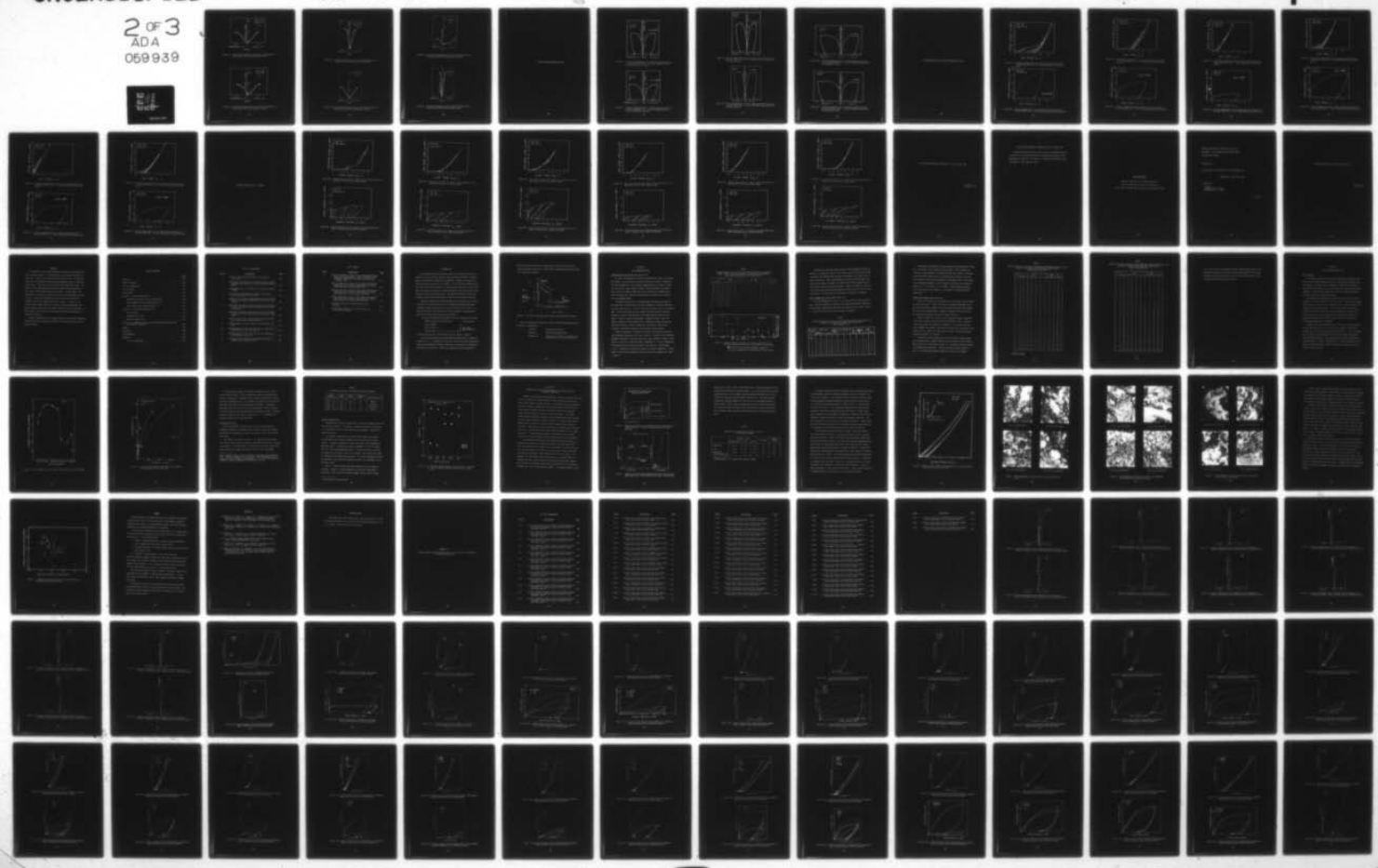
The above reasoning would appear to explain the increase in shear strength above 4 kbars confining pressure. The uniaxial strain path is expected to show similar increases. Future tests at confining pressures above 4 kbars should include pore pressure measurements.

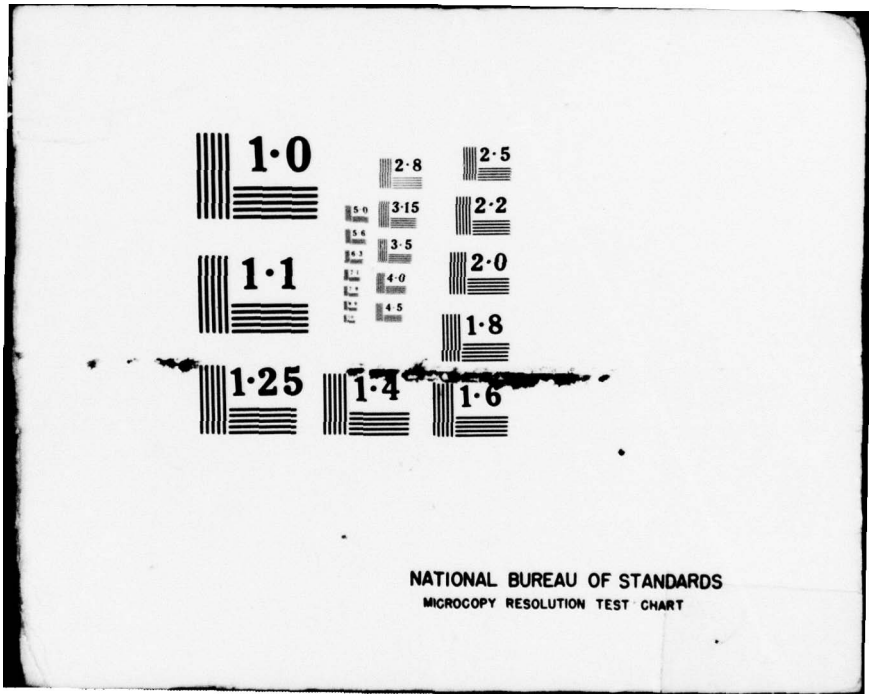
APPENDIX

UNCONFINED COMPRESSION TESTS

AD-A059 939 TERRA TEK INC SALT LAKE CITY UTAH F/G 18/3
MATERIAL PROPERTIES OF NEVADA TEST SITE TUFF AND GROUT--WITH EM--ETC(U)
NOV 77 D S GARDINER, D O ENNISS, S W BUTTERS DNA001-76-C-0351
UNCLASSIFIED TR-77-96 DNA-4528F NL

2 OF 3
ADA
059939




1·0
1·1
1·25
1·4
1·6
1·8
2·0
2·2
2·5
2·8
3·15
3·5
4·0
4·5
5·0
NATIONAL BUREAU OF STANDARDS
MICROCOPY RESOLUTION TEST CHART

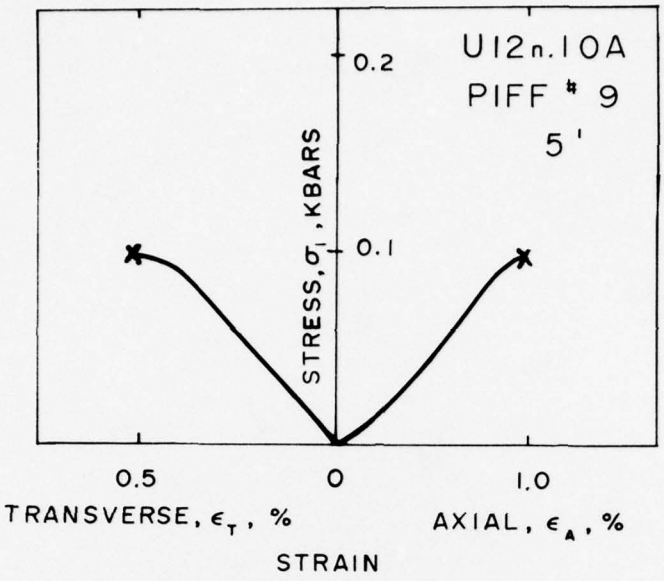


Figure A1. Unconfined compression test on U12n.10A PIFF#9 tuff -- stress versus axial and transverse strains.

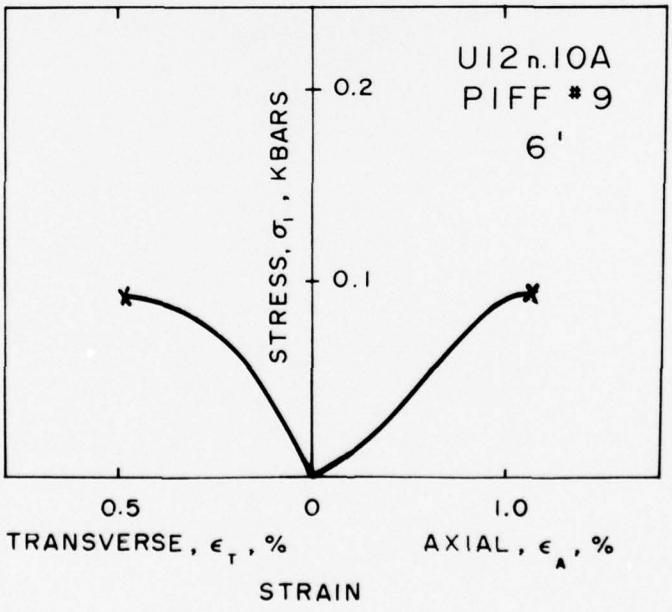


Figure A2. Unconfined compression test on U12n.10A PIFF#9 tuff -- stress versus axial and transverse strains.

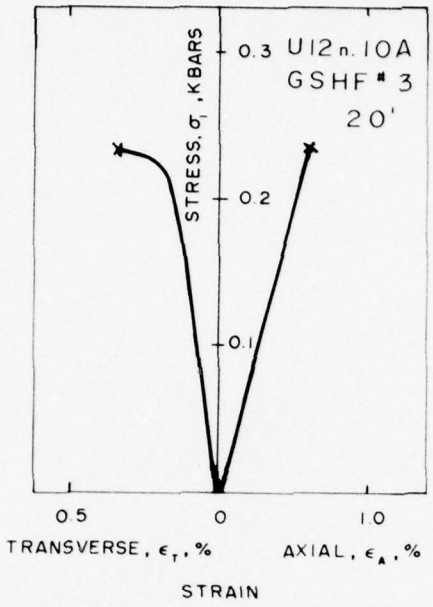


Figure A3. Unconfined compression test on U12n.10A GSHF#3 tuff -- stress versus axial and transverse strains.

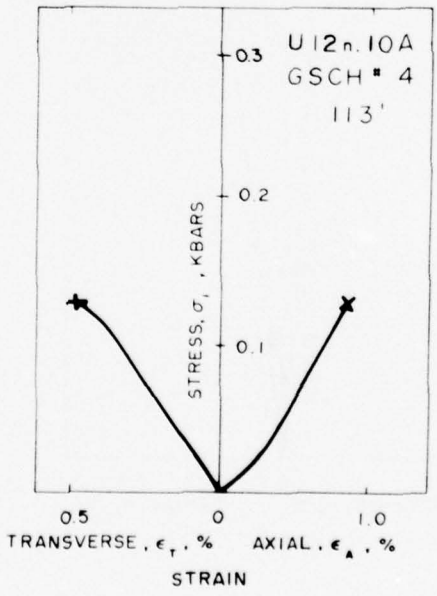


Figure A4. Unconfined compression test on U12n.10A GSCH#4 tuff -- stress versus axial and transverse strains.

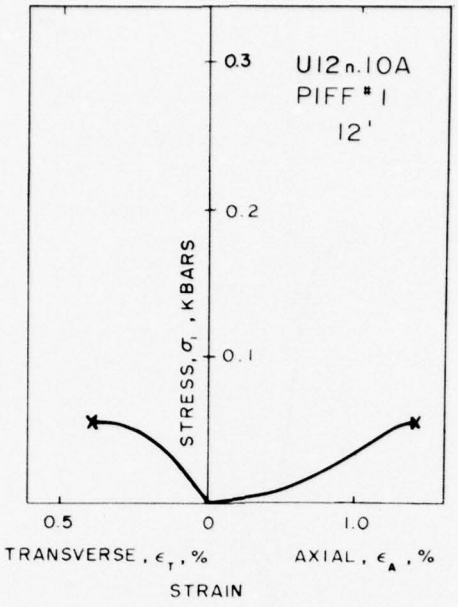


Figure A5. Unconfined compression test on U12n.10A PIFF#1 tuff -- stress versus axial and transverse strains.

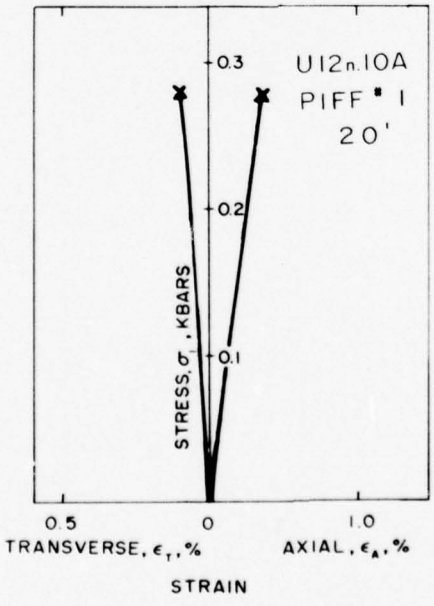


Figure A6. Unconfined compression test on U12n.10A PIFF#1 tuff -- stress versus axial and transverse strains.

4 KBAR TRIAXIAL COMPRESSION TESTS

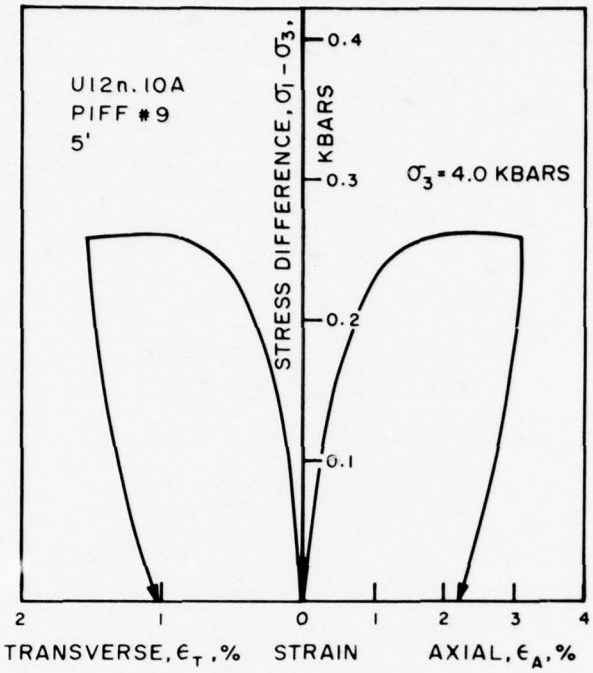


Figure A7. Triaxial compression test at 4 kbars confining pressure on U12n.10A PIFF#9 tuff -- stress difference versus axial and transverse strains.

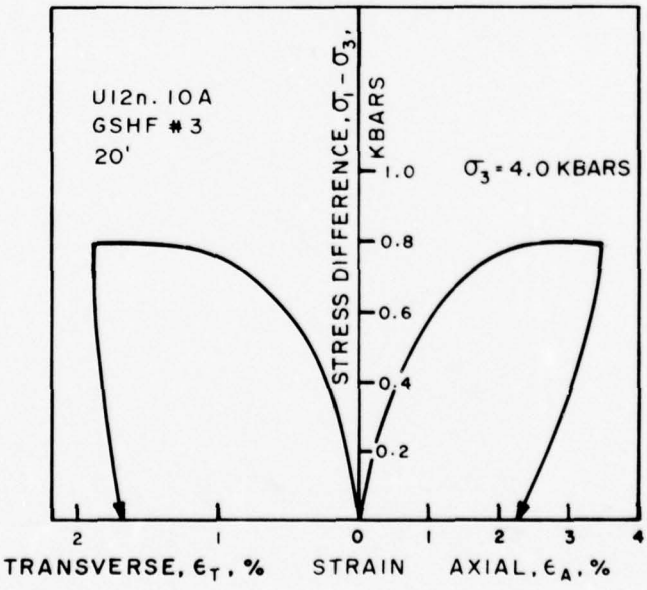


Figure A8. Triaxial compression test at 4 kbars confining pressure on U12n.10A GSHF#3 tuff -- stress difference versus axial and transverse strains.

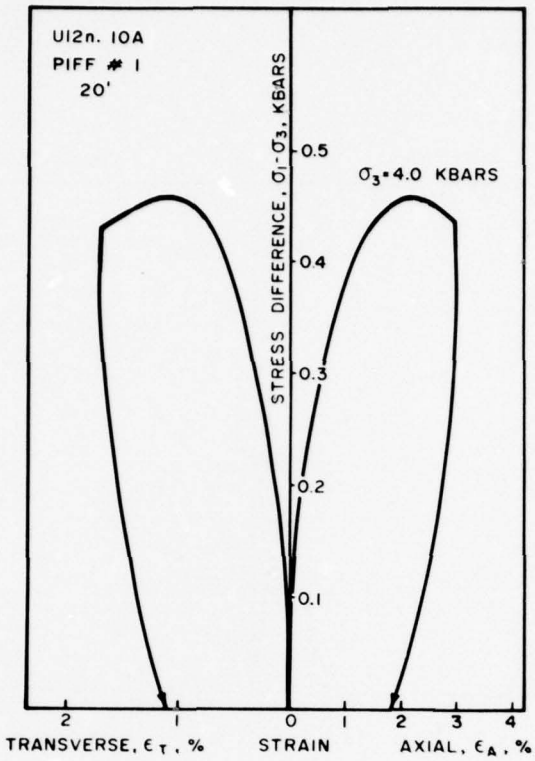


Figure A9. Triaxial compression test at 4 kbars confining pressure on U12n.10A PIFF#1 tuff -- stress difference versus axial and transverse strains.

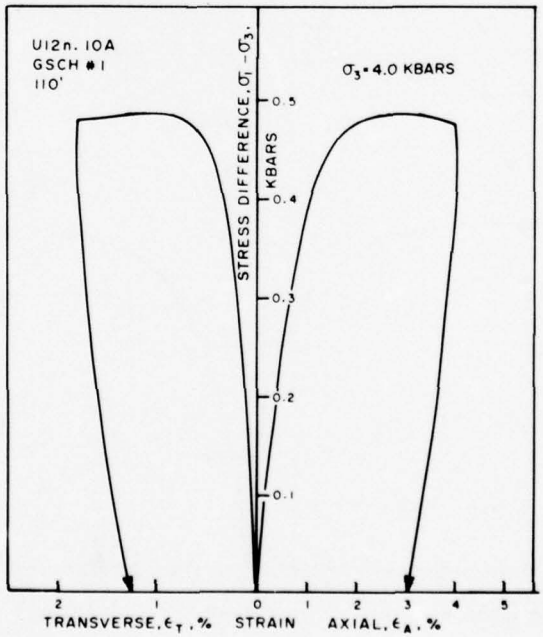


Figure A10. Triaxial compression test at 4 kbars confining pressure on U12n.10A GSCH#1 tuff -- stress difference versus axial and transverse strains.

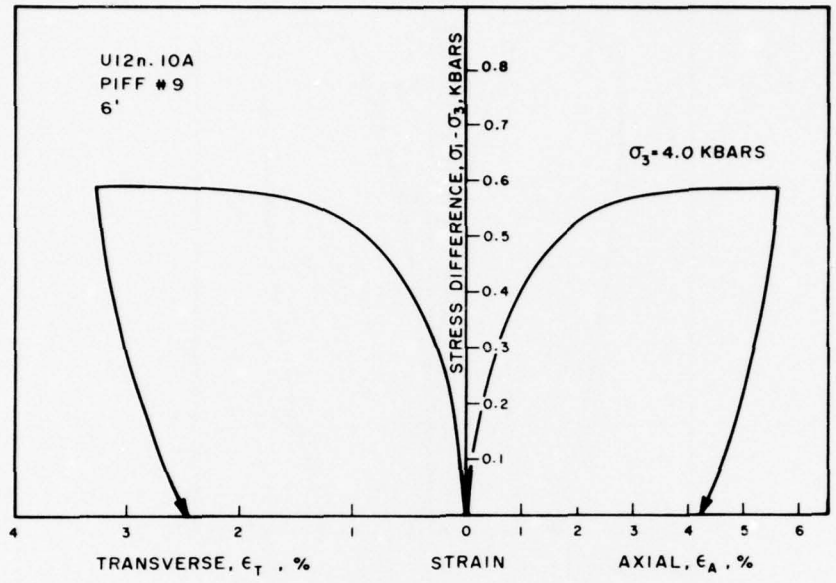


Figure A11. Triaxial compression test at 4 kbars confining pressure on U12n.10A PIFF#9 tuff -- stress difference versus axial and transverse strains.

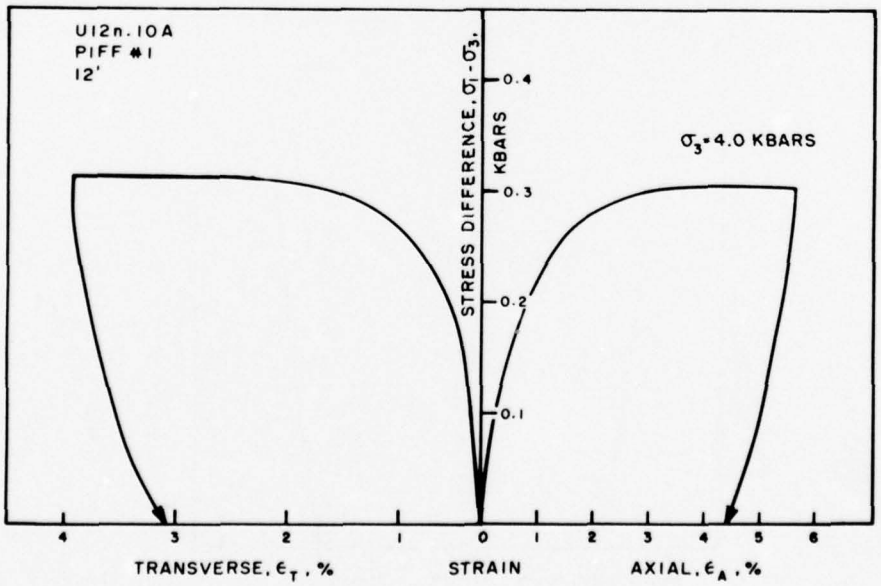


Figure A12. Triaxial compression test at 4 kbars confining pressure on U12n.10A PIFF#1 tuff -- stress difference versus axial and transverse strains.

8 KBAR HYDROSTATIC AND TRIAXIAL COMPRESSION TESTS

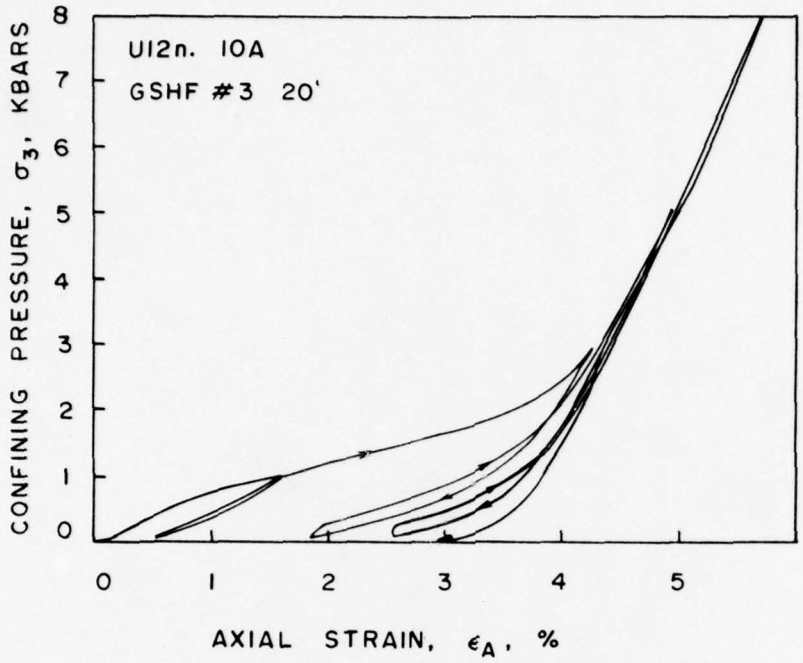


Figure A13. Hydrostatic compression test to 8 kbars confining pressure on U12n.10A GSHF#3 tuff -- confining pressure versus axial strain.

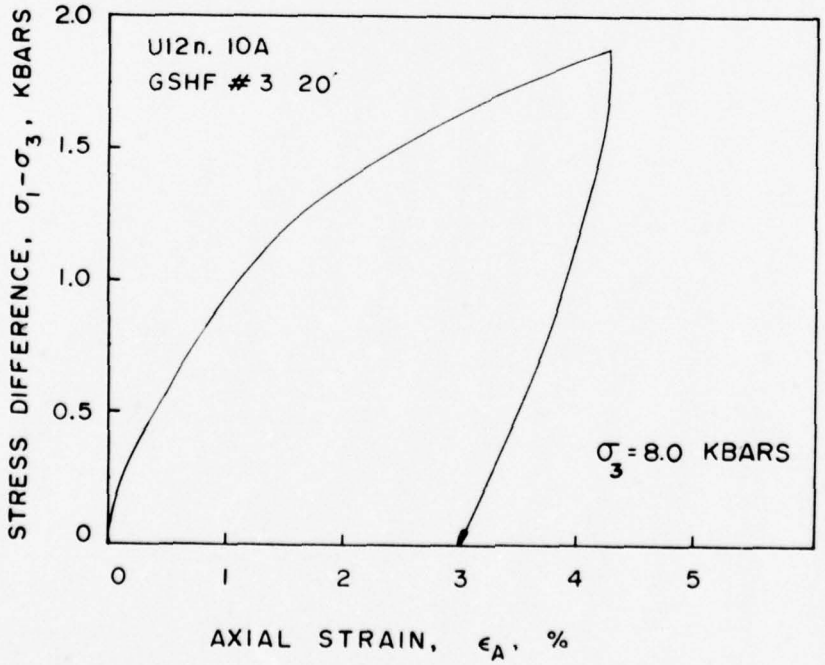


Figure A14. Triaxial compression test at 8 kbars confining pressure on U12n.10A GSHF#3 tuff -- stress difference versus axial strain.

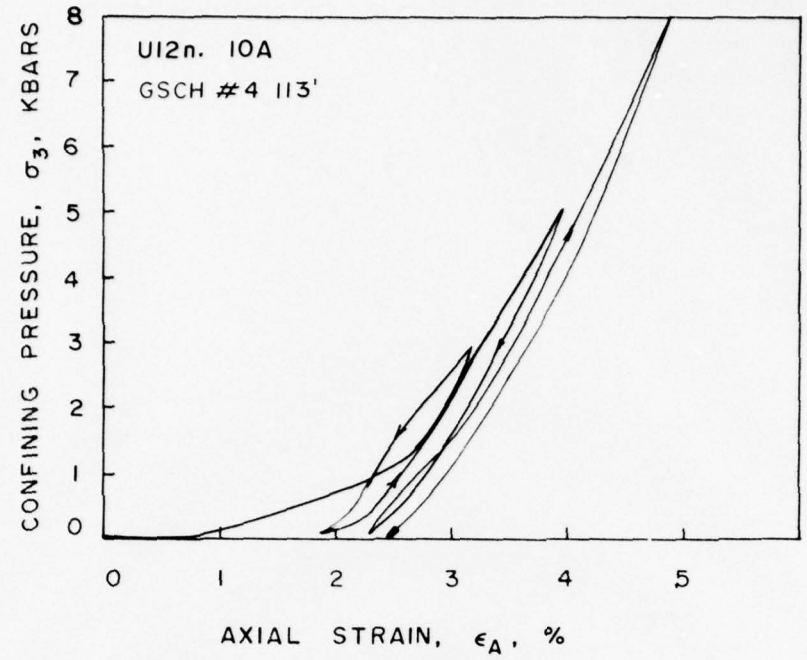


Figure A15. Hydrostatic compression test to 8 kbars confining pressure on U12n.10A GSCH#4 tuff -- confining pressure versus axial strain.

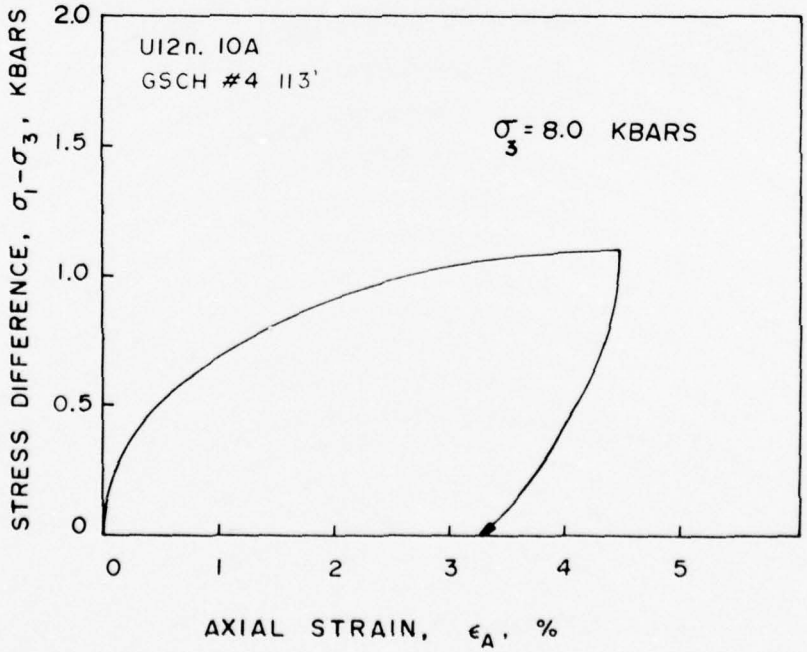


Figure A16. Triaxial compression test at 8 kbars confining pressure on U12n.10A GSCH#4 tuff -- stress difference versus axial strain.

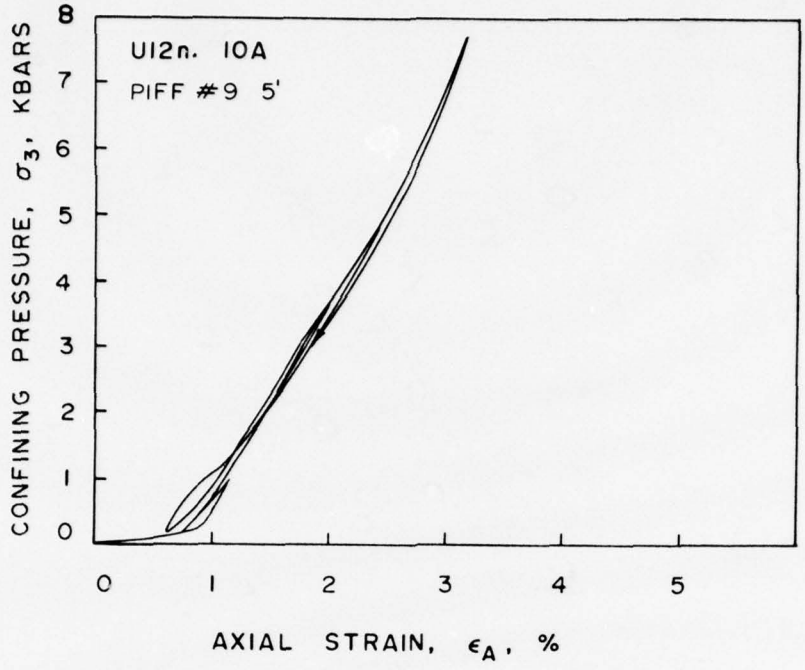


Figure A17. Hydrostatic compression test to 8 kbars confining pressure on U12n.10A PIFF#9 tuff -- confining pressure versus axial strain.

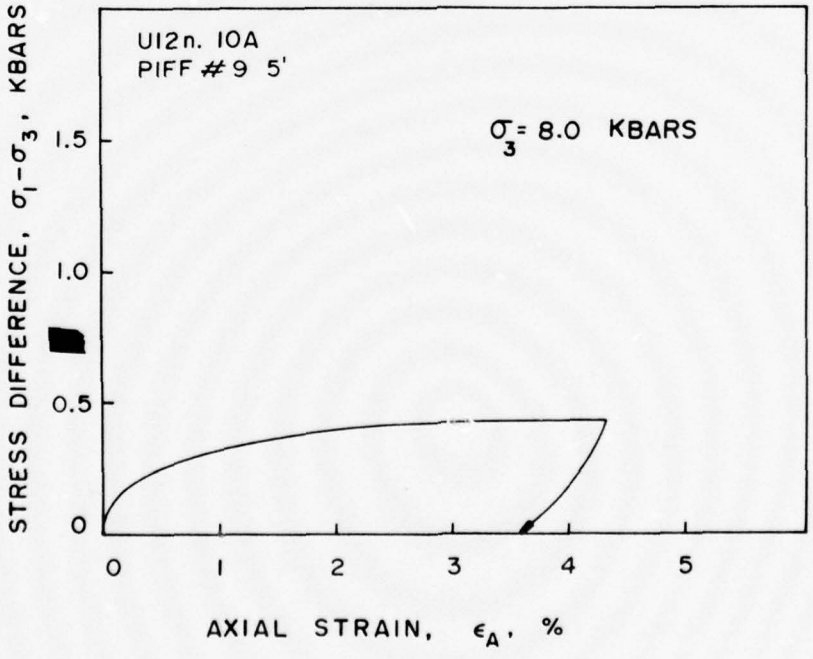


Figure A18. Triaxial compression test at 8 kbars confining pressure on U12n.10A PIFF#9 tuff -- stress difference versus axial strain.

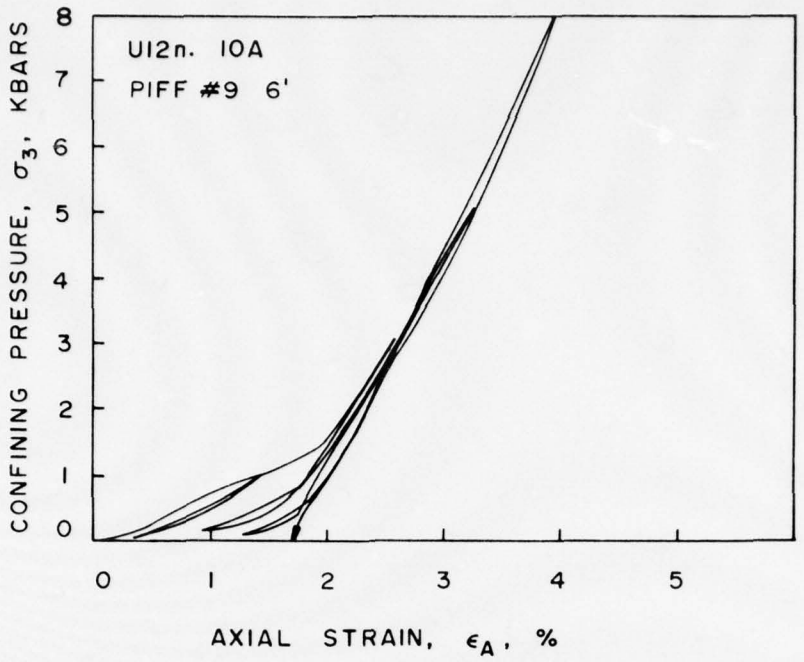


Figure A19. Hydrostatic compression test to 8 kbars confining pressure on U12n.10A PIFF#9 tuff -- confining pressure versus axial strain.

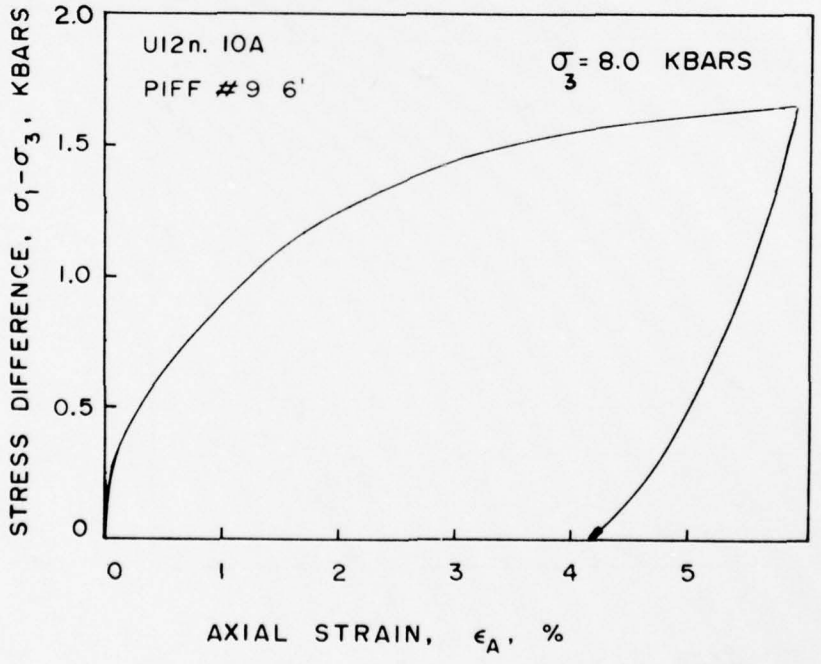


Figure A20. Triaxial compression test at 8 kbars confining pressure on U12n.10A PIFF#9 tuff -- stress difference versus axial strain.

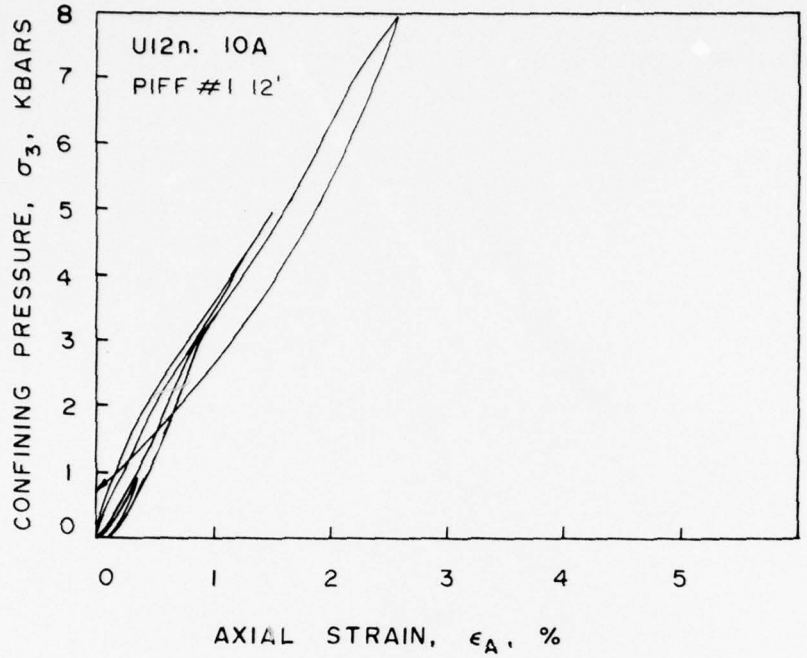


Figure A21. Hydrostatic compression test to 8 kbars confining pressure on U12n.10A PIFF#1 tuff -- confining pressure versus axial strain.

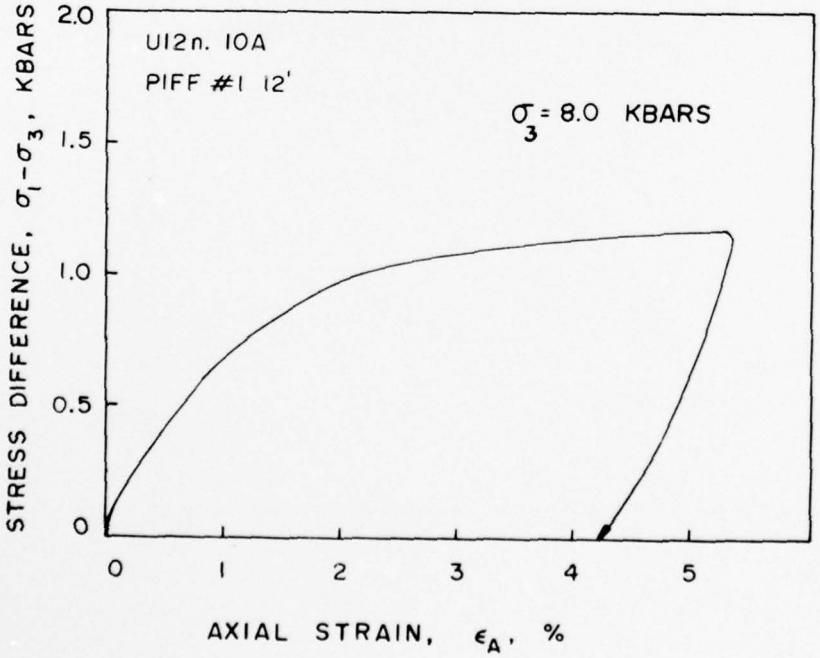


Figure A22. Triaxial compression test at 8 kbars confining pressure on U12n.10A PIFF#1 tuff -- stress difference versus axial strain.

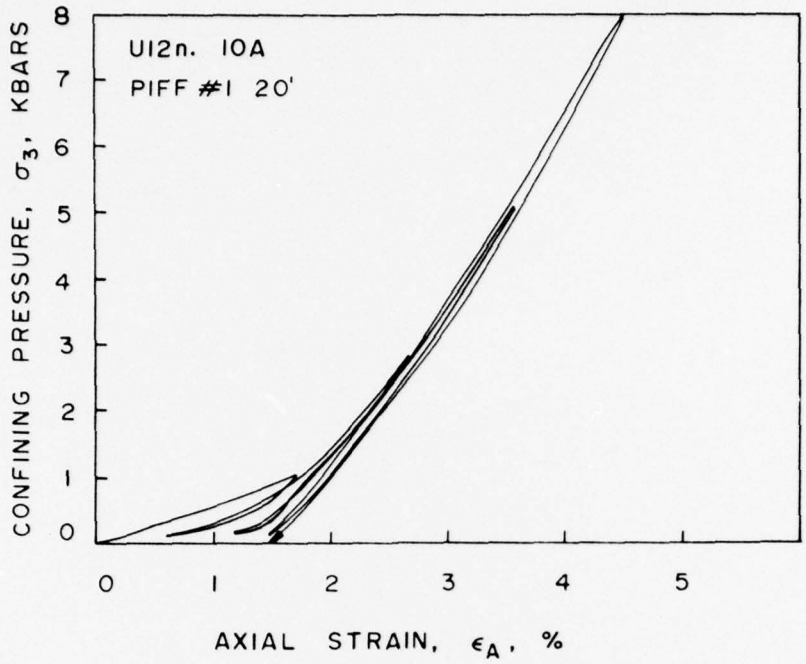


Figure A23. Hydrostatic compression test to 8 kbars confining pressure on U12n.10A PIFF#1 tuff -- confining pressure versus axial strain.

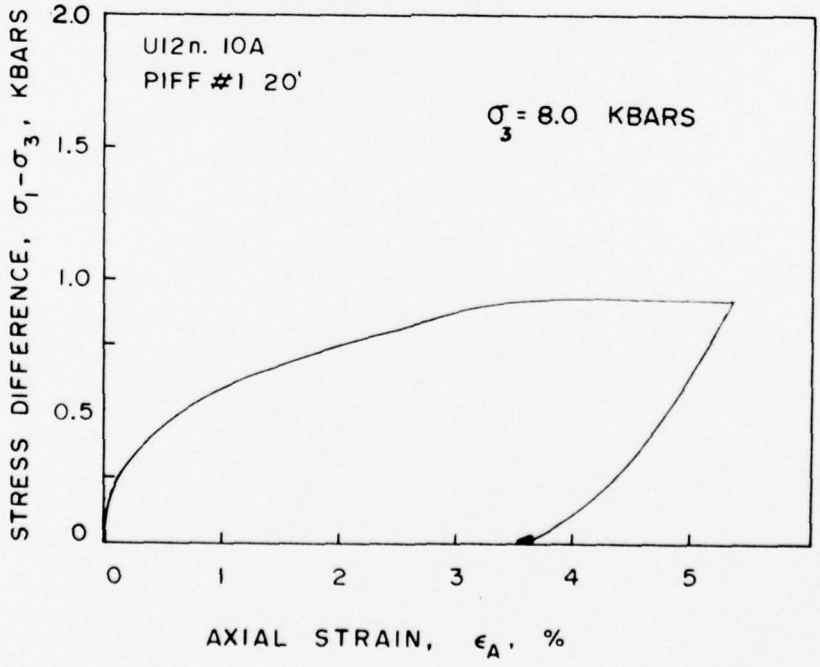


Figure A24. Triaxial compression test at 8 kbars confining pressure on U12n.10A PIFF#1 tuff -- stress difference versus axial strain.

UNIAXIAL STRAIN TEST TO ~8 KBARS

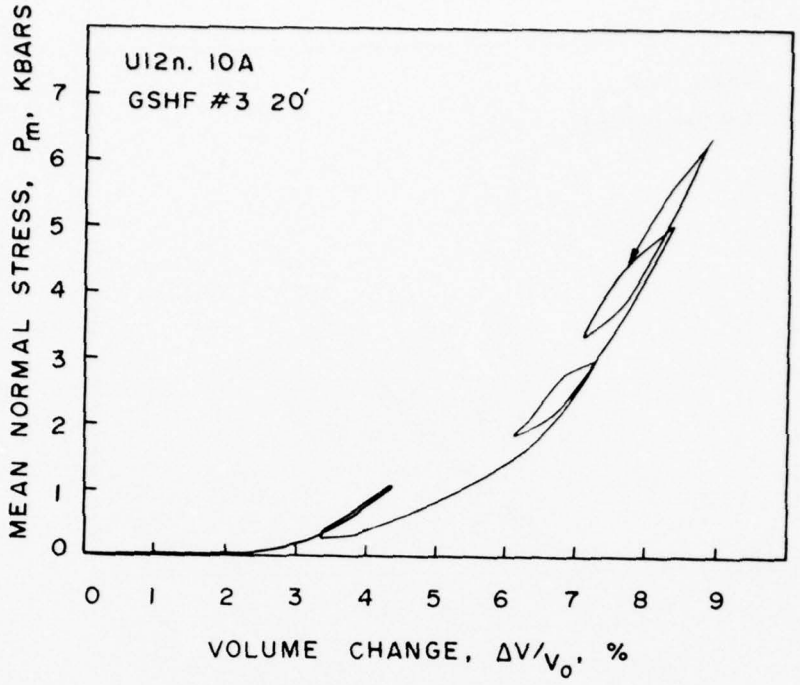


Figure A25. Uniaxial strain test to 6.5 kbars on U12n.10A GSHF#3 tuff -- mean normal stress versus volume change.

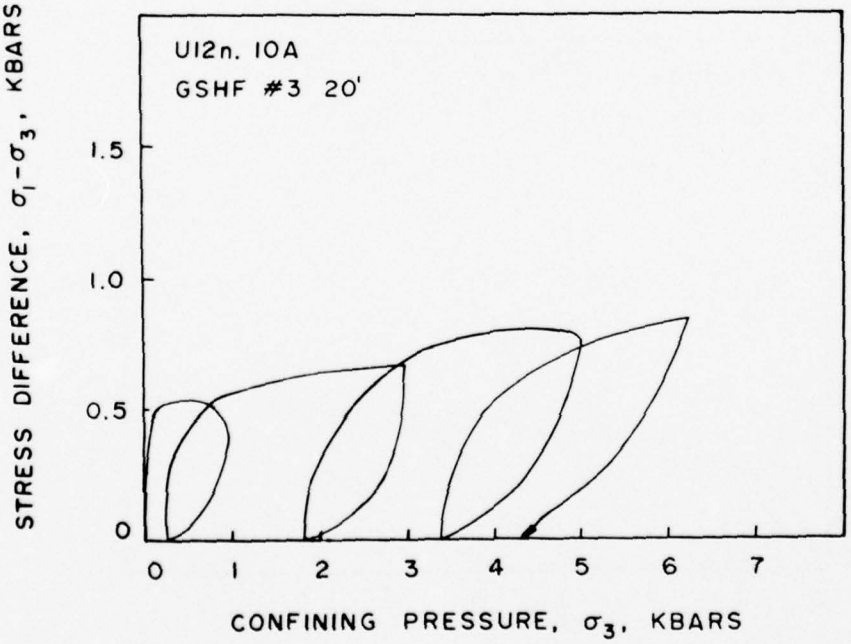


Figure A26. Uniaxial strain test to 6.5 kbars on U12n.10A GSHF#3 tuff -- stress difference versus confining pressure.

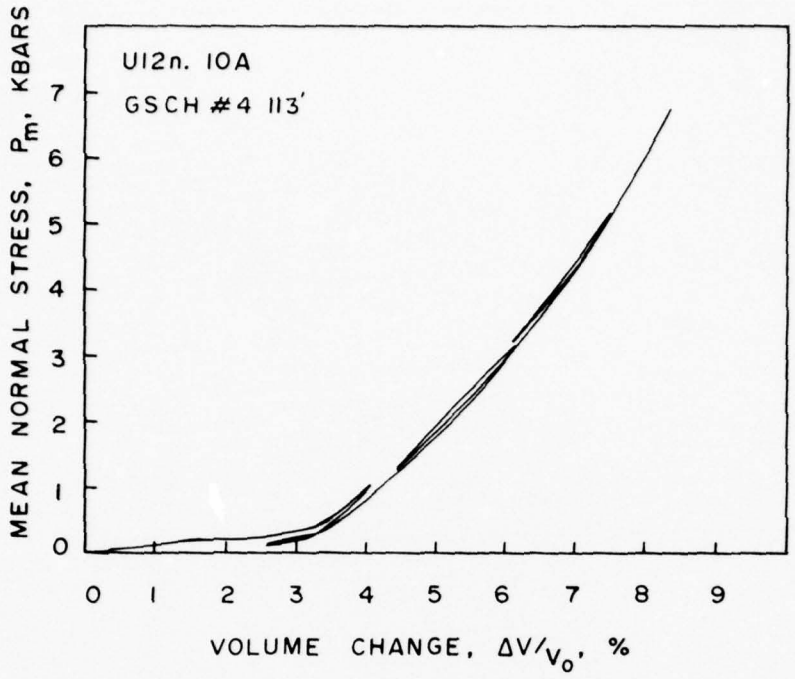


Figure A27. Uniaxial strain test to 7 kbars on U12n.10A GSCH#4 tuff -- mean normal stress versus volume change.

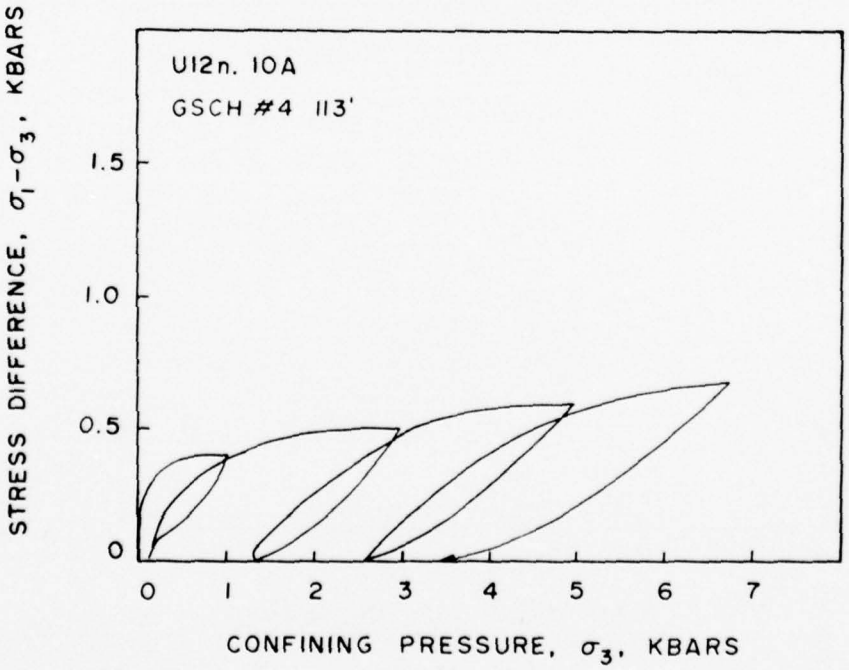


Figure A28. Uniaxial strain test to 7 kbars on U12n.10A GSCH#4 tuff -- stress difference versus confining pressure.

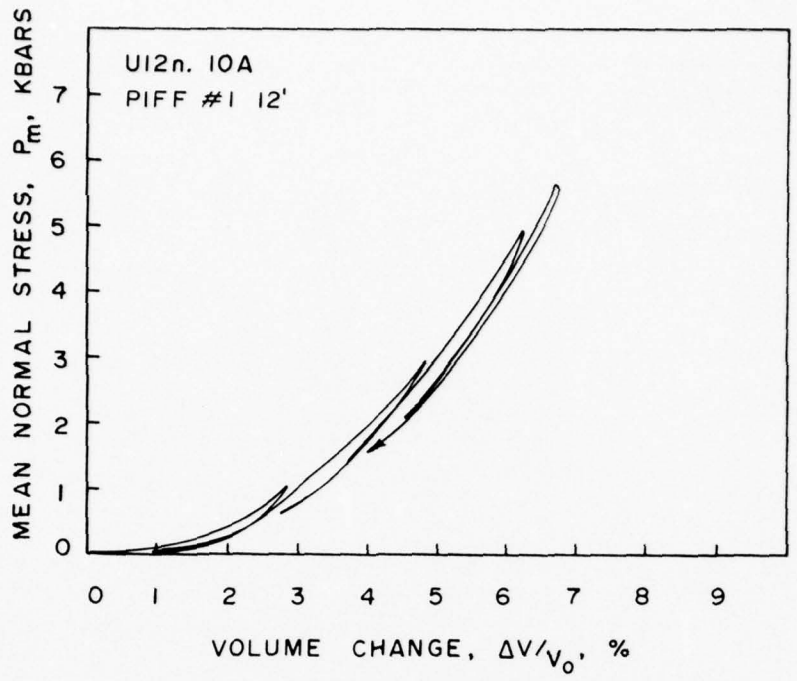


Figure A29. Uniaxial strain test to 6 kbars on U12n.10A PIFF#1 tuff -- mean normal stress versus volume change.

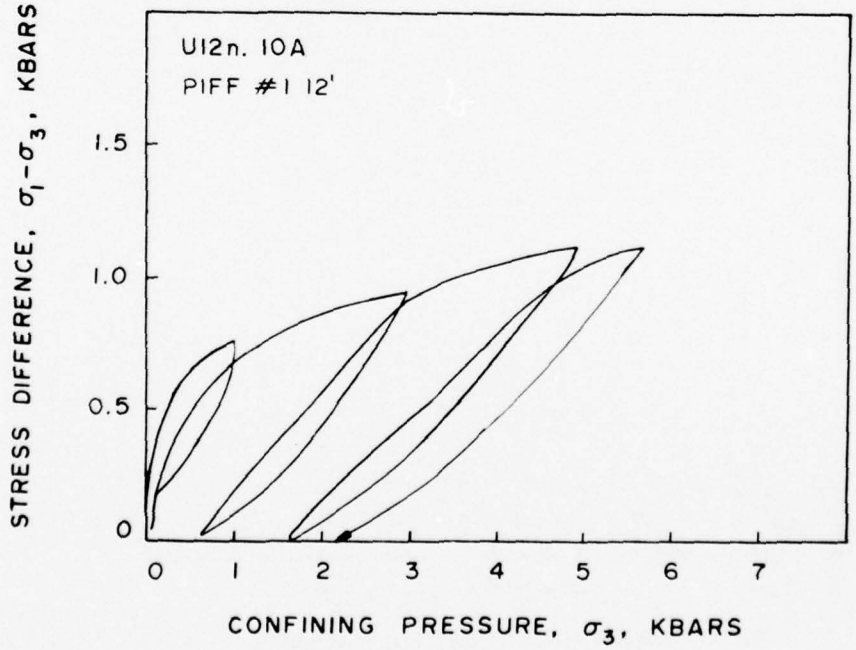


Figure A30. Uniaxial strain test to 6 kbars on U12n.10A PIFF#1 tuff -- stress difference versus confining pressure.

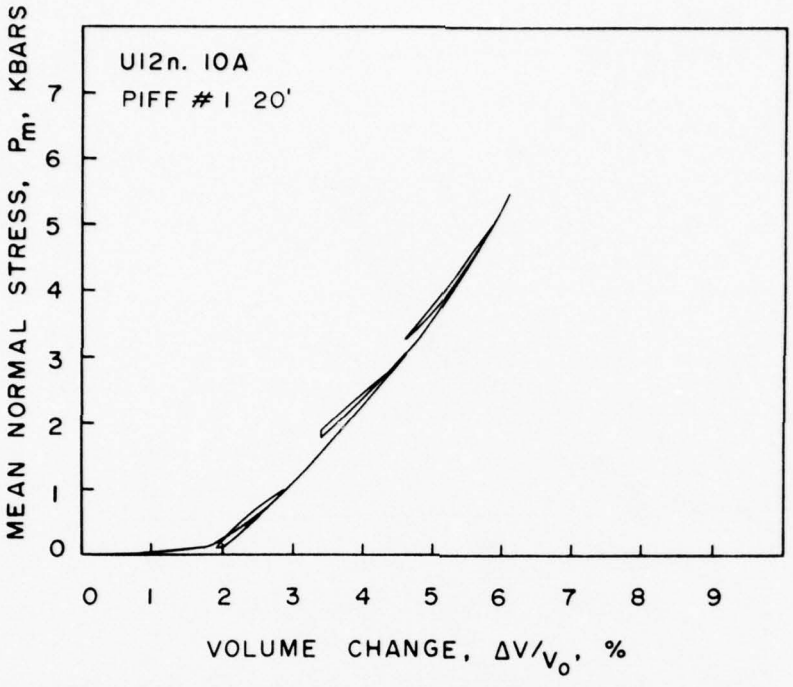


Figure A31. Uniaxial strain test to 6 kbars on U12n.10A PIFF#1 tuff -- mean normal stress versus volume change.

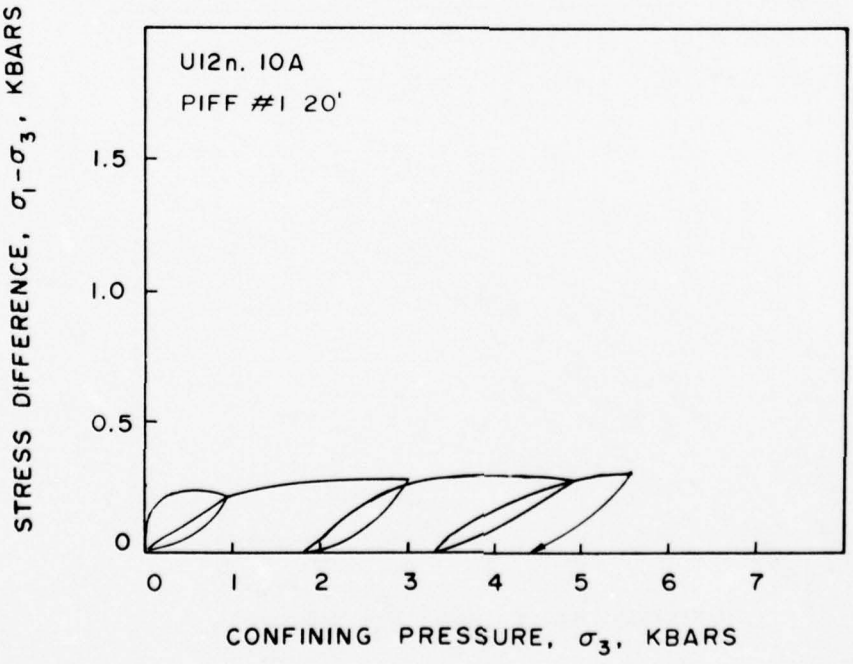


Figure A32. Uniaxial strain test to 6 kbars on U12n.10A PIFF#1 tuff -- stress difference versus confining pressure.

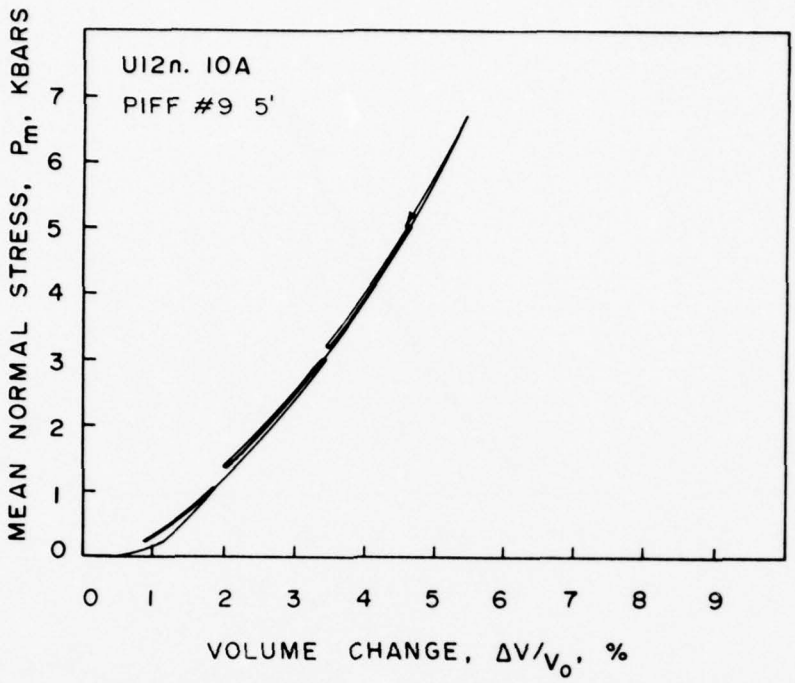


Figure A33. Uniaxial strain test to 7 kbars on U12n.10A PIFF#9 tuff -- mean normal stress versus volume change.

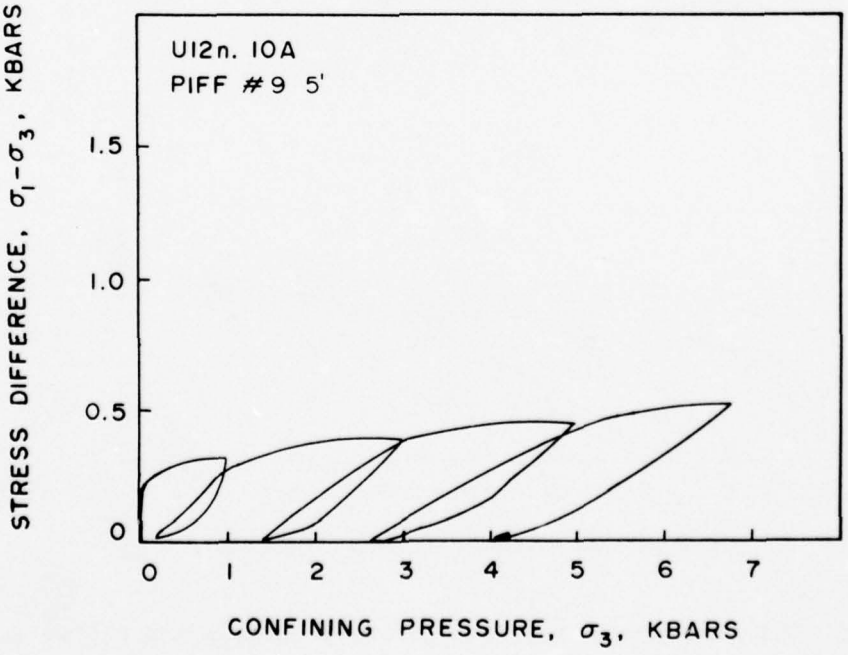


Figure A34. Uniaxial strain test to 7 kbars on U12n.10A PIFF#9 tuff -- stress difference versus confining pressure.

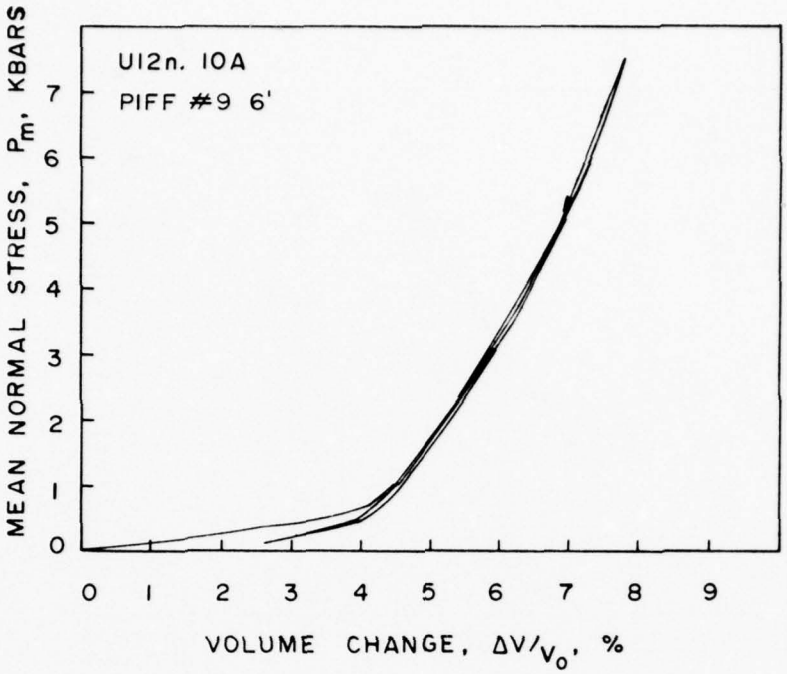


Figure A35. Uniaxial strain test to 7.5 kbars on U12n.10A PIFF#9 tuff -- mean normal stress versus volume change.

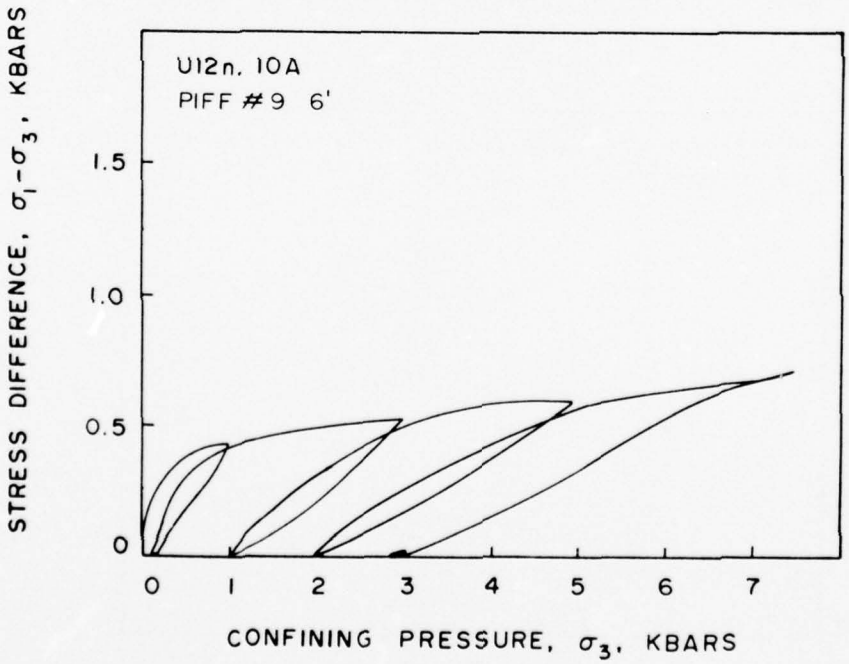


Figure A36. Uniaxial strain test to 7.5 kbars on U12n.10A PIFF#9 tuff -- stress difference versus confining pressure.

HIGH PRESSURE MECHANICAL PROPERTIES OF LAPIS LUSTRE SAND

TR 77-70
September 1977

HIGH PRESSURE MECHANICAL PROPERTIES OF LAPIS LUSTRE SAND

Laboratory testing of Lapis Lustre sand is all completed with the exception of a few additional tests for documenting the actual field emplacement of the sand. The report will therefore be published upon completion of those remaining tests.

HYBLA GOLD EVENT

Material Properties for the Hybla Gold Event

Material Properties of U12e.20 Tuff Overcores

Water and Air Permeability of Concrete from Hybla Gold Pipe

MATERIAL PROPERTIES OF NEVADA TEST SITE TUFF AND GROUT -- WITH EMPHASIS ON THE DIABLO HAWK AND HYBLA GOLD EVENTS

November 1977

Final Report for Period August 1976--September 1977

CONTRACT NO. DNA 001-76-C-0351

Prepared for

Director
Defense Nuclear Agency
Washington, D.C. 20305

TR 77-96

MATERIAL PROPERTIES FOR THE HYBLA GOLD EVENT

TR 77-46
August 1977

ABSTRACT

The location of the forthcoming Hybla Gold event at the Nevada Test Site is unique in that it is located close to a previously executed nuclear test. Typical site characterization usually assumes that material properties are reasonably consistent and predictable within a given geological layer. This could not be assumed for the Hybla Gold event. The material (tuff) surrounding the Hybla Gold event had been subjected to shock waves from the previous Dining Car event. The magnitude of the shock waves is obviously a function of distance from the Dining Car working point. Recent work completed by Terra Tek for the "two-for-one" concept[1] (multi use of common facilities) suggested, although no conclusions could be made because of a paucity of data, that material properties changes could result from shock loading or from cavity growth. In either case, it was necessary to characterize the Hybla Gold media as a function of location.

The media characterization included mechanical and physical properties. Comparisons are also drawn on the effects of the Dining Car event on the Hybla Gold media.

TABLE OF CONTENTS

	Page
Abstract	124
Table of Contents	125
List of Illustrations	126
List of Tables	127
Introduction	128
Section I - Site Evaluation Tests	130
UE12e#1 Vertical Drill Hole (Pre-Dining Car)	130
U12e.18 DNRE#1 Drill Hole (Post-Dining Car)	132
U12e.20 Drill Holes (Post-Dining Car)	133
Section II - Select Miscellaneous Tests	137
Gas Flow Tests	137
Atterberg Limit Tests	140
Wet/Dry Permeabilities	141
Section III - Comparison of Dining Car and Hybla Gold (Post-Dining Car) Material Properties	143
Summary	153
References	154
Acknowledgments	155
Appendix A	156
List of Illustrations	157

LIST OF ILLUSTRATIONS

Figure	Description	Page
1	Plan view of the Hybla Gold tunnels and selected drill holes	129
2	Selected data from UE12e#1 core samples--uniaxial strain permanent compaction and triaxial compression failure points	131
3	Gas permeability of dry UE12e#1 tuffs versus drill hole footage	138
4	Gas flow tests through select UE12e#1 core samples--driving pressure versus flow rate	139
5	Comparison of wet and dry gas permeabilities on selected U12e.20 core samples--permeability versus drill hole/footage	142
6	Comparison of preshot and postshot uniaxial strain tests on Hybla Gold tuffs--stress difference versus confining pressure	144
7	Comparison of preshot and postshot uniaxial strain tests on Hybla Gold tuffs--mean normal stress versus volume change	144
8	Typical uniaxial strain and hydrostatic compression/uniaxial strain tests on Hybla Gold tuff	147
9	ESM photographs of virgin ash-fall tuff from Hybla Gold Site	148
10	ESM photographs of Hybla Gold ash-fall tuff subjected to shock wave from a nuclear explosion	149
11	ESM photographs of Hybla Gold ash-fall tuff subjected to 4 kb uniaxial strain test	150
12	Ultrasonic P-wave velocity versus moisture content for random area 12 tunnel bed tuffs	152

LIST OF TABLES

Table	Description	Page
1	Physical Properties, Uniaxial Strain Measured Permanent Compaction, Young's Moduli, Tensile Strengths, and Ultrasonic Longitudinal and Shear Wave Velocities of UE12e#1 Tuffs	131
2	Physical Properties, Uniaxial Strain Measured Permanent Compaction, and Ultrasonic Longitudinal and Shear Wave Velocities of U12e.18 DNRE#1 Tuff	132
3	Physical Properties, Uniaxial Strain Measured Permanent Compaction, and Ultrasonic Longitudinal and Shear Wave Velocities of U12e.20 UG#1,2,&3 Tuffs	134
4	Physical Properties, Uniaxial Strain Measured Permanent Compaction, and Ultrasonic Longitudinal and Shear Wave Velocities of U12e.20 HF#1-10A Tuffs	135
5	Atterberg Limit Tests on Selected U12e.20 Core Samples	141
6	Average Select Properties of Preshot Dining Car and Hybla Gold Medias	145

INTRODUCTION

The forthcoming Hybla Gold nuclear event at the Nevada Test Site required, as for past events, material characterization and hence a material model, for predicting stemming and containment. However, the Hybla Gold configuration was unusual for two reasons: 1) the Hybla Gold working point and drifts were within 300 feet of a previous event (Dining Car) and 2) the Hybla Gold event was expected to behave differently than the "standard" DNA horizontal line-of-sight-pipe event. The Hybla Gold characterization was therefore conducted with consideration given to these unusual conditions.

Material properties have been determined on pre-Dining Car core samples from a single vertical drill hole located approximately 350 feet southwest of the working point and on post-Dining Car core samples (i.e. Hybla Gold samples) from several drill holes located in the horizontal plane of the U12e.20 main and auxiliary drifts.

Tests were conducted on core samples from the following drill holes:

UE12e#1 (vertical from Mesa top)	Pre Dining Car
U12e.18 DNRE#1	Hybla Gold (Post Dining Car)
U12e.20 UG#1, 2, 3	
U12e.20 HF#1, 2, 3, 4, 5, 6, 7, 8, 9, 10A	

The relative locations of these drill holes are shown in Figure 1.

Site characterization was accomplished by determination of mechanical properties (i.e., a combination of uniaxial strain and triaxial compression tests) and measurement of physical properties and ultrasonic longitudinal and shear wave velocities. Select core samples were also subjected to

tensile tests, gas flow tests, Atterberg Limit (plasticity) tests and scanning electron microscopy in order to more completely characterize specific locations of interest.

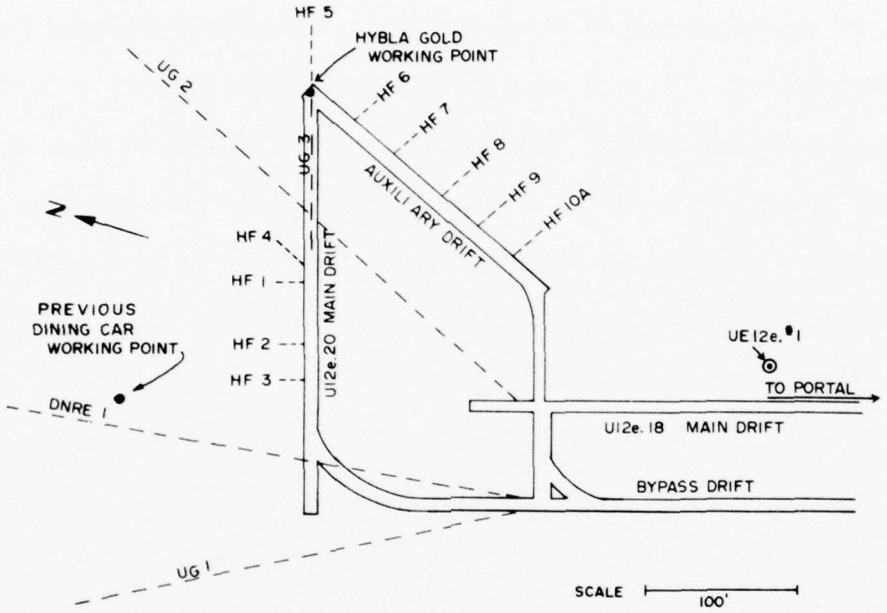


Figure 1. Plan view of the Hybla Gold tunnels and selected drill holes

Data is presented in graphic and tabular form with written discussion by section as shown below:

Section I	Site Evaluation Tests
Section II	Select Miscellaneous Tests
Section III	Comparison of Dining Car and Hybla Gold (Post-Dining Car) Material Properties

SECTION I

SITE EVALUATION TESTS

UE12e#1 Vertical Drill Hole (Pre-Dining Car)

In order to evaluate the effects of the Dining Car event on the Hybla Gold media, it was necessary to establish Dining Car material properties. For select properties, this had been accomplished with a number of tests on pre-Dining-Car core samples,[2] however, tests on UE12e#1 core samples were required to address properties such as porosities, permeabilities, shear strengths and ultrasonic velocities over a greater cross-section of the containment media.

The UE12e#1 vertical drill hole penetrates the horizontal plane of the U12e.20 drift approximately 350 feet southwest of the Hybla Gold working point (see Figure 1). The drill hole was collared on top of the Rainier Mesa. Cores were tested over the interval 241 feet through 1248 feet, therefore, giving a cross-section of the bedding planes above the main tunnel. Physical property measurements included densities, total and effective porosities and permeabilities. Mechanical properties were obtained via tension, triaxial compression, and uniaxial strain tests. Ultrasonic longitudinal and shear velocities were also measured.

Physical properties, ultrasonic velocities, and uniaxial strain measured permanent compaction are listed in Table 1. Uniaxial strain measured permanent compaction is plotted versus drill hole footage in Figure 2 (the uniaxial strain test curves are shown in Appendix A). Triaxial compression failure points are also shown in Figure 2 for each drill hole footage. Triaxial compression stress-strain curves are shown in Appendix A. Young's moduli (from triaxial compression tests) and tensile strengths are listed in Table 1.

TABLE 1

Physical Properties, Uniaxial Strain Measured Permanent Compaction, Young's Moduli, Tensile Strengths, and Ultrasonic Longitudinal and Shear Wave Velocities of UE12e#1 Tuffs

FOOTAGE	DENSITY (gm/cc) AS-RECEIVED	DRY	GRAIN	WATER BY WET WEIGHT (%)	POROSITY (%)	EFFECTIVE GAS POROSITY (%)	SATURATION (%)	CALC. AIR VOIDS (%)	MEAS. PERMANENT COMP. (%)	VELOCITY (ft/sec) LONG	SHEAR	YOUNG'S MODULUS (KB)	TENSILE STRENGTH (BARS)
241	2.25	2.13	2.50	5.5	15.1	13.7	82.7	2.6	0.1	13790	7880	217.4	19.0
298	1.66	1.36	2.43	18.1	43.9	43.4	68.3	13.9	10.0	8790	3760	16.6	0.3
400	1.79	1.42	2.52	20.6	43.6	39.5	84.6	6.7	3.5	--	--	6.7	0.3
489	1.56	1.25	2.39	20.1	47.9	45.2	65.5	16.5	13.7	3950	2300	22.2	2.0
644	1.85	1.62	2.49	12.2	34.9	33.1	64.9	12.2	4.2	3320	--	14.3	0.7
699	1.76	1.42	2.50	19.1	43.0	41.5	78.3	9.3	6.1	3320	1990	9.1	0.3
801	1.78	1.43	2.61	19.8	45.3	40.0	77.8	10.0	4.0	8570	4490	25.0	0.7
904	1.82	1.45	2.41	20.3	39.9	35.9	92.7	2.9	4.6	11920	6680	88.9	19.0
980	1.99	1.64	2.60	17.6	37.0	34.0	94.9	1.9	0.7	8960	3840	16.7	5.2
1100	1.91	1.62	2.44	15.3	33.7	30.8	86.7	4.4	3.4	10990	6030	83.3	9.0
1201	1.82	1.47	2.46	19.4	40.3	38.2	87.4	5.1	1.7	8360	3900	50.0	9.0
1248	1.96	1.71	2.43	12.7	29.6	26.4	84.3	4.6	0.7	11210	6200	133.3	23.1

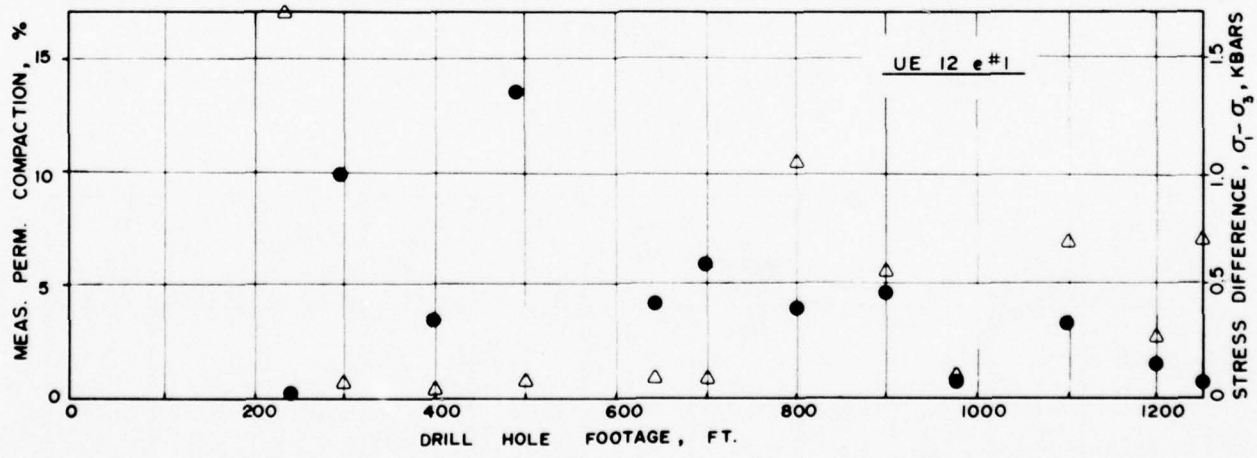


Figure 2. Selected data from UE12e#1 core samples--uniaxial strain permanent compaction and triaxial compression failure points.

● Uniaxial strain measured permanent compaction

△ Triaxial compression (σ_3=0.069 kbars) failure points

Examination of the data reveals that the region between 298 feet and 904 feet is a region of high air void content (up to 10 percent by volume in places) with average shear and tensile strengths of 0.2 kbars and 0.7 bars, respectively. Cores tested below this region exhibited higher compressive and tensile strengths (0.5 kbars and 13.5 bars average) and air voids under 2 percent with two exceptions. Material property variations, as just described, have been encountered in other vertical drill hole samples and are, for the most part, attributed to changes in lithology.

U12e.18 DNRE#1 Drill Hole (Post-Dining Car)

The U12e.18 DNRE#1 drill hole is a re-entry hole into the Dining Car area. Physical properties, uniaxial strain measured permanent compaction and ultrasonic longitudinal and shear wave velocities are listed in Table 2. Uniaxial strain test curves are shown in Appendix A.

TABLE 2

Physical Properties, Uniaxial Strain Measured Permanent Compaction, and Ultrasonic Longitudinal and Shear Wave Velocities of U12e.18 DNRE#1 Tuff

DRILL HOLE FOOTAGE	DENSITY (gm/cc)			WATER BY WET WEIGHT (%)	POROSITY (%)	SATURATION (%)	CALC. AIR VOIDS (%)	MEAS. PERMANENT COMP. (%)	VELOCITY (km/sec)	
	AS-RECEIVED	DRY	GRAIN						LONG	SHEAR
U12e.18 DNRE#1										
40	1.97	1.64	2.52	16.7	34.9	94.3	2.0	1.0	2.72	1.29
69	1.80	1.40	2.49	22.5	44.0	92.1	3.5	2.4	2.24	1.13
81	1.87	1.49	2.44	20.1	38.9	96.7	1.3	0.8	2.38	1.19
101	1.89	1.53	2.51	19.2	39.2	92.7	2.9	1.1	2.67	1.41
122	1.89	1.52	2.50	19.6	39.3	94.2	2.3	1.0	2.11	1.43
146	1.79	1.40	2.47	22.0	43.5	90.6	4.1	2.7	1.70	--
169	1.77	1.33	2.47	24.6	46.0	94.7	2.4	1.2	--	--

Some changes were apparent from the properties established pre Dining Car. The stress-stress response during uniaxial strain loadings are "shallow" (shear strength is considerably lower than normal at confining pressures under 4 kbars) much like the second cycle curves of the two-cycle uniaxial strain tests conducted on Diablo Hawk tuffs.[3] Also noted are considerable decreases in the ultrasonic velocities from preshot to postshot $\sim$ 2.7 - 2.8 km/sec to $\sim$ 2.3 km/sec. These changes and others will be discussed in more detail in the section on "Preshot-Postshot Comparisons".

U12e.20 Drill Holes (Post-Dining Car)

U12e.20 drill holes are all located in the horizontal plane surrounding the working point. Short drill holes were emplaced perpendicular to the main and auxiliary tunnels and long oblique holes were cored farther out into the surrounding media. Relative locations of the drill holes with respect to the tunnel layout are shown in Figure 1.

Physical properties, uniaxial strain measured permanent compaction and ultrasonic wave velocities are listed in Tables 3 and 4. Uniaxial strain test curves are contained in Appendix A. As explained for the U12e.18 DNRE#1 core samples, the effects of Dining Car can be seen in the shallow uniaxial strain test stress-stress curves. Measured permanent compaction averages ~1.0 percent.

In addition to the standard uniaxial strain tests, selected cores were hydrostatically loaded to 800 psi prior to uniaxial strain loading. These tests will be discussed in detail in a following section on preshot and postshot data comparison. The test results are seen in Tables 3 and 4 in the measured permanent compaction column as two numbers

TABLE 3

Physical Properties, Uniaxial Strain Measured Permanent Compaction, and Ultrasonic Longitudinal and Shear Wave Velocities of U12e.20 UG#1,2,&3 Tuffs

DRILL HOLE FOOTAGE	DENSITY (gm/cc)			WATER BY WET WEIGHT (%)	POROSITY (%)	SATURATION (%)	CALC AIR VOIDS (%)	MEAS PERMANENT COMP. (%)	VELOCITY (km/sec)	
	AS-RECEIVED	DRY	GRAIN						LONG	SHEAR
U12e.20 UG#1										
35	1.89	1.56	2.53	18.1	38.5	89.3	4.1	0.9	2.24	0.95
68	2.08	1.82	2.47	12.3	26.0	98.3	0.4	0.5	3.37	1.82
91 m.s.*	1.98	1.65	2.54	16.8	35.0	94.9	1.8	---	--	--
98	1.77	1.29	2.63	27.1	50.9	94.3	2.9	1.7	2.42	1.20
115	1.78	1.32	2.66	26.1	50.5	91.8	4.1	1.9	2.44	1.40
139	1.74	1.31	2.53	24.6	48.0	88.9	5.3	1.9	1.91	0.93
160 m.s.*	1.80	1.38	2.49	23.3	44.5	94.2	2.6	---	--	--
187 m.s.*	1.74	1.30	2.51	25.4	48.3	91.5	4.1	---	--	--
201	1.83	1.42	2.54	22.6	44.2	93.7	2.8	0.1	1.91	0.73
228	1.94	1.60	2.48	17.7	35.6	96.4	1.3	1.1	2.28	1.24
U12e.20 UG#2										
21	1.95	1.62	2.48	17.0	34.7	95.5	1.6	---	3.18	1.87
46	1.89	1.56	2.46	17.4	36.5	90.0	3.7	1.0	2.44	1.18
69	1.95	1.59	2.49	18.3	36.0	99.1	0.3	0.4	2.87	1.39
98	1.98	1.66	2.51	16.2	33.9	94.8	1.8	0.4	2.98	1.40
123	1.82	1.38	2.50	24.0	44.6	97.7	1.1	0.6	2.35	0.99
150	1.88	1.48	2.50	21.1	40.6	97.4	1.0	1.1	2.25	1.15
174	1.89	1.48	2.53	21.8	41.6	99.0	0.4	0.3	2.47	1.37
200	1.92	1.53	2.52	20.1	39.2	98.8	0.5	0.6	2.08	1.13
225	1.91	1.50	2.55	21.6	41.3	100.0	0	0.4	2.21	1.20
249	1.88	1.49	2.50	20.9	40.5	96.9	1.3	0.7	2.19	1.10
272	1.99	1.65	2.60	16.9	36.4	92.3	2.8	0.7	2.43	1.12
300	1.92	1.55	2.53	19.4	38.8	95.8	1.6	1.2	2.29	1.15
350	1.88	1.49	2.49	20.6	40.1	96.8	1.3	1.6	2.43	1.40
374	1.95	1.57	2.55	19.4	38.4	98.7	0.5	0.3	2.30	1.12
398	1.88	1.48	2.47	21.0	39.9	99.0	0.4	0.2	2.51	1.30
U12e.20 UG#3								HYD/1-D		
2	1.92	1.55	2.56	19.1	39.3	93.2	2.6	0.8	2.62	1.36
5	1.93	1.55	2.57	19.6	39.6	95.4	1.8	0.8/0.2	2.39	1.27
11	1.89	1.50	2.54	20.4	40.8	94.6	2.2	0.1	2.22	1.49
18	1.86	1.45	2.56	22.0	43.3	94.4	2.4	0.6/0.1	2.32	1.30
24	1.88	1.49	2.55	20.8	41.6	94.0	2.5	0.7	2.30	1.52
30	1.89	1.49	2.53	21.2	41.1	97.4	1.1	0.4/0.8	2.04	1.16
35	1.93	1.56	2.54	19.1	38.6	95.7	1.7	0.5	2.30	1.48
39	1.93	1.55	2.55	19.6	39.1	96.6	1.3	0.3/0.3	2.26	1.35
43	1.91	1.52	2.51	20.5	39.5	99.1	0.3	0.2	2.50	1.37
49	1.93	1.57	2.56	18.8	38.8	93.6	2.5	1.3/0.2	2.22	1.34
54	1.90	1.52	2.52	20.2	39.9	96.3	1.4	0.1	2.82	1.21
60	1.98	1.62	2.57	18.3	37.1	97.8	0.8	0.5/0.2	2.53	1.51
64	1.96	1.58	2.49	18.8	36.4	100.0	0	1.8	3.07	1.49
69	1.93	1.56	2.54	19.4	38.8	96.6	1.3	0.7/-0.1	2.33	1.48
74	1.96	1.59	2.49	18.6	36.2	100.0	0	0.5	2.51	1.46
79	1.93	1.56	2.53	19.3	38.4	96.9	1.2	0.8/-0.1	2.65	1.54
84	1.88	1.48	2.51	21.2	41.0	97.3	1.1	0.3	2.86	1.29
89	1.85	1.45	2.52	21.4	42.3	93.6	2.7	1.3/-0.1	2.53	1.38
95	1.89	1.51	2.46	20.2	38.7	98.7	0.5	0.5	2.53	1.41
99	1.89	1.52	2.56	19.8	40.8	91.7	3.4	0.9/-0.1	2.31	1.27
106	1.91	1.55	2.48	19.1	37.7	96.8	1.2	0.6	2.51	1.28
109	1.73	1.27	2.42	26.8	47.7	97.3	1.3	0.7/-0.1	2.19	1.27
113	1.74	1.30	2.42	25.5	46.3	95.8	2.3	0.6	2.67	1.36
118	1.95	1.59	2.48	18.5	35.9	100.0	0	0.7	2.91	1.46
121	1.94	1.59	2.57	17.8	38.1	90.6	3.1	0.4/-0.1	2.39	1.43

* Moisture sample

TABLE 4

Physical Properties, Uniaxial Strain Measured Permanent Compaction, and Ultrasonic Longitudinal and Shear Wave Velocities of U12e.20 HF#1-10A Tuffs

DRILL HOLE FOOTAGE	DENSITY (gm/cc)			WATER BY WET WEIGHT (%)	POROSITY (%)	SATURATION (%)	CALC AIR VOIDS (%)	MEAS PERMANENT COMP (%)	VELOCITY (km/sec)	
	AS-RECEIVED	DRY	GRAIN						LONG	SHEAR
U12e.20 HF#1										
6	1.89	1.50	2.52	20.7	40.5	96.5	1.4	0.9/-0.1	2.14	1.26
16	1.88	1.49	2.50	20.5	40.2	95.8	1.7	M.S.	M.S.	M.S.
U12e.20 HF#2										
10	1.80	1.39	2.47	3.0	43.7	94.7	2.7	0.8/-0.1	1.93	1.07
U12e.20 HF#3										
5	1.79	1.35	2.49	24.6	45.8	96.1	1.8	0.3/0.4	1.80	1.20
U12e.20 HF#4										
1	1.94	1.57	2.55	19.1	38.4	96.4	1.4	0.8/0.4	2.16	1.26
9	1.96	1.60	2.55	18.4	37.3	96.7	1.4	0.9/-0.1	1.98	1.12
21	1.87	1.45	2.49	22.4	41.7	100.0	0	0.5	2.13	1.12
25	1.89	1.49	2.52	20.9	40.7	97.1	1.2	0.7	1.76	0.82
U12e.20 HF#5										
1	1.94	1.59	2.54	17.9	37.3	93.2	2.6	0.6	2.60	1.33
5	1.93	1.57	2.49	18.5	36.8	96.8	1.2	0.7/-0.1	2.48	1.33
9	1.90	1.52	2.50	19.8	39.0	96.3	1.4	0.5	2.42	1.35
15	1.90	1.52	2.50	20.1	39.3	97.3	1.1	0.6/-0.1	2.57	1.36
22	1.92	1.54	2.51	19.6	38.5	97.8	0.8	1.2	2.72	1.45
28	1.92	1.56	2.51	18.6	37.7	94.7	2.0	0.7/0.4	2.73	1.36
32	1.79	1.39	2.44	22.4	43.1	93.1	3.0	1.1	2.62	1.50
37	1.74	1.31	2.46	24.9	46.8	92.6	3.5	1.0/-0.1	2.18	1.23
41	1.97	1.63	2.48	17.3	34.4	99.4	0.2	0.5	2.83	1.59
44	1.92	1.54	2.46	19.6	37.3	100.0	0	0.6/-0.1	2.67	1.38
49	2.03	1.71	2.55	15.9	33.1	97.7	0.8	0.4	2.60	1.17
55	1.99	1.67	2.46	16.2	32.2	100.0	0	0.3/-0.1	2.56	1.19
59	2.06	1.75	2.57	15.2	32.0	97.8	0.7	0.4	2.66	1.19
66	2.03	1.71	2.60	16.0	34.4	94.4	1.9	0.7/0.1	2.31	1.04
69	1.99	1.66	2.54	16.5	34.6	94.9	1.7	0.7	2.23	1.05
U12e.20 HF#6										
6	1.82	1.40	2.49	22.9	43.7	95.5	2.0	0.8/0	2.06	1.10
16	1.87	1.51	2.46	19.4	38.7	93.7	2.4	0.4	2.12	1.41
U12e.20 HF#7										
4	1.94	1.59	2.53	18.3	38.0	93.8	1.4	0.4/0	2.52	1.50
11	1.87	1.48	2.49	20.9	40.6	96.1	1.6	0.7	2.38	1.41
17	1.91	1.55	2.52	19.0	38.6	93.9	2.4	0.5/0	2.03	1.34
U12e.20 HF#8										
5	1.96	1.62	2.42	17.2	32.9	100.0	0	1.0	2.69	1.70
13	1.95	1.59	2.57	18.5	38.2	94.7	2.0	0.7/0.2	2.24	1.78
19	1.96	1.60	2.54	18.2	36.9	96.9	1.2	0.7	2.59	1.14
U12e.20 HF#9										
4	1.85	1.44	2.52	22.3	43.0	96.0	1.8	0.7/0.5	2.35	1.47
11	1.85	1.44	2.50	22.4	42.6	97.3	1.1	0.9	2.42	1.35
18	1.87	1.46	2.55	21.6	42.5	95.1	2.1	1.1/0.1	2.61	1.25
U12e.20 HF#10a										
5	2.00	1.67	2.46	16.3	32.0	100.0	0	0.5	3.06	1.75
13	1.94	1.56	2.52	19.4	37.9	99.0	0.4	0.9/0.4	2.31	1.40
20	1.89	1.53	2.45	18.9	37.4	95.4	1.7	1.5	2.73	1.58

(i.e. 0.8/0.2), the first number being the volume change resulting from hydrostatic compression to 800 psi and the second number is the volume compaction due to uniaxial strain to 4 kilobar confining pressure upon initiation at 800 psi confining pressure.

SECTION II

SELECT MISCELLANEOUS TESTS

Gas Flow Tests

Dry UE12e#1 vertical drill hole tuff samples were subjected to gas flow tests to generate supportive data for the computer hydrofrac code. The purpose of the tests was to determine if choked flow occurred at some gas driving pressure (i.e. no increased flow with increased driving pressure). The tests were conducted to verify an apparent choking of flow that occurred in recent field tests.

Test samples were prepared by recoring and saw cutting the core samples to a 1.8 inch diameter, 1.75 inch length. They were then bonded with epoxy to the inside of an aluminum ring so as to prevent gas flow between the ring and the sample. O-ring sealed steel end caps were placed over each end of the ring and the assembly was inserted into a small load frame. Gas was supplied to one face of the sample from a regulated nitrogen bottle (2500 psi maximum pressure) and flow was measured downstream with a flowmeter.

Permeabilities were determined for all samples initially by measuring the flow resulting from a 20 psi driving pressure. Approximate permeabilities for each footage are shown in Figure 3. The high pressure gas flow tests were conducted only on the lower permeability samples below the 900 foot depth. These samples were tested by increasing the driving pressure in 200 psi increments up to a maximum 2000 psi or up to where the sample fractured. Results are shown in Figure 4 as driving pressure versus flow rate.

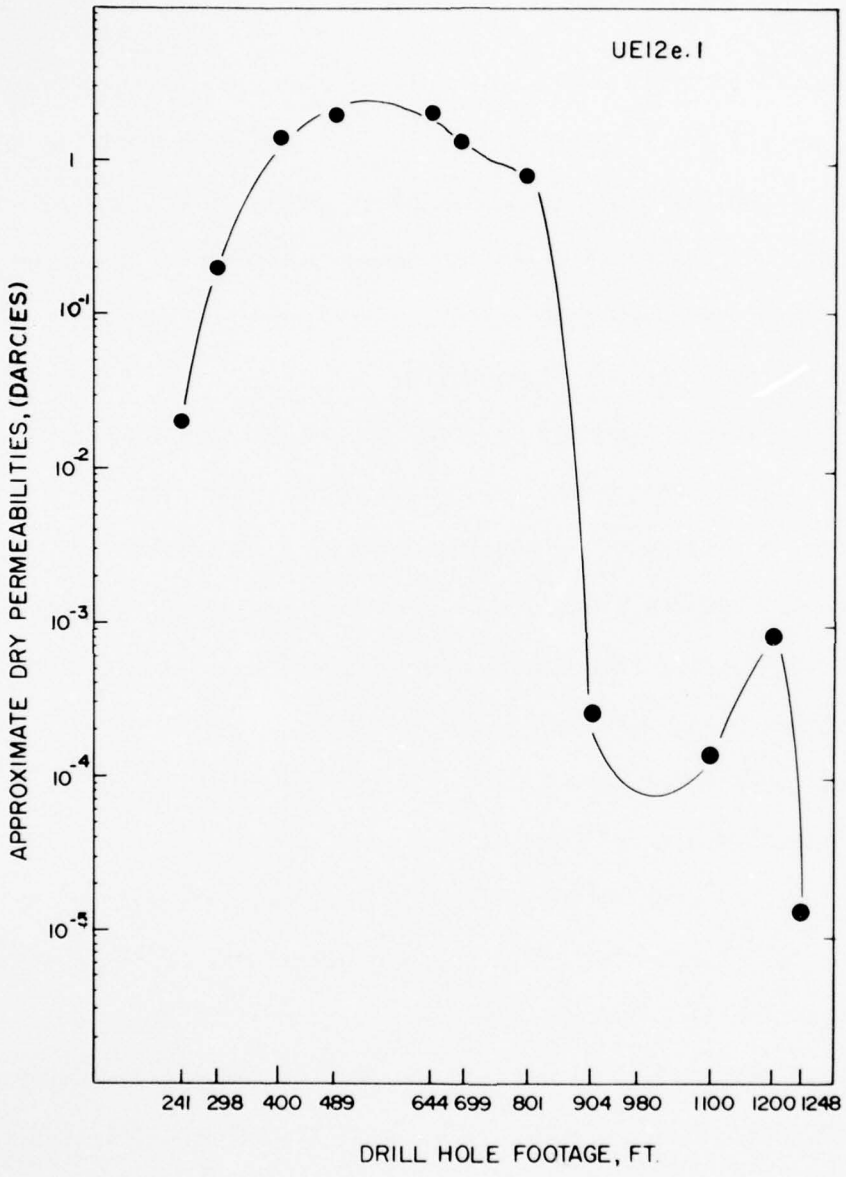


Figure 3. Gas permeability of dry UE12e#1 tuffs versus drill hole footage.

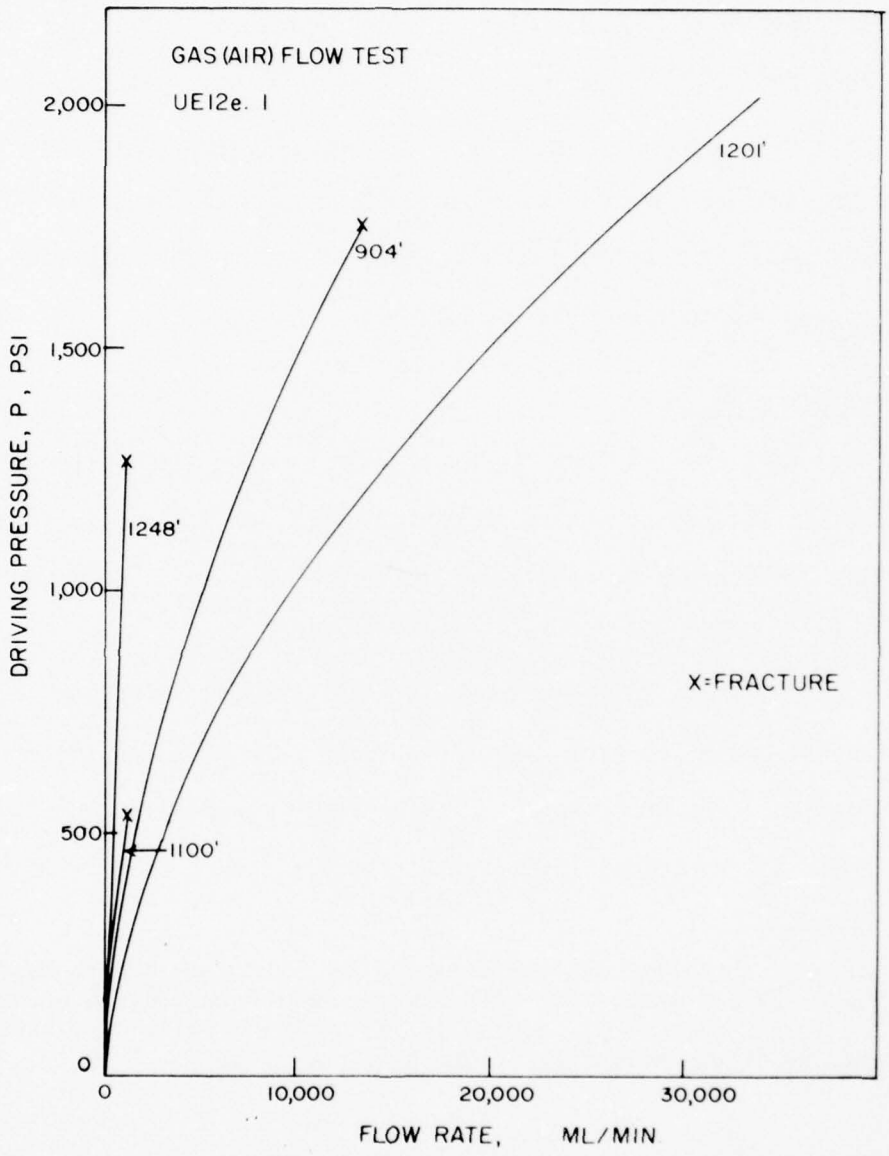


Figure 4. Gas flow tests through select UE12e#1 core samples--driving pressure versus flow rate.

The test results suggest that choked flow does not occur in this driving pressure range. In fact, rather than showing no increase with pressure, flow tends to increase with the square of the pressure according to the permeability law. Also, samples fractured in all but one case well before the 2000 psi maximum pressure was reached. It should be noted that these tests are not truly representative of field flow tests in that the tuff was dry and unconfined (no overburden stress). The data, therefore, should not be used as a measure of *in situ* permeability or pressure required to cause hydrofracture.

Atterberg Limit Tests

Select core samples from the Hybla Gold site were subjected to Atterberg Limit* tests to determine their respective plasticity indexes. Cores from four separate drill holes, U12e.20 UG#3, HF#1, HF#2 and HF#5 were tested.

Test results are listed in Table V. All samples, with the exception of HF#5, had a positive plasticity index number indicating a "plastic" classification. The HF#5 sample is classified "non-plastic" because the sample could not be molded into a ball, the first test requirement.

---

*These "Atterberg Limits" are not intented to represent data produced on soils. Special procedures for tuff require intial mechanical crushing and pulverizing followed by reconsolidation. The "Limits" obtained are, therefore, relative indicators of the behavior of tuff.

TABLE 5

Atterberg Limit Tests* on Selected U12e.20 Core Samples

Sample Designation	Liquid Limit	Plastic Limit	Plasticity Index	Classification
HF#1 - 16'	29.7	27.7	2.0	Plastic
HF#2 - 10'	33.8	32.7	1.1	Plastic
HF#5 - 5'	29.3	--	---	Non-Plastic
UG#3 - 109'	38.2	37.9	0.3	Plastic

Wet/Dry Permeabilities

Permeabilities to air were determined on select core samples from the U12e.20 UG#3 and HF#1, 2, 3 locations. Samples were tested in their wet or "as-received" condition, then oven dried and retested. Results are shown in Figure 5.

As expected, permeabilities increased significantly upon drying. The magnitude of the increase, however, was much larger for the UG#3 samples. A possible explanation for the difference is the permeability mechanism itself. The UG#3 tuff samples appeared to be a fairly competent tuff with interconnected porosity. In the wet condition, the pores are largely full of water so flow is restricted. Upon oven drying, water is removed and flow becomes unrestricted. This type of permeability would be considered a pore connected permeability and is very dependent on the saturation state.

HF#1, 2, 3 tuffs, on the other hand, appeared to have a number of fractures, resulting in higher permeability relatively independent of saturation. Thus a smaller difference between the wet and dry samples.

---

* See footnote on previous page.

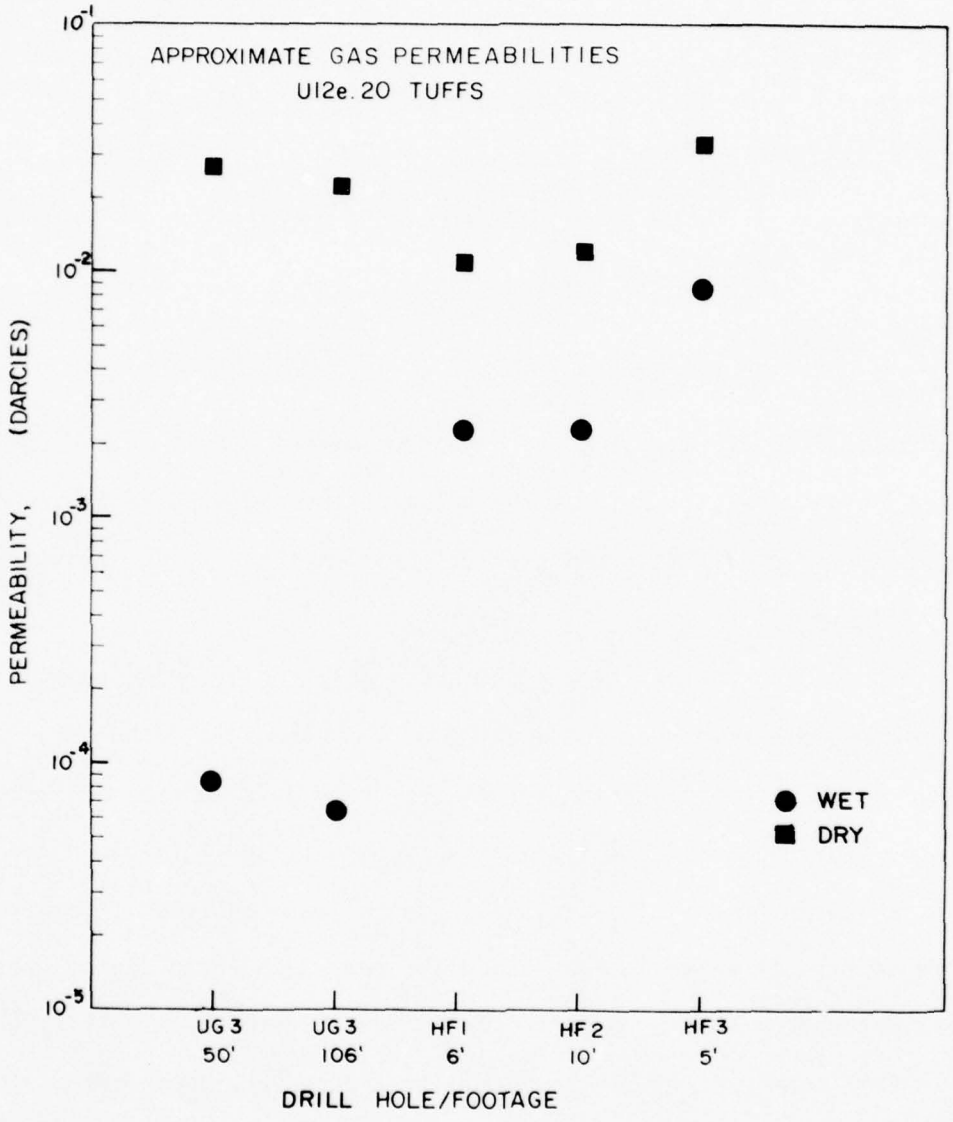


Figure 5. Comparison of wet and dry gas permeabilities on selected U12e.20 core samples--permeability versus drill hole/footage.

SECTION III

COMPARISON OF DINING CAR AND HYBLA GOLD (POST-DINING CAR) MATERIAL PROPERTIES

Interest in the effects of the Dining Car event on the Hybla Gold site led to a comparison of preshot (UE12e#1, U12e.14 and U12e.15) and postshot (U12e.18 DNRE#1 and U12e.20) data. The effects were first observed in the U12e.18 DNRE#1 re-entry drill hole and early Hybla Gold drill holes (U12e.20 UG#1 and UG#2) in which the uniaxial strain tests produced lower stress differences for given confining pressures. This lower stress difference becomes immediately apparent when preshot and postshot data are plotted together as shown in Figure 6. Uniaxial strain volume change curves also show a marked difference between preshot and postshot tuffs. When test results are plotted on an expanded scale, postshot tuffs have a significantly larger "foot" than do preshot tuffs, as shown by Figure 7. Strangely enough, however, the postshot tuffs produced lower uniaxial strain permanent volume compactions than did the preshot.

It was reasoned that the above described differences might be explained by the presence of numerous microcracks in the postshot tuff.[4] That is, the preshot tuff apparent air void contents are primarily due to air filled pore porosity. Thus, the relatively small "foot" associated with the usual permanent volume compaction of 1 to 2% by volume. The apparent air void content of the postshot tuff, on the other hand, is thought to be due to shock-induced microcracks which have been "opened" when relieved of overburden stress and are closed easily at low stresses -- reference the "foot" on the postshot samples. The postshot samples either

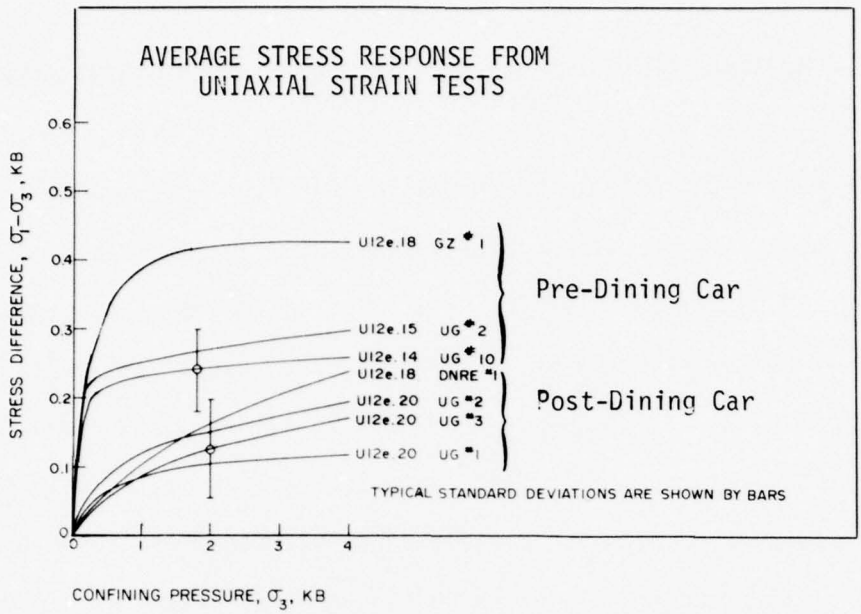


Figure 6. Comparison of preshot and postshot uniaxial strain tests on Hybla Gold tuffs -- stress difference versus confining pressure.

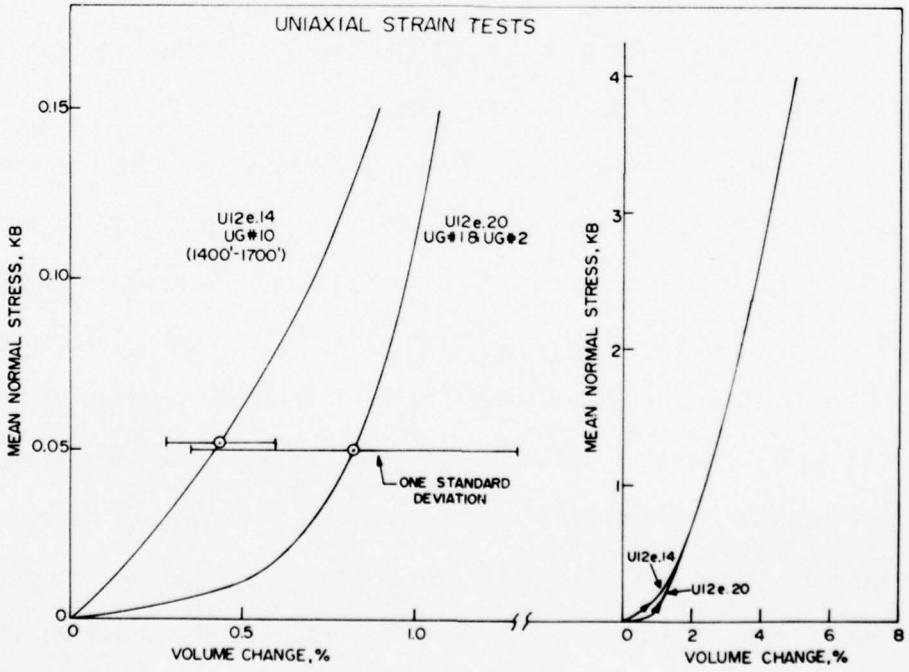


Figure 7. Comparison of preshot and postshot uniaxial strain tests on Hybla Gold tuffs -- mean normal stress versus volume change.

contain very little, if any, of the original air-filled pore porosity or the existing pores have been filled with water. This latter possibility has been suggested by data on the preshot and postshot Ming Blade tuff[1] and is also reflected in the data contained herein, see Table 6*. The bed 4J numbers represent the average properties of that rock unit throughout the Area 12 tunnel complex. Bed 4J shows different densities but identical porosities and moisture contents from that of the Dining Car media (also 4J) but both have noticeably lower porosities and moisture contents than the Hybla Gold media.

TABLE 6

Average Select Properties of Preshot Dining Car and Hybla Gold Medias

	Density, gm/cc			Porosity %	Moisture Content %
	As-Received	Dry	Grain		
Dining Car	1.93	1.59	2.44	35	18
(4J)	1.96	1.63	2.47	35	18
Hybla Gold (Post Dining Car)	1.90	1.51	2.52	40	20.3

*compiled by Mr. J. W. LaComb, DNA, Mercury, Nevada

To address these gas-filled void changes, select postshot samples were hydrostatically loaded to estimated overburden stresses followed by uniaxial strain loading. It was observed that the foot was virtually eliminated and measured permanent compaction from the uniaxial strain portion of the test was reduced substantially (Tables 3 and 4). Typical tests are shown in Figure 8. This observation suggested that microcracks do apparently close when overburden stresses are applied. Similar tests were conducted on a few preshot tuff samples to determine if the initial hydrostatic compression would eliminate any permanent compaction. The data, however, was not sufficient to draw any conclusions. Further tests comparing preshot and postshot tuff are needed to answer these questions of overburden stress and microcrack effect on material properties.

To investigate microcrack presence, several preshot and postshot tuff samples were subjected to microscopic examination using a scanning electron microscope. Preshot tuff samples were thoroughly examined and few microcracks were observed. Pore structure appeared undamaged and the zeolite web-like structures often found in the pores were still intact. Representative preshot photographs are shown in Figure 9. Postshot tuff samples were examined equally thoroughly and a large number of microcracks were present in all cases. The zeolite webbing was partially broken down in some cases and cleavage planes were occasionally present. Photographs of postshot tuffs are shown in Figure 10. An examination was also made of preshot tuff subjected to a 4 kbar uniaxial strain test. Figure 11 shows photographs of post uniaxial strain tuff. There is some indications of damage although not as obvious as in the postshot material.

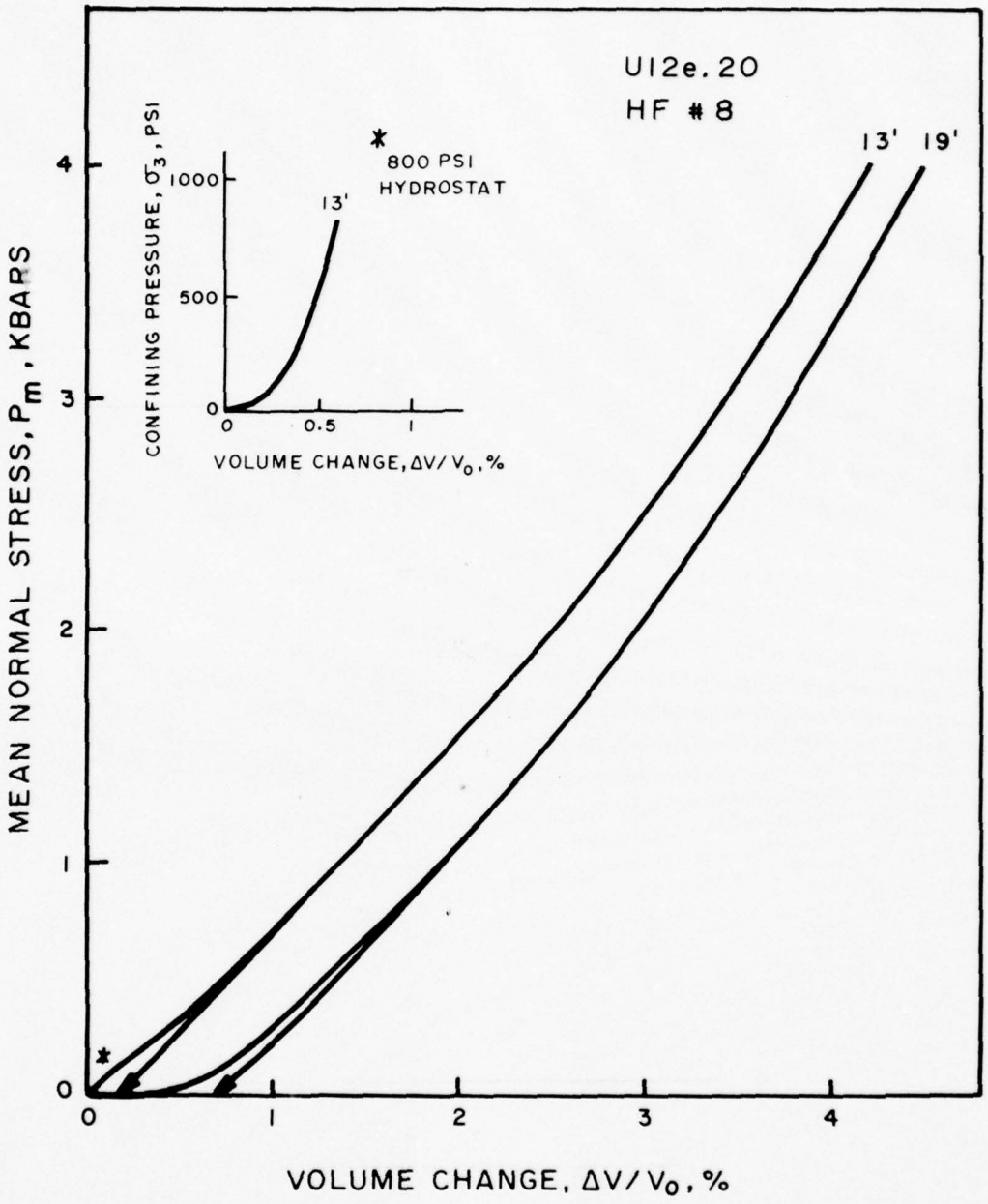
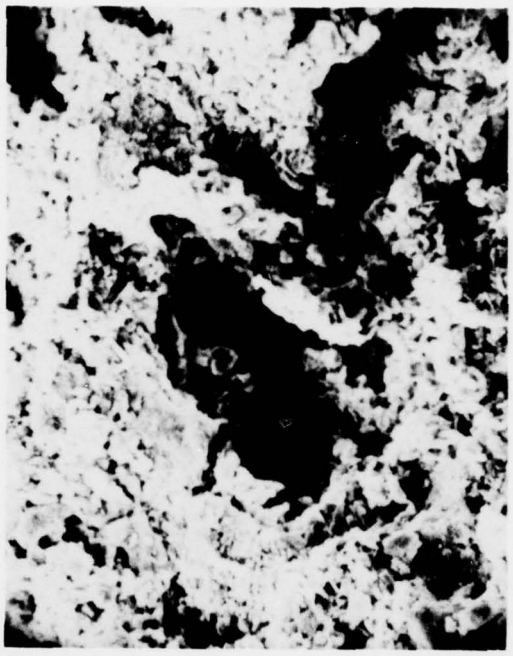


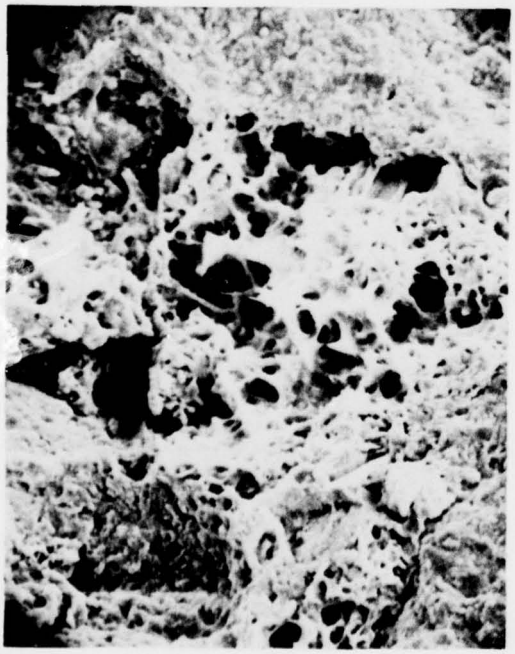
Figure 8. Typical uniaxial strain and hydrostatic compression/uniaxial strain tests on Hybla Gold tuff.



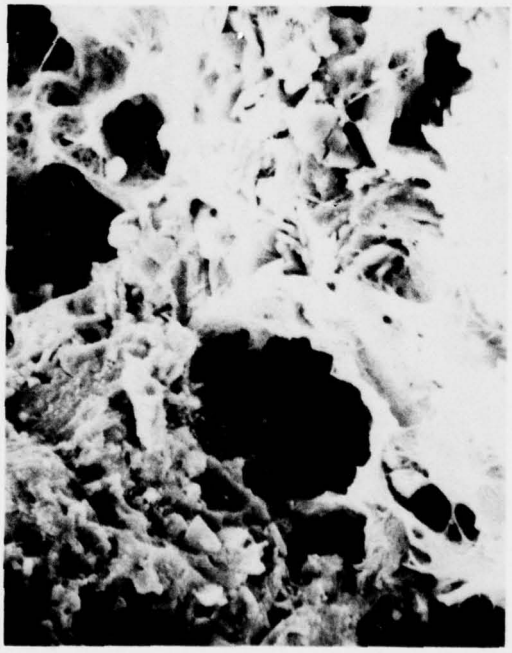
50 Microns



50 Microns



50 Microns



25 Microns

Figure 9. ESM photographs of virgin ash-fall tuff from Hybla Gold Site.

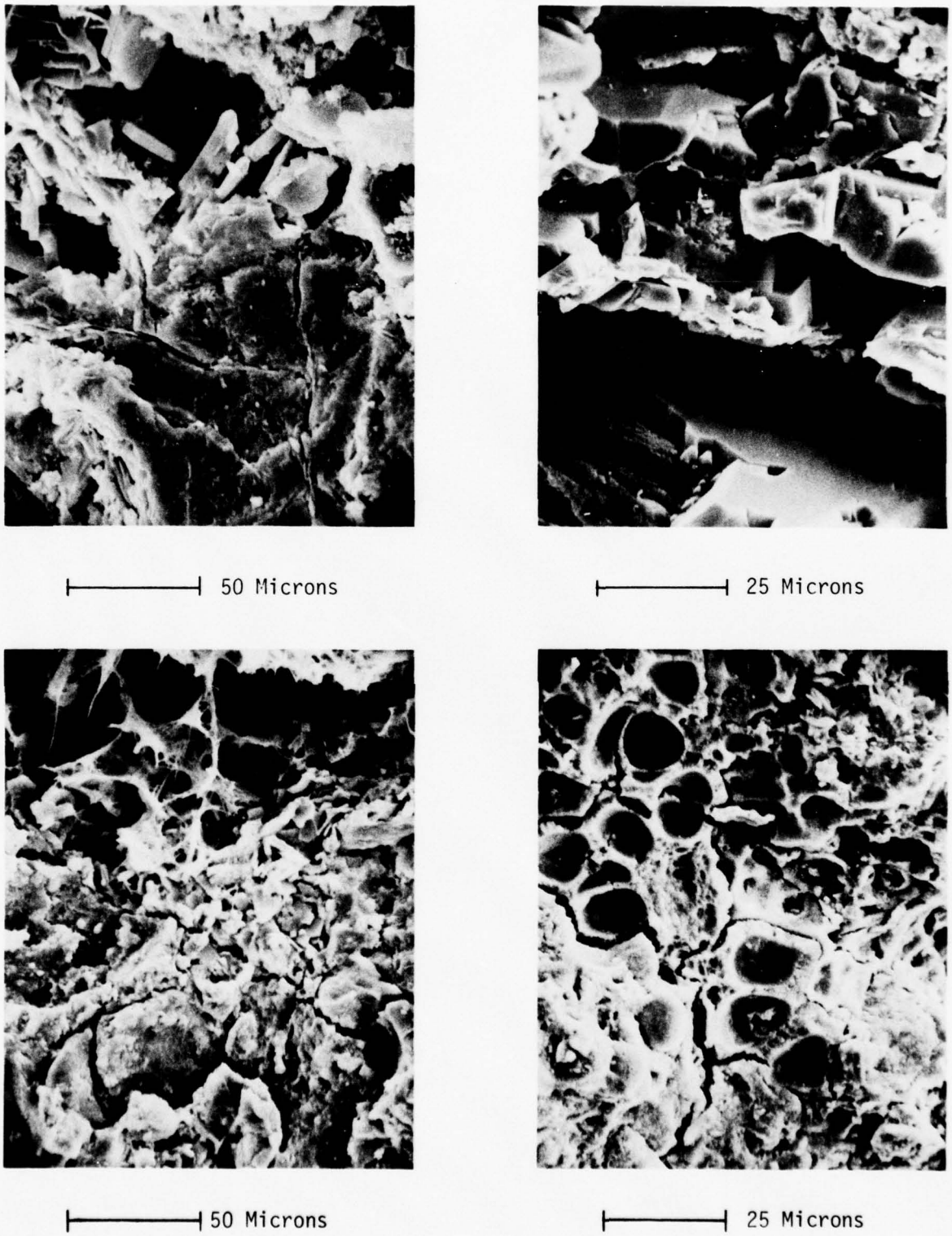
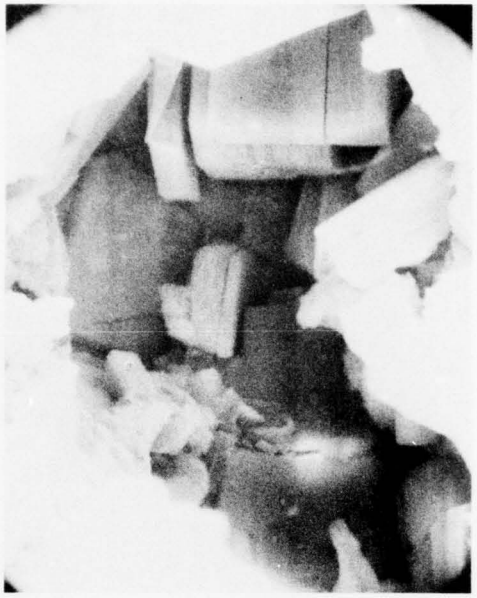


Figure 10. ESM photographs of Hybla Gold ash-fall tuff subjected to shock wave from a nuclear explosion.



12.5 Microns



50 Microns



25 Microns



50 Microns

Figure 11. ESM photographs of Hybla Gold ash-fall tuff subjected to 4 kb uniaxial strain test.

So far, changes in physical properties and the existence of microcracks have been documented. Their effect on the gas-filled void content has also been discussed and partially verified. The mechanisms behind the changes in shear stress response and ultrasonic velocities are at this time mostly speculation, although supportive test data are available.

The lower stress-stress response during the uniaxial strain tests, Figure 6, could be a result of both the microcracks and the physical properties changes. Tests have been conducted in which samples were subjected to two cycles of uniaxial strain loading to roughly simulate fractured postshot samples.[5] Many of the samples produced a lower stress-stress curve on the second cycle. There is evidence, therefore, that the existence of microcracks can lessen the shear stress carrying capacity of the material. Likewise, a material with high porosity, high moisture content (i.e., preshot to postshot changes) and, hence, a lower effective stress, will also exhibit lower shear stresses.

The decrease in the ultrasonic velocities from preshot to postshot Dining Car could also be a result of both the microcracks and the physical properties changes. Test results generated at Terra Tek show ultrasonic longitudinal (P-wave) velocity decreases of up to 25% as a result of fracturing by uniaxial compression loading and direct shearing.[6] With regard to the physical properties changes (primarily the increase in porosity and moisture content) Figure 12 shows P-wave plotted versus moisture content for random tunnel bed tuff samples. Although there is considerable scatter, the data does suggest lower P-wave velocities with higher water contents.

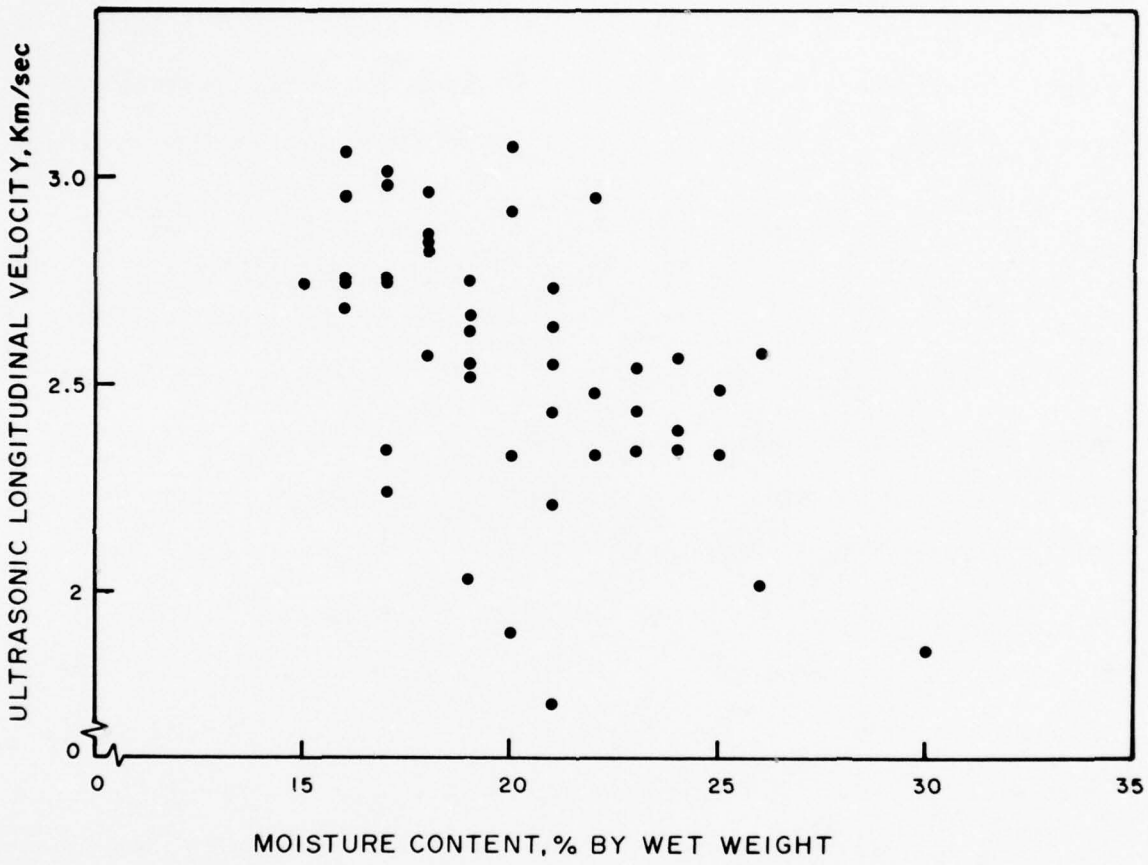


Figure 12. Ultrasonic P-wave velocity versus moisture content for random area 12 tunnel bed tuffs.

SUMMARY

Characterization of the Hybla Gold media was conducted with emphasis on the effect of the past Dining Car event. Some changes in material properties were noted, as discussed below; however, the Hybla Gold media properties are considered adequate for containment.

In the course of characterizing the Hybla Gold tuff, it became apparent that some material properties were different than those established pre-Dining Car. Of significance were:

1) changes in the characteristics of volume strain and permanent volume compaction during uniaxial strain tests,
2) an apparent decrease in the shear stress capacity during uniaxial strain loading, and
3) a decrease in the ultrasonic P and S wave velocities.

Further examination produced evidence that densities, porosities and moisture contents had increased, suggesting fluid migration into existing or induced cracks and pores. Also, subsequent electron scanning microscope pictures showed numerous microcracks in the postshot material.

The mechanical properties changes (numbers 1 through 3) appear to be explainable via the changes in the physical characteristics. In most cases, data are presented to verify the proposed relationships between the changes.

In conclusion, the Hybla Gold characterization has been successful in documenting the effect of a nuclear event on the close-in media. The results and theories presented should prove very beneficial in light of future "two-for-one" tests.

REFERENCES

1. Butters, S. W., Snow, C. N., Jones, A. H., "Nevada Test Site "Two-In-One Concept" Evaluation" Comparison of Preshot and Postshot Material Properties," Terra Tek REport TR 76-61, August 1976.

2. Butters, S. W., Dropek, R. K., Green, S. J., Jones, A. H., "Material Properties in Support of the Nevada Test Site Nuclear Test Program," June, 1975.

3. Gardiner, D. S., Butters, S. W., "Material Properties for Diablo Hawk Event," Terra Tek Report TR 77-43, June 1977.

4. Mr. J. W. LaComb, Defense Nuclear Agency Field Command, Mercury, Nevada, Personal Communication, July 1977.

5. Gardiner, D. S., Butters, S. W., "Material Properties for Diablo Hawk Event," Terra Tek Report TR 77-43, June 1977.

6. Lingle, R., Rosso, R. S., Buchholdt, L. M., "An Investigation to Determine the Effect of Fracture on the Ultrasonic Velocities in Ash-Fall Tuff," Terra Tek Report 75-20, DNA Contract No. 001-75-C-0260, May 1975.

ACKNOWLEDGMENTS

The authors would like to make note of their appreciation for the assistance and guidance of the Contracting Officer Representative - Mr. J. W. LaComb - during the course of this work.

APPENDIX A

Triaxial Compression and Uniaxial Strain Test Curves on Tuffs Relating to the Hybla Gold Event

LIST OF ILLUSTRATIONS

Figure	Description	Page
A-1	Triaxial compression test at 1000 psi confining pressure on UE12e#1 core samples--stress difference versus individual strains	162
A-2	Triaxial compression test at 1000 psi confining pressure on UE12e#1 core samples--stress difference versus individual strains	162
A-3	Triaxial compression test at 1000 psi confining pressure on UE12e#1 core samples--stress difference versus individual strains	163
A-4	Triaxial compression test at 1000 psi confining pressure on UE12e#1 core samples--stress difference versus individual strains	163
A-5	Triaxial compression test at 1000 psi confining pressure on UE12e#1 core samples--stress difference versus individual strains	164
A-6	Triaxial compression test at 1000 psi confining pressure on UE12e#1 core samples--stress difference versus individual strains	164
A-7	Triaxial compression test at 1000 psi confining pressure on UE12e#1 core samples--stress difference versus individual strains	165
A-8	Triaxial compression test at 1000 psi confining pressure on UE12e#1 core samples--stress difference versus individual strains	165
A-9	Triaxial compression test at 1000 psi confining pressure on UE12e#1 core samples--stress difference versus individual strains	166
A-10	Triaxial compression test at 1000 psi confining pressure on UE12e#1 core samples--stress difference versus individual strains	166
A-11	Triaxial compression test at 1000 psi confining pressure on UE12e#1 core samples--stress difference versus individual strains	167
A-12	Triaxial compression test at 1000 psi confining pressure on UE12e#1 core samples--stress difference versus individual strains	167

Figure	Description	Page
A-13a	Uniaxial strain tests on UE12e#1 core samples--mean normal stress versus volume change	168
A-13b	Uniaxial strain tests on UE12e#1 core samples--stress difference versus confining pressure	168
A-14a	Uniaxial strain tests on UE12e#1 core samples--mean normal stress versus volume change	169
A-14b	Uniaxial strain tests on UE12e#1 core samples--stress difference versus confining pressure	169
A-15a	Uniaxial strain tests on UE12e#1 core samples--mean normal stress versus volume change	170
A-15b	Uniaxial strain tests on UE12e#1 core samples--stress difference versus confining pressure	170
A-16a	Uniaxial strain tests on U12e.18 DNRE#1 core samples--mean normal stress versus volume change	171
A-16b	Uniaxial strain tests on U12e.18 DNRE#1 core samples--stress difference versus confining pressure	171
A-17a	Uniaxial strain tests on U12e.18 DNRE#1 core samples--mean normal stress versus volume change	172
A-17b	Uniaxial strain tests on U12e.18 DNRE#1 core samples--stress difference versus confining pressure	172
A-18a	Uniaxial strain tests on U12e.20 UG#1 core samples--mean normal stress versus volume change	173
A-18b	Uniaxial strain tests on U12e.20 UG#1 core samples--stress difference versus confining pressure	173
A-19a	Uniaxial strain tests on U12e.20 UG#1 core samples--mean normal stress versus volume change	174
A-19b	Uniaxial strain tests on U12e.20 UG#1 core samples--stress difference versus confining pressure	174
A-20a	Uniaxial strain tests on U12e.20 UG#2 core samples--mean normal stress versus volume change	175
A-20b	Uniaxial strain tests on U12e.20 UG#2 core samples--stress difference versus confining pressure	175
A-21a	Uniaxial strain tests on U12e.20 UG#2 core samples--mean normal stress versus volume change	176

Figure	Description	Page
A-21b	Uniaxial strain tests on U12e.20 UG#2 core samples--stress difference versus confining pressure	176
A-22a	Uniaxial strain tests on U12e.20 UG#2 core samples--mean normal stress versus volume change	177
A-22b	Uniaxial strain tests on U12e.20 UG#2 core samples--stress difference versus confining pressure	177
A-23a	Uniaxial strain tests on U12e.20 UG#2 core samples--mean normal stress versus volume change	178
A-23b	Uniaxial strain tests on U12e.20 UG#2 core samples--stress difference versus confining pressure	178
A-24a	Uniaxial strain tests on U12e.20 UG#3 core samples--mean normal stress versus volume change	179
A-24b	Uniaxial strain tests on U12e.20 UG#3 core samples--stress difference versus confining pressure	179
A-25a	Uniaxial strain tests on U12e.20 UG#3 core samples--mean normal stress versus volume change	180
A-25b	Uniaxial strain tests on U12e.20 UG#3 core samples--stress difference versus confining pressure	180
A-26a	Uniaxial strain tests on U12e.20 UG#3 core samples--mean normal stress versus volume change	181
A-26b	Uniaxial strain tests on U12e.20 UG#3 core samples--stress difference versus confining pressure	181
A-27a	Uniaxial strain tests on U12e.20 UG#3 core samples--mean normal stress versus volume change	182
A-27b	Uniaxial strain tests on U12e.20 UG#3 core samples--stress difference versus confining pressure	182
A-28a	Uniaxial strain tests on U12e.20 UG#3 core samples--mean normal stress versus volume change	183
A-28b	Uniaxial strain tests on U12e.20 UG#3 core samples--stress difference versus confining pressure	183
A-29a	Uniaxial strain tests on U12e.20 HF#1,2,3 core samples--mean normal stress versus volume change	184

Figure	Description	Page
A-29b	Uniaxial strain tests on U12e.20 HF#1,2,3 core samples--stress difference versus confining pressure	184
A-30a	Uniaxial strain tests on U12e.20 HF#4 core samples--mean normal stress versus volume change	185
A-30b	Uniaxial strain tests on U12e.20 HF#4 core samples--stress difference versus confining pressure	185
A-31a	Uniaxial strain tests on U12e.20 HF#5 core samples--mean normal stress versus volume change	186
A-31b	Uniaxial strain tests on U12e.20 HF#5 core samples--stress difference versus confining pressure	186
A-32a	Uniaxial strain tests on U12e.20 HF#5 core samples--mean normal stress versus volume change	187
A-32b	Uniaxial strain tests on U12e.20 HF#5 core samples--stress difference versus confining pressure	187
A-33a	Uniaxial strain tests on U12e.20 HF#5 core samples--mean normal stress versus volume change	188
A-33b	Uniaxial strain tests on U12e.20 HF#5 core samples--stress difference versus confining pressure	188
A-34a	Uniaxial strain tests on U12e.20 HF#6 core samples--mean normal stress versus volume change	189
A-34b	Uniaxial strain tests on U12e.20 HF#6 core samples--stress difference versus confining pressure	189
A-35a	Uniaxial strain tests on U12e.20 HF#7 core samples--mean normal stress versus volume change	190
A-35b	Uniaxial strain tests on U12e.20 HF#7 core samples--stress difference versus confining pressure	190
A-36a	Uniaxial strain tests on U12e.20 HF#8 core samples--mean normal stress versus volume change	191
A-36b	Uniaxial strain tests on U12e.20 HF#8 core samples--stress difference versus confining pressure	191
A-37a	Uniaxial strain tests on U12e.20 HF#9 core samples--mean normal stress versus volume change	192

Figure	Description	Page
A-37b	Uniaxial strain tests on U12e.20 HF#9 core samples--stress difference versus confining pressure	192
A-38a	Uniaxial strain tests on U12e.20 HF#10A core samples--mean normal stress versus volume change	193
A-38b	Uniaxial strain tests on U12e.20 HF#10A core samples--stress difference versus confining pressure	193

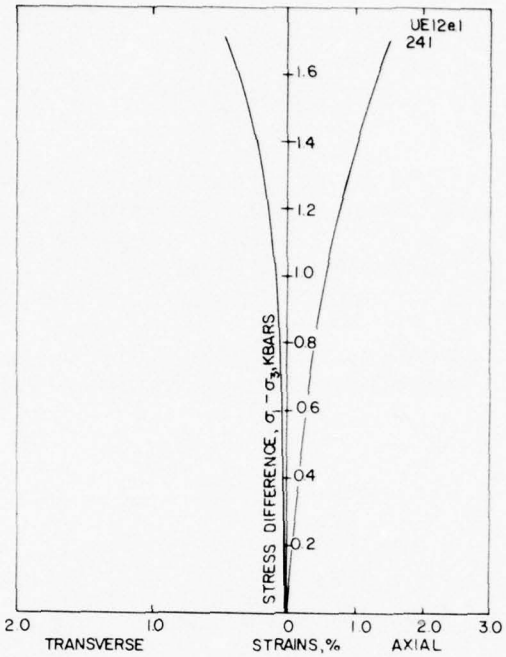


Figure A-1. Triaxial compression test at 1000 PSI confining pressure on UE12e#1 core samples--stress difference versus individual strains.

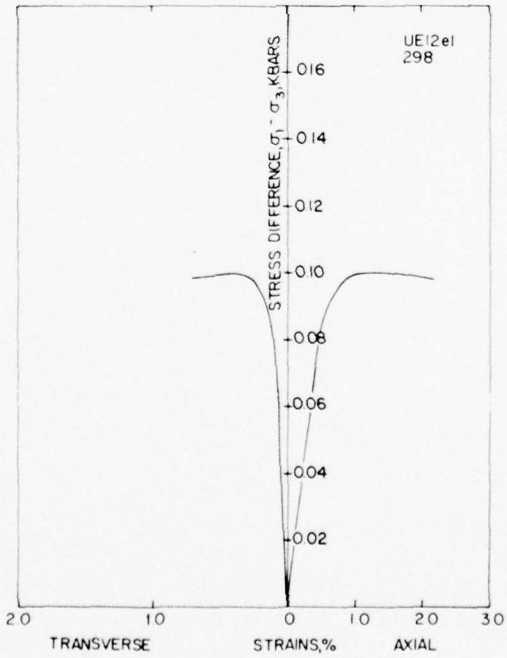


Figure A-2. Triaxial compression test at 1000 PSI confining pressure on UE12e#1 core samples--stress difference versus individual strains.

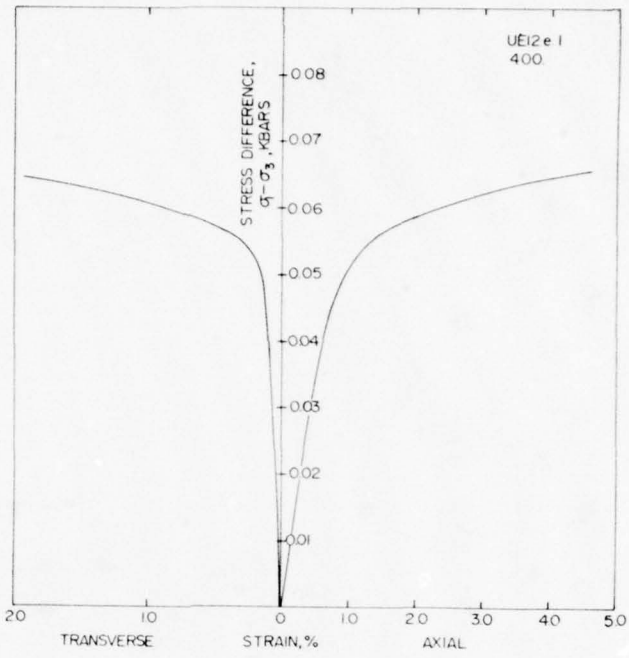


Figure A-3. Triaxial compression test at 1000 PSI confining pressure on UE12e#1 core samples--stress difference versus individual strains.

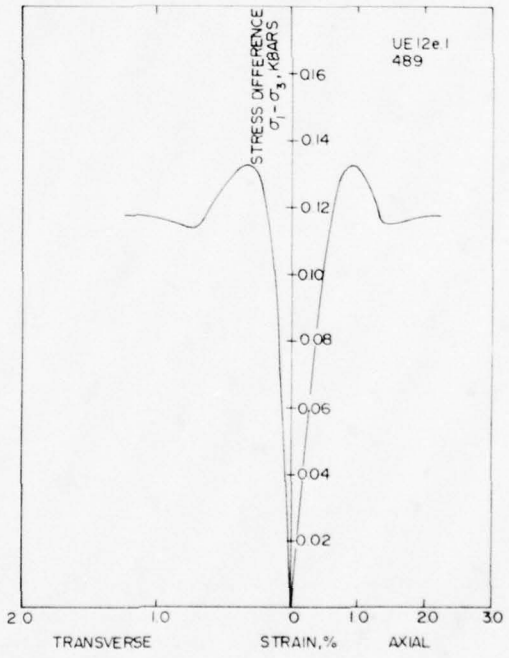


Figure A-4. Triaxial compression test at 1000 PSI confining pressure on UE12e#1 core samples--stress difference versus individual strains.

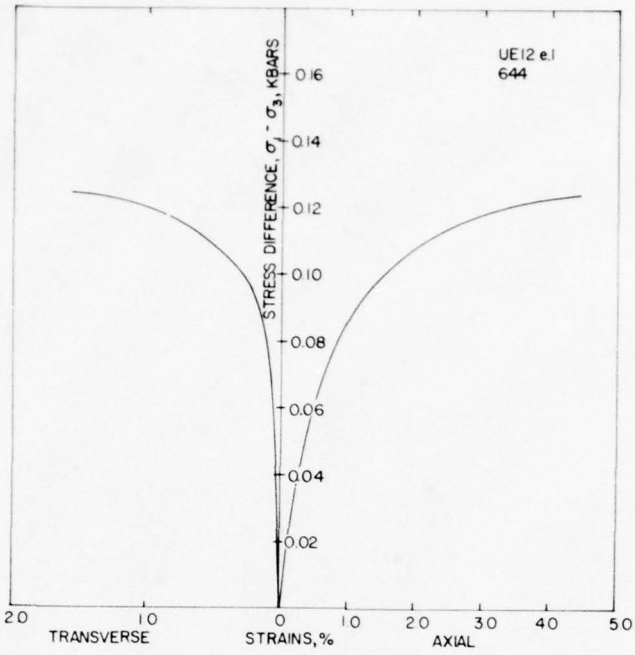


Figure A-5. Triaxial compression test at 1000 PSI confining pressure on UE12e#1 core samples--stress difference versus individual strains.

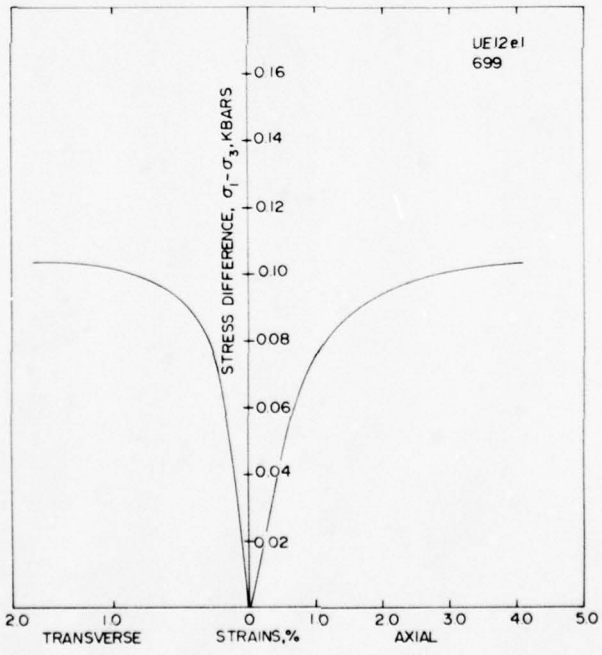


Figure A-6. Triaxial compression test at 1000 PSI confining pressure on UE12e#1 core samples--stress difference versus individual strains.

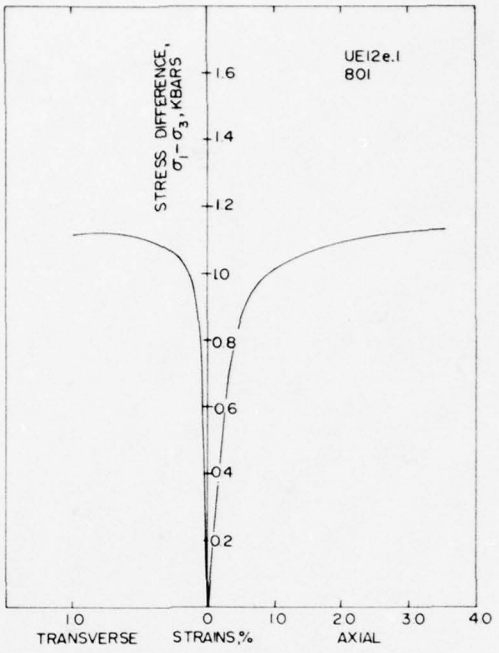


Figure A-7. Triaxial compression test at 1000 PSI confining pressure on UE12e#1 core samples--stress difference versus individual strains.

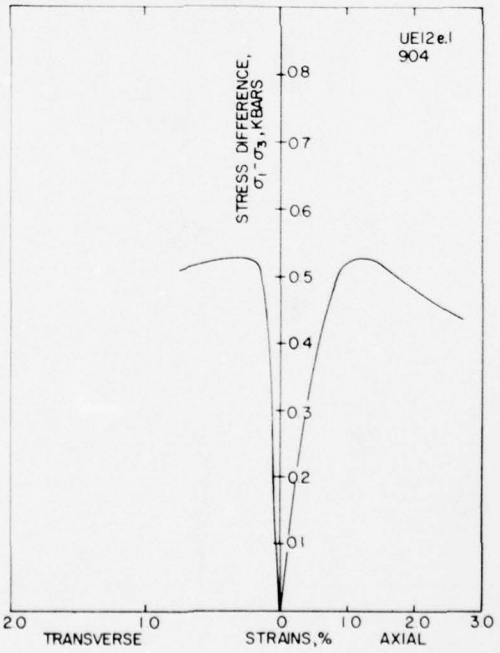


Figure A-8. Triaxial compression test at 1000 PSI confining pressure on UE12e#1 core samples--stress difference versus individual strains.

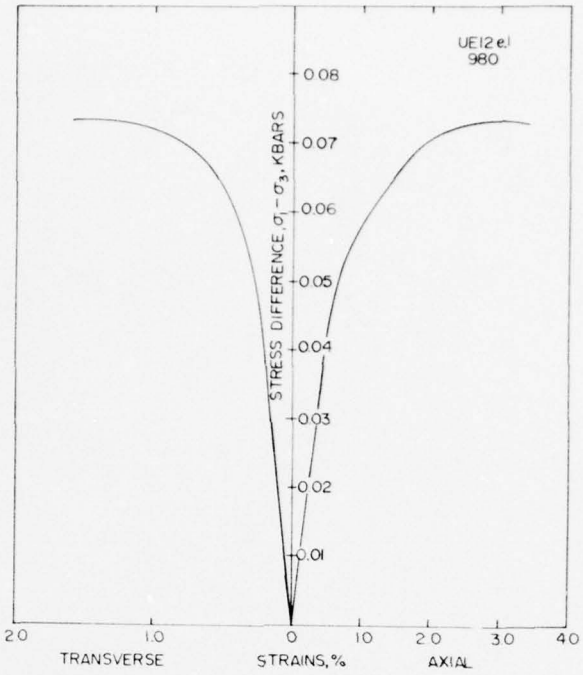


Figure A-9. Triaxial compression test at 1000 PSI confining pressure on UE12e#1 core samples--stress difference versus individual strains.

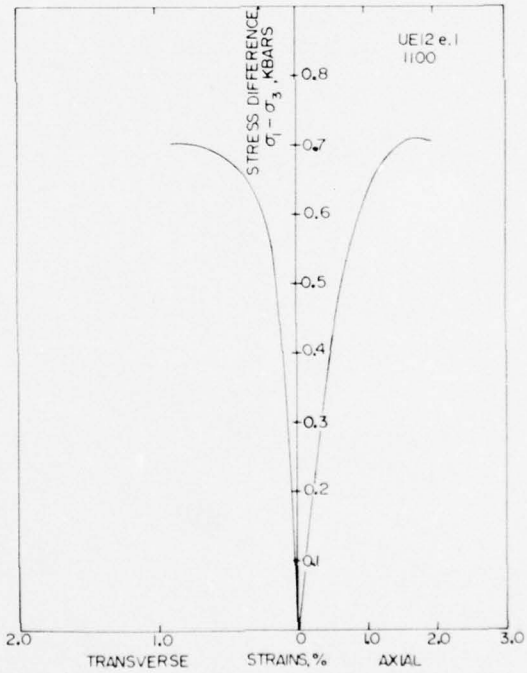


Figure A-10. Triaxial compression test at 1000 PSI confining pressure on UE12e#1 core samples--stress difference versus individual strains.

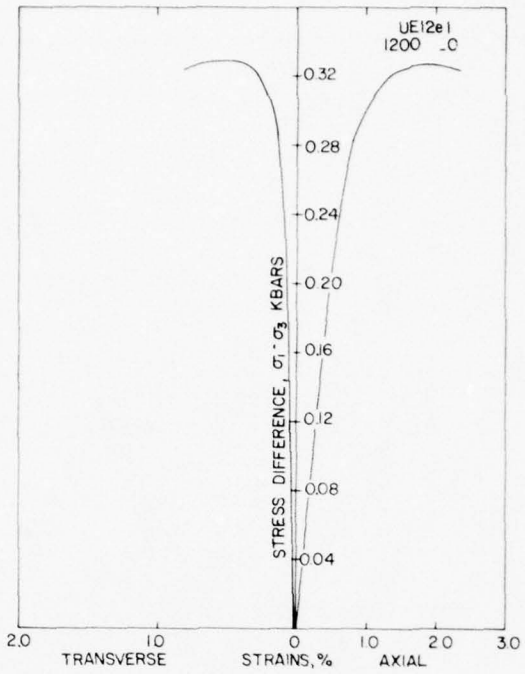


Figure A-11. Triaxial compression test at 1000 PSI confining pressure on UE12e#1 core samples--stress difference versus individual strains.

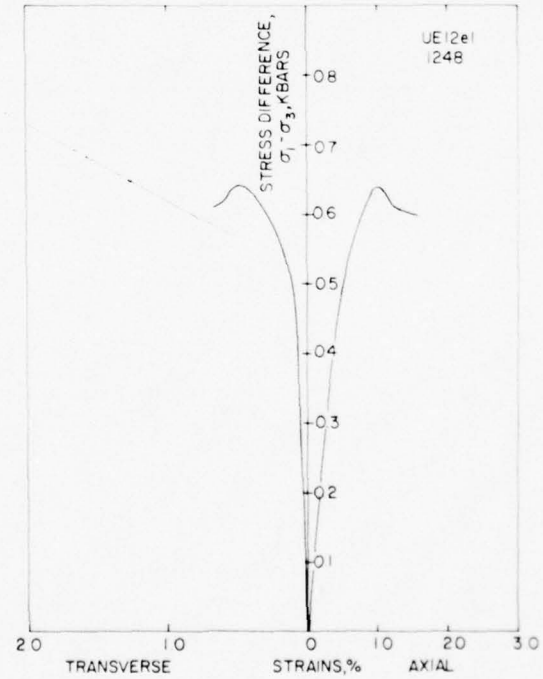


Figure A-12. Triaxial compression test at 1000 PSI confining pressure on UE12e#1 core samples--stress difference versus individual strains.

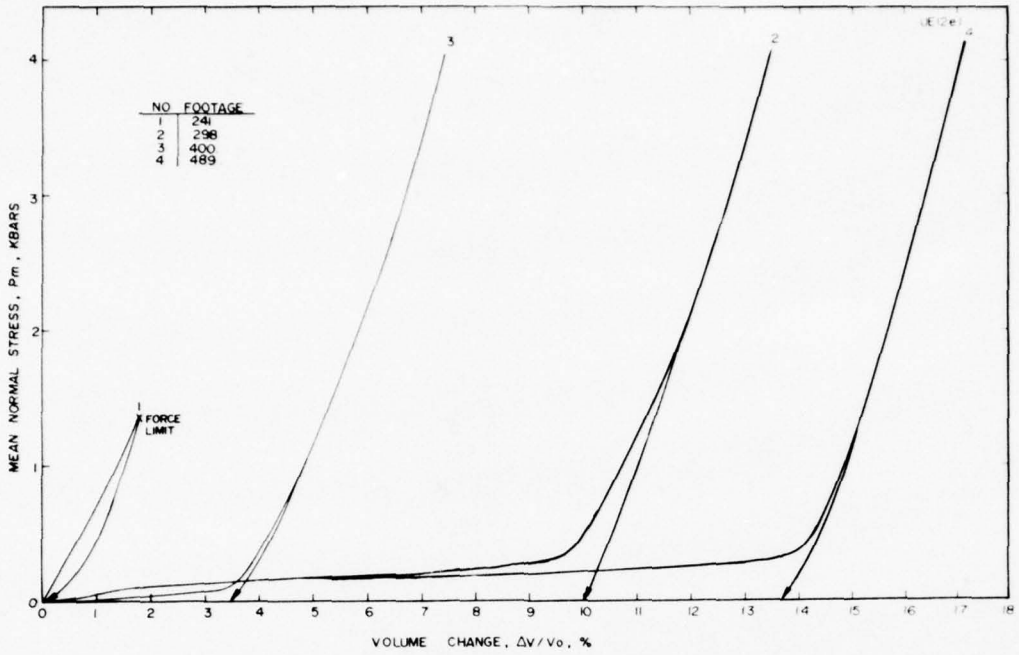


Figure A-13a. Uniaxial strain tests on UE12e#1 core samples--mean normal stress versus volume change.

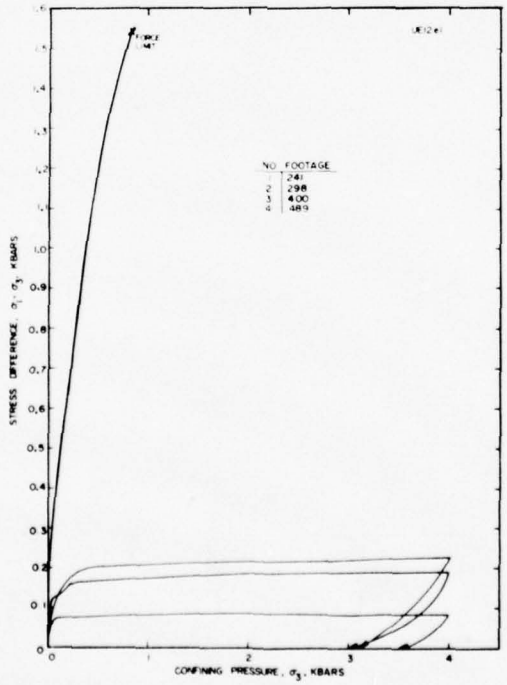


Figure A-13b. Uniaxial strain tests on UE12e#1 core samples--stress difference versus confining pressure.

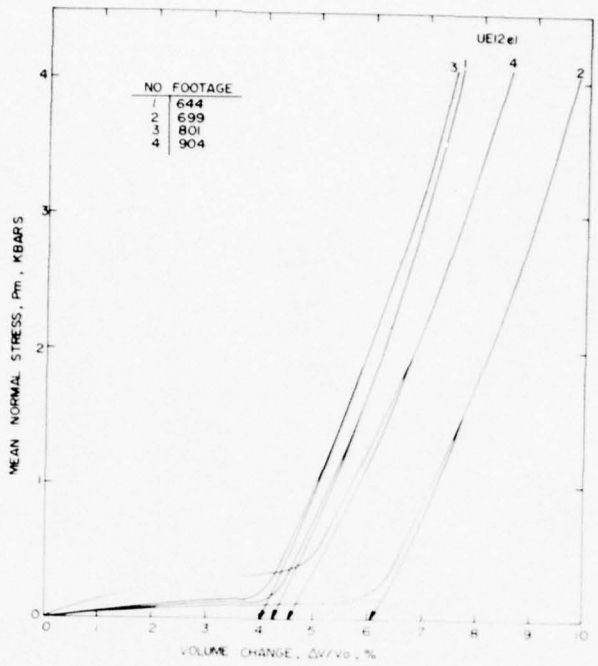


Figure A-14a. Uniaxial strain tests on UE12e#1 core samples--mean normal stress versus volume change.

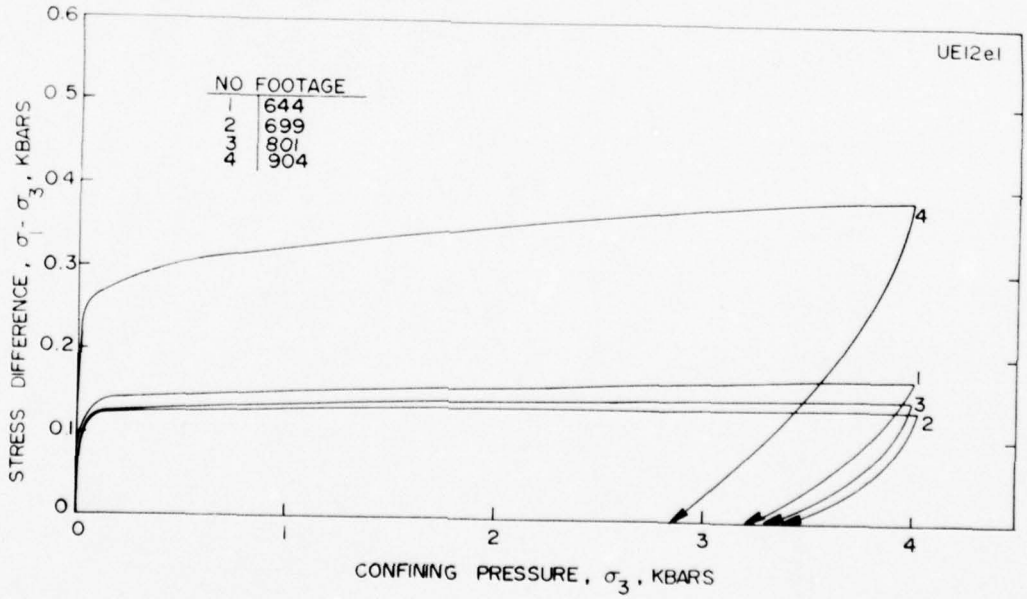


Figure A-14b. Uniaxial strain tests on UE12e#1 core samples--stress difference versus confining pressure.

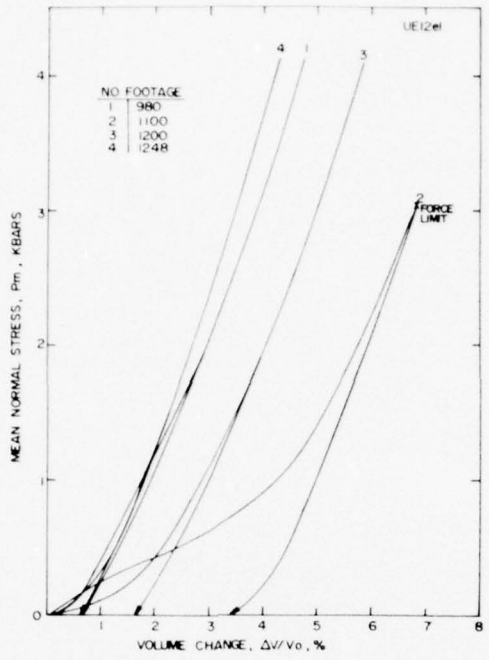


Figure A-15a. Uniaxial strain tests on UE12e#1 core samples--mean normal stress versus volume change.

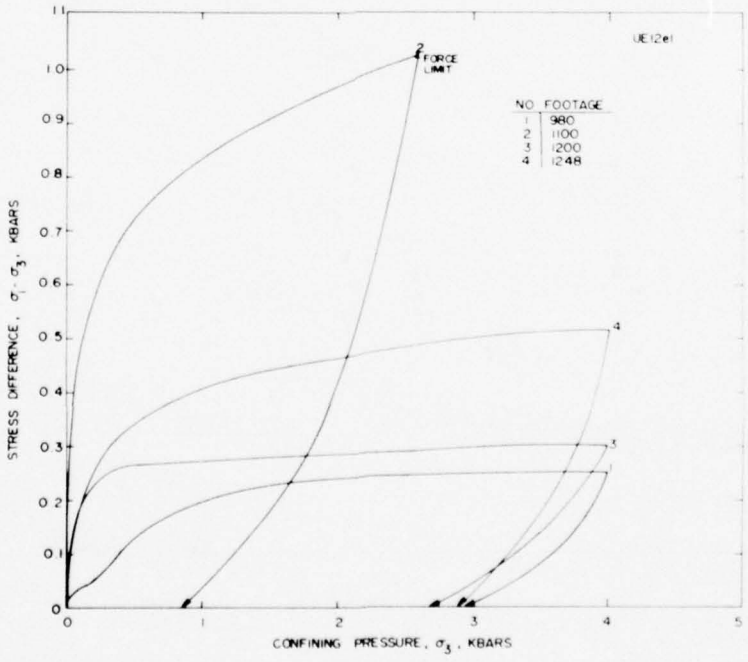


Figure A-15b. Uniaxial strain tests on UE12e#1 core samples--stress difference versus confining pressure.

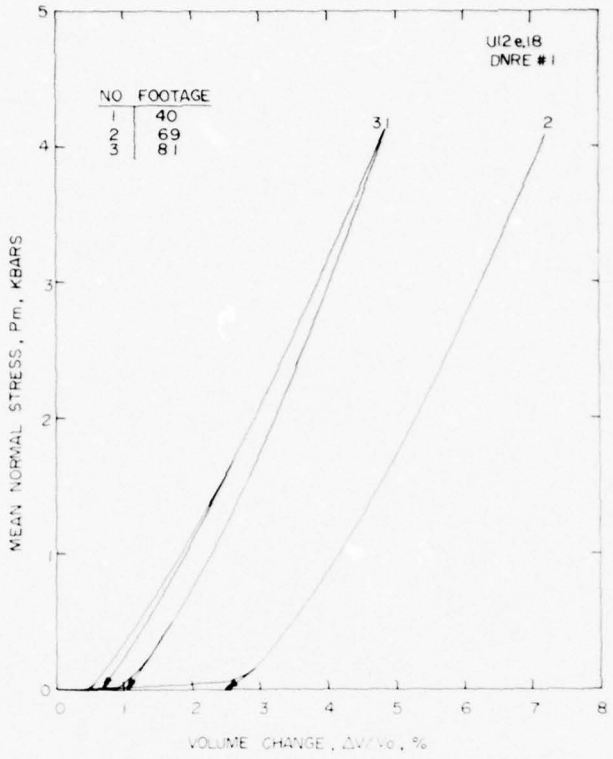


Figure A-16a. Uniaxial strain tests on U12e.18 DNRE#1 core samples--mean normal stress versus volume change.

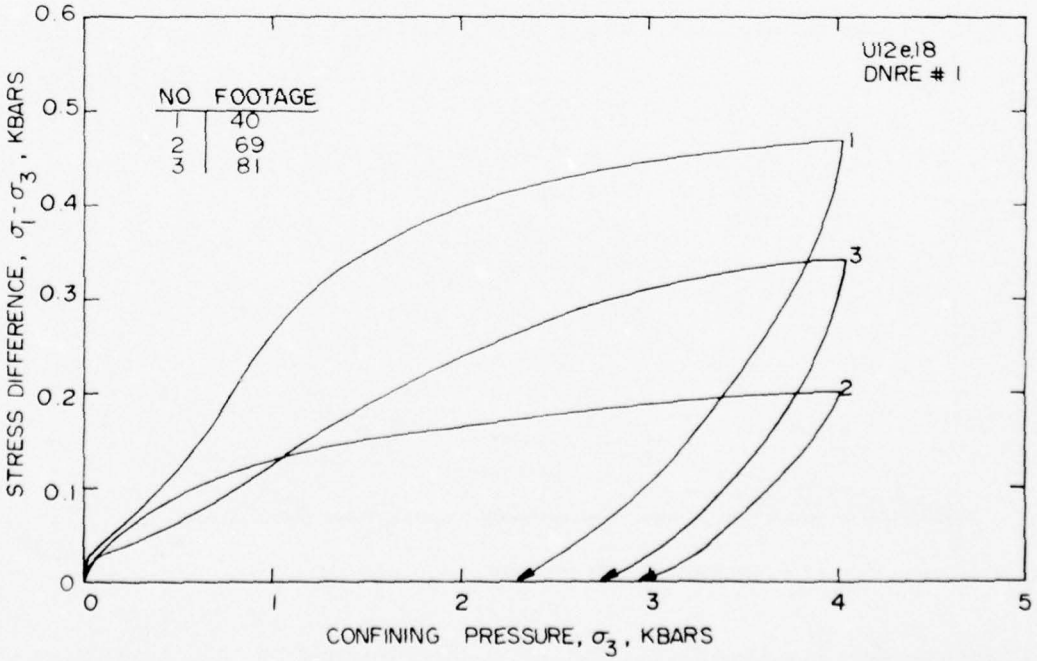


Figure A-16b. Uniaxial strain tests on U12e.18 DNRE#1 core samples--stress difference versus confining pressure.

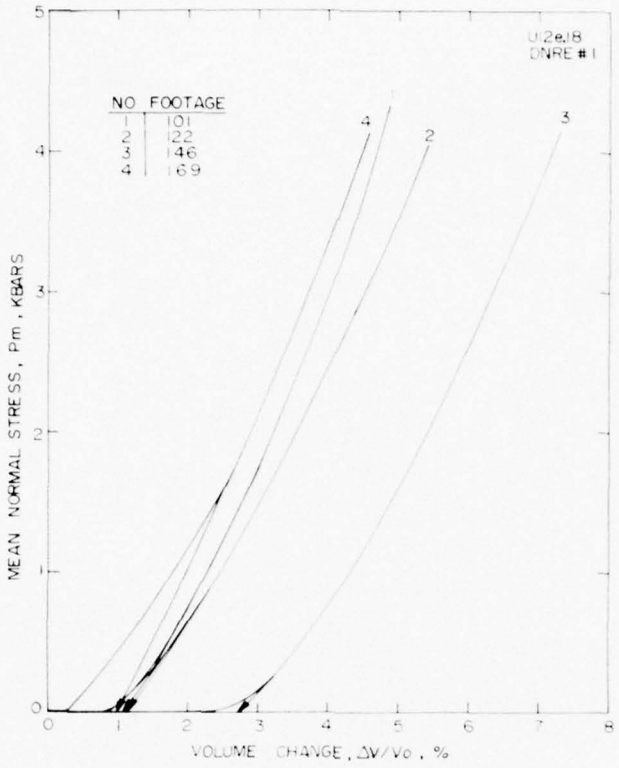


Figure A-17a. Uniaxial strain tests on U12e.18 DNRE#1 core samples--mean normal stress versus volume change.

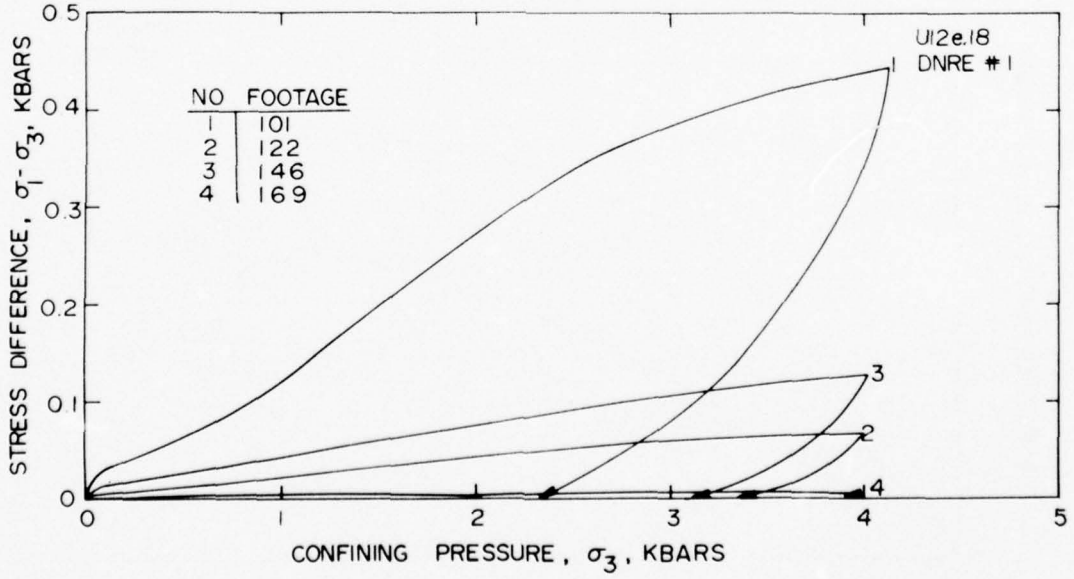


Figure A-17b. Uniaxial strain tests on U12e.18 DNRE#1 core samples--stress difference versus confining pressure.

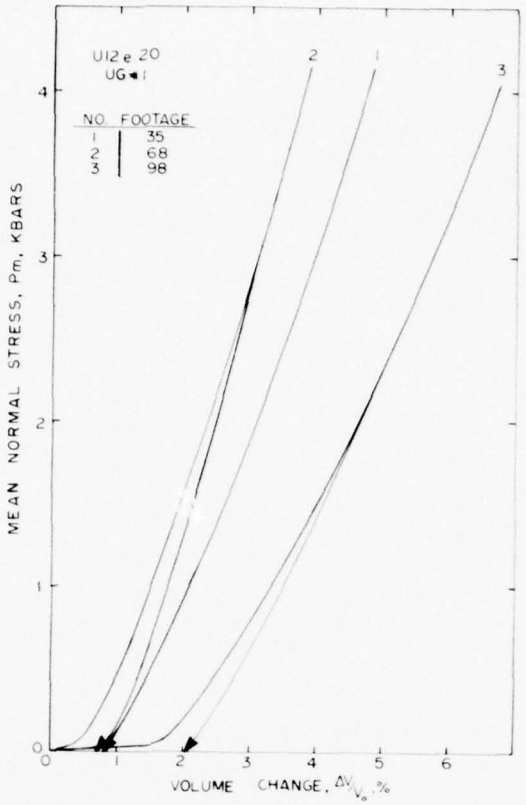


Figure A-18a. Uniaxial strain tests on U12e.20 UG#1 core samples--mean normal stress versus volume change.

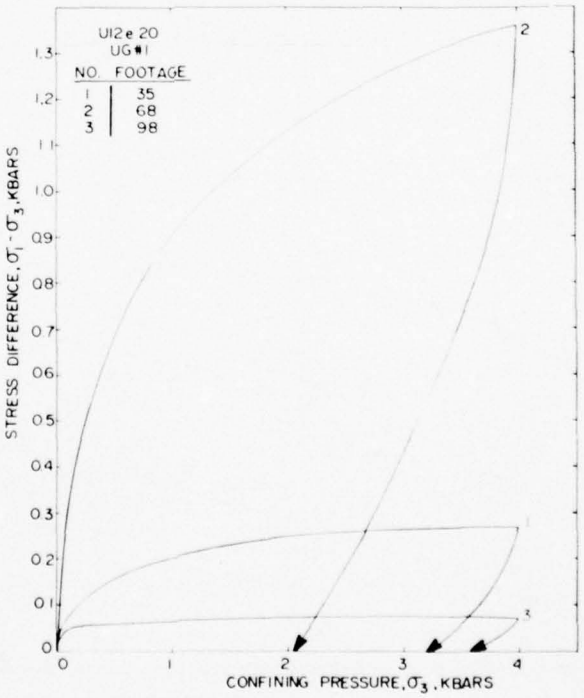


Figure A-18b. Uniaxial strain tests on U12e.20 UG#1 core samples--stress difference versus confining pressure.

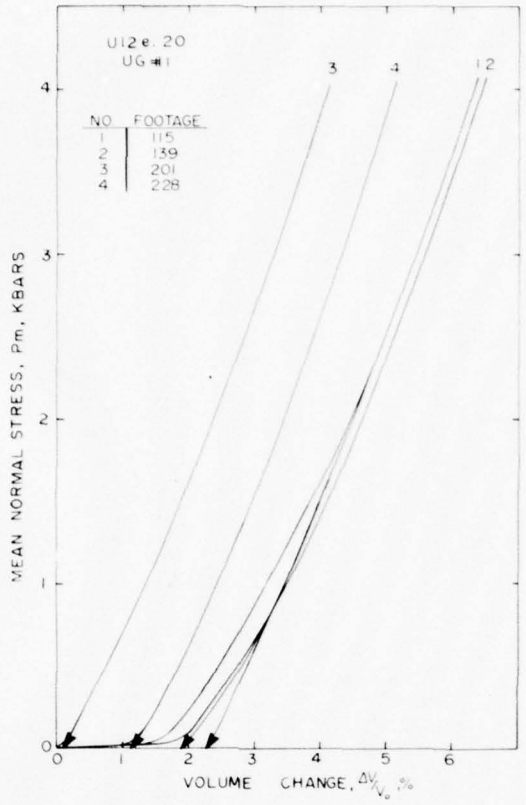


Figure A-19a. Uniaxial strain tests on U12e.20 UG#1 core samples--mean normal stress versus volume change.

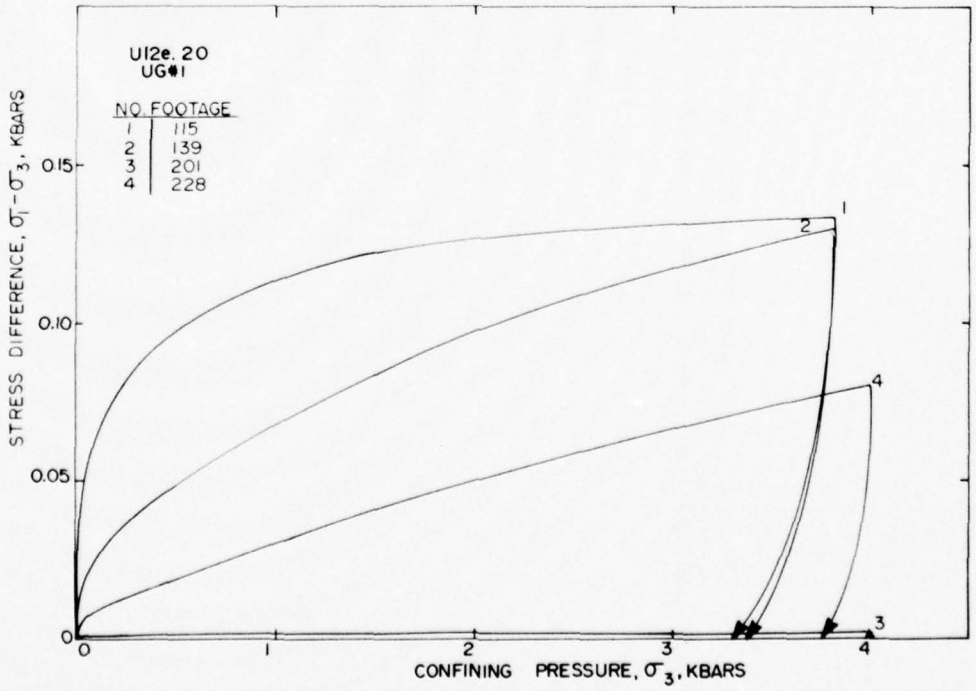


Figure A-19b. Uniaxial strain tests on U12e.20 UG#1 core samples--stress difference versus confining pressure.

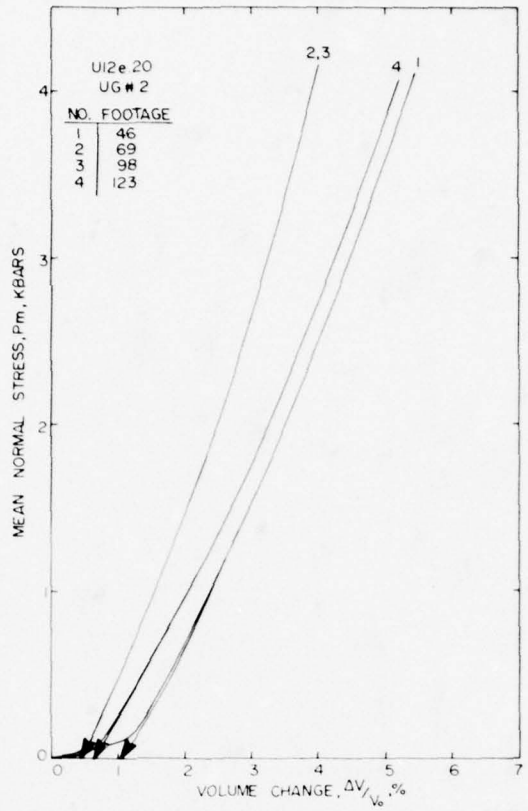


Figure A-20a. Uniaxial strain tests on U12e.20 UG#2 core samples--mean normal stress versus volume change.

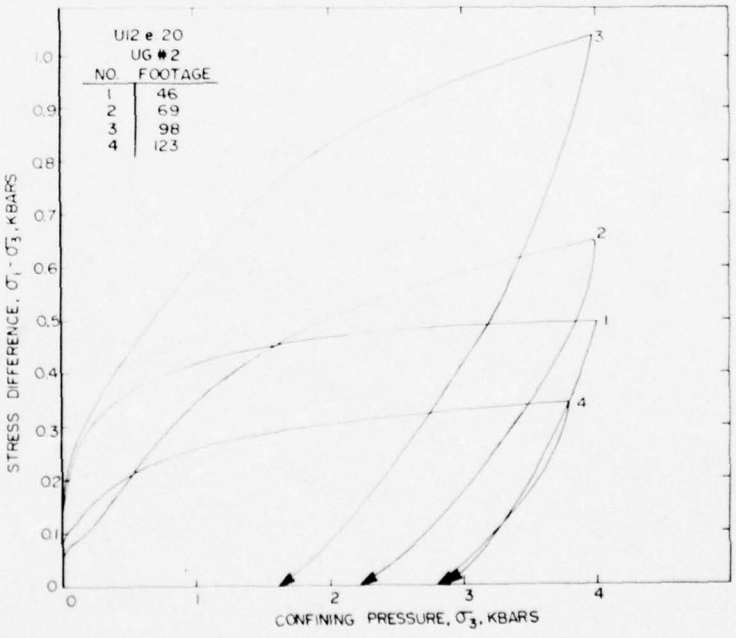


Figure A-20b. Uniaxial strain tests on U12e.20 UG#2 core samples--stress difference versus confining pressure.

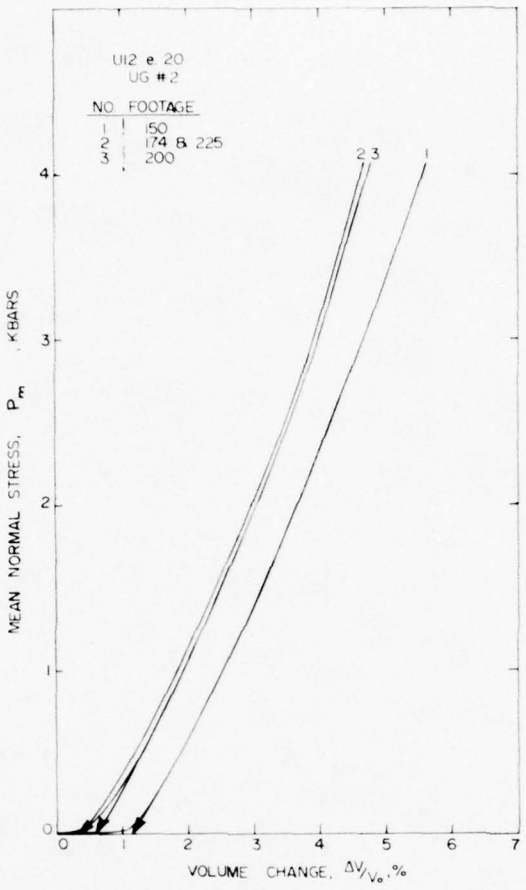


Figure A-21a. Uniaxial strain tests on U12e.20 UG#2 core samples--mean normal stress versus volume change.

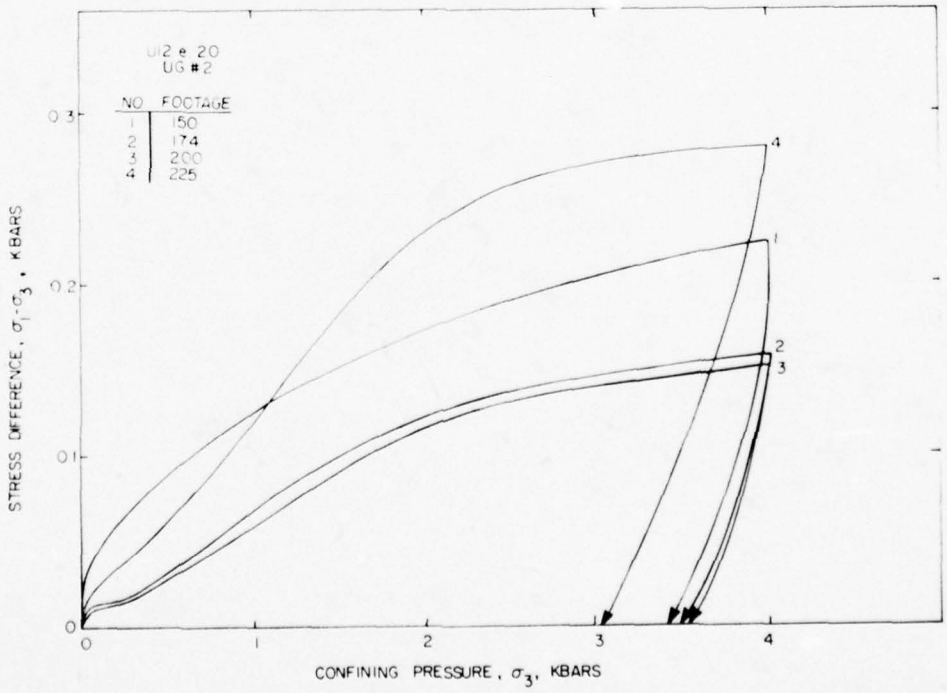


Figure A-21b. Uniaxial strain tests on U12e.20 UG#2 core samples--stress difference versus confining pressure.

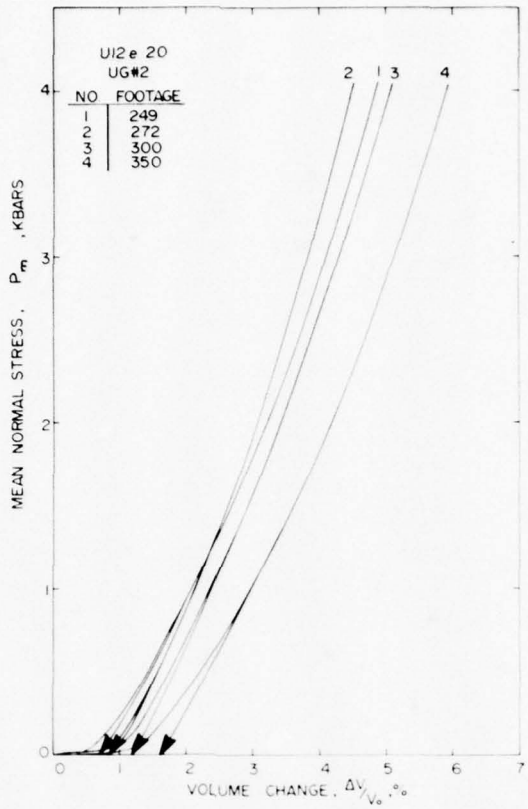


Figure A-22a. Uniaxial strain tests on U12e.20 UG#2 core samples--mean normal stress versus volume change.

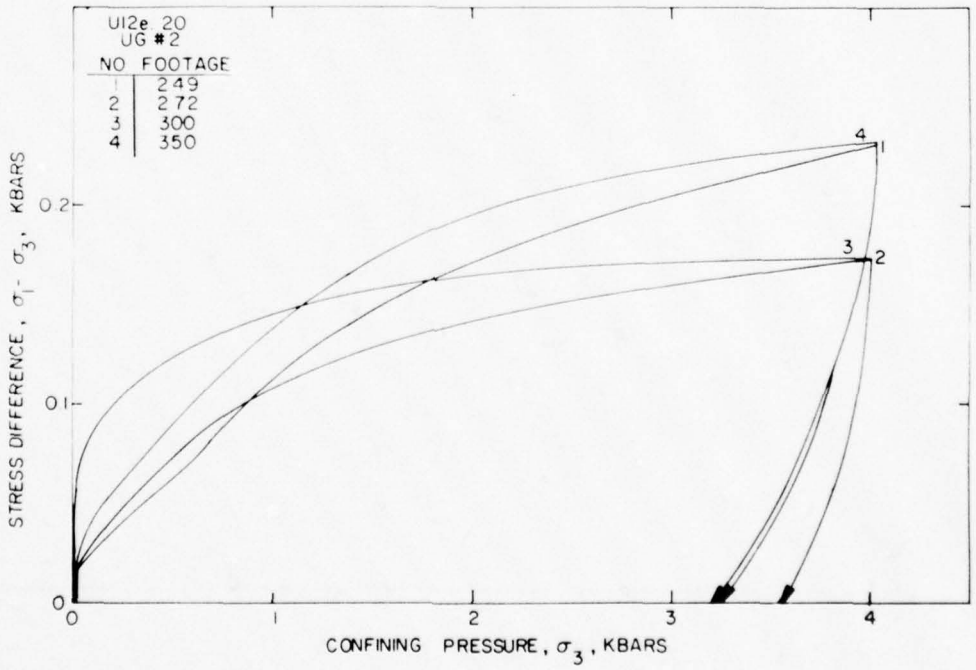


Figure A-22b. Uniaxial strain tests on U12e.20 UG#2 core samples--stress difference versus confining pressure.

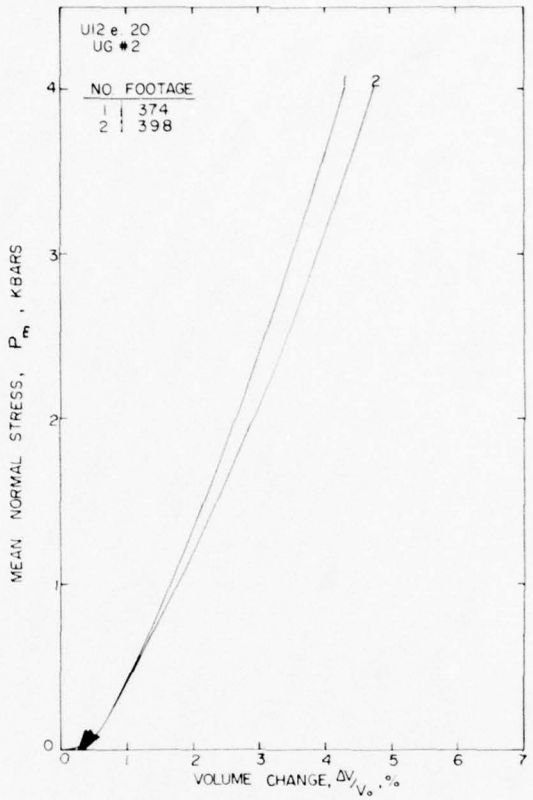


Figure A-23a. Uniaxial strain tests on U12e.20 UG#2 core samples--mean normal stress versus volume change.

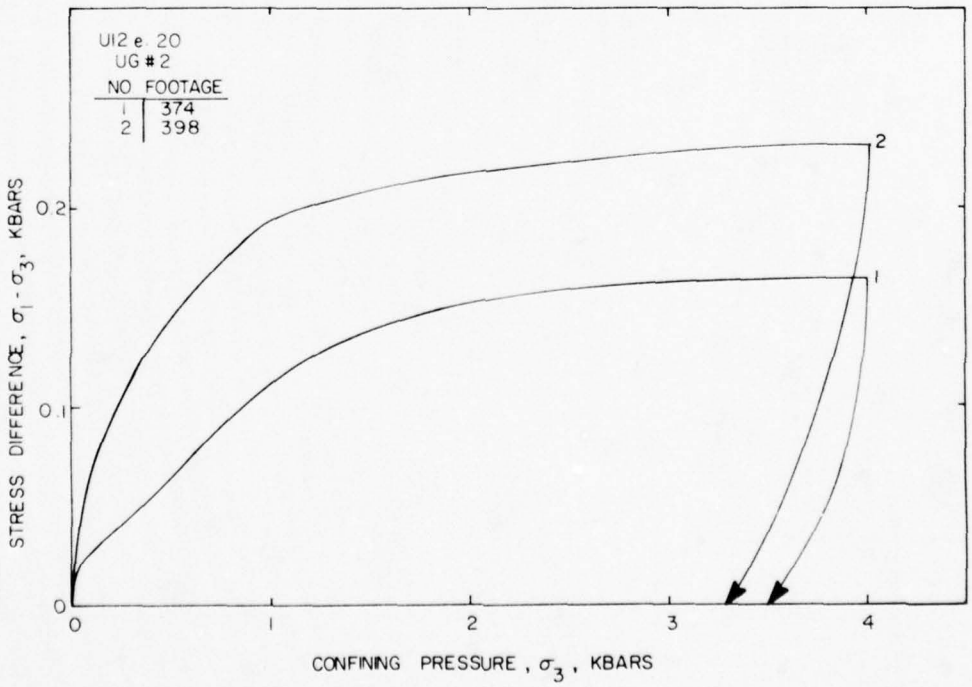


Figure A-23b. Uniaxial strain tests on U12e.20 UG#2 core samples--stress difference versus confining pressure.

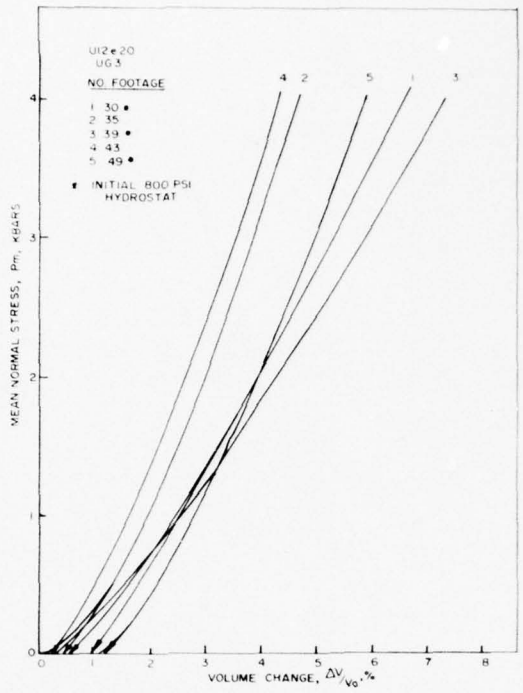


Figure A-24a. Uniaxial strain tests on U12e.20 UG#3 core samples--mean normal stress versus volume change.

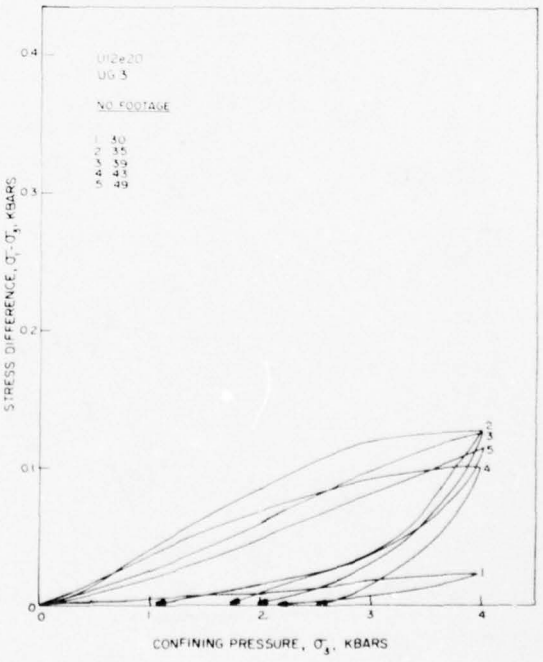


Figure A-24b. Uniaxial strain tests on U12e.20 UG#3 core samples--stress difference versus confining pressure.

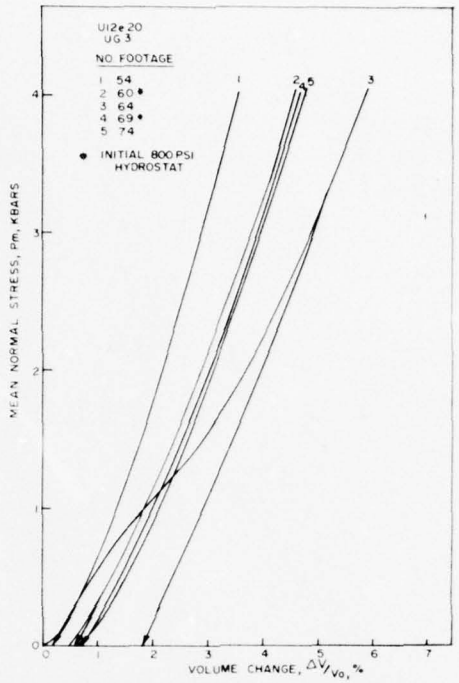


Figure A-25a. Uniaxial strain tests on U12e.20 UG#3 core samples--mean normal stress versus volume change.

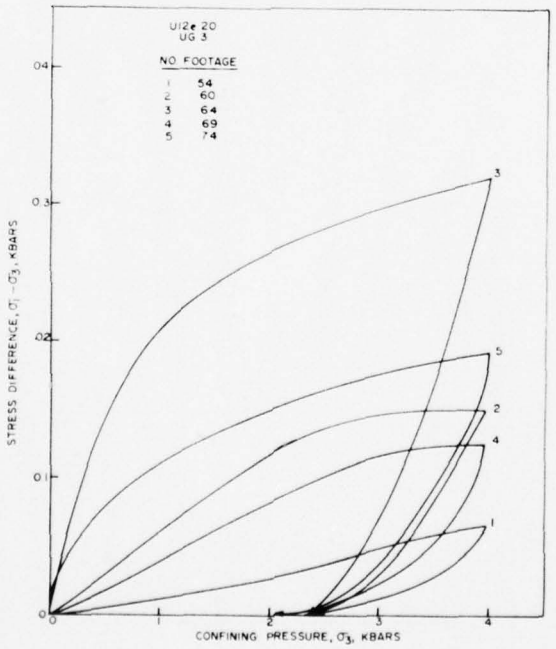


Figure A-25b. Uniaxial strain tests on U12e.20 UG#3 core samples--stress difference versus confining pressure.

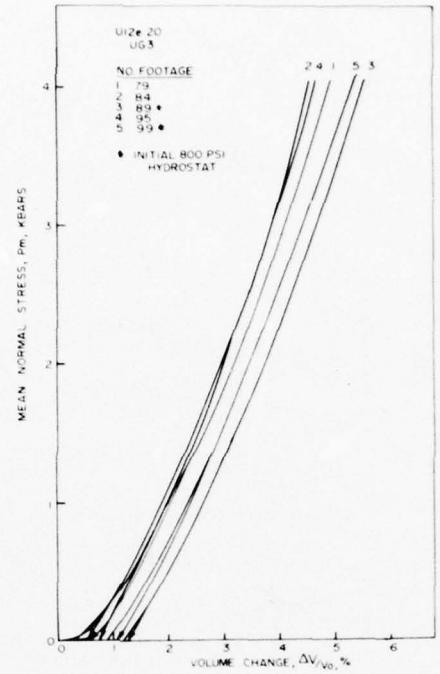


Figure A-26a. Uniaxial strain tests on U12e.20 UG#3 core samples--mean normal stress versus volume change.

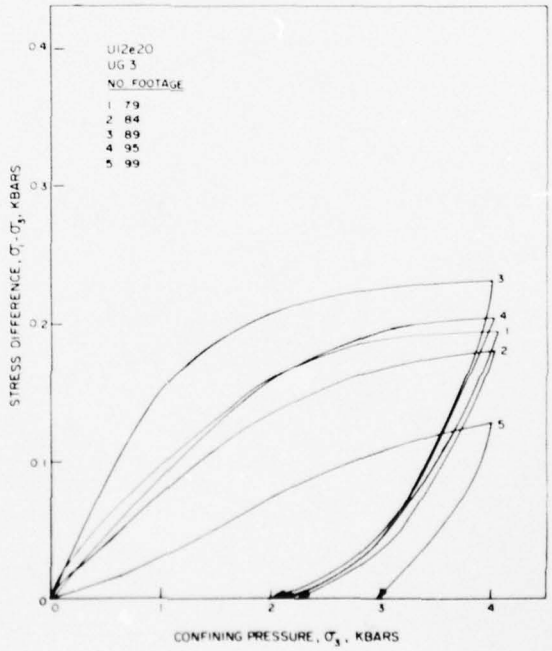


Figure A-26b. Uniaxial strain tests on U12e.20 UG#3 core samples--stress difference versus confining pressure.

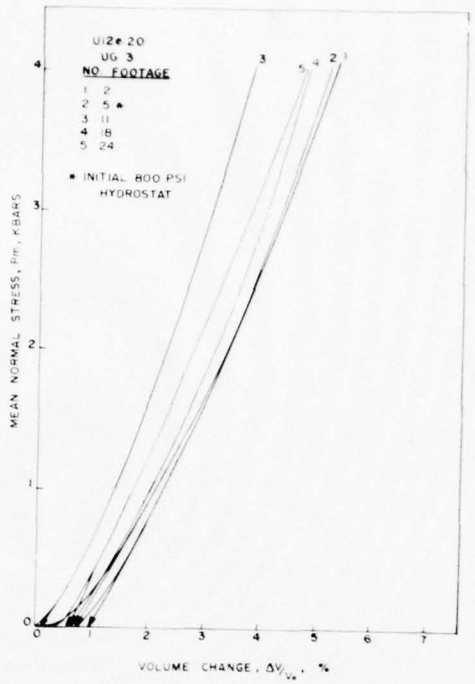


Figure A-27a. Uniaxial strain tests on U12e.20 UG#3 core samples--mean normal stress versus volume change.

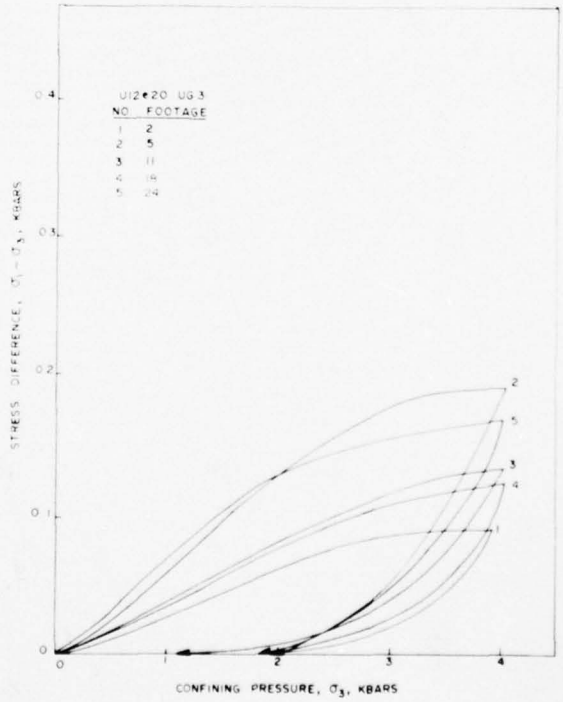


Figure A-27b. Uniaxial strain tests on U12e.20 UG#3 core samples--stress difference versus confining pressure.

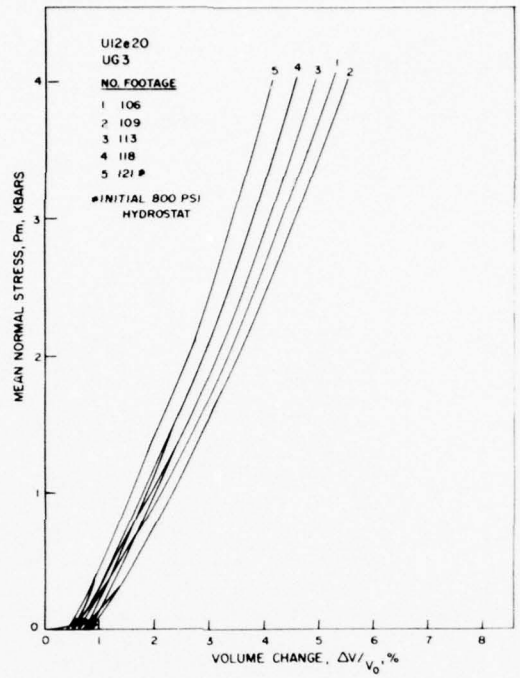


Figure A-28a. Uniaxial strain tests on U12e.20 UG#3 core samples--mean normal stress versus volume change.

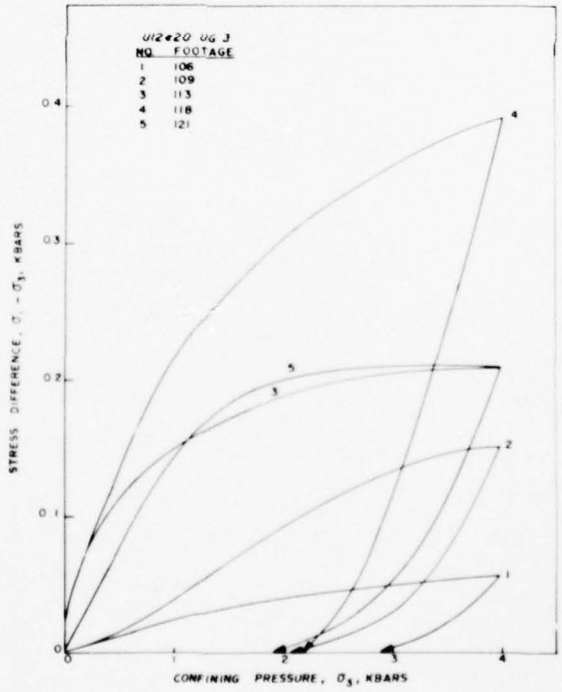


Figure A-28b. Uniaxial strain tests on U12e.20 UG#3 core samples--stress difference versus confining pressure.

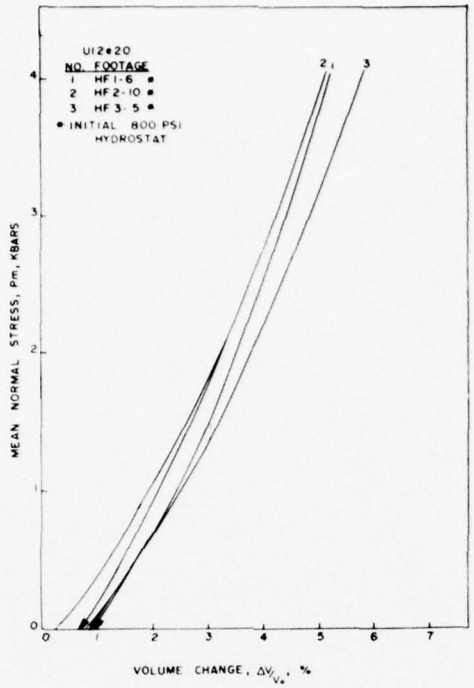


Figure A-29a. Uniaxial strain tests on U12e.20 HF#1,2,3 core samples--mean normal stress versus volume change.

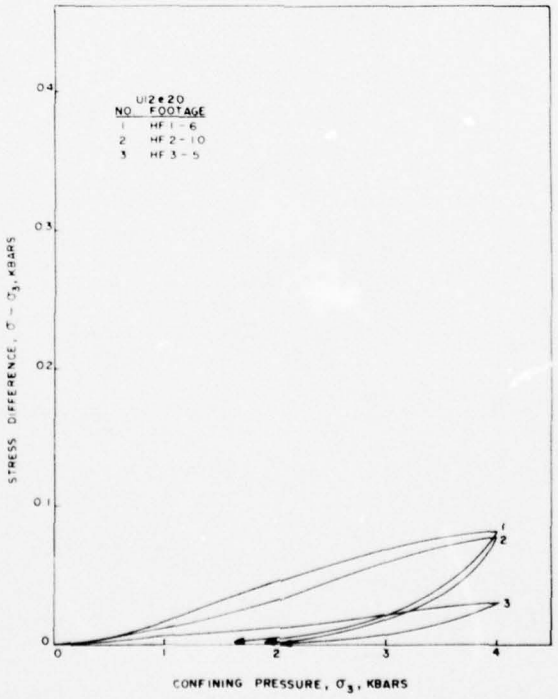


Figure A-29b. Uniaxial strain tests on U12e.20 HF#1,2,3 core samples--stress difference versus confining pressure.

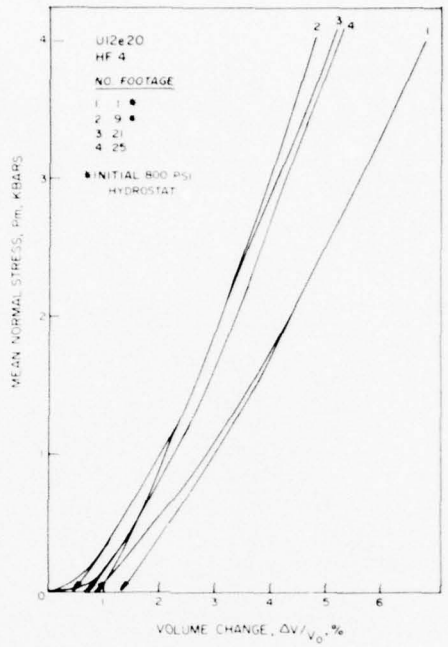


Figure A-30a. Uniaxial strain tests on U12e.20 HF#4 core samples--mean normal stress versus volume change.

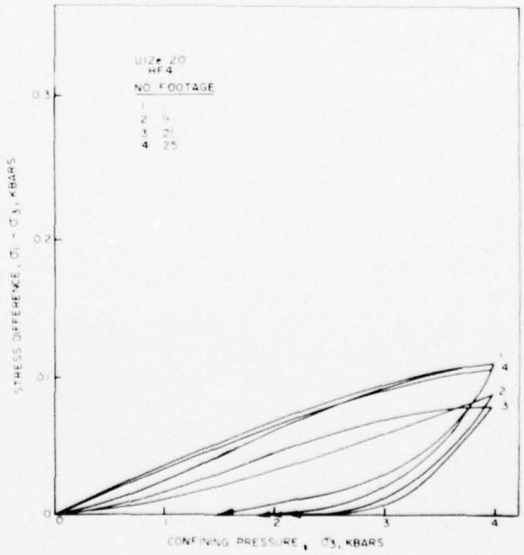


Figure A-30b. Uniaxial strain tests on U12e.20 HF#4 core samples--stress difference versus confining pressure.

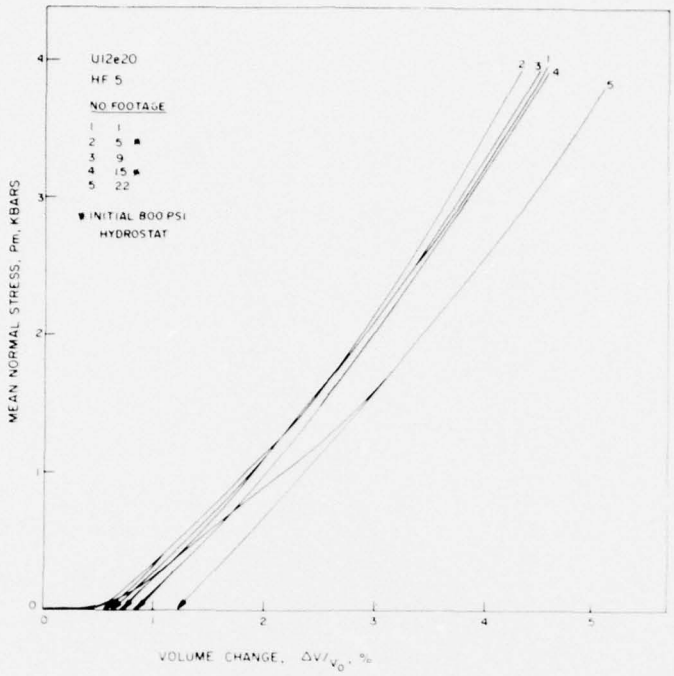


Figure A-31a. Uniaxial strain tests on U12e.20 HF#5 core samples--mean normal stress versus volume change.

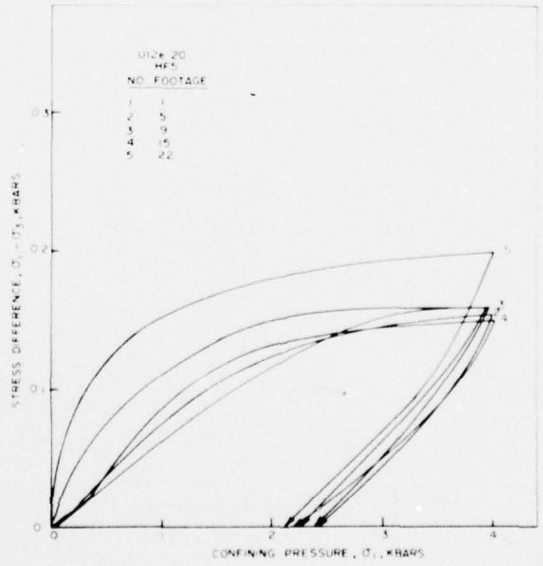


Figure A-31b. Uniaxial strain tests on U12e.20 HF#5 core samples--stress difference versus confining pressure.

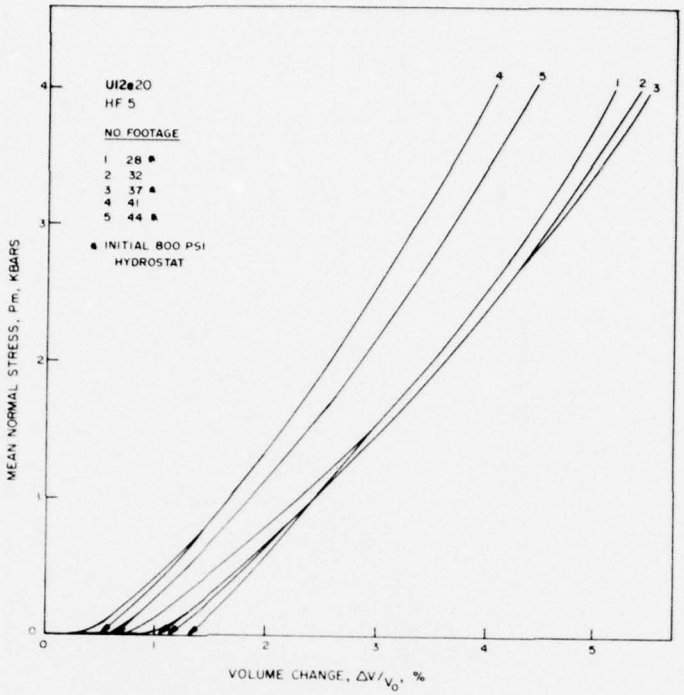


Figure A-32a. Uniaxial strain tests on U12e.20 HF#5 core samples--mean normal stress versus volume change.

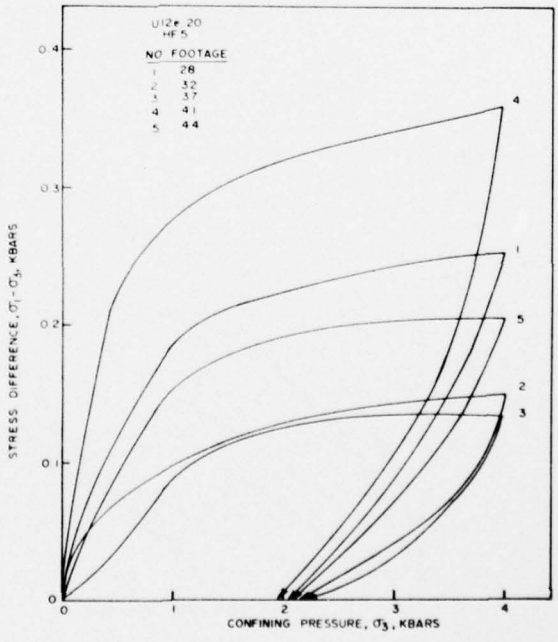


Figure A-32b. Uniaxial strain tests on U12e.20 HF#5 core samples--stress difference versus confining pressure.

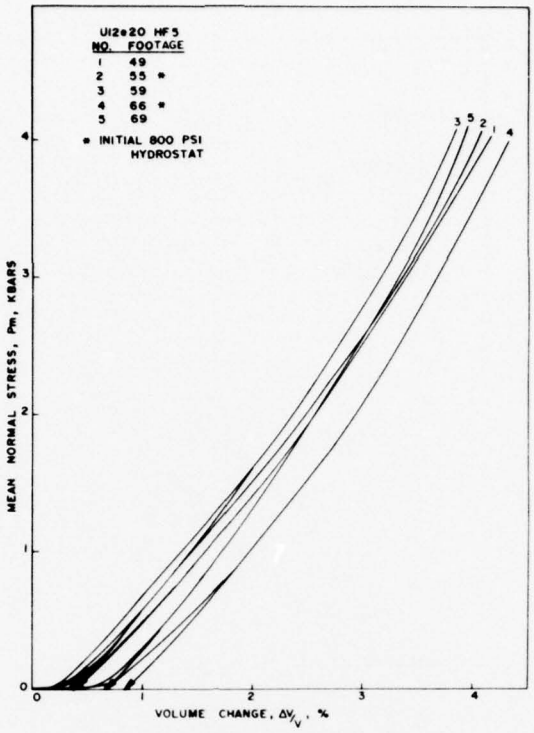


Figure A-33a. Uniaxial strain tests on U12e.20 HF#5 core samples--mean normal stress versus volume change.

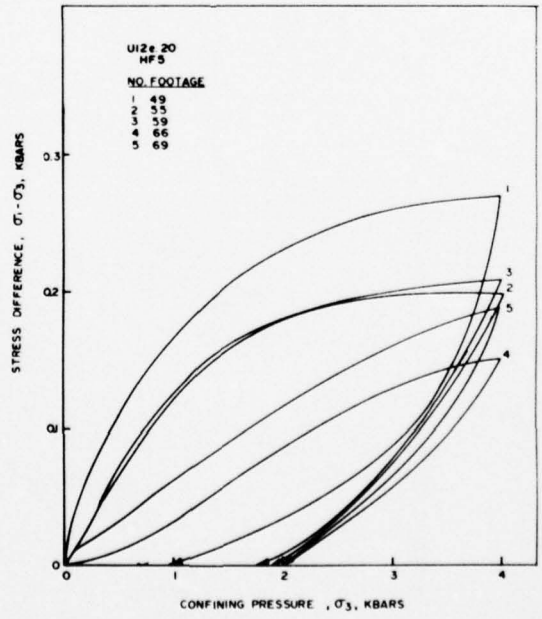


Figure A-33b. Uniaxial strain tests on U12e.20 HF#5 core samples--stress difference versus confining pressure.

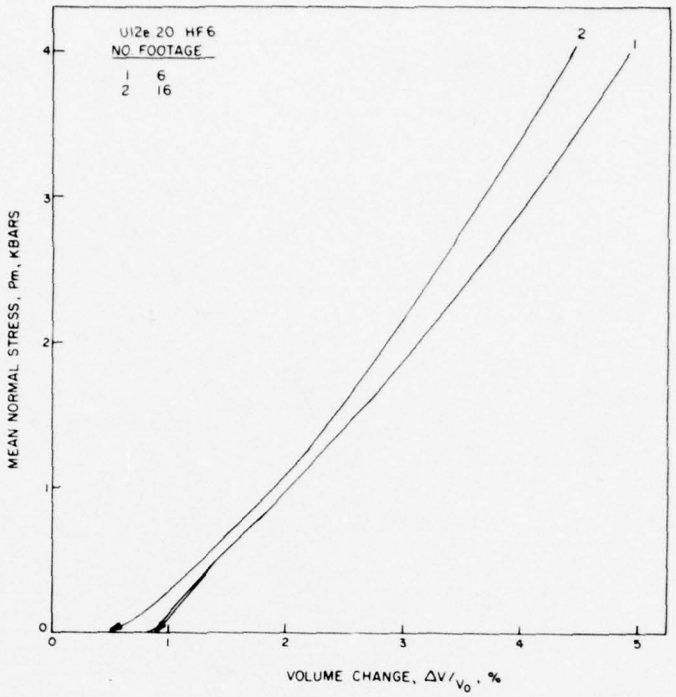


Figure A-34a. Uniaxial strain tests on U12e.20 HF#6 core samples--mean normal stress versus volume change.

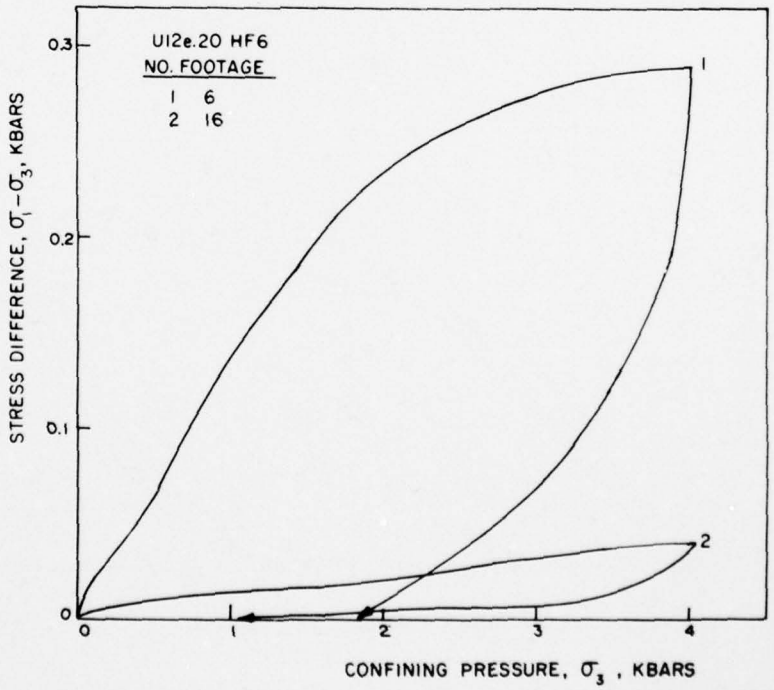


Figure A-34b. Uniaxial strain tests on U12e.20 HF#6 core samples--stress difference versus confining pressure.

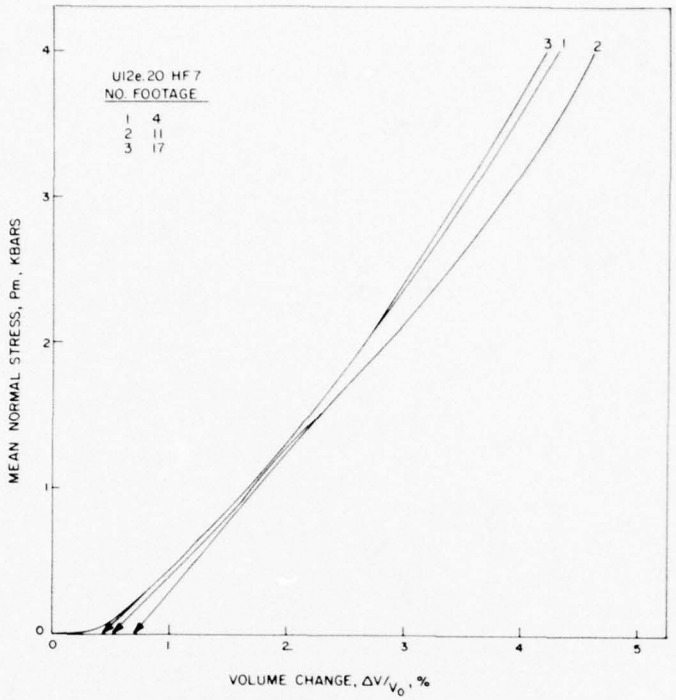


Figure A-35a. Uniaxial strain tests on U12e.20 HF#7 core samples--mean normal stress versus volume change.

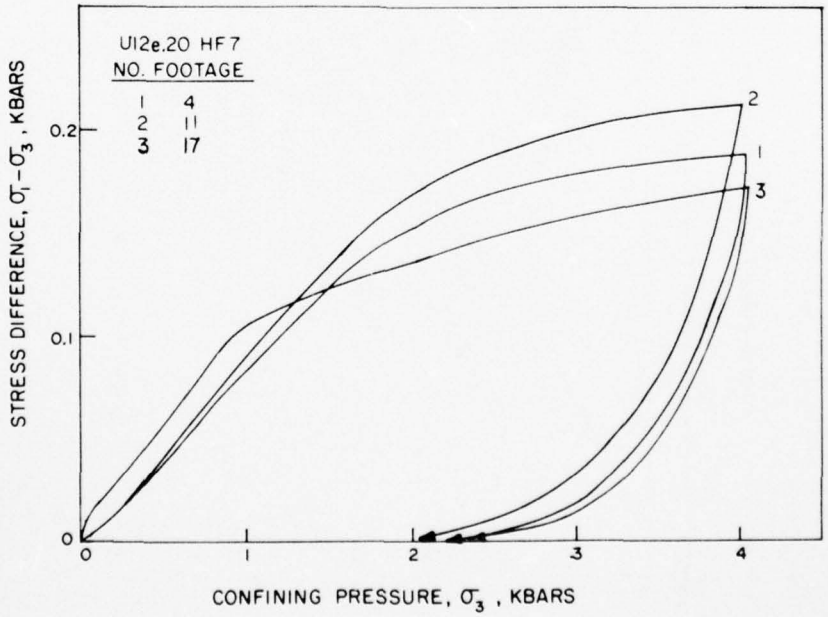


Figure A-35b. Uniaxial strain tests on U12e.20 HF#7 core samples--stress difference versus confining pressure.

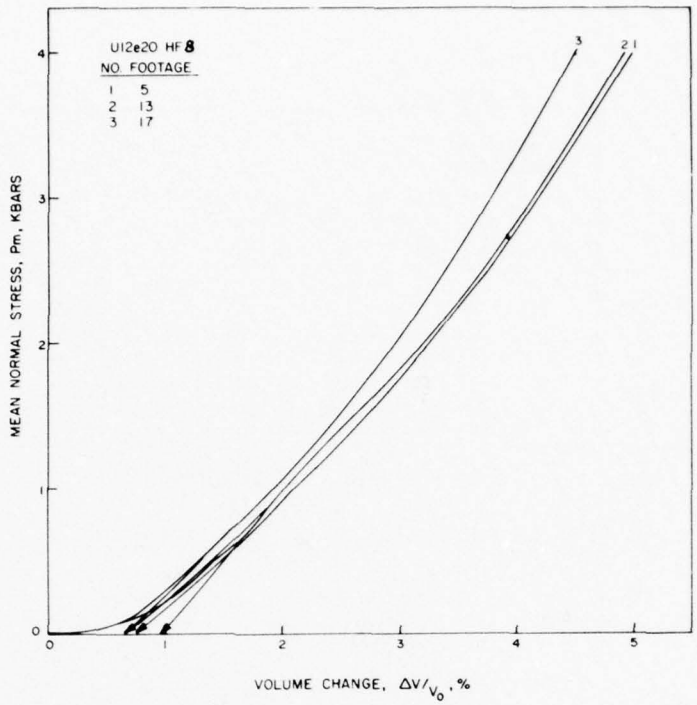


Figure A-36a. Uniaxial strain tests on U12e.20 HF#8 core samples--mean normal stress versus volume change.

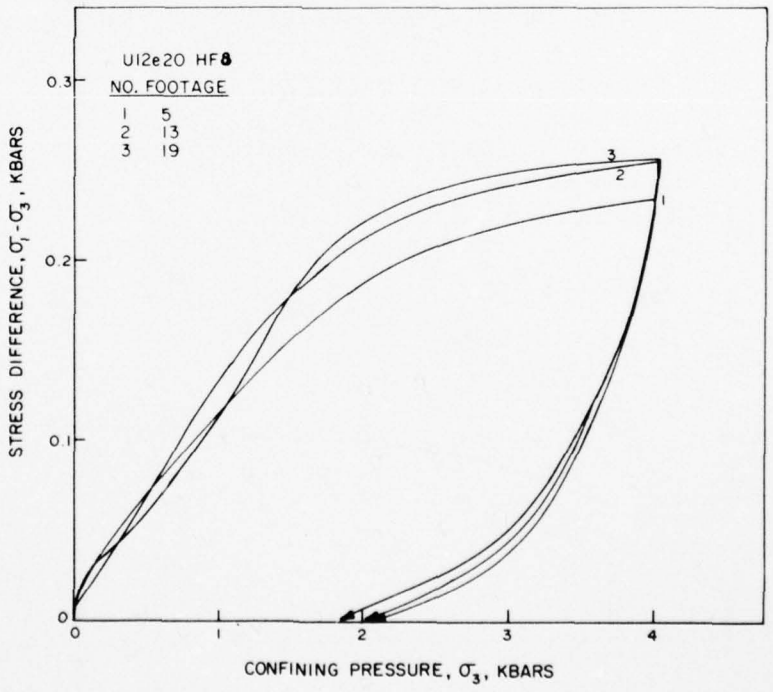


Figure A-36b. Uniaxial strain tests on U12e.20 HF#8 core samples--stress difference versus confining pressure.

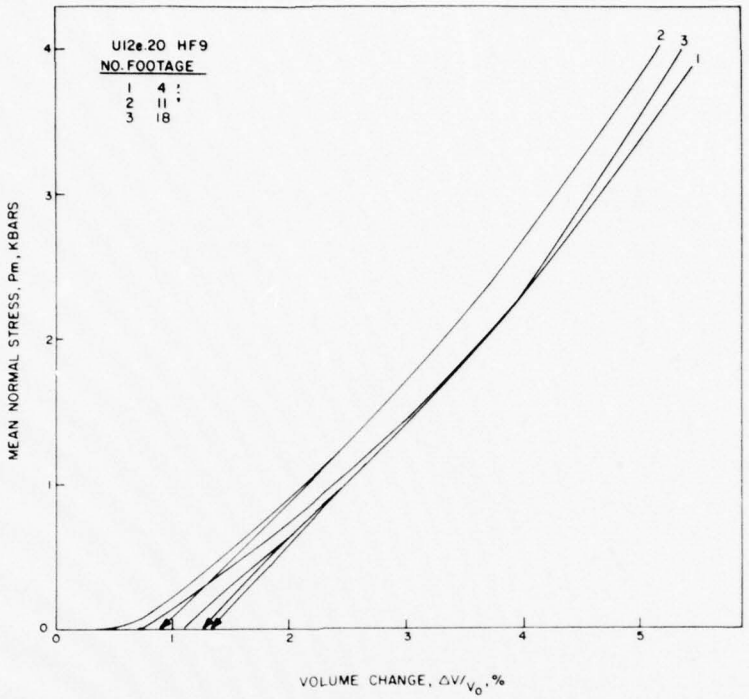


Figure A-37a. Uniaxial strain tests on U12e.20 HF#9 core samples--mean normal stress versus volume change.

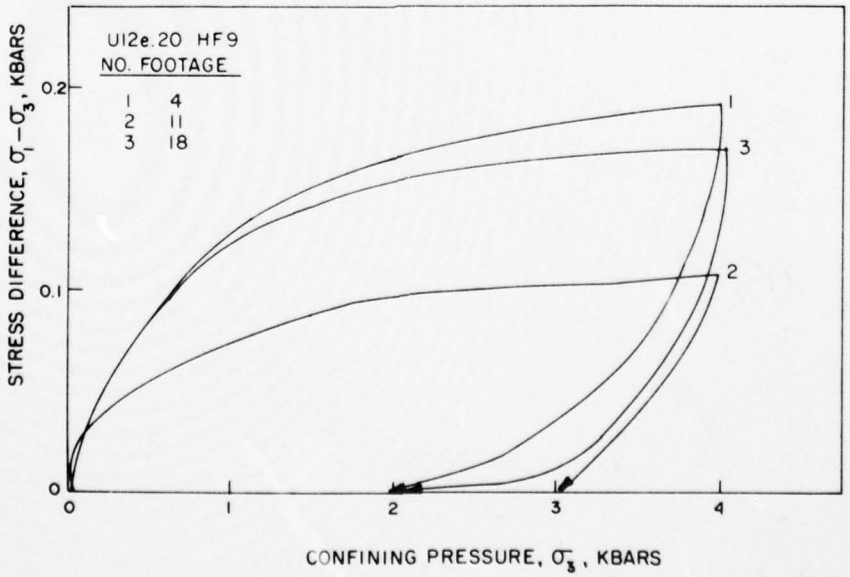


Figure A-37b. Uniaxial strain tests on U12e.20 HF#9 core samples--stress difference versus confining pressure.

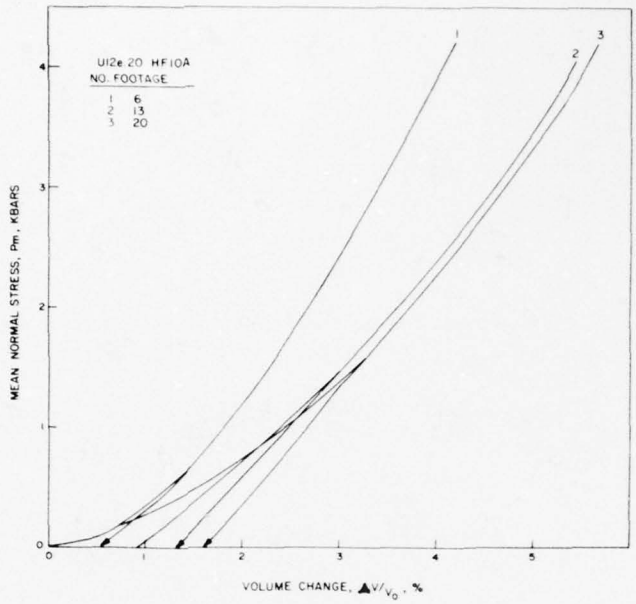


Figure A-38a. Uniaxial strain tests on U12e.20 HF#10A core samples--mean normal stress versus volume change.

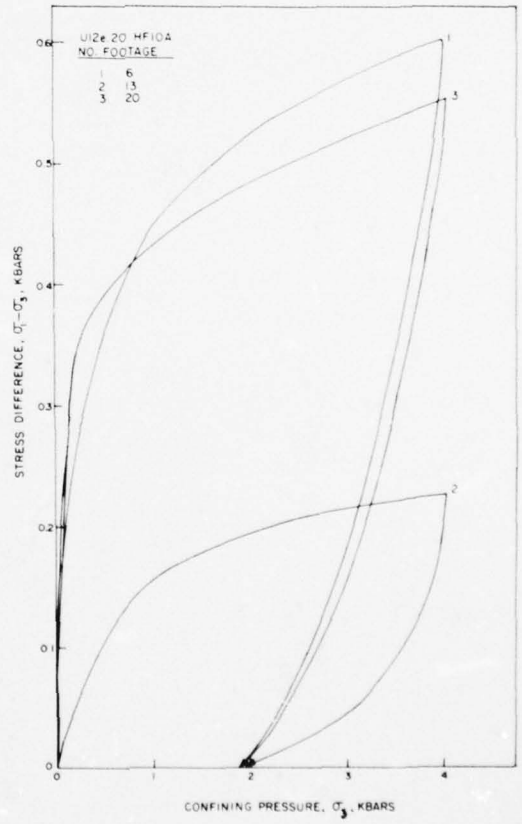


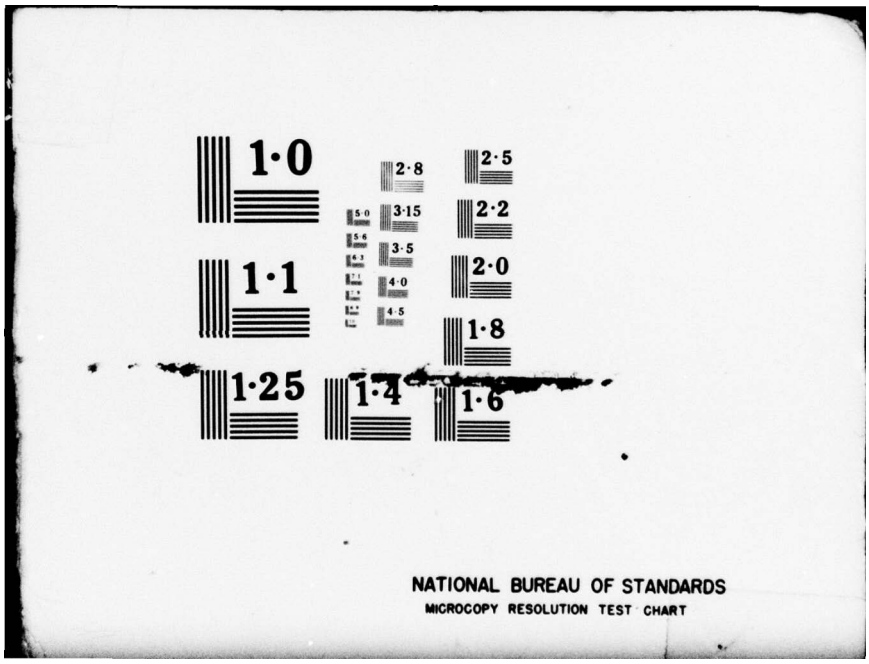
Figure A-38b. Uniaxial strain tests on U12e.20 HF#10A core samples--stress difference versus confining pressure.

AD-A059 939 TERRA TEK INC SALT LAKE CITY UTAH F/G 18/3
MATERIAL PROPERTIES OF NEVADA TEST SITE TUFF AND GROUT--WITH EM--ETC(U)
NOV 77 D S GARDINER, D O ENNISS, S W BUTTERS DNA001-76-C-0351
UNCLASSIFIED TR-77-96 DNA-4528F NL

3 OF 3
ADA
059939



END
DATE
FILMED
12-78
DDC


1·0
1·1
1·25
1·4
1·6
1·8
2·0
2·2
2·5
2·8
3·15
3·5
4·0
4·5
5·0
5·6
NATIONAL BUREAU OF STANDARDS
MICROCOPY RESOLUTION TEST CHART

MATERIAL PROPERTIES OF U12e.20 TUFF OVERCORES

PRECEDING PAGE BLANK-NOT FILMED

TerraTek

August 1, 1977

Mr. J. W. LaComb
Defense Nuclear Agency
Nevada Test Site
Mercury, NV 89023

Dear Joe:

U12e.20 overcore tuff samples were subjected to mechanical tests to determine the elastic moduli for use in evaluating "in situ" stresses. Cores from five separate overcores designated ISS#1, 2, 3, 7A, and 9 were tested. Samples were prepared by recoring to a 2 inch diameter and cutting ends parallel to a 2½ inch length.

Triaxial compression tests were performed at 34.5 bars (500 psi). Young's moduli were scaled directly from the stress-strain curves in the initial elastic portion. Poisson's ratio were calculated from axial and lateral strain increments in the same region. Table I lists the Young's modulus and Poisson's ratio for each overcore. Stress-strain curves are shown in Figure 1.

Overcores ISS#2, 3 and 7A all had Young's moduli around 14 kbars. These modulus values seem to confirm both your's and Bill Ellis' preconceived estimates. Young's moduli for ISS#1 and #9 were about 4 kilobars and ½ kilobars, respectively.

Sincerely,

Don Gardiner

D. S. Gardiner
Research Engineer

DSG/jlg

Enclosure

cc: Bill Ellis

TABLE I

Young's Moduli and Poisson's Ratios from Triaxial Compression at 34.5 Bars Confining Pressure

U12e.20 Overcore No./Footage		Young's Modulus E(KB)	Poisson's Ratio* ν
ISS#1	7'	3.85	0.44
ISS#2	14'	14.81	0.16-0.21
ISS#3	4'	13.79	0.18-0.20
ISS#7A	8'	13.33	0.16-0.18
ISS#9		0.40	-

* The range given for Poisson's ratio was derived from the difference in the two lateral strain measurements.

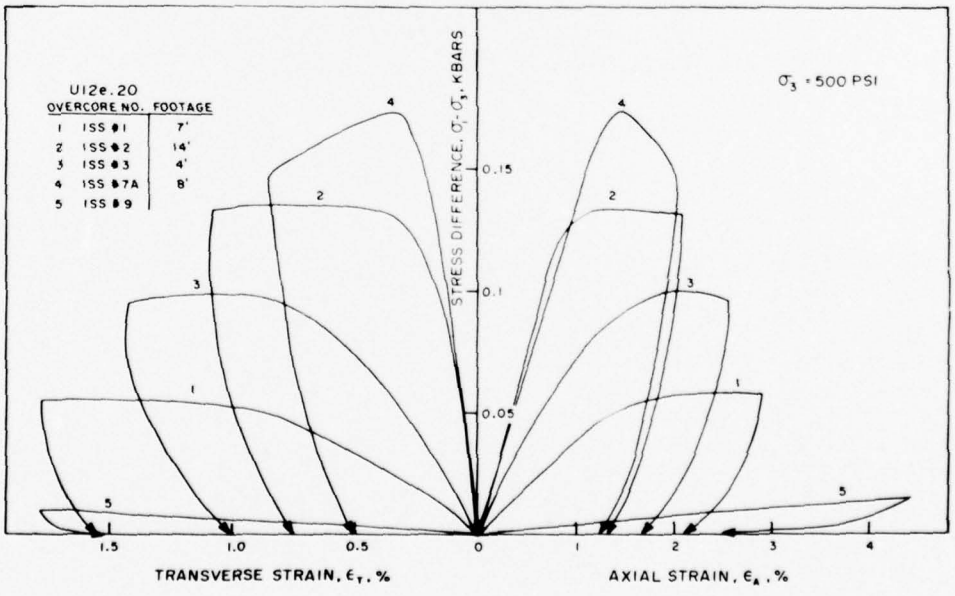


Figure 1. Stress-strain curves for U12e.20 overcores.

WATER AND AIR PERMEABILITY OF CONCRETE FROM HYBLA GOLD PIPE

PRECEDING PAGE BLANK-NOT FILMED

TerraTek

September 2, 1977

Mr. J. W. LaComb
Defense Nuclear Agency
Nevada Test Site
Mercury, Nevada 89023

Dear Joe:

Hybla Gold concrete samples from A, B&C, D and E pipes were tested for permeability to air (nitrogen) and water. Permeability to air was measured by pressurizing one face of a cylindrical sample and measuring the flow at the downstream face (steady-state method). Permeability to water was measured by monitoring the pressure decay of a given volume of pressurized water at one end of the sample (transient method). Driving pressures were 100 psi for the air tests and 100 and 200 psi for the water tests. Additionally, water test specimens were pressurized up to the point where fracturing occured. All samples were ~1.0 inches in length and 1.74 inches in diameter.

Test results are listed in Table I. Results show all the concrete specimens to be in the microdarcy permeability range. No significant differences in permeabilities resulted from the different driving pressures. Samples fractured at around 1000 psi driving pressure.

Sincerely,

Don Gardiner

D. S. Gardiner
Research Engineer

UNIVERSITY RESEARCH PARK · 420 WAKARA WAY · SALT LAKE CITY, UTAH 84108 · (801) 582-2220

TABLE I

Air/Water Permeabilities-Hybla Gold Concrete

Pipe	Permeability to Air Microdarcies	Permeability to Water Microdarcies	Driving Pressure at Fracture PSI
A	3	20	1040
B&C	870	700	
D	40	600	
E	1	6	987

MATERIAL PROPERTIES FOR CORES FROM EXPLORATORY DRILL HOLE U12n.11 UG#1

TR 77-42
June 1977

PRECEDING PAGE BLANK-NOT FILMED

BACKGROUND

Site exploration is an essential part of the nuclear test program at the Nevada Test Site, Mercury, Nevada. The constant need for new test sites dictates continual exploration. Exploratory drill holes are an economical means of determining site usability for a nuclear test prior to extending tunnels into an area.

Site potential can be determined by examining the material properties of exploratory drill hole cores and comparing results with data from previously tested sites. Of particular interest are percent air void values derived from permanent volume compactions, after uniaxial strain tests to 4 kb confining pressure.

U12n.11 UG#1 DRILL HOLE SUMMARY

Both the physical and mechanical properties were determined for ash-fall tuff cores from exploratory drill hole U12n.11 UG#1. The cores were from 1006 feet through 1526 feet, with tests performed on samples spaced 25 feet apart. The derived physical properties and measured ultrasonic velocities are listed in Table I. Figure 1 is a plot of permanent-volume compaction (from uniaxial strain tests) versus drill hole footage for all the samples tested. Individual uniaxial strain test results are shown in Figures 2 through 7 as mean-normal stress versus volume change and stress difference versus confining pressure.

The results indicate a tuff saturated to in excess of 98 percent thereby exhibiting low permanent-volume compaction. Ultrasonic velocity measurements confirm the mechanical test data. Except for the sample from 1027 foot depth, shear strength lies within 0.2 to 0.8 kbar. The 1027 foot sample exhibited shear strength on the order of 1.7 kbar at 3 kbar confining pressure. For this sample the shear strength increased at the rate 0.3 kb/kbar confining pressure at 3 kbar confining pressure. Further pore collapse could have occurred with increased loads.

TABLE I

Physical Properties, Uniaxial Strain Permanent Volume Compaction and Ultrasonic Wave Velocities of U12n.11 UG#1 Cores

DRILL HOLE FOOTAGE U12n.11 UG#1	DENSITY (gm/cc)			WATER BY WET WEIGHT (%)	POROSITY (%)	SATURATION (%)	CALC. AIR VOIDS (%)	MEAS. PERMANENT COMP. (%)	VELOCITY (Km/sec)	
	AS-RECEIVED	DRY	GRAIN						LONG	SHEAR
1006	1.78	1.35	2.46	23.9	45.0	94.8	2.3	1.0	2.38	1.09
1027	1.92	1.61	2.36	16.3	31.9	98.1	0.6	0.3	3.30	1.72
1050	1.87	1.50	2.42	19.9	38.1	97.6	0.9	0.7	2.95	1.49
1073	1.87	1.50	2.41	19.9	37.9	98.3	0.6	0.4	2.89	1.41
1100	1.89	1.59	2.39	16.0	33.6	90.1	3.3	1.0	3.29	1.64
1124	1.82	1.44	2.37	20.8	39.2	96.6	1.3	1.2	3.31	1.81
1151	1.82	1.45	2.33	20.4	37.8	98.2	0.7	0.7	3.03	1.59
1176	1.79	1.38	2.39	23.0	42.3	97.3	1.1	0.5	2.78	1.35
1201	1.78	1.38	2.39	22.3	42.1	94.2	2.4	1.2	2.67	1.26
1225	1.88	1.52	2.47	19.0	38.4	93.2	2.6	1.5	3.26	1.96
1250	1.96	1.62	2.49	17.2	34.8	96.8	1.1	0.4	3.10	1.53
1273	1.92	1.56	2.48	18.6	37.0	96.6	1.2	0.9	3.05	1.39
1301	2.00	1.69	2.49	15.6	32.2	96.9	1.0	1.8	3.14	1.51
1327	1.97	1.63	2.50	17.5	35.0	98.5	0.5	0.6	2.79	1.30
1351	1.87	1.51	2.46	19.3	38.6	93.4	2.5	1.6	3.20	1.67
1374	1.83	1.43	2.44	21.5	41.2	95.2	2.0	0.9	3.01	1.60
1404	1.89	1.56	2.40	17.7	35.1	95.5	1.6	0.5	3.16	1.69
1430	1.87	1.49	2.44	20.1	38.7	97.1	1.1	0.4	2.76	1.37
1452	1.93	1.58	2.49	17.9	36.4	95.0	1.8	0.7	2.94	1.50
1476	1.85	1.46	2.43	21.3	40.1	98.3	0.7	0.8	2.50	1.19
1498	1.81	1.40	2.45	22.7	42.9	95.8	1.8	1.3	2.32	1.29
1526	1.89	1.52	2.49	19.7	38.9	95.9	1.6	0.6	2.69	1.41

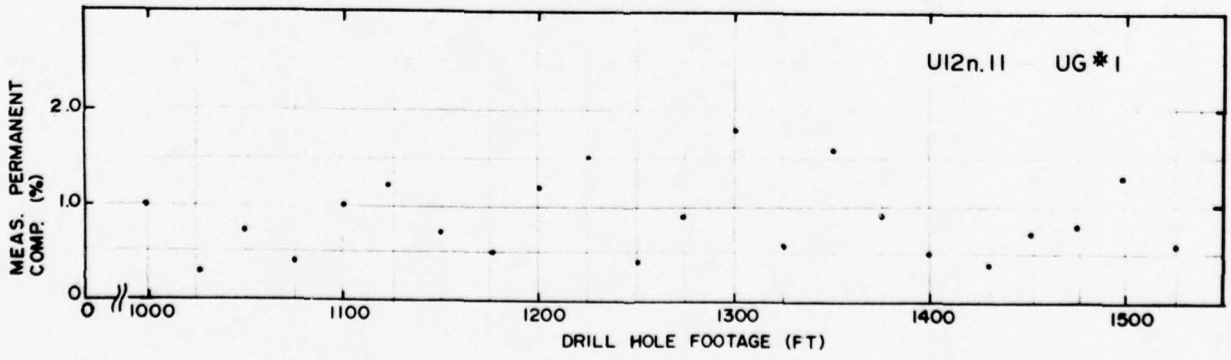


Figure 1. Measured permanent compaction versus drill hole footage.

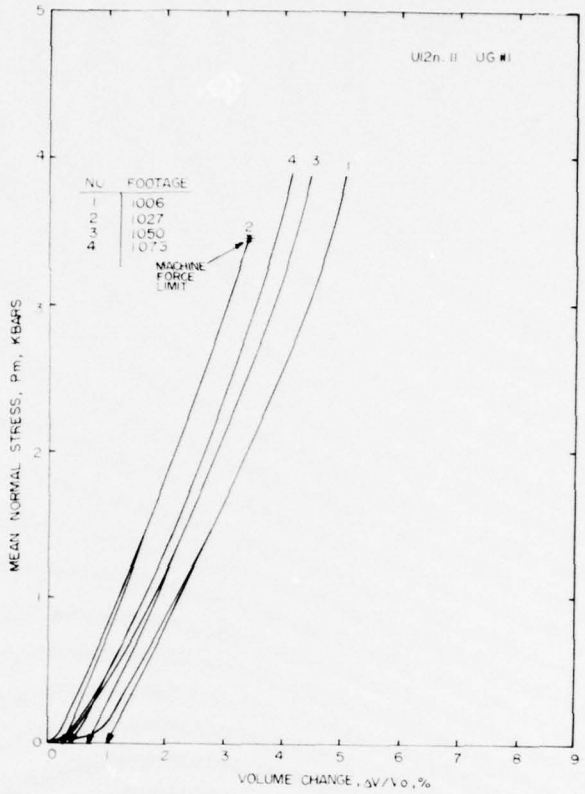


Figure 2a. Uniaxial strain test--mean normal stress versus volume change.

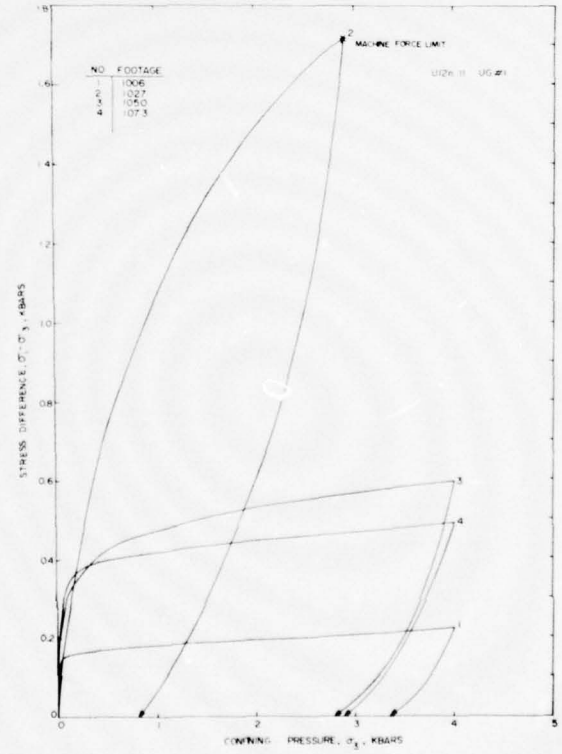


Figure 2b. Uniaxial strain test--stress difference versus confining pressure.

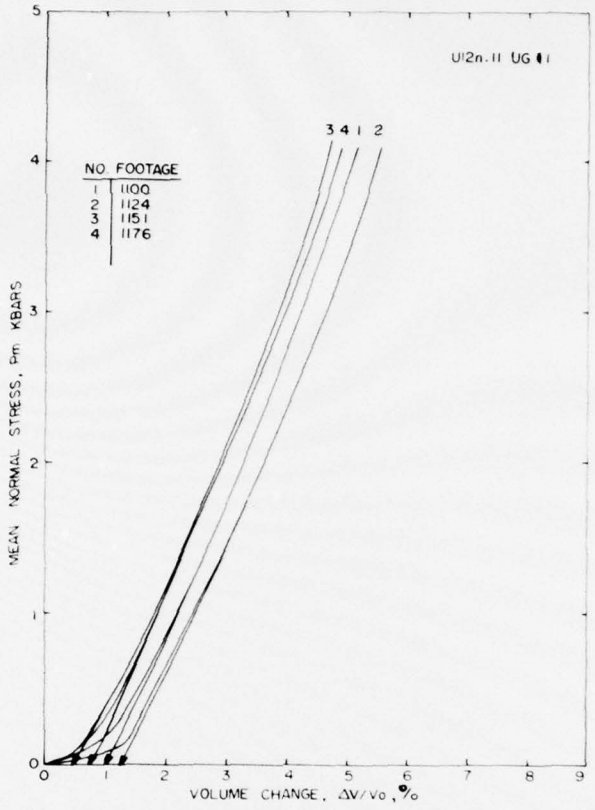


Figure 3a. Uniaxial strain test--mean normal stress versus volume change.

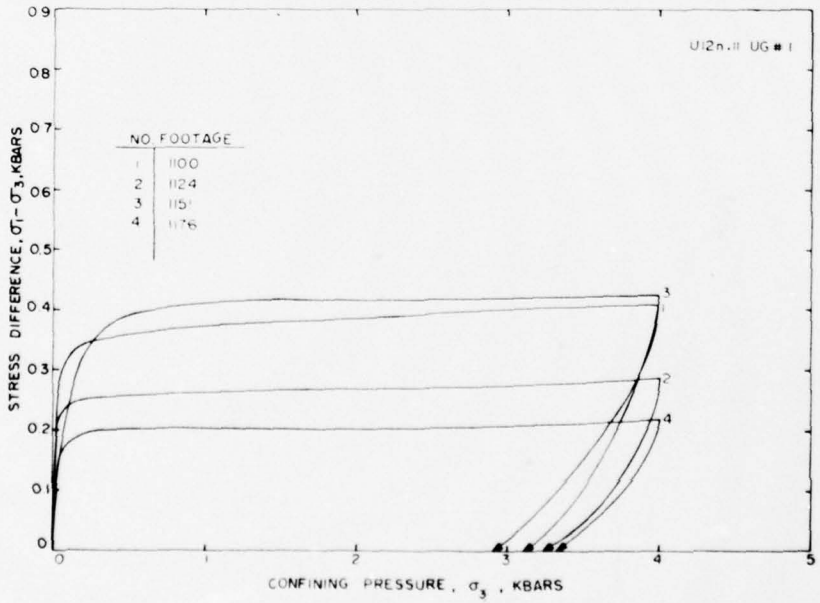


Figure 3b. Uniaxial strain test--stress difference versus confining pressure.

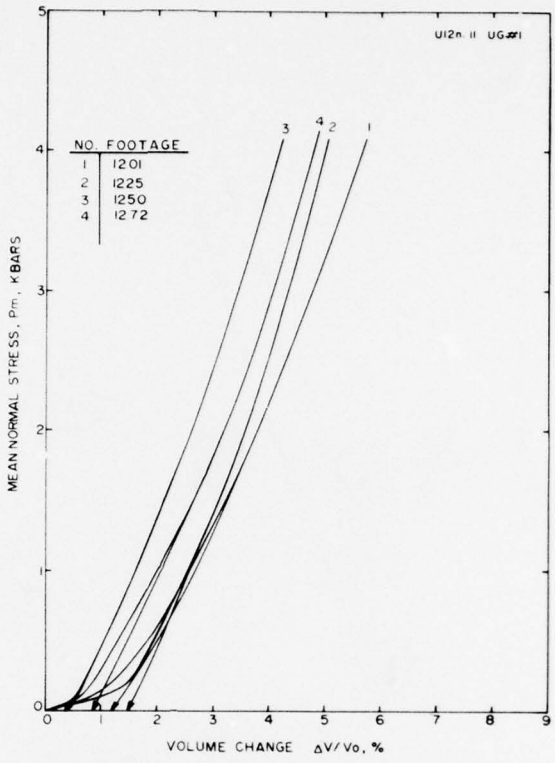


Figure 4a. Uniaxial strain test--mean normal stress versus volume change.

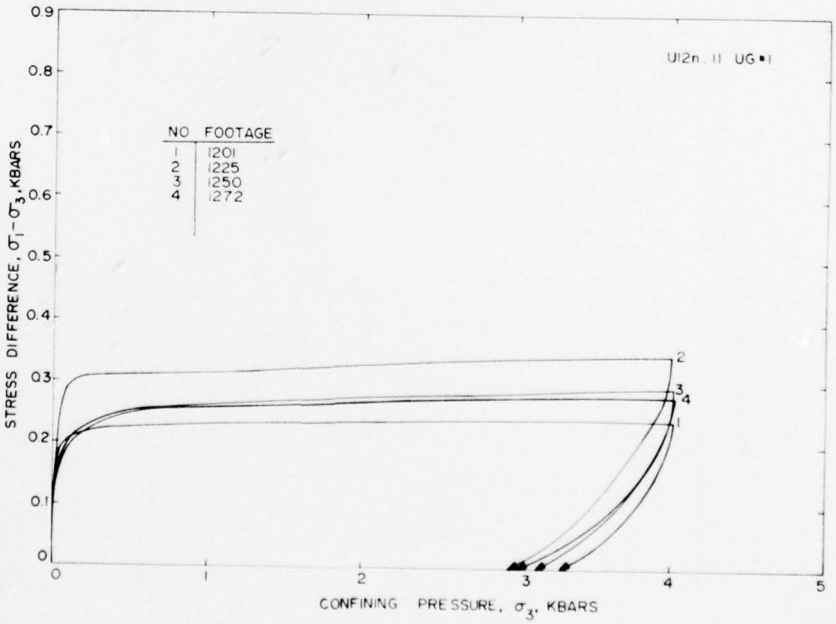


Figure 4b. Uniaxial strain test--stress difference versus confining pressure.

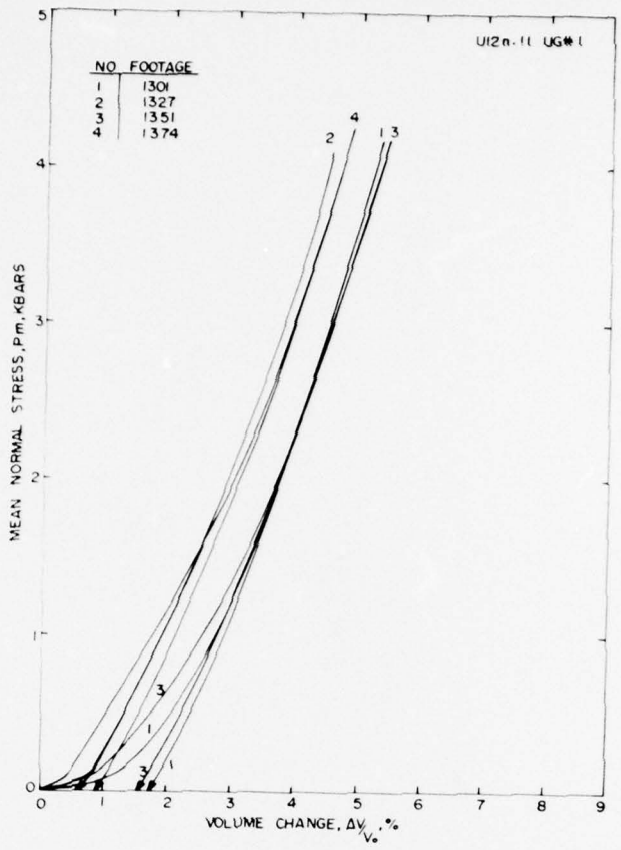


Figure 5a. Uniaxial strain test--mean normal stress versus volume change.

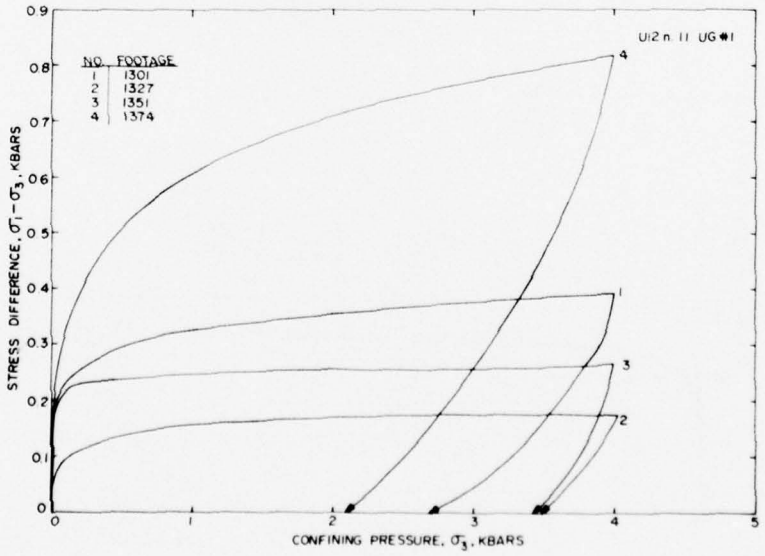


Figure 5b. Uniaxial strain test--stress difference versus confining pressure.

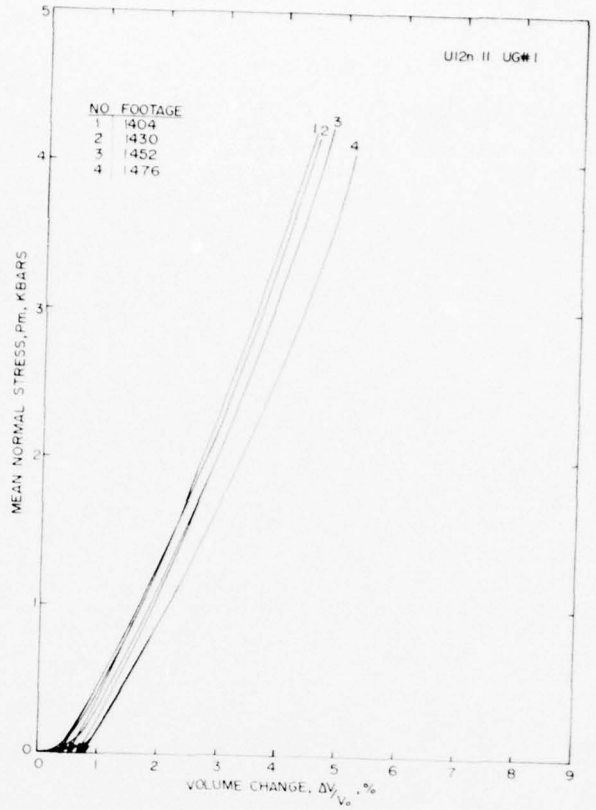


Figure 6a. Uniaxial strain test--mean normal stress versus volume change.

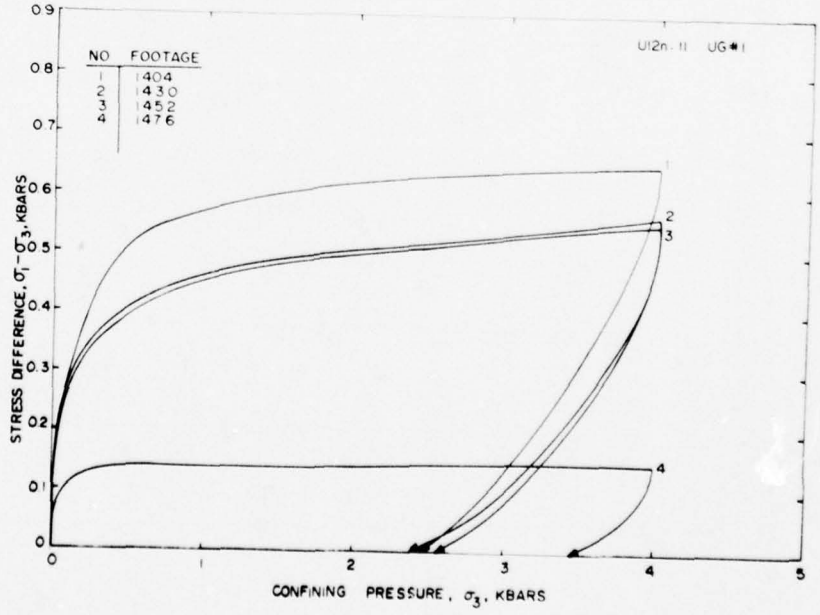


Figure 6b. Uniaxial strain test--stress difference versus confining pressure.

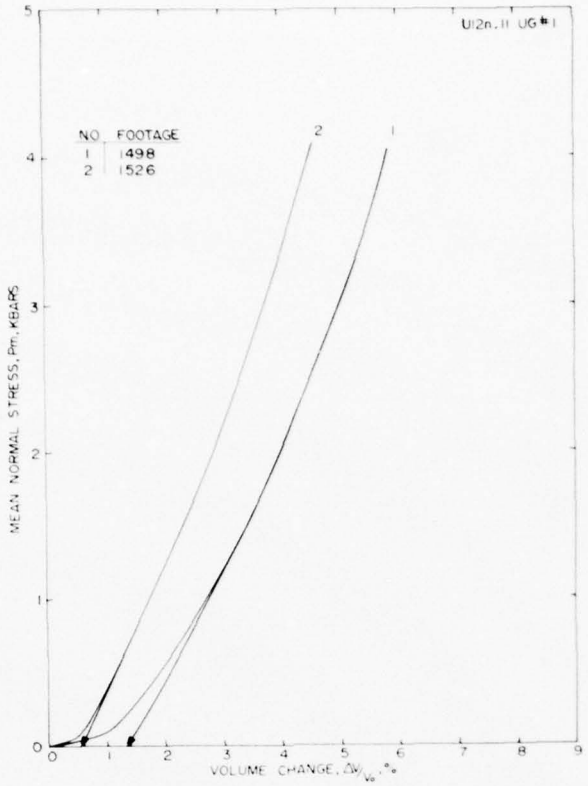


Figure 7a. Uniaxial strain test--mean normal stress versus volume change.

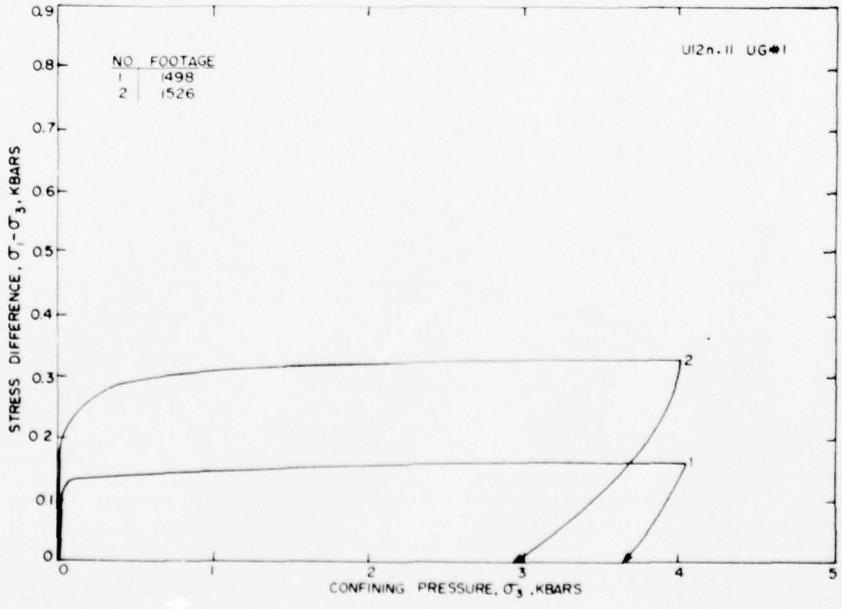


Figure 7b. Uniaxial strain test--stress difference versus confining pressure.

MECHANICAL PROPERTIES OF MIGHTY EPIC GROUT (POSTSHOT)

TR 76-43
August 1976

INTRODUCTION

Grout samples were retrieved from Mighty Epic Site (U12n.10 A, B and C drifts) after the nuclear event detonation. Both physical and mechanical properties of these postshot grouts were determined and compared with those of preshot grout[1]. Comparisons are made of physical properties, ultrasonic velocities, and uniaxial strain response to 4 kbars confining pressure.

---

1. Butters. S. W., Stowe, R. L., LaComb, J. W., "Characterization of Tuff and Development of Grouts for Mighty Epic Structures Program," Terra Tek Report TR 76-21, April 1976.

TEST RESULTS

Physical properties, uniaxial strain measured permanent compaction, and ultrasonic velocity measurements are listed in Table 1. Uniaxial strain test results are shown in Figures 1 and 2 as mean normal stress versus volume change and stress difference versus confining pressure. Average pre-Mighty Epic grout data are shown as dashed lines.

TABLE 1

Physical Properties, Uniaxial Strain Measured Permanent Compaction and Ultrasonic Velocities of Mighty Epic Postshot Grout

DRIFT	DRILL HOLE FOOTAGE	DENSITY (gm/cc) AS-RECEIVED	DRY	GRAIN	WATER BY WET WEIGHT (%)	POROSITY (%)	SATURATION (%)	CALC AIR VOIDS (%)	MEAS. PERMANENT COMP. (%)	VELOCITY (ft/sec) LONG	SHEAR
	U12 n 10										
B	#1A 0-13"	2.18	1.76	3.20	19.1	44.8	93.0	3.1	3.3	10213	5685
B	#1A 13-25"	2.16	1.76	3.15	18.6	44.2	90.9	4.1	2.8	10428	5695
B	# 4 0-12"	2.18	1.80	3.10	17.7	42.1	91.6	3.5	2.4	10512	5812
B	# 4 12-23"	2.20	1.80	3.13	18.2	42.6	94.2	2.5	2.3	10010	5583
A	# 6 0-12"	2.21	1.80	3.17	18.7	43.4	95.3	2.1	1.7	10230	5759
A	# 6 23-36"	2.13	1.71	3.18	19.7	46.2	90.9	4.2	2.4	10075	5607
C	# 2 0-12"	2.25	1.92	3.06	14.6	37.1	88.5	4.3	1.6	16875	9278
C	# 3 0-13"	2.27	1.94	3.04	14.4	36.1	90.5	3.4	1.5	12251	6571
C	# 6 0-13"	2.10	1.83	3.01	13.0	39.3	69.5	11.9	2.7	11739	6383
C	#6A 0-13"	2.15	1.79	3.04	16.6	40.9	87.3	5.2	2.6	9848	5729
C	#6B 13-26"	2.11	1.73	3.01	18.2	42.6	90.0	4.3	2.2	10648	5836
C	# 7 0-12"	2.22	1.87	3.03	15.6	38.2	90.7	3.6	3.2	11410	6904
C	#7A 12-25"	2.21	1.85	3.03	16.4	39.0	92.8	2.8	2.7	11071	6148
	Pre-Shot ME8-11R Grout	2.09-2.19	1.73-1.83	2.94-3.07	16.5-18.1	41-43	87-93	3.9-6.6	4.0-5.4	9570-11260	5179-5600

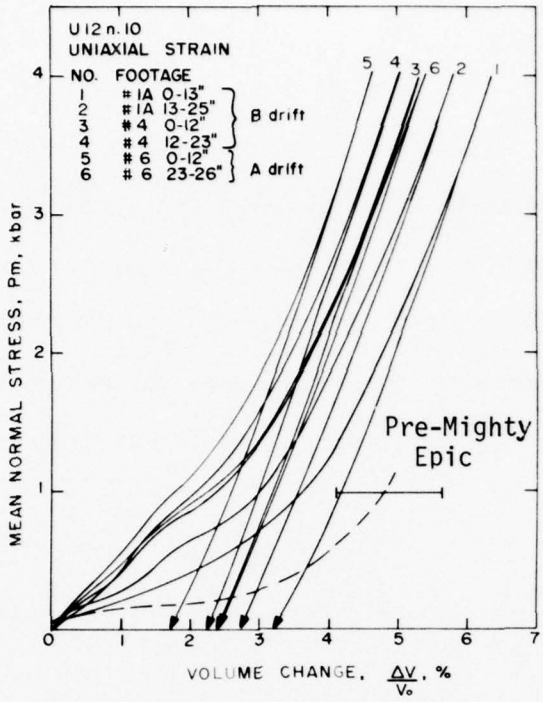


Figure 1a. Uniaxial strain test on U12n.10 A and B drift grouts -- mean normal stress versus volume change.

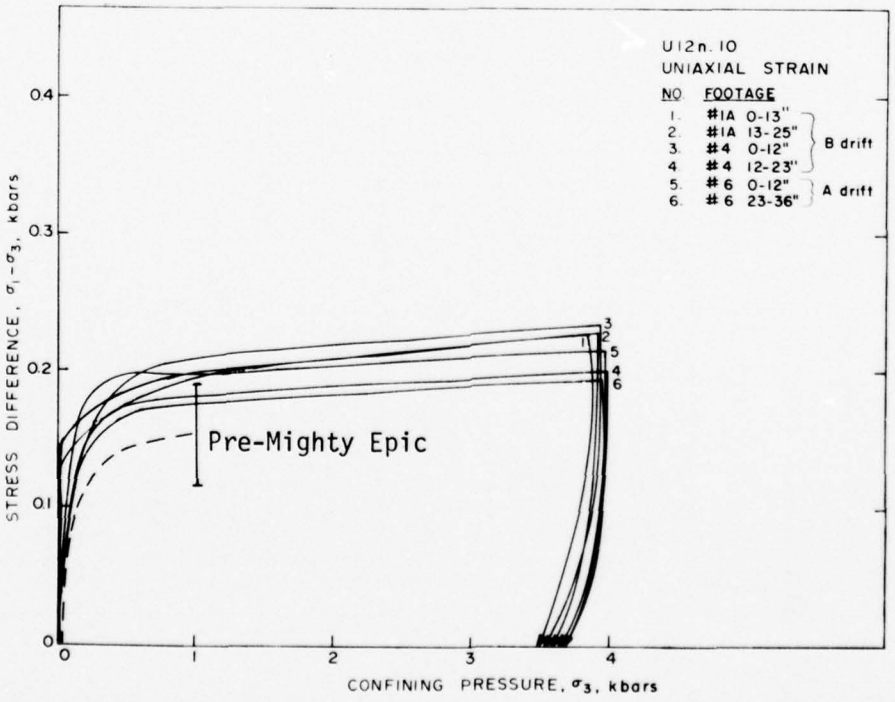


Figure 1b. Uniaxial strain test on U12n.10 A and B drift grouts -- stress difference versus confining pressure.

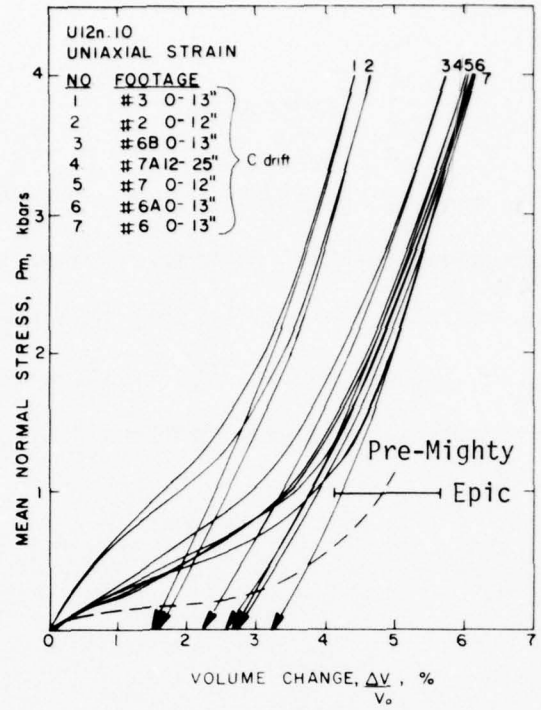


Figure 2a. Uniaxial strain test on U12n.10 C drift grout -- mean normal stress versus volume change.

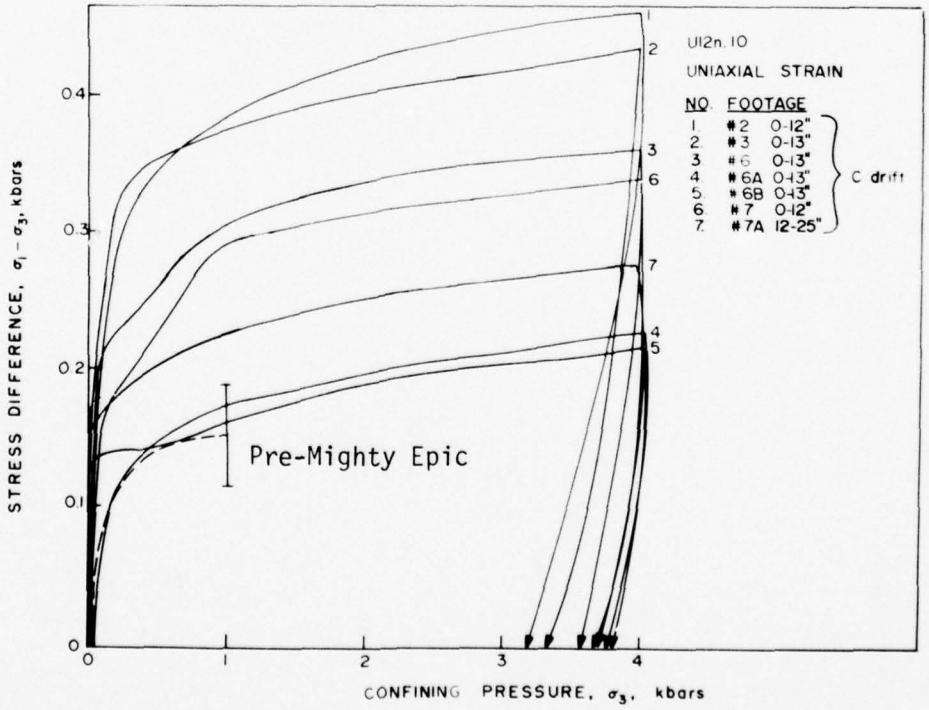


Figure 2b. Uniaxial strain test on U12n.10 C drift grout -- stress difference versus confining pressure.

DISCUSSION

In general, the postshot grouts have lower calculated air voids (2-5%) than did the preshot grout (4-6%). Permanent compaction resulting from the uniaxial strain test is also lower (1.5-3.3%) than the preshot grout (4.0-5.4%). Postshot grout appears to be slightly stronger (20%) than preshot grout with C drift grouts exhibiting higher shear strengths and considerably more scatter.

RESIDUAL STRESS IN THICK-WALLED CYLINDERS OF ASH-FALL TUFFS AND TUFF MATCHING GROUTS SUBJECTED TO INTERNAL PRESSURIZATION

TR 76-67
December 1977

INTRODUCTION

After underground nuclear events, it is mandatory that the radioactive gases not be vented to the atmosphere. One of the primary considerations in evaluating the containment potential of a site is the ability to contain these residual radioactive cavity gases. It is believed that a compressive residual stress field in the region surrounding the post-shot cavity can be beneficial to this containment process[1,2].

Laboratory containment tests have been conducted by Florence and Kennedy[3] in which 12 inch (30.5 cm) diameter grout spheres were explosively pressurized (internally) while hydraulically confined (externally) to simulate an overburden stress. Test results show agreement with analytical models predicting compressive residual stress formation following this type of loading. However, this testing has been limited to testing in an artificial medium (grout) as opposed to actual site materials (ash-fall tuffs).

Modeling studies have been undertaken by N. Rimer[4] which have analytically demonstrated that the magnitude of the residual stress field created is dependent on the site media physical properties. It is desirable, therefore, that a laboratory test program be developed that would allow verification of residual stress formation in ash-fall tuffs and also address the effects of varying physical properties on the residual stress. As a first step in the development of this type of testing capability, Terra Tek conducted a number of internal pressurization tests on thick-walled cylinders of tuff and tuff-matching grout. The initial objective of this test program is to determine whether a residual stress is

actually being formed in the laboratory samples of tuff. If the residual stress field is consistently produced, the physical property dependence can be addressed.

SAMPLE PREPARATION AND TEST PROCEDURES

The initial cylinder pressurization tests were conducted on tuff-matching grout samples (ME8-11); the second group of tests was conducted on samples of ash-fall tuff from the Nevada Test Site. The tuff was designated U12t.02 UG#7, and was selected primarily because of available length and material consistency.

Both groups of test samples were prepared identically. Each test samples was 2.0 ± 0.05 inches (5.1 ± 0.13 cm) in diameter, 2.25 inches (5.72 cm) in length. A hole of 0.32 inches (0.81 cm) diameter (0.20 inches in the case of samples with no internal jacketing) was then bored through each sample along its longitudinal axis. The ends of the sample were ground to a standard overall sample length of 2.0 ± 0.05 inches (5.1 ± 0.13 cm). A minimum outer diameter to inner diameter ratio of 6.25:1 was maintained on all internally jacketed test samples. Samples without the internal jacketing have a larger diameter ratio of 10:1. Prior to testing, each sample was inspected for visually apparent non-homogeneities and evidence of large stress concentrators such as voids, nicks, cracks, etc. All samples were tested in a saturated state.

The internally jacketed burst tests* were conducted using the apparatus shown in Figure 1. A steel shaft, 0.250 inches (0.64 cm) diameter,

---

* The internal bores of the rock cylinders were jacketed during the initial investigations. These "jacketed" type pressurization tests have been shown by Clifton, *et al*[5], to be easier to control as crack growth does go through a stable region. Later testing included samples with unjacketed internal bores to supply data more readily comparable to field data obtained through hydro-fracture testing.

completely wrapped with a thin vinyl tubing, was placed through the internal bore of the test specimen. The vinyl tubing acts as a jacket isolating the sample from the pressurizing fluid. Mild steel end caps are then attached and the exterior of the sample sealed with a polyurethane jacket to prevent sample contact with the confining fluids.

Non-internally jacketed tests were conducted without the use of the steel shafts and inner liner. O-rings were placed on each end of the sample. The steel end caps held against these O-rings by a small axial force effectively isolated the internal bore of the test sample.

Each sample was then placed into a pressure vessel which supplied the external pressure for the confined tests. A small axial stress of approximately 50 psi was applied to the sample to maintain pressure sealing of the internal bore. This axial stress was maintained constant throughout the test and was experienced by all test samples.

Test Procedures

Two basic series of internal pressurization tests were conducted; uncycled and cycled. In the uncycled testing, the interior of the test sample was pressurized while no external confining pressure was applied. The internal pressure at which the test sample fails is termed the uncycled, unconfined burst pressure. For the cycled tests an external confining pressure was used to simulate an overburden stress. With this confining pressure applied, the interior pressure of the sample is increased to a value between the applied confining pressure and the bursting pressure for that particular confining pressure. The pressures are then

removed and the interior pressure increased again with no confining pressure until a catastrophic failure of the sample occurs. The internal pressure at which this failure occurs is termed the cycled, unconfined burst pressure.

A comparison can be made between the uncycled and the cycled behavior of test samples from the same material. The effect of residual stresses created during the initial pressurization of a cycled sample, if any, will be apparent as a change in the unconfined burst pressure.

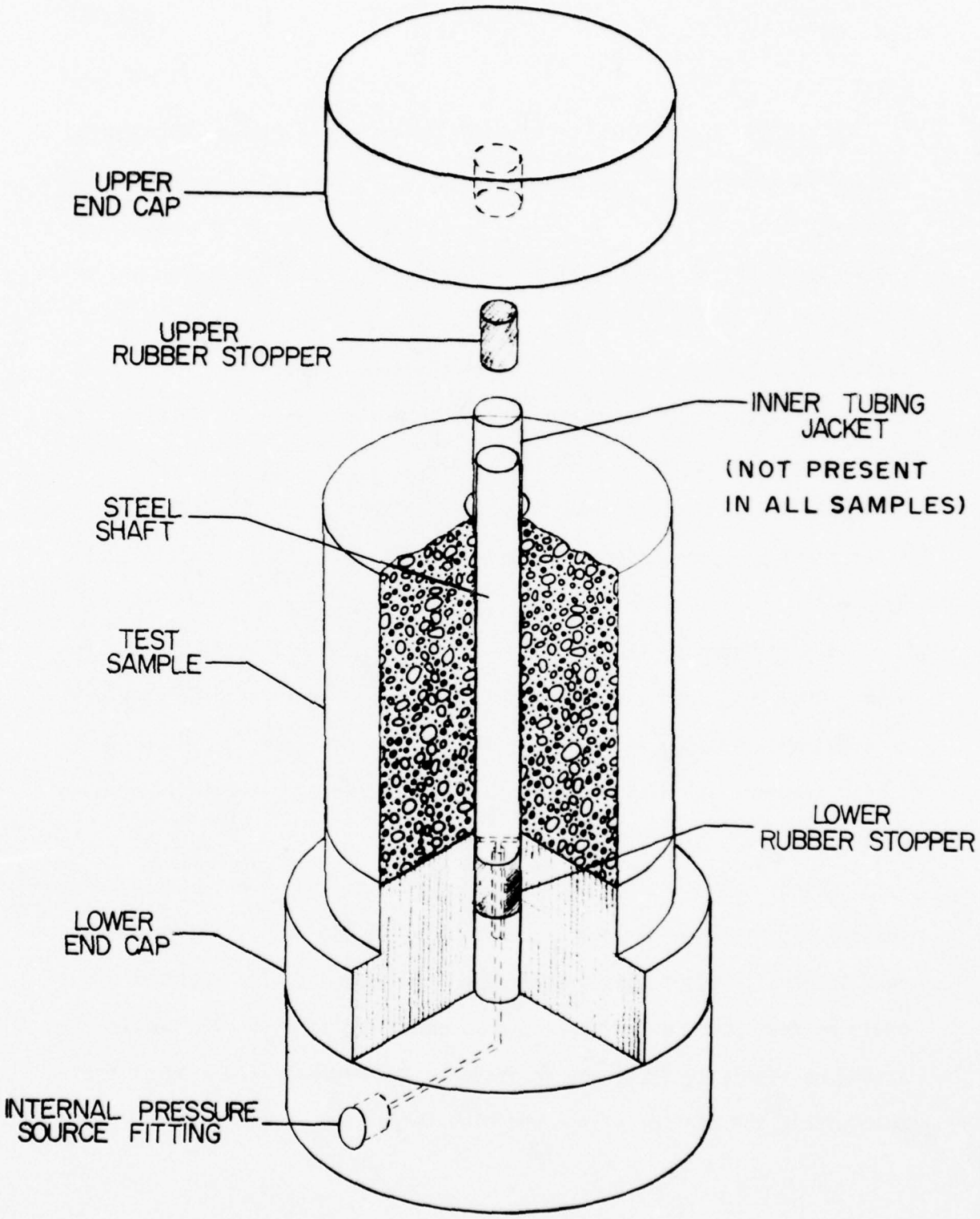


Figure 1. Burst Test Apparatus.

EXPERIMENTAL RESULTS

Grout

Uncycled: The initial testing was conducted on tuff-matching grout samples in an effort to reduce variation in test results due to material scatter. Initially, nine uncycled, unconfined pressurization tests on internally jacketed samples were conducted. The mean burst pressure of these nine tests was 77 bars with a standard deviation of 8 bars. A summary of all uncycled grout tests is contained in Table 1. The tests are designated according to the type of test and the sample material, e.g. UGB-1 designates uncycled grout burst #1.

UGB-10 was burst while confined. This test established the confined burst pressure, approximately 210 bars, for a sample confined at 30 bars.

Also included in Table 1 are the results of UGB-11 and UGB-12 which were also burst uncycled. These tests differed from the previous uncycled grout bursts in that they did not have an inner jacket present during pressurization and that the diameter ratio of outer to inner was somewhat larger; 10.0 versus 6.25.

Cycled: The effect of a cylical pressurization on an unconfined sample was determined on sample CGB-1. The sample was cycled to 60 bars internal pressure while unconfined to determine if a residual stress could be developed in the absence of a confining stress. The sample showed no significant changes in response and demonstrated a burst pressure within the scatter of the uncycled tests.

TABLE 1

Uncycled Grout Burst Pressure Data

Sample Designation	Internal Pressure Cycle		Pressure at Failure		Diameter Ratio (Do/Di)	Comments
	External (bars)	Internal (bars)	External (bars)	Internal (bars)		
UGB-1 (Grout)	--	--	0	74	6.25/1	Unconfined Burst*
UGB-2 (Grout)	--	--	0	70	6.25/1	Unconfined Burst
UGB-3 (Grout)	--	--	0	66	6.25/1	Unconfined Burst
UGB-4 (Grout)	--	--	0	68	6.25/1	Unconfined Burst
UGB-5 (Grout)	--	--	0	89	6.25/1	Unconfined Burst
UGB-6 (Grout)	--	--	0	80	6.25/1	Unconfined Burst
UGB-7 (Grout)	--	--	0	89	6.25/1	Unconfined Burst
UGB-8 (Grout)	--	--	0	86	6.25/1	Unconfined Burst
UGB-9 (Grout)	--	--	0	84	6.25/1	Unconfined Burst
UGB-10(Grout)	--	--	30	208	6.25/1	Not Cycled: Burst While Confined
UGB-11(Grout)	--	--	0	58	10.0/1	Unconfined Burst: Internal Bore Not Jacketed
UGB-12(Grout)	--	--	0	52	10.0/1	Unconfined Burst: Internal Bore Not Jacketed

* All internal bores were jacketed unless noted otherwise

During the cycled grout tests the samples were internally pressurized to 120 bars while confined at 30 bars confining pressure (burst failure would occur at approximately 210 bars at this confining pressure as established by UGB-10). The internal pressure was then relaxed and the confining pressure lowered. Samples were burst at an unconfined state. The samples tested after being cycled in this manner consistently showed a higher unconfined burst pressure than uncycled samples. The three grout samples tested had a mean burst pressure of 117 bars with a standard deviation of 12 bars. This amounted to an approximately 40 bar increase in burst pressure over the 77 bar mean burst pressure of the uncycled samples. A summary of the cycled burst tests on tuff-matching grout samples is contained in Table 2.

TABLE 2

Cycled Grout Burst Pressure Data

Sample Designation	Internal Pressure Cycle		Pressure at Failure		Diameter Ratio (Do/Di)	Comments
	External (bars)	Internal (bars)	External (bars)	Internal (bars)		
CGB-1 (Grout)	0	60	0	88	6.25/1	Unconfined Burst: Cycled* Internal Pressure
CGB-2 (Grout)	30	120	0	124	6.25/1	Internal Pressure Cycled While Confined; Burst Unconfined
CGB-3 (Grout)	30	120	0	103	6.25/1	Internal Pressure Cycled While Confined; Burst Unconfined
CGB-4 (Grout)	30	120	0	125	6.25/1	Internal Pressure Cycled While Confined; Burst Unconfined

* All internal bores were jacketed unless noted otherwise

Tuff

Uncycled: Two uncycled, unconfined burst tests were conducted on the tuff cylinders identical to those conducted on the grout cylinders. These tests, designated UTB-1 and UTB-2, burst at pressures of 74 bars and 78 bars, respectively. Two uncycled tuff tests were conducted without the inner jacket and are designated UTB-3 and UTB-4.

Cycled: Two cycled tests were conducted on the tuff samples, CTB-1 and CTB-2. After confining at 30 bars and internally pressurizing to 120 bars, the samples showed no significant increase in strength when burst unconfined. The test samples failed at 79 bars and 80 bars. Two additional samples (CTB-3 and CTB-4) were prepared from the same footage and cycled at internal pressures of 179 and 204 bars. They, in turn, burst unconfined at 80 and 78 bars, respectively. The last of the confined

tuff tests, CTB-5 was confined at 70 bars and cycled to 220 bars internal pressure. The sample showed no significant increase in burst pressure and failed when burst unconfined at 85 bars.

Tables 3 and 4 contain summaries of uncycled and cycled burst data for the ash-fall tuffs, respectively.

TABLE 3

Uncycled Tuff Burst Pressure Data

Sample Designation	Internal Pressure Cycle		Pressure at Failure		Diameter Ratio (Do/Di)	Comments
	External (bars)	Internal (bars)	External (bars)	Internal (bars)		
UTB-1 (Tuff)	--	--	0	74	6.25/1	Unconfined Burst*
UTB-2 (Tuff)	--	--	0	78	6.25/1	Unconfined Burst
UTB-3 (Tuff)	--	--	0	30	10.0/1	Unconfined Burst: Internal Bore Not Jacketed
UTB-4 (Tuff)	--	--	0	34	10.0/1	Unconfined Burst: Internal Bore Not Jacketed

* All internal bores were jacketed unless noted otherwise

TABLE 4

Cycled Tuff Burst Pressure Data

Sample Designation	Internal Pressure Cycle		Pressure at Failure		Diameter Ratio (Do/Di)	Comments
	External (bars)	Internal (bars)	External (bars)	Internal (bars)		
CTB-1 (Tuff)	30	120	0	79	10.0/1	Internal Pressure Cycled While Confined: Burst Unconfined*
CTB-2 (Tuff)	30	120	0	80	10.0/1	Internal Pressure Cycled While Confined: Burst Unconfined
CTB-3 (Tuff)	30	179	0	80	6.25/1	Internal Pressure Cycled While Confined; Burst Unconfined
CTB-4 (Tuff)	30	204	0	78	6.25/1	Internal Pressure Cycled While Confined; Burst Unconfined
CTB-5 (Tuff)	70	220	0	85	6.25/1	Internal Pressure Cycled While Confined; Burst Unconfined

* All internal bores were jacketed unless noted otherwise

CONCLUSIONS

Most of this preliminary work has been conducted on grout samples with some tests on Nevada Test Site ash-fall tuffs. Unconfined, uncycled burst tests on the grout samples were repeatable. Significant increases in burst pressure were noted for the cycled grout samples. These increases would tend to support the argument that a residual stress field had been formed.

The tuff samples showed uncycled behavior similar to the grout samples. The cycled behavior differed quite significantly, however. The increase in unconfined burst pressure that was apparent in the post-cycled grout samples did not appear in the tuff samples. The tuffs also demonstrated multiple fractures upon failure. The grout samples fractured into two pieces via diametrically opposite wall fractures.

The exact reason for the dissimilar cycled behavior of these two materials has not yet been determined. The shear stress levels reached during the cycled tuff tests were high enough to have initiated permanent deformation in most tuff material. During test CTB-4, for instance, shear stress at the inner wall exceeded 2800 psi (~0.20 kb). Typical shear stress values for ash-fall tuffs at compressive failure range from 0.05 kb to 0.10 kb. Tuff material can of course demonstrate considerable variation in strength. Further testing should include detailed mechanical response testing of proposed burst test samples.

The difference in cycled behavior could lie in the nature of the damage incurred. In the cycled grouts, plastic failure could have occurred at the inner bore surface. The damage in the tuff material could have

occurred in a more brittle manner. The resulting stress relaxation at the internal bore in this case would result from micro-cracking and perhaps major crack opening. In any case there appears to be a lack of a residual compressive stress build up upon relaxation of pressures applied to the sample.

Experimentation is currently being planned to determine the mechanisms involved in this dissimilar behavior. Detailed microscopic analysis should aid in a better understanding of this phenomenon. Once the residual stress field can be consistently established in tuff samples the test program can be expanded to verify that the testing approach is analytically sound and that this testing technique can be continued to address the effects of physical properties and time dependency.

REFERENCES

1. W.L. Ellis, U.S.G.S., letter to J. LaComb, December, 1975.

2. R.E. Duff, K. H. Lie, and W.Z. Savage, "Residual Stress Fields in the Vicinity of an Explosion-Produced Cavity and Related Topics", Systems, Science and Software Report, SSS-R-75-2533, June 1975.

3. A.L. Florence and T.C. Kennedy, "A Simple Analysis for Containment Studies", Stanford Research Institute Report, TR 76-3701-1, August, 1976.

4. N. Rimer, "The Relationship Between Material Properties, Residual Stresses and Cavity Radius Due to a Nuclear Explosion", *Systems, Science and Software Report*, SSS-R-76-2907, May, 1976.

5. R.J. Clifton, E.R. Simonson, A.H. Jones and S.J. Green, "An Application of Linear Elastic Fracture Mechanics to Pressurized Thick Walled Vessels", Terra Tek Report, TR 74-51, October, 1974.

HIGH TEMPERATURE GAS FLOW TESTS ON RECONSTITUTED TUFF

TR 77-48
June 1977

INTRODUCTION

At the request of DNA a series of special tests were devised and conducted to determine the thermal response of an altered tuff material exposed to sustained high temperature gas flow. The tuff material used in these tests is representative of the altered material in the chimney region following a nuclear event.

The apparatus constructed for this testing was designed to meet several specific objectives. The principal objective was the monitoring of the temperature response of a column of crushed and reconstituted tuff to a pressurized hot gas applied at one end. The column was designed to simulate one dimensional conditions for both the gas flow and the heat transfer. Temperature profiles were monitored as a function of time by embedded thermocouples.

Another design objective was the definition of mass flow rate of the gas through the column as a function of time. This flow history, when used in conjunction with the temperature profile, can establish a volumetric heat transfer coefficient for a particular sample representing a specific density, saturation and composition. Also, special attention was given to possible alteration of the tuff due to exposure to the hot gas flow, e.g., permeability changes, particle degradation, etc.

This report outlines the test procedures employed in this test series and includes the data obtained to date.

SAMPLE PREPARATION AND TEST APPARATUS

Because of the difficulties encountered in obtaining core samples in a chimney region, the altered chimney material was simulated by compacting crushed tuff materials to appropriate densities. The values chosen for these densities were those considered representative of chimney areas. Tuff samples were broken up in a jaw crusher to particle sizes ranging from 0.250 in. (0.64 cm) diameter to 0.0021 in. (U.S. standard 270 sieve) diameter. Figure 1 shows the typical particle size breakdown for the crushed material used as a control sample. Sample moisture contents were also determined prior to testing.

Table 1 contains a summary of the important sample properties. The location of the core used is included along with the reconstituted test sample density and moisture content. For reference, the density of the virgin material (prior to crushing) is also included as is the percentage of the original density achieved in the compaction process.

The test apparatus used in the hot gas flow tests is shown in a cross-sectional drawing in Figure 2. The flow gas is dry-grade nitrogen. Gas head pressure is maintained by a regulator and monitored by a pressure transducer. The transducer (not shown in Figure 2) is placed as close as possible to the sample face, but at a location cool enough to avoid any deleterious effects of the high temperatures. The gas passes through a volumetric flow meter and then into the heating area. A 2,400 watt heating element capable of supplying 1,000°F (538°C) gas at the sample face at flow rates up to 2 CFM (56.6 LPM) is used to heat the gas. Gas temperature is monitored by a thermocouple located approximately 0.375 in. (0.1 cm)

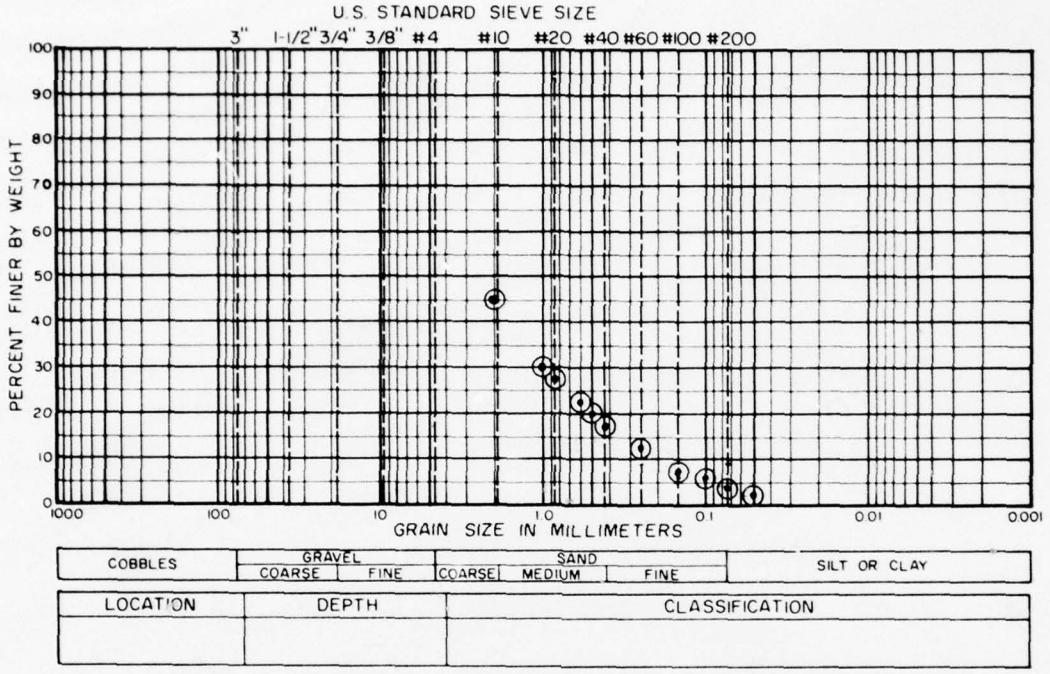


Figure 1. Particle size distribution in crushed samples.

TABLE 1

Reconstituted Sample Physical Properties

Test No.	Material	Sample Dimension	Virgin Tuff Density gm/cc	Reconstituted Sample		
				Density gm/cc	% of "Pre-crushed" Density	Moisture Content %
#1	U12n.10 GSCH#1 90.3'	2.5" dia. x 5.0" L	1.87	1.56	83	18
#2	U12n.10A GSIC#6 28'	2.5" dia. x 5.0" L	1.79	1.58	88	17.3
#3	U12n.10 DNCH#1	2.5" dia. x 20" L	1.97	1.51	77	17

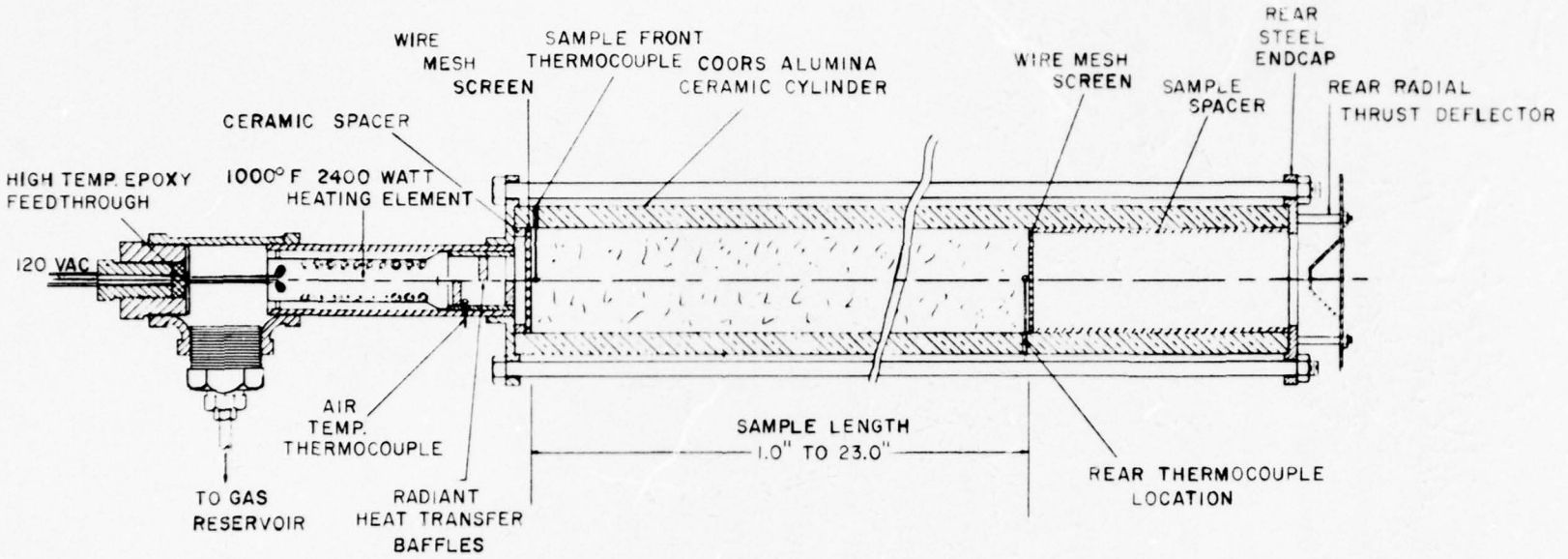


Figure 2. Test apparatus sectional drawing.

in front of the sample face. The ceramic baffle section is designed to shield the face of the sample and the flow temperature thermocouple from any radiant heat transfer from the heating elements.

The sample is contained in an alumina ceramic tube selected for its high strength and low thermal conductivity. At the sample face a stainless steel wire screen maintains sample integrity and also allows sample compaction in the ceramic tube. The sample tube exterior was insulated with a ceramic fiber insulation to minimize heat transfer through the walls (not shown). Sample length ranged from 1 to 23 inches (2.54 to 58.2 cm) with a diameter of 2.5 inches (6.35 cm).

Thermocouples placed through the ceramic cylinder wall and embedded at desired locations in the sample were used to monitor temperature; both radial and axial gradients were defined. The thermocouple sheathing was cemented to the ceramic tube to assure pressure seal. Exit temperature of the flow was also monitored as it exhausted to atmospheric pressure.

Additional design features currently under consideration include techniques for monitoring moisture movement within and out of the sample as a function of time. The capability to introduce controlled amounts of moisture to the inlet flow is also being planned.

TEST RESULTS

Thermal Flow Test #1

In this test a 2.5 inch (6.35 cm) diameter, 5.0 inch (12.70 cm) long sample of crushed tuff (U12n.10 GSCH#1 90.3') was subjected to the 1000°F (538°C) nitrogen gas flow. The compacted sample density was 1.56 gm/cm^3, approximately 83 percent of the virgin material density. A head pressure of 3 psig (0.02 MPa) was established at the sample face resulting in an initial flow rate of 1.02 CFM (29.0 LPM). Exhaust pressure was atmospheric.

Thermocouples were placed within the sample at the locations shown in Figure 3. All probes are located on the center axis of the sample. The temperature profile is shown as a function of time in Figure 4. Figure 5 contains the corresponding flow history, also plotted as a function of time.

As can be seen from Figure 4, thermocouple 2, located 0.375 inches (0.95 cm) from the face of the sample, shows an almost immediate temperature rise. The overshoot in the flow temperature (thermocouple 1) is also reflected by the thermocouple at location 2. The thermocouples at locations 3, 4, and 5 show a general temperature increase to 122°F (50°C), but remain constant at that value until the temperature at location 3 rises sharply at approximately 30 minutes after start-up. The exhaust flow temperature shows the next increase occurring at approximately 62 minutes after start-up.

Gas flow through the sample at a constant head pressure shows a general decrease in flow with time (Figure 5). Initial flow volumes measured 1.02 CFM (29.0 LPM) and decreased over the 100 minute duration of the test to 0.61 CFM (17.0 LPM).

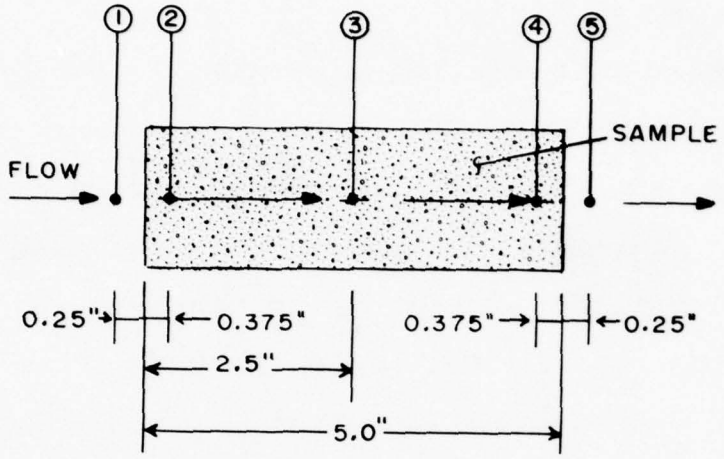


Figure 3. Thermocouple placement for thermal flow test #1.

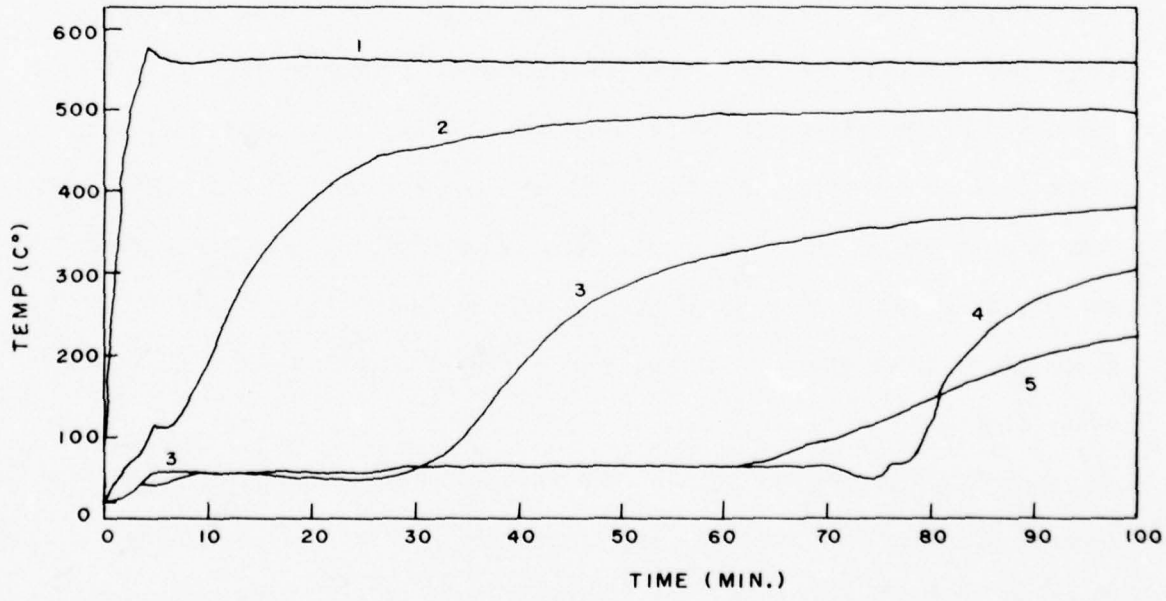


Figure 4. Thermal flow history, test #1.

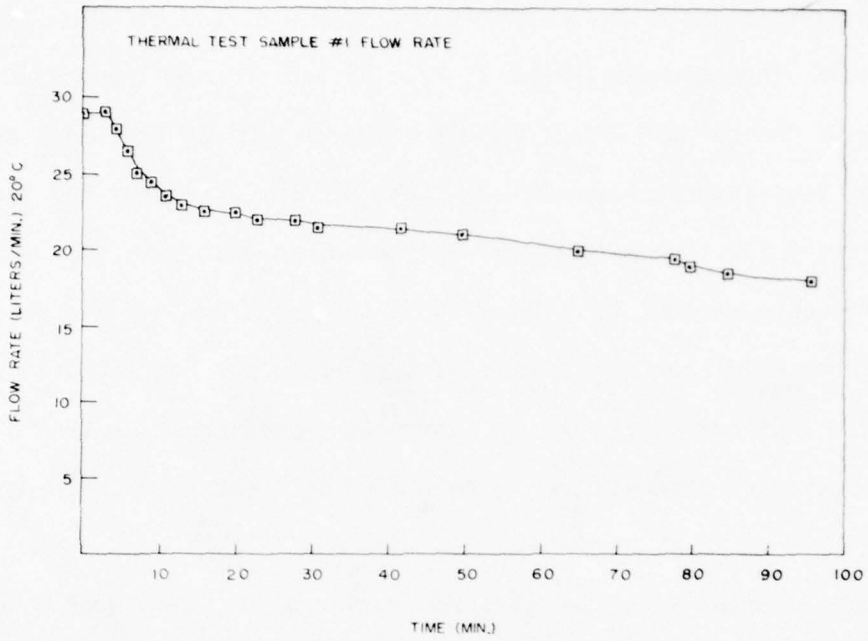


Figure 5. Flow rate history, test #1.

Gas flow was terminated at 100 minutes with the system not having reached steady state. The sample exposed to the flow was removed and tested for moisture content. No moisture was present in the post-test sample.

Thermal Flow Test #2

This test was conducted on a 2.5 inch (6.35 cm) diameter, 5.0 inch (12.70 cm) long sample of crushed tuff from U12n.10A GSIS#6 28'. Compacted density of this sample was 1.58 gm/cm^3, approximately 88 percent of the virgin material density. An initial head pressure of 4 psig (0.03 MPa) was placed at the front face of the sample resulting in a flow of approximately 0.88 CFM (25.0 LPM). Exhaust pressure for this test was atmospheric.

Thermocouples were placed within the sample at the locations shown in Figure 6. Thermocouple probes 2, 4, 6, 8 and 10 were located at the periphery of the ceramic tube. Probes 2 and 10 monitor the inlet and exhaust flow temperatures respectively. The probes located on the perimeter are inserted 0.250 inches (0.64 cm) inside the ceramic tube.

Thermocouple probes 1, 3, 5, 7 and 9 are located along the center of the sample at axial location identical to probes 2, 4, 6, 8 and 10, respectively. This configuration was chosen to determine the extent of the radial temperature gradient and to determine if a radial gas flow gradient exists.

Figure 7 contains the temperature profile of the sample as a function of time. Probes 1 and 2 represent the gas flow temperature at the sample face. Initially probe 2, located on the periphery, showed a temperature somewhat less than at the center. This temperature difference is due to the heat flow into the endcaps and ceramics and disappears after these components heat up to operating temperature, approximately 25 minutes later. Probes 3 and 4, both located 0.375 inches (0.95 cm) from the front of the sample show the largest radial temperature gradient. The temperature difference appears to be a result of an entrance effect of the gas flow entering the sample. The area of probe 4 having a smaller flow volume would experience less convective heat transfer. The area would heat slowly by conduction. Future testing will include alterations of the entrance endcaps to verify that this is a localized entrance effect.

Probes 5 and 6 were located at the sample midpoint. Probe 5 was placed on the sample axis and probe 6 was located on the perimeter of the sample. The temperature at probe 6 rises somewhat earlier with the

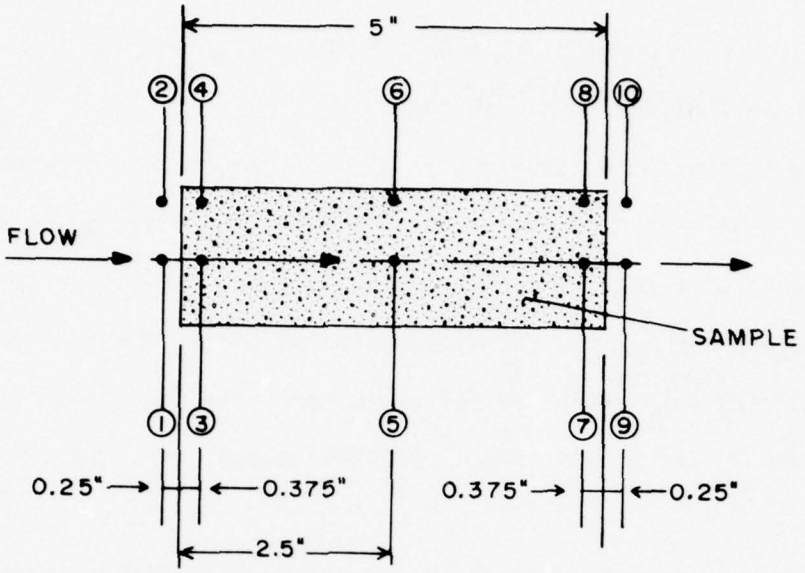


Figure 6. Thermocouple placement for thermal flow test #2.

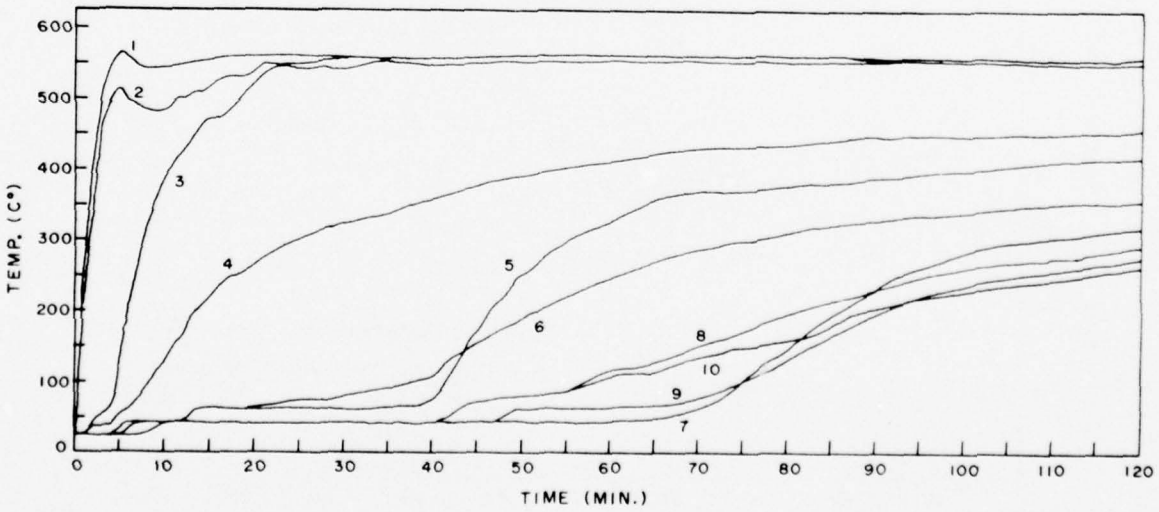


Figure 7. Thermal flow history, test #2.

probe 5 temperature eventually equalizing and surpassing it. A temperature gradient of approximately 144°F (80°C) exists between these two probes for most of the test duration.

The gas flow at the sample exit shows a temperature gradient is present. The flow on the perimeter (probes 8 and 10) rises quicker than the corresponding center axis (probes 7 and 9). The temperature just inside the sample end eventually stabilized with the center probe (#7) approximately 45°F (25°C) higher than the perimeter probe (8). A smaller gradient exists in the exhaust flow. At termination, this gradient measured 22°F (12°C).

The flow history for this test is contained in Figure 8. The initial flow rate was 0.88 CFM (25.0 LPM). The flow rate showed a general decline until approximately 35 minutes from start-up. Flow began increasing to

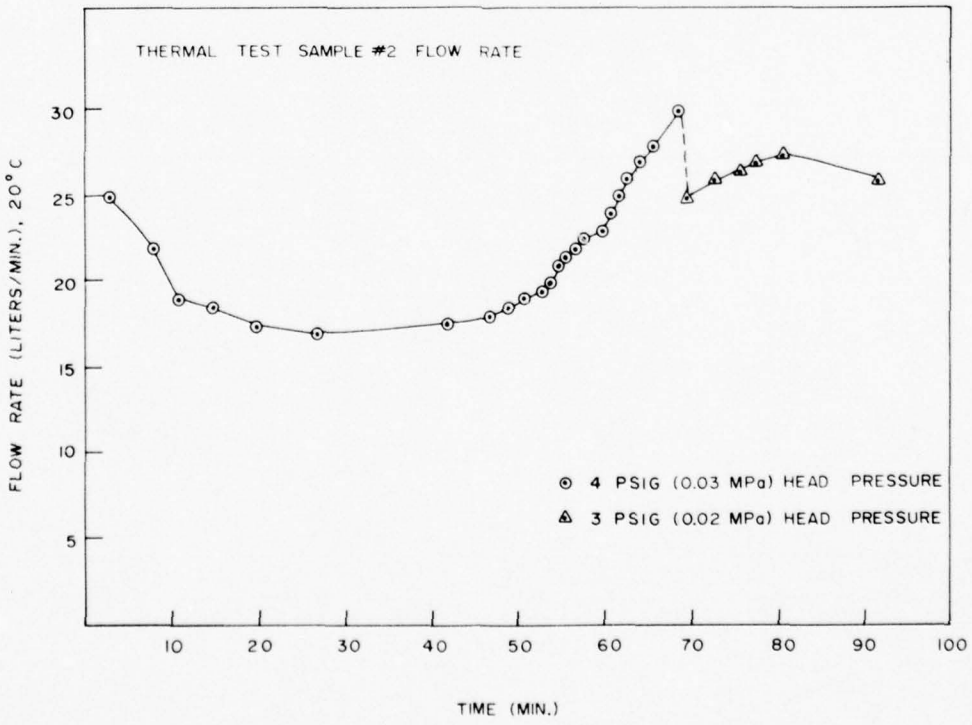


Figure 8. Flow rate history, test #2.

1.06 CFM (30.0 LPM) flow at 66 minutes from start-up. This value was approaching the upper limit of the flowmeter and required a reduction in head pressure for continued flow measurement. Head pressure was lowered from 4 psig to 3 psig for the remainder of the test.

The flow was stopped after 120 minutes. After cooling, the sample was removed and the moisture content measured. No moisture was present. The post test sample was then compared to a control sample in a sieve analysis. There does not appear to be any differences in particle size that cannot be attributed to population sampling scatter in the sieve analysis.

Thermal Flow Test #3

In this test a much longer sample was tested than either two of the previous tests. A 2.5 inch (6.35 cm) diameter, 20 inch (50.8 cm) long sample, composed of U12n.10 DNCH#1 material, was compacted from crushed tuff. Compacted density was 1.51 gm/cm^3, approximately 77 percent of virgin material density. The sample contained 17 percent moisture by wet weight at the time of testing. A pressure head of 8 psig (0.06 MPa) was established at the face of the sample and resulted in a 0.60 CFM (17.0 LPM) initial flow. Exhaust pressure was atmospheric.

The thermocouple probe configuration for this test is shown in Figure 9. Probes 1, 2, 4, 6, 8, 9 and 10 are located along the central axis. Probe 3 monitors the temperature profile of the tuff at a position axially equivalent to probe 4 but is placed on the perimeter of the sample. Probes 5 and 7 are embedded in the ceramic cylinder wall and are at the same axial location as probes 4 and 6, respectively.

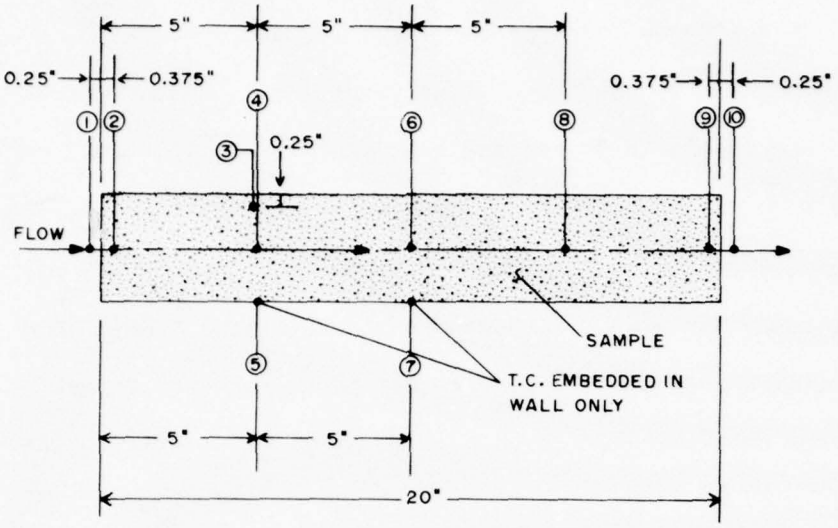


Figure 9. Thermocouple placement for thermal flow test #3.

The temperature profile for this test is shown in Figure 10. The temperature at probe 2, located at a distance of 0.375" (0.95 cm) from the sample front face, rises very quickly and approaches the input gas temperature. Probes 3, 4 and 5 are located in the same plane normal to the gas flow. Probes 3 and 5 rise together. Probe 4 (sample center), responds somewhat slower initially. The radial temperature gradient in this plane for the majority of the test is approximately 36°F (20°C).

Probes 6 and 7, are located in the same plane normal to the flow and show similar temperature histories. The wall probe, 7, rises somewhat quicker than probe 6 at first. At test termination, however, a smaller radial gradient exists with probe 6 at the center, 18°F (10°C) hotter than the wall probe, 7.

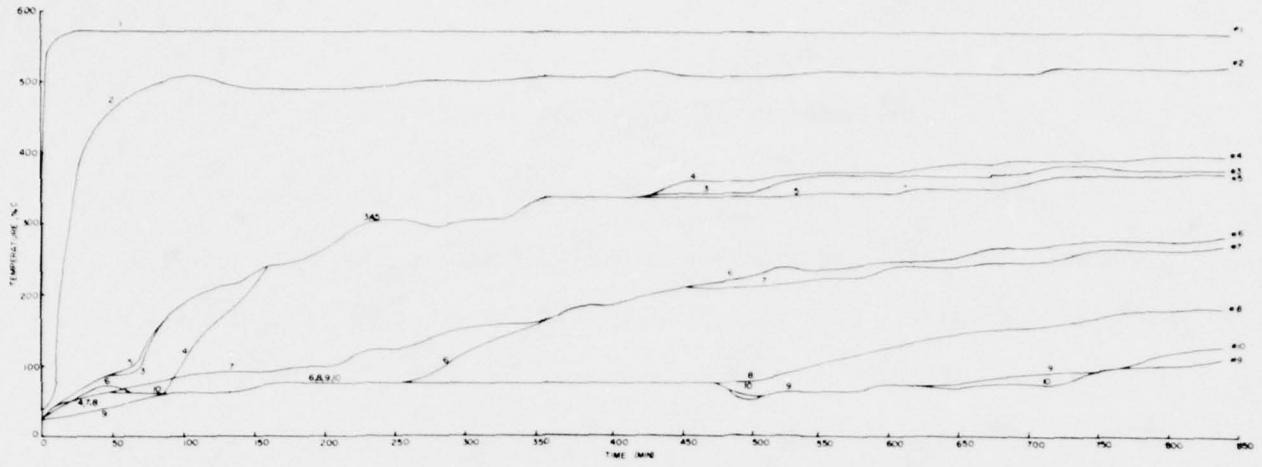


Figure 10. Thermal flow history, test #3.

The flow history for this test is contained in Figure 11. The 8 psig (0.06 MPa) head pressure created an initial 0.56 CFM (16.0 LPM) flow followed by a decrease during the first 40 minutes and then a rapid increase. To avoid exceeding the range of the flowmeter the heat pressure was dropped to 4 psig where it remained for the duration of the test.

The test was terminated at 850 minutes (14 hours); the sample was removed and cooled. Analysis of the post test sample showed there was no change in grain size distribution. The sample appeared dry although no moisture measurement was obtained.

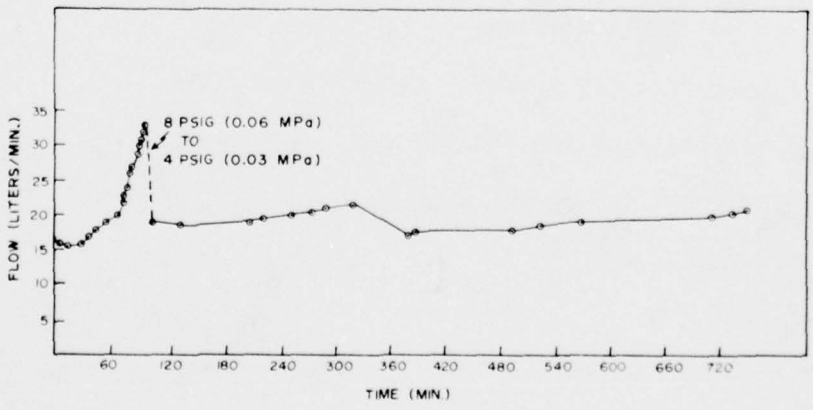


Figure 11. Flow rate history, test #3.

DISCUSSION OF THE FLOW RATE HISTORY RESULTS

In each of the three flow tests, the gas flow rate varied continuously throughout the test. In flow test #1 (Figure 5) the flow rate showed a continuous decline. Flow test #2 (Figure 8) experienced first decline of flow rate, followed by a very pronounced increase to a flow rate higher than the original. A leveling trend followed showing a slight declining trend at test conclusion. A similar flow history was measured for flow test #3 (Figure 11).

Each of these flow histories can be explained in terms of the linear gas flow equation[1]:

$$Q_{sc} = \frac{(0.00296)\ T_{sc}\ A\ K\ (P_1^2 - P_2^2)}{P_{sc}\ T_m\ Z\ L\ \mu} \qquad \text{where;} \qquad (1)$$

Q_{sc} = flow rate at standard conditions, liter/minute

T_{sc} = standard temperature, °K

P_{sc} = standard pressure, MPa

T_m = mean temperature of the sample, °K

P_1, P_2 = upstream and downstream pressures, MPa

A = cross-sectional area of the sample, cm^2

Z = non-ideal gas behavior factor, dimensionless

μ = viscosity of the flowing gas, centipoise

K = permeability of the sample, darcy

L = length, cm

The gas flow rate as expressed by this equation is governed by three time dependent variables: (1) mean temperature of the sample, T_m, (2) viscosity of the flowing gas, μ, and (3) permeability of the sample, K. The whole phenomenon of the flow rate variation can be conceptually idealized as shown in Figure 12. In this figure the qualitative aspects of permeability and flow rate variation can be examined. The behavior can be subdivided into four major periods as indicated on the figure.

Period I: The flow rate remains initially constant for the first several minutes after startup. Both temperature and viscosity changes are small and therefore do not seriously affect the flow rate. Permeability changes during this period are also very small although increasing slightly. The sample shows an overall permeability very close to its pre-heated value.

Period II: During this period permeability increases slightly. The rapid increase of the mean temperature (T_m) and the subsequent increase in gas viscosity (μ) dominate this period. These two terms are in the denominator of equation 1 and therefore result in an overall decline in gas flow rate, (Q_{sc}).

Period III: It is in this period that the major drying of the sample occurs and the permeability (K) to gas increases very rapidly overshadowing the smaller increases in mean temperature (T_m) and gas viscosity (μ). When boiling occurs in the sample, fluid movement is complicated by the presence of multiple phases. The crushed rock is more permeable to steam or dry gas than to steam-water mixture or water alone. This trend is illustrated by the curves of Botset[2] for the flow of liquid-gas mixtures through unconsolidated sand (Figure 13). As the vapor fraction increases

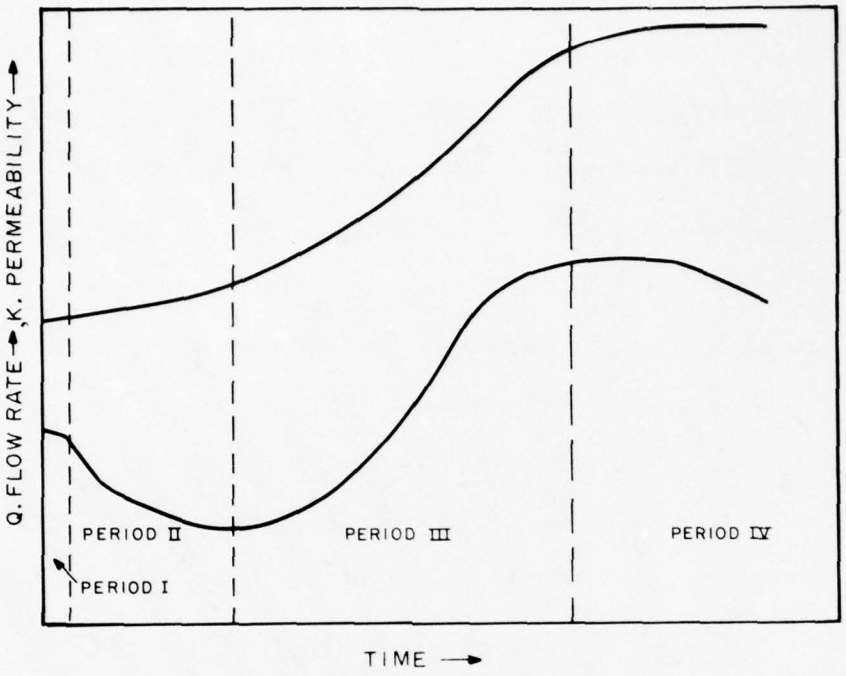


Figure 12. Idealized permeability and flow rate history.

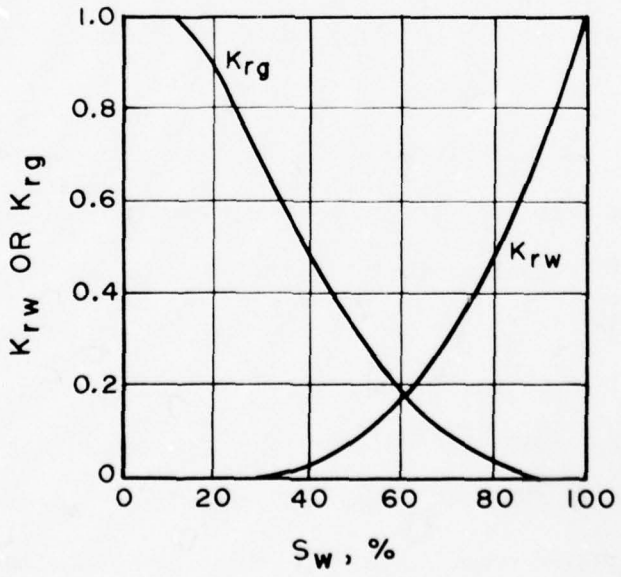


Figure 13. Relative permeability to gas and water. Unconsolidated sand (after Botset[2]).

with boiling, the permeability to the water phase decreased rapidly. For instance, at a saturation of 40 percent the permeability to gas is 10-15 times that of water. It is the permeability increase that dominates the flow in this period accounting for the sharp increases in flow rate.

Period IV: This period represents the completion of the sample drying. The sample permeability now remains constant. At this point a slightly decreasing flow rate is anticipated due to the continued increase of mean temperature and viscosity.

Figures 14, 15 and 16 contain plots of gas flow rate and permeability as functions of time. The periods discussed previously are designated where appropriate.

Flow test #1 exhibits both periods I and II as shown. Periods III and IV are not demonstrated by this test principally due to the short duration. This sample also had the highest recompaction density of all three samples. This could have resulted in extensive blockage of pore space and delayed the increase in permeability expected in period III.

Flow test #2 contains four very well defined periods. Period I lasts approximately 1.5 minutes before the beginning of the flow rate decline. This decreasing flow rate is characteristic of period II. At approximately 33 minutes from start-up period III begins and continues until approximately 80 minutes. A distinct period IV follows. At location A shown on Figure 15 the differential pressure had to be reduced so as not to exceed the range of the flowmeter. The apparent decrease in flow rate from A to B should not be confused as a trend -- it is an instantaneous decrease. Instead of the apparent curve connecting points ABC, visualizing the path AB'BC more clearly defines the true behavior.

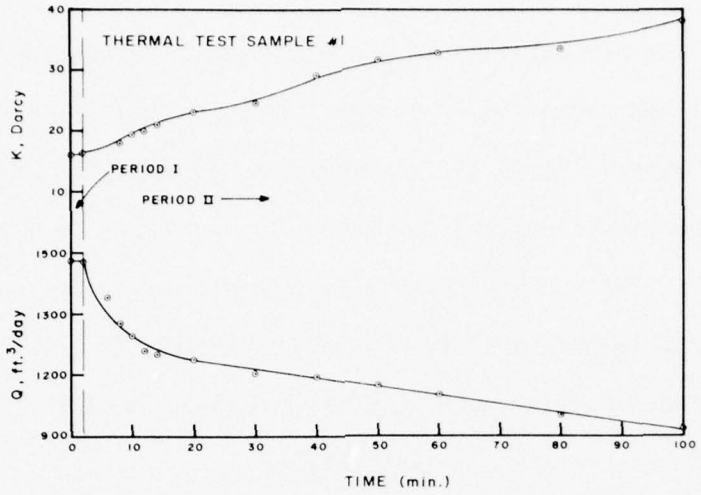


Figure 14. Permeability and flow rate history, test #1.

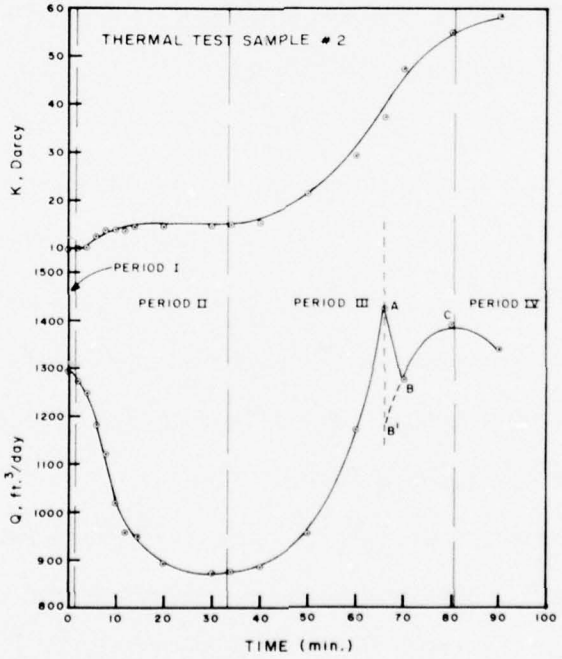


Figure 15. Permeability and flow rate history, test #2.

On test #3, Figure 16, periods I, II, and III are quite well defined. Because of the large sample size the test duration of 800 minutes did not allow for a distinct period IV. A similar effect of the differential pressure reduction is seen in this figure at points A, B and B'. Between locations X and Y as designated on the figure a flow anomaly occurs which is not presently understood.

The flow histories for all three tests although somewhat varied are governed by the linear gas flow equation. Discrepancies in flow behavior can be linked to test duration or to sample material peculiarities.

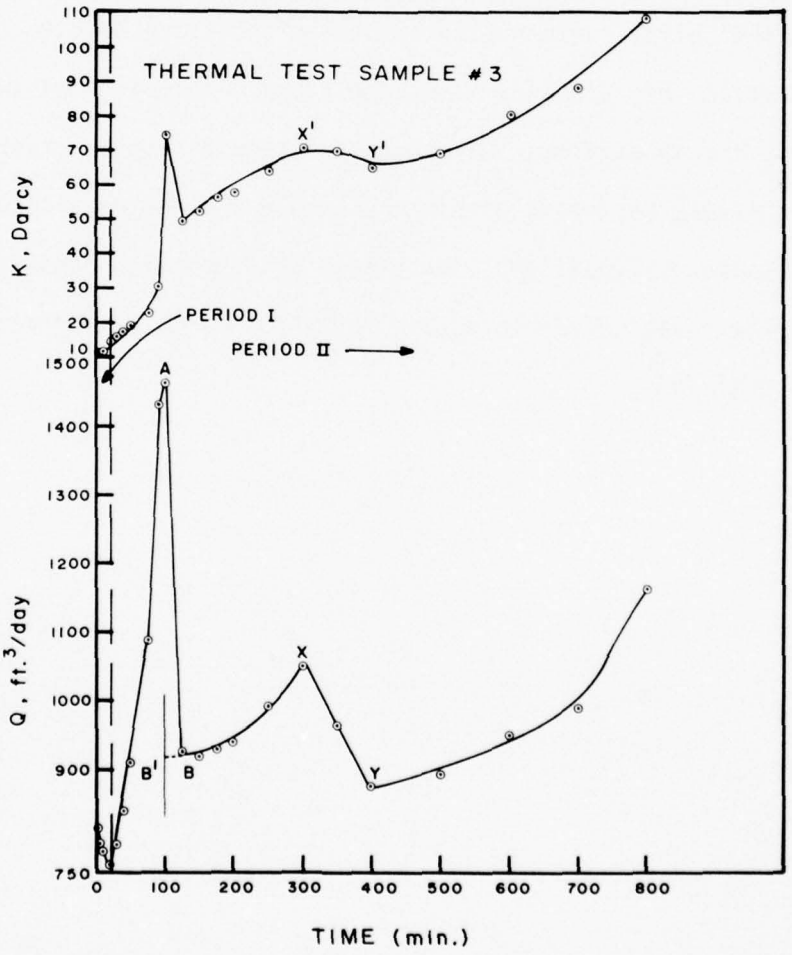


Figure 16. Permeability and flow rate history, test #3.

SUMMARY

The three hot gas flow tests conducted to date represent the initial phase of this test program. The design approach was verified, in that the thermal and flow states required were achieved. Refinements in the apparatus to further minimize the extent of the radial gradients and to eliminate the need of changing flow head pressure to accomodate the flow measurement can now be initiated.

From this point, further experimental efforts can be directed toward better simulation of actual *in situ* conditions, including moisture introduction into the inlet flow. Consideration should also be given to the effect of moisture movements within the sample and the resulting changes in flow rate and permeability. The effect of compaction density variation should also be investigated to more clearly relate this laboratory work to the field conditions.

REFERENCES

1. Craft, B. C. and Hawkins, M. F., "Applied Petroleum Reservoir Engineering," Prentice-Hall, Inc., Englewood Cliffs, New Jersey, 1959.

2. Botset, H. G., "Flow of Gas Liquid Mixtures Through Consolidated Sand," Trans. AIME, Vol. 136, 1940.

PHYSICAL AND MECHANICAL PROPERTIES OF RECONSTITUTED TUFF

TR 77-94
October 1977

PRECEDING PAGE BLANK-NOT FILMED

INTRODUCTION

To attain maximum utilization of facilities, it is desirable to site nuclear tests closer than previous practice. For this reason, it is important to characterize the "rubble zone" which exists in the "chimney" regions of previous events. The "rubble zone" is a highly broken region of material which is a result of cavity growth followed by cavity collapse and subsequent plunge downward of a significant volume of material.

Field measurements have revealed some material properties (densities and permeabilities) of chimney tuffs; laboratory testing was needed to more completely characterize the material. Since "chimney" region cores are difficult to obtain, "chimney like" samples were prepared from recompacted, crushed and/or pulverized tuff. Two sample types were tested, one composed of pulverized (~0.006 inch inch particle size, i.e. 100 mesh) and one composed of crushed (<0.25 inch particle size) tuff, both recompacted to a density considered representative of the *in situ* chimney material (i.e. about 95 percent of intact cores, "as-received" density). These samples were hydrostatically compressed to 1000 psi (simulated overburden stress) and tested in triaxial compression. Densities were typically 97 to 99 percent of the "as-received" density of intact cores at the end of this hydrostatic compression.

Permeability tests conducted on the reconstituted tuffs prior to further mechanical tests were used to design and evaluate the chimney material heat transfer phenomena[1].

---

1. Enniss, D. O., Butters, S. W., "High Temperature Gas Flow Tests on Reconstituted Tuff," Terra Tek Report TR 77-48, June 1977.

SAMPLE PREPARATION

Virgin - Virgin samples were prepared in the standard manner by saw cutting the core samples (already ~2 inch diameter) to a 2.5 inch length; care was taken to retain the *in situ* moisture content. An 18 mil thick polyurethane jacket was wrapped around the sample and steel endcaps bonded on each end. The sample was then sealed by attaching the jacket to the endcaps with rubber tape and lock wire.

Crushed (particle size less than 0.25 inches) - Crushed tuff samples were obtained by placing virgin tuff in a jaw crusher. After crushing, the tuff was poured into a 2 inch diameter polyurethane jacket affixed to a steel endcap on the bottom and supported laterally by a cylindrical mold. The material was compressed (to about 5000 psi) in 1/2 inch thick layers until the desired length and, therefore, density (i.e. ~95% of the virgin material as-received density) was obtained. The upper endcaps were then emplaced and the sample was sealed, ready for triaxial testing.

Permeability samples were prepared by pouring crushed tuff into an aluminum ring and compacting it to the desired density. O-ring sealed steel endcaps were emplaced and the assembly was inserted into a small load frame for testing.

Pulverized (particle size ~0.006 inches) - Pulverized tuff samples were obtained by crushing and pulverizing virgin tuff. Construction of the sample followed the same procedure as described for the crushed tuff. In each case, care was taken to insure moisture content was the same as that of the virgin tuff.

TEST RESULTS

Triaxial compression test results are shown as stress-strain curves for two different core samples (A and B) composed of virgin, crushed and pulverized tuff -- Figures 1 and 2. Table 1 lists the respective rigidity modulus and shear strength for each sample type. Figures 3 and 4 show the same data plotted in graphic form. Permeability test results are shown in Figure 5 on a semi-log plot as reconstituted density versus permeability.

TABLE 1

Ridigity Modulus and Shear Strength for UE12e.1 ~980' Virgin, Crushed, and Pulverized Tuff

Sample Type		Density(gm/cc) ρ	Ridigity Modulus(KB) G	Shear Strength(Bars) $*_\tau$
Virgin	A	1.96	40	85
Crushed	A	1.90	18	55
Pulverized	A	1.91	13	45
Virgin	B	1.82	20	83
Crushed	B	1.80	17	60
Pulverized	B	1.80	8	40

$*_\tau = (\sigma_1 - \sigma_3) / 2$

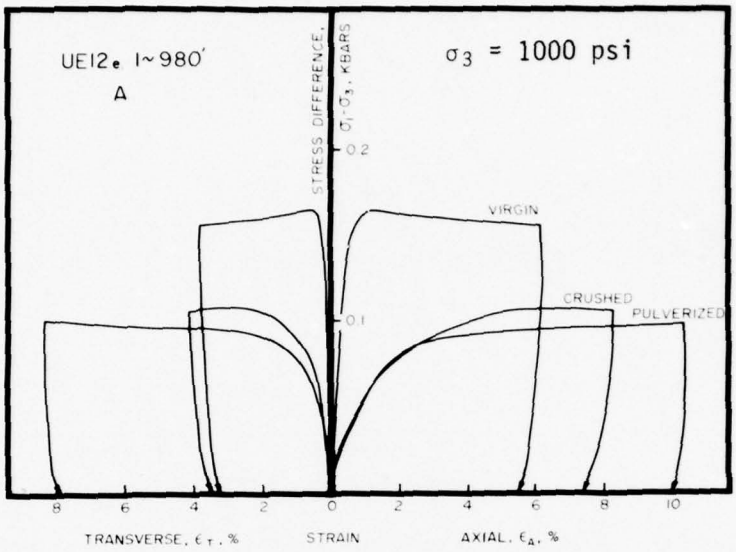


Figure 1. Triaxial compression tests -- stress difference versus axial and transverse strains.

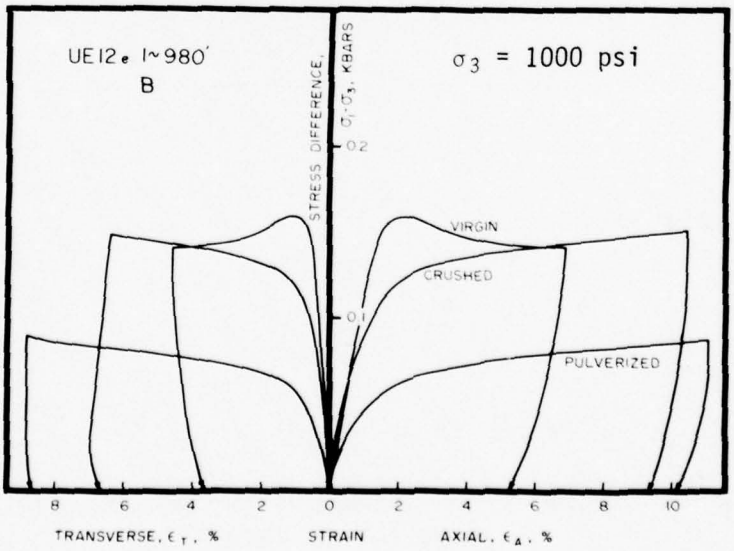


Figure 2. Triaxial compression tests -- stress difference versus axial and transverse strains.

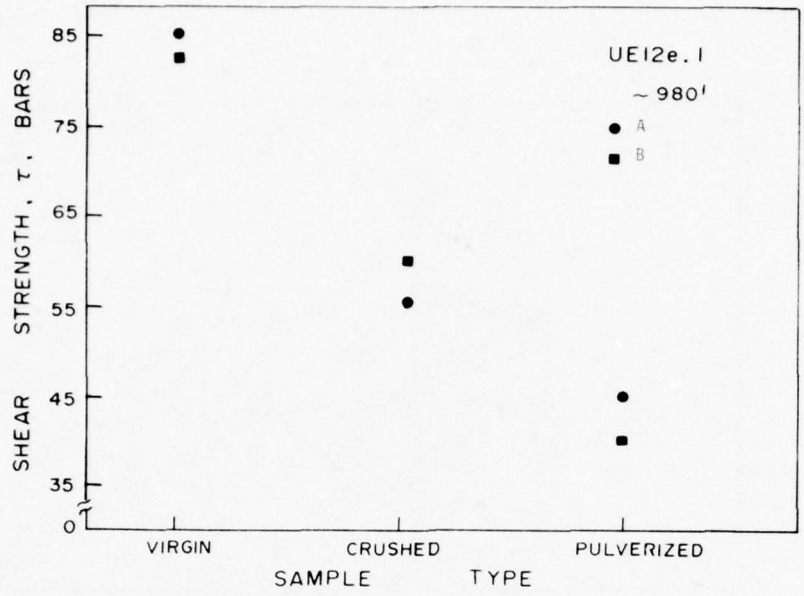


Figure 3. Shear strengths of virgin, crushed and pulverized UE12e.1 ~980' core samples.

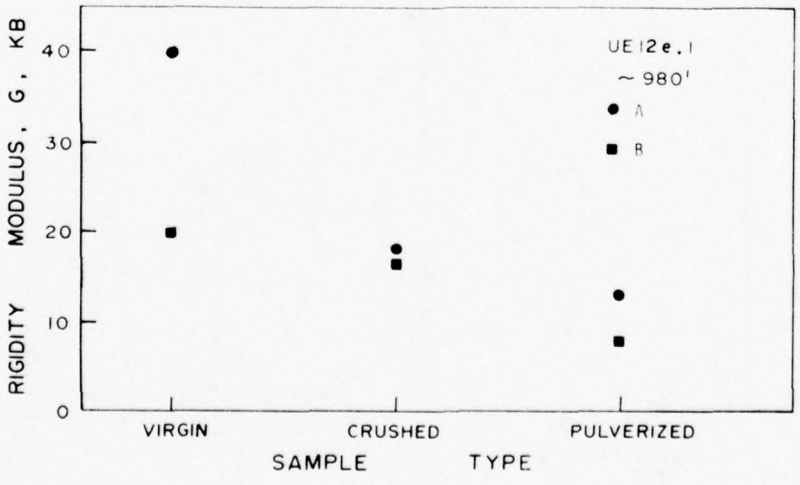


Figure 4. Rigidity modulus of virgin, crushed and pulverized UE12e.1 ~980' core samples.

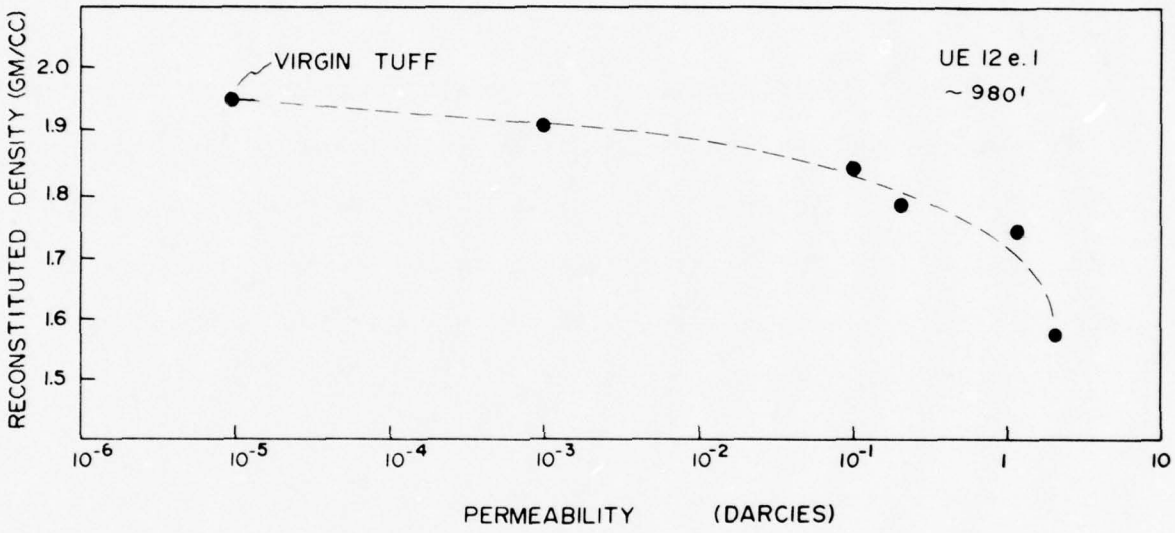


Figure 5. Permeabilities of UE12e.1 ~980' reconstituted samples of varying densities.

DISCUSSION AND CONCLUSIONS

Test results show that both shear strength and rigidity modulus decrease as the particle size decreases. Crushed samples exhibited a 20-30 percent decrease in rigidity modulus and shear strength while pulverized samples showed a 50 percent decrease. Also, as particle size decreased, the samples exhibited a more ductile type behavior (see Figures 1 and 2).

The above described decreases in the moduli and strength and increases in the porosity (and air void content) have been utilized in containment calculations which have shown that they will not be detrimental to containment. Additionally, the increases in porosity and permeability may even make the "chimney" acceptable as a "dump" to release cavity pressures.

This work was successful in producing data useful in predicting general chimney behavior. Further tests will be helpful with the increasing role of the "chimney" in future nuclear events and as more information is gathered about the *in situ* chimney properties.

STANFORD RESEARCH INSTITUTE GROUT

Material Properties of Stanford Research Institute Grout

Material Properties of SRI Rock Matching Grout and Modified Granite Simulant

MATERIAL PROPERTIES OF STANFORD RESEARCH INSTITUTE GROUT

TR 76-41
July 1976

PRECEDING PAGE BLANK-NOT FILMED

INTRODUCTION

Samples of rock matching grout (RMG 2C3) prepared by Stanford Research Institute (SRI) were tested for physical and mechanical properties. The grout is being used by SRI in a containment experiment in which a small explosive devise is detonated inside a grout sphere[1]. Grout properties were needed for calculation purposes. Two separate grout batches were characterized on days corresponding to the SRI tests (7 and 14 July 1976).

---

1. Florence, A. L., "Laboratory Investigation of Stemming and Containment in Underground Nuclear Tests," Final Report DNA 4149F, October 1976.

TEST RESULTS

The physical properties and the measured longitudinal and shear wave velocities are listed in Table 1. The test number corresponds to the date that the sample arrived at Terra Tek. The triaxial compression tests were conducted at 0.5 and 4.0 kbars confining pressure. The results are plotted as stress difference versus the individual strains in Figure 1.

The uniaxial strain test results are plotted as mean normal stress versus percent volume change in Figure 2a and stress difference versus confining pressure in Figure 2b.

TABLE 1

Physical Properties, Uniaxial Strain Measured Permanent Compaction and Ultrasonic Velocities

TEST NO.	DRILL HOLE FOOTAGE	DENSITY (gm/cc)			WATER BY WET WEIGHT (%)	POROSITY (%)	SATURATION (%)	CALC. AIR VOIDS (%)	MEAS. PERMANENT COMP. (%)	VELOCITY (ft/sec)	
		AS-RECEIVED	DRY	GRAIN						LONG	SHEAR
070176	SRI RMG 2C3	2.15	1.78	2.99	17	40	92	3.2	1.3	10557	5735
070976	SRI RMG 2C3	2.14	1.73	3.02	19	43	96	1.5	1.8	10717	5914

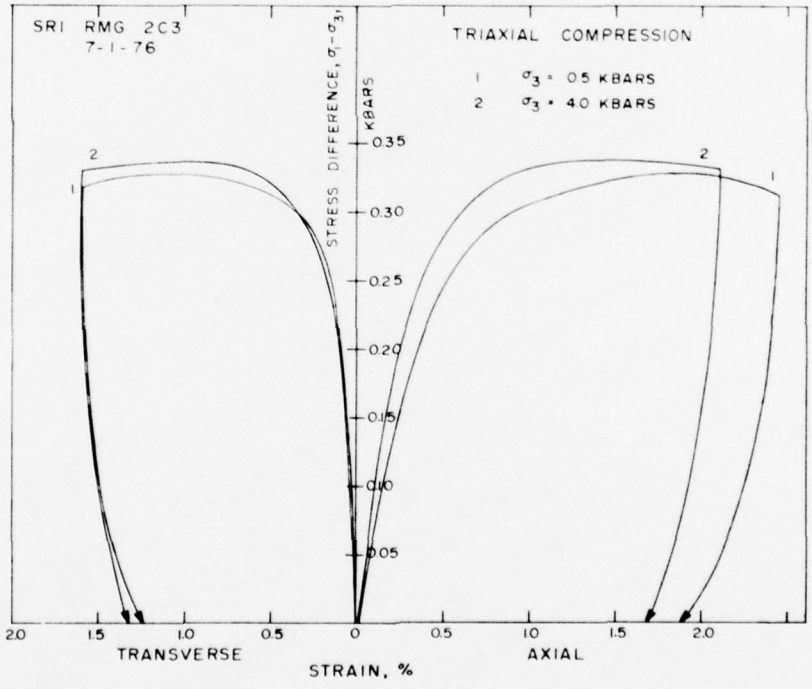


Figure 1. Triaxial compression test -- stress difference versus individual strains.

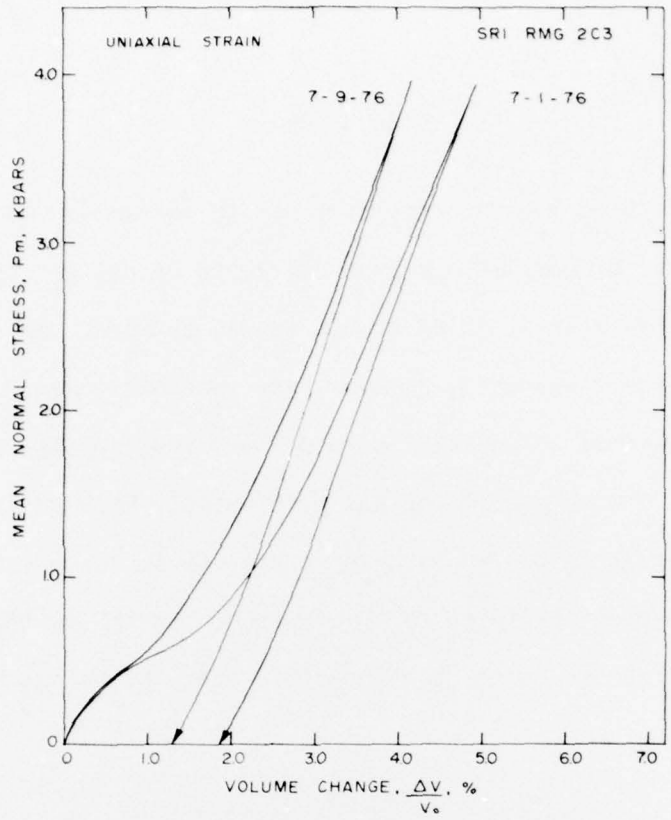


Figure 2a. Uniaxial strain test -- mean normal stress versus volume change.

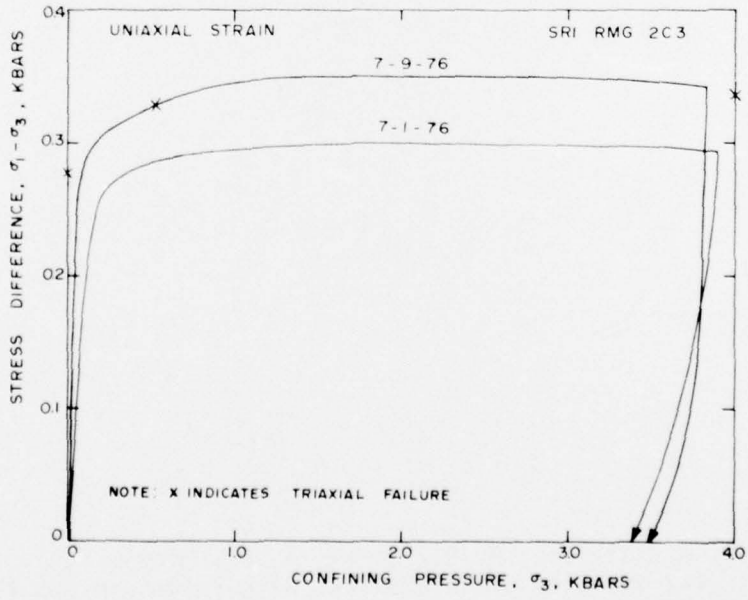


Figure 2b. Uniaxial strain test -- stress difference versus confining pressure.

DISCUSSION

Test results show the two grout batches to be similar in both physical and mechanical properties. Mechanical response appears to be consistent with other SRI rock matching grouts tested by Terra Tek[2]. Grain densities and percent moisture, however, are somewhat lower.

Material response to uniaxial strain shows the typical initial elastic response followed by pore collapse and stiffening. Pore collapse appears to be complete at about 0.7 kbars mean normal stress. The uniaxial strain stress-stress response is in reasonable agreement with the triaxial compression shear strength observed at both 0.5 and 4.0 kbars confining pressure (Figure 2b).

---

2. Butters, S. W., Nielsen, R. R., Jones, A. H., Green, S. J., "Mechanical and Physical Properties of Nevada Test Site Tuffs and Grouts from Exploratory Drill Holes," Terra Tek Report TR 73-69, December 1973.

MATERIAL PROPERTIES OF SRI ROCK MATCHING GROUT AND MODIFIED GRANITE SIMULANT

TerraTek

August 16, 1977

Dr. Alexander Florence
Stanford Research Institute
333 Ravenswood Ave.
Menlo Park, CA 94025

Dear Alex:

As per your request, we have determined selected material properties on the Modified Granite Simulant "tube 3A" that you supplied. Mechanical tests included triaxial compression and uniaxial strain tests to 0.5 kbars confining pressure. Tests were conducted on 4 August 1977 in accordance with your request. The triaxial compression test results are shown in Figure 1 as stress difference versus individual strains. Uniaxial strain test results are shown in Figures 2 and 3. Physical properties and ultrasonic wave velocities were also measured and are listed in Table I.

The stress difference was 1.62 kbars at failure during triaxial compression. Maximum stress difference in uniaxial strain was 1.1 kbars with a resulting measured permanent compaction of 0.5 percent. Physical property measurements indicate the sample to be somewhat under saturated with 3.5 percent air voids. The discrepancy between the measured permanent compaction and the percent air voids was investigated by rerunning the physical property tests only to produce the same results. Apparently the 0.5 kbar uniaxial strain test did not collapse all the air voids.

Sincerely,

D. S. Gardiner
Research Engineer

DSG/jlg

Enclosures

cc: J. W. LaComb
C. Keller

TABLE I

Stanford Research Institute Modified Granite Simulant

SAMPLE DESIGNATION	DENSITY (gm/cc)			WATER BY WET WEIGHT (%)	POROSITY (%)	SATURATION (%)	CALC. AIR VOIDS (%)	MEAS. PERMANENT COMP. (%)	VELOCITY (km/sec)	
	AS-RECEIVED	DRY	GRAIN						LONG	SHEAR
3A	2.42	2.27	2.80	6.3	18.8	81.6	3.5	0.5	4.82	2.75

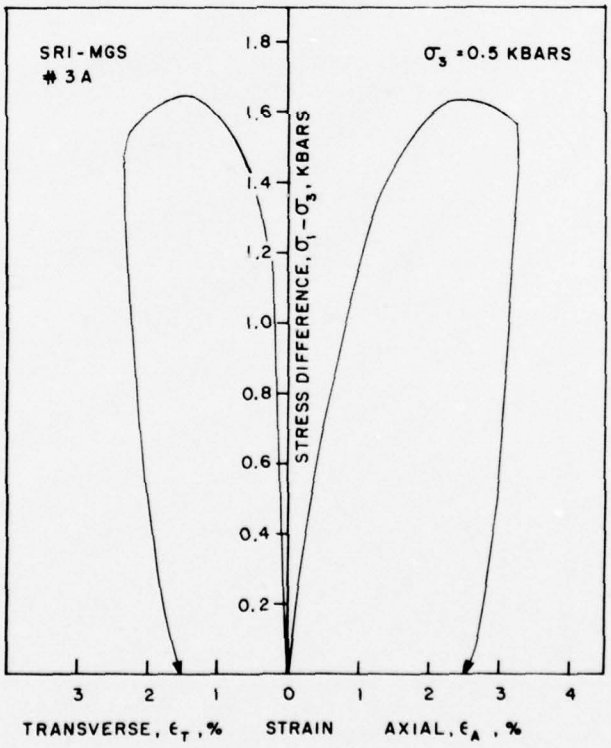


Figure 1. Triaxial compression test--stress difference versus individual strains.

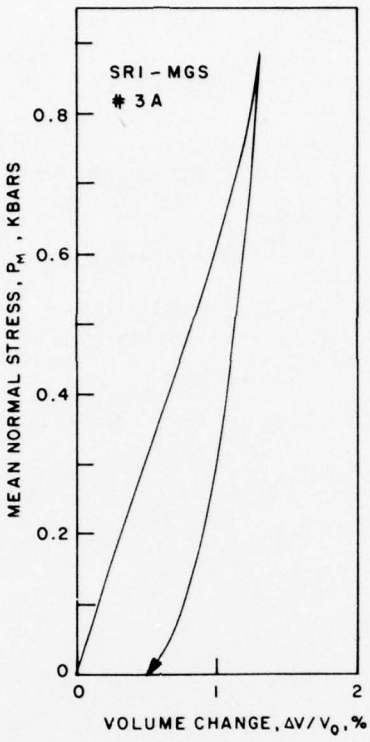


Figure 2. Uniaxial strain test--mean normal stress versus volume change.

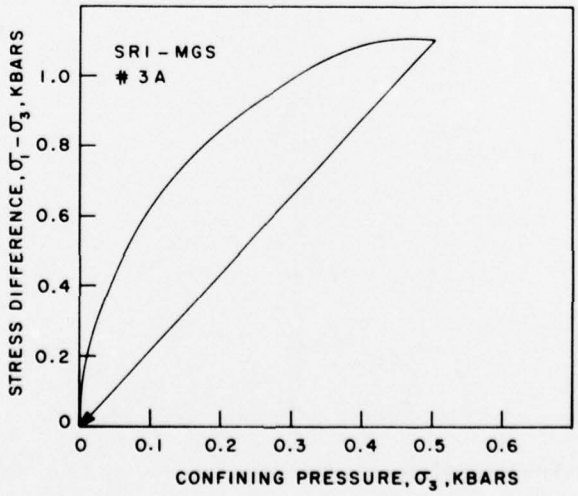


Figure 3. Uniaxial strain test--stress difference versus confining pressure.

TerraTek

July 8, 1977

Dr. Alexander Florence
Stanford Research Institute
333 Ravenwood Ave.
Menlo Park, CA 94025

Dear Alex:

As per your request, we have conducted material property testing on the samples of rock matching grout (RMG 2C4) that you supplied. Physical property and ultrasonic wave velocity measurements were conducted on samples from batches 1A, 2A, and 3A to verify batch consistency. Mechanical property tests were conducted on batches 1A and 3A. Mechanical tests included triaxial compression and uniaxial strain tests to 0.5 kbars confining pressure. Tests were conducted on 1 July 1977 to coincide with your test date.

Triaxial test results are shown in Figure 1 as stress difference versus individual strains. Uniaxial strain test results are shown in Figures 2 and 3. Table I lists the physical properties and ultrasonic wave velocities.

Test results show that both mechanical and physical properties are similar to the rock matching grout (RMG 2C3) previously tested[1]. Maximum stress difference at 0.5 kbar confining pressure is 0.32 kbars for the triaxial compression test which is in good agreement with the stress difference during the uniaxial strain test. Permanent volume strain resulting from the uniaxial strain test is 0.7 percent by volume.

Physical property measurements show the grout batches to be totally saturated with similar densities and porosities.

Sincerely,

Don Gardiner

D. S. Gardiner
Project Engineer

DSG/jlg

---

1. TR 76-41, "Material Properties of Stanford Institute Grout, July 1976.

UNIVERSITY RESEARCH PARK · 420 WAKARA WAY · SALT LAKE CITY, UTAH 84108 · (801) 582-2220

TABLE I

Stanford Research Institute Rock Matching Grout

SAMPLE DESIGNATION	DENSITY (gm/cc)			WATER BY WET WEIGHT (%)	POROSITY (%)	SATURATION (%)	CALC. AIR VOIDS (%)	MEAS. PERMANENT COMP. (%)	VELOCITY (km/sec)	
	AS-RECEIVED	DRY	GRAIN						LONG	SHEAR
2C4-1A	2.15	1.76	2.90	18.1	39.4	98.9	0.5	---	3.30	1.82
2C4-2A	2.15	1.75	2.87	18.6	39.2	100.0	0	---	3.23	1.81
2C4-3A	2.18	1.79	2.88	17.7	37.7	100.0	0	---	3.28	1.82

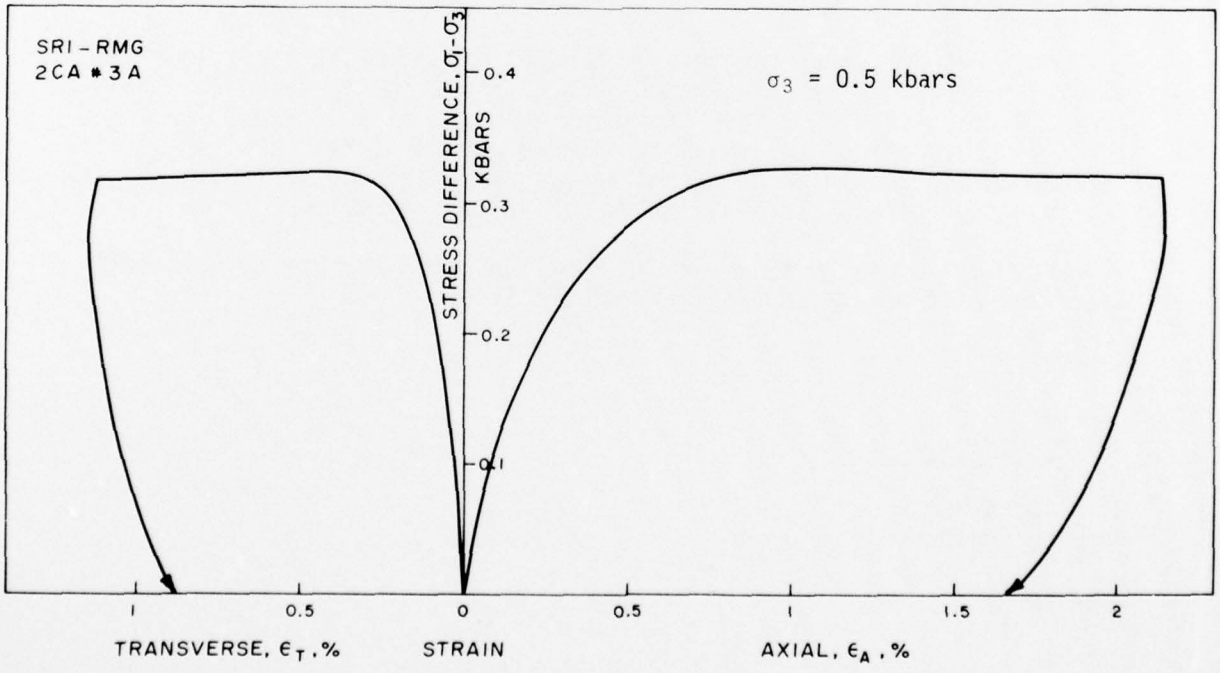


Figure 1. Triaxial compression test--stress difference versus individual strains.

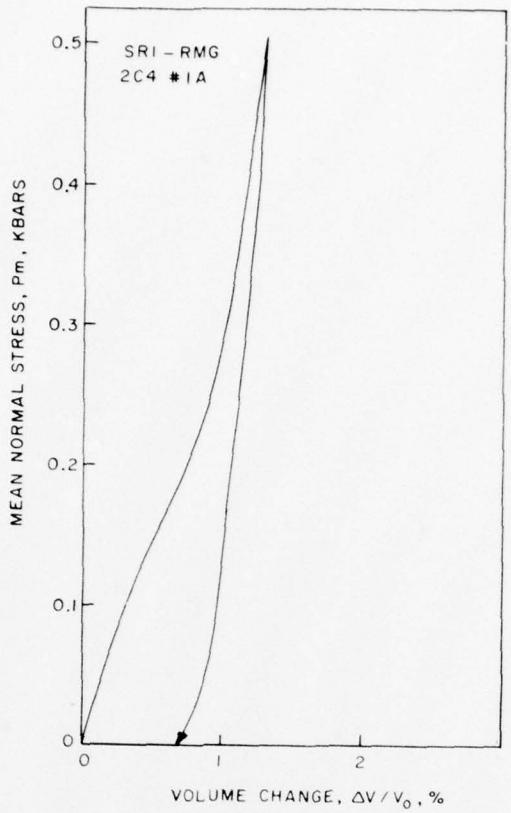


Figure 2. Uniaxial strain test--mean normal stress versus volume change.

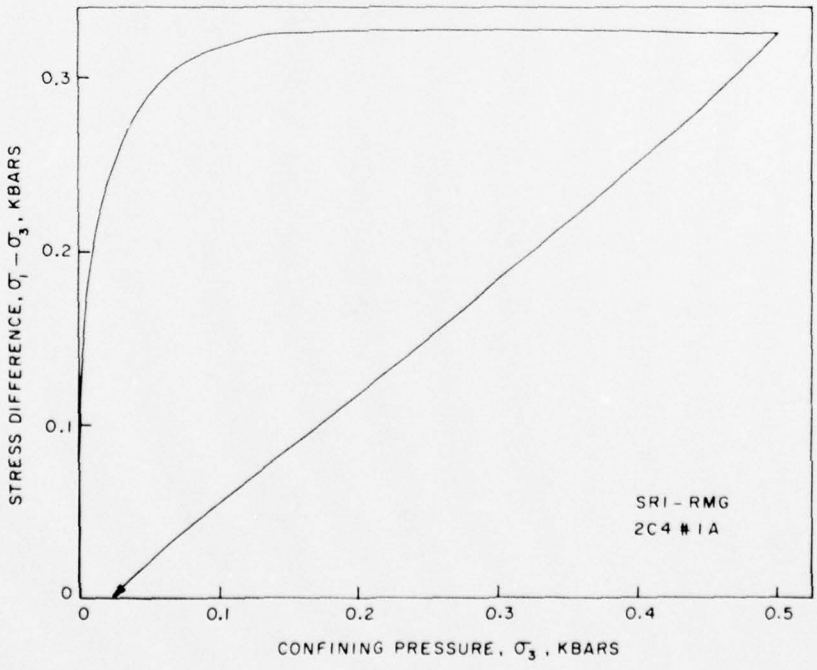


Figure 3. Uniaxial strain test--stress difference versus confining pressure.

DISTRIBUTION LIST

DEPARTMENT OF DEFENSE

Assistant to the Secretary of Defense
Atomic Energy
ATTN: Executive Assistant

Defense Documentation Center
Cameron Station
12 cy ATTN: TC

Defense Nuclear Agency
ATTN: DDST
ATTN: STSP
2 cy ATTN: SPTD
3 cy ATTN: SPSS
4 cy ATTN: TITL

Field Command, Defense Nuclear Agency
ATTN: FCTMO
ATTN: FCTMC, Dr. Ristvet
ATTN: FCT, G. Vavra
ATTN: FCTME, Major Johnson
ATTN: FCPR
10 cy ATTN: FCTMC, C. Keller
10 cy ATTN: FCTCE, J. LaComb

Livermore Division, Field Command, DNA
Lawrence Livermore Laboratory
ATTN: FCPRL
ATTN: Document Control

Weapons Systems Evaluation Group
ATTN: Technical Library

Under Sec. of Def. for Rsch. & Engrg.
ATTN: Strategic & Space Systems (OS)

DEPARTMENT OF THE ARMY

Deputy Chief of Staff for Rsch.
Development and Acquisition
ATTN: Nuclear Team

Explosive Excavation Research Lab.
ATTN: Document Control

Harry Diamond Laboratories
ATTN: DELHD-NP

U.S. Army Engineer Center
ATTN: ATSEN-SV-L

U.S. Army Engineer Waterways Experiment Station
ATTN: D. Day
ATTN: J. Zelasko
ATTN: W. Flathau
ATTN: L. Ingram
ATTN: P. Hadala
ATTN: J. Jackson
ATTN: J. Ehrgotz
ATTN: R. Bendinelli
ATTN: Library

DEPARTMENT OF THE NAVY

Office of Naval Research
ATTN: Technical Library

DEPARTMENT OF THE NAVY (Continued)

Naval Research Laboratory
ATTN: Code 1065

Civil Engineering Laboratory
Naval Construction Battalion Center
ATTN: J. Allgood
ATTN: Code L31

Naval Ordnance Station
ATTN: Code 121

Naval Surface Weapons Center
ATTN: F-30

DEPARTMENT OF THE AIR FORCE

AF Geophysics Laboratory, AFSC
ATTN: LWW, K. Thompson

AF Weapons Laboratory, AFSC
ATTN: DE-I
ATTN: DEV-G, J. Bratton
ATTN: DEV, M. Plamondon
ATTN: DEX
ATTN: SES, R. Henning
ATTN: SUL

DEPARTMENT OF ENERGY

Los Alamos Scientific Laboratory
ATTN: J. McQueen
ATTN: R. Sharp, Jr.
ATTN: A. Davis
ATTN: A. Cos
ATTN: R. Brownlee
ATTN: B. Killian
ATTN: L. Germain
ATTN: J. House
ATTN: Reports Library

Sandia Laboratories
ATTN: C. Gulick
ATTN: W. Vollendorf
ATTN: C. Broyles
ATTN: W. Weart

Department of Energy
Nevada Operations Office
ATTN: R. Newman
ATTN: Library

Lawrence Livermore Laboratory
ATTN: J. Hearst
ATTN: Mr. McKague
ATTN: H. Rodean
ATTN: V. Wheeler

OTHER GOVERNMENT AGENCIES

Bureau of Mines
Twin Cities Research Center
ATTN: T. Ricketts
ATTN: T. Atchison

PRECEDING PAGE BLANK-NOT FILMED

OTHER GOVERNMENT AGENCIES (Continued)

Department of Interior
Bureau of Mines
ATTN: L. Obert

Department of Interior
U.S. Geological Survey, Special Projects Center
ATTN: R. Carroll
ATTN: W. Twenhofel

DEPARTMENT OF DEFENSE CONTRACTORS

Agbabian Associates
ATTN: Document Control
ATTN: C. Bagge

Boeing Company
ATTN: K. Fridell

EG&G, Inc.
San Ramon Operations
ATTN: G. Preston

Engineering Decision Analysis Co., Inc.
ATTN: R. Kennedy

General Electric Company-TEMPO
Center for Advanced Studies
ATTN: DASIAC

H Tech Laboratories, Inc.
ATTN: B. Hartenbaum

Holmes and Narver, Inc.
ATTN: A. Patton
ATTN: F. Fuhriman

Ken O'Brien and Associates
ATTN: D. Donegan

Massachusetts Institute of Technology
ATTN: W. Brace

Merritt CASES, Inc.
ATTN: J. Merritt

Pacifica Technology
ATTN: D. Patch
ATTN: J. Kent

DEPARTMENT OF DEFENSE CONTRACTORS (Continued)

Physics International Company
ATTN: C. Vincent

R & D Associates
ATTN: C. Knowles
ATTN: R. Shaeffer

Reynolds Electrical and Engineering Co., Inc.
ATTN: W. Flangas

Shock Hydrodynamics, Inc.
ATTN: K. Kreyenhagen

SRI International
ATTN: A. Florence
ATTN: H. Lindberg

Systems, Science & Software, Inc.
ATTN: R. Duff
ATTN: D. Grine
ATTN: Document Control

Terra Tek, Inc.
ATTN: D. Gardiner
ATTN: D. Enniss
ATTN: S. Butters
ATTN: A. Jones
25 cy ATTN: S. Green

TRW Defense and Space Systems Group
ATTN: P. Lieberman
ATTN: P. Dai

University of Illinois
ATTN: N. Newmark

University of Michigan
ATTN: R. McLaughlin

University of Wisconsin
Milwaukee Dept. of Geological Services
ATTN: D. Willis

Weidlinger Associates
Consulting Engineers
ATTN: M. Baron